Universiteit
Leiden
The Netherlands

Experimental optical imaging during pancreatic cancer interventions

Manen, L. van

Citation
Manen, L. van. (2023, December 13). *Experimental optical imaging during pancreatic cancer interventions*. Retrieved from https://hdl.handle.net/1887/3672215

Version:	Publisher's Version
License:	Licence agreement concerning inclusion of doctoral thesis in the Institutional Repository of the University of Leiden
Downloaded from:	https://hdl.handle.net/1887/3672215

Note: To cite this publication please use the final published version (if applicable).

Experimental optical imaging during pancreatic cancer interventions

Labrinus van Manen

ISBN: 978-90-9037887-9

© L. van Manen 2023

All rights reserved. No parts of this thesis may be reproduced, distributed, stored in a retrieval system or transmitted in any form or by any means, without prior written permission of the author.

Cover design, lay-out and printing by Memorise Reclame en Marketing BV | www.memorise.nl

Financial support by Chipsoft B.V., Horlogerie van Manen, KARL STORZ Endoscopie Nederland B.V., Mobula-IGM B.V., MSB Gouda and Universitaire Bibliotheken Leiden for the printing of this thesis is gratefully acknowledged.

Experimental optical imaging during pancreatic cancer interventions

Proefschrift

ter verkrijging van
de graad van doctor aan de Universiteit Leiden,
op gezag van rector magnificus prof. dr. ir. H. Bijl,
volgens besluit van het college voor promoties
te verdedigen op woensdag 13 december 2023
klokke 16.15 uur

door

Labrinus van Manen
geboren te Veenendaal
in 1994

Promotor:	Prof. dr. J.F. Hamming
Co-promotores:	Dr. J. Dijkstra Dr. J.S.D. Mieog
Promotiecommissie:	Prof. dr. S. Hernot (Vrije Universiteit Brussel, België) Prof. dr. J.E. van Hooft Dr. S. Keereweer (Erasmus MC, Rotterdam) Prof. dr. S. Kruijff (UMCG, Groningen)

Voor Jan-Willem

TABLE OF CONTENTS

Chapter 1 General introduction and thesis outline 13

Part I: Biomarkers in pancreatic cancer

Chapter 2 Elevated CEA and CA19-9 serum levels independently predict advanced pancreatic cancer at diagnosis 23

Chapter 3 Stage-specific value of Carbohydrate Antigen 19-9 and Carcinoembryonic Antigen serum levels on survival and recurrence in pancreatic cancer: a single center study and meta-analysis 41

Part II: Exogenous contrast imaging in pancreatic cancer

Chapter 4 A practical guide for the use of indocyanine green and methylene blue in fluorescence guided abdominal surgery 63

Chapter 5 Intraoperative detection of the remnant cystic duct during robot-assisted surgery using near-infrared fluorescence imaging: a case report 93

Chapter 6 Latest developments in molecular tracers for fluorescence image-guided cancer surgery 101

Chapter 7 Near-infrared fluorescence imaging of pancreatic cancer using a fluorescently labelled anti-CEA nanobody probe: a preclinical study 125

Part III: Endogenous contrast imaging in pancreatic cancer

Chapter 8 The clinical usefulness of optical coherence tomography during cancer interventions 141

Chapter 9 Validation of full-field optical coherence tomography in distinguishing malignant and benign tissue in resected pancreatic cancer specimens 167

Chapter 10 Single fiber reflectance spectroscopy for pancreatic cancer detection during endoscopic ultrasound guided fine needle biopsy: a prospective cohort study 183

Chapter 11 Detection of cutaneous oxygen saturation using a novel snapshot hyperspectral camera: a feasibility study 197

Part IV: Summary and appendices

Chapter 12 Summary and discussion 213

Chapter 13 Nederlandse samenvatting 223

List of publications 227

Curriculum Vitae 229

Dankwoord 230

Chapter 1

General introduction and thesis outline

Pancreatic cancer

Pancreatic cancer is an aggressive cancer associated with a poor prognosis as approximately 80% of the patients have either locally advanced disease or metastatic spread at the time of diagnosis.[1] Compared to other cancer types, the incidence of pancreatic cancer is still increasing, whereas the survival has not significantly been improved the last decades, despite the advances in treatment i.e. new chemotherapeutic agents, immunotherapy and/or radiotherapy. This will result in an increase of projected pancreatic-cancer-related deaths in the future (Figure 1). Currently only patients with localized pancreatic tumors can undergo surgery, which is the cornerstone in the treatment of pancreatic cancer, whether or not preceded by neoadjuvant (chemo/radio)therapy. Recently neoadjuvant chemoradiotherapy using gemcitabine, followed by surgery and adjuvant chemotherapy could improve the survival of a patient with localized pancreatic cancer compared, compared to upfront surgery and adjuvant chemotherapy.[2]

Current challenges

The diagnostic work-up of a patient with pancreatic cancer consists of preoperative staging using dedicated imaging techniques, of which Computed tomography (CT) is currently the predominant imaging modality. Additional diagnostics include biomarker testing, Magnetic Resonance Imaging (MRI), Positron Emission Tomography CT, and acquiring histology by either endoscopic ultrasound-guided fine needle aspiration (EUS-FNA), endoscopic retrograde cholangiopancreatography (ERCP), or sometimes using a diagnostic laparoscopy.[3] Tumor markers, such as cancer antigen 19-9 (CA19-9) and carcinoembryonic antigen (CEA) can be used to predict biological behavior of pancreatic cancer.[4] Strong associations between serum values and resectability, prognosis and/or disease recurrence are reported, however clinical guidelines on how to interpret serum values are still disputable. In the diagnostic work-up, EUS-FNA plays an important role to obtain histology and confirm the diagnosis. It is nowadays routinely performed and has a diagnostic accuracy up to 95%, although it has certain limitations, such as multiple tissue punctures and the need for rapid onsite evaluation.[5] Therefore, the introduction of fine needle biopsy (FNB), that is capable to acquire tissue cores using special designed needles, has shown improvement in the diagnostic accuracy compared to EUS-FNA.[6] Nevertheless, in case of severe surrounding pancreatitis, it is still difficult to acquire tissue with viable tumor cells, confirming the suspected diagnosis.[7,8]

Intraoperatively, the pancreatic surgeon has to deal with certain challenges, such as adequate intraoperative judgement of the extent of the tumor and/or detection of metastases, of which the last is currently considered as contraindication for resection. The presence of peritumoral inflammation or tissue fibrosis after neoadjuvant therapy makes the distinction with cancerous tissue even more challenging.[9] Currently, no intraoperative imaging techniques have been proven to add significant value, which means that the surgeon has to rely on visual inspection and palpation, of which the latter is only possible during open surgery. The patients' prognosis after surgery mainly depends on the completeness of surgical resection. Currently, pancreatic surgeons perform high-risk surgeries (5% mortality; 50% major complications), resulting in up to 75% irradical resections, which certainly demonstrates that the field of pancreatic surgery should make a major step forward.[10]

Clinical implementation of novel imaging modalities which are quantitative, comprehensive, standardized, sensitive, having a high resolution and having minimal interference in the clinical workflow, could be of outmost importance during both the diagnostic workup and intraoperatively, in order to improve the care of pancreatic cancer patients.[11]

Optical imaging techniques

In the past years, novel intraoperative optical techniques have been assessed for several applications. An overview of image-guided surgery modalities (conventional *vs* novel optical techniques described in this thesis) are represented in Figure 2.[12] Advantages of optical techniques are detection of smaller lesions, providing direct feedback and most of them could be directly related to the surgical field of view. Nevertheless, optical imaging techniques have also limitations, such as limited penetration depth due to scattering and absorption of photons.[13]

Humans are able to detect light in the visual light spectrum (400-750 nm) with a high resolution, although they are not able to differentiate between spectra with a small separation in wavelengths. During surgery it is difficult for oncologic surgeons to distinguish tumor tissue from surrounding inflammatory tissue, as both tissues have the same color. Near infrared (NIR) light (750-1000 nm) has the advantage of deeper tissue penetration and less disturbing autofluorescence signals (i.e. scattering, absorption) compared to visible light, making this a more optimal window for optical imaging.[14] However, for detection of NIR light specialized detectors are necessary. By illuminating tissue with light at fixed wavelengths or wavelength bands one can detect the reflection at certain wavelengths, which can provide information about the tissue composition on molecular level, which cannot be detected by the human eye. Besides imaging based on endogenous reflectance, one can also use exogenous contrast agents (fluorescent probes) to improve signal-to-noise ratios. The optical techniques evaluated in this thesis are in brief described below.

Near-infrared fluorescence imaging

Near-infrared fluorescence (NIRF) imaging or sometimes called fluorescence-guided surgery is a technique based on imaging in the NIR window of the electromagnetic spectrum. It requires an imaging system that is able to excite (using laser or light-emitting diodes) and detect the emitted fluorescence of the administrated NIR fluorophore. NIR fluorophores could be administration either intravenously, topically, or surrounding the tumor in order to visualize the target tissue.[15] With the recent introduction of targeted fluorescent tracers, by conjugating a NIR fluorophore to a targeting molecule (monoclonal antibody, antibody fragments, protein scaffolds, peptides or small molecules), tissues of interest could be visualized more specifically. After tracer administration, the targeted cells, most often cancer cells, will light up, whereas the background fluorescence will become significantly less once the unbound tracer has been cleared by either the kidneys and/or liver.

Optical coherence tomography

Optical coherence tomography (OCT), which is often denoted as the optical analog of ultrasonography, is a technique that uses the interference of light to generate two-dimensional

cross-sectional images.[16] However, compared to ultrasound, it detects back-reflected light, instead of sound, from tissues. OCT can be used to image minimal-invasively and without the need for tissue preparation, thereby providing microscopic images of tissue architecture comparable to low-resolution histology images. To provide higher resolution imaging, focusing on cellular details, high definition OCT (HD-OCT) and full-field OCT (FF-OCT) have been developed, however, its current application is limited to *ex vivo* imaging, due to the longer acquisition times.

Reflectance spectroscopy

Using reflectance spectroscopy one can measure the light reflected from the tissue after scattering and absorption by tissue chromophores in a very small tissue volume. It requires a spectrophotometer to measure the white light reflectance, a light source and one or more optical fibers that are being used for the contact measurements. This technique has the advantage to acquire a complete spectral fingerprint at the point of contact, thereby providing real-time quantitative information on the tissue pathophysiology.[17]

Hyperspectral imaging

Hyperspectral imaging is an optical technology allowing the imaging of an object with full spectral resolution (wavelengths dependent on the used camera sensors) noninvasively and without the need to contact the tissue in contrast to for instance reflectance spectroscopy and OCT. A hyperspectral camera device detects the remaining spectrum of light reflected from tissues after it has been scattered and absorbed by tissue chromophores, such as haemoglobin, fat, melanin or water illuminated with a full spectrum light source. Therefore it provides a complete spectral fingerprint of the tissue at pixel level, which contains important quantitative diagnostic information about tissue pathophysiology.[18] In the last years, advances in costs, hyperspectral camera quality, image analysis methods, and computational power enabling application of this technique in the medical field.

Thesis outline

A schematic overview of this thesis has been illustrated in Figure 4.

Part I discusses the clinical implications of the biomarkers CA19-9 and CEA in patients with pancreatic cancer. **Chapter 2** describes the diagnostic accuracy of these biomarkers for prediction of advanced PDAC and proposes implementation of CEA and CA19-9 serum levels as additional tools for establishing tumor resectability during multidisciplinary team meetings. **Chapter 3** analyses the prognostic value of CA19-9 and CEA as tumor markers for survival and recurrence in PDAC patients in a retrospective cohort study and additionally these findings were compared with existing literature.

Part II focusses on optical imaging of pancreatic cancer using exogenous contrast agents for intraoperative imaging in the near-infrared (NIR) region. **Chapter 4** provides a practical guide on NIR fluorescence imaging using non-targeted fluorophores during abdominal surgery. **Chapter 5** shows an example of successful intraoperative visualization of bile duct anatomy and illustrates

that NIR fluorescence imaging using ICG during difficult robot-assisted surgical procedures of the bile ducts is effective and therefore highly recommended. **Chapter 6** discusses the preclinical evidence, ongoing clinical trials and the latest developments in the field of molecular NIR tracers for fluorescence-guided cancer surgery. In **Chapter 7** a CEA-targeted nanobody conjugated to the zwitterionic dye ZW800-1 has been preclinically evaluated for intraoperative visualization of pancreatic cancer.

Part III outlines optical imaging of pancreatic cancer using endogenous contrast agents. **Chapter 8** provides an overview on the clinical usefulness of optical coherence tomography (OCT) during cancer interventions. In **Chapter 9** the use of high resolution (Full-Field) OCT is described for distinguishing malignant from benign pancreatic tissue in resected specimens, showing its potential for intraoperative frozen section analysis. **Chapter 10** contains the results of a prospective cohort study, which evaluates the diagnostic accuracy of single fiber reflectance spectroscopy during EUS of the pancreas for detection of PDAC. **Chapter 11** discusses the first in-human study of a novel hyperspectral snapshot camera system for detection of intraoperative oxygen tissue saturation, paving the way for future studies and implementation during pancreatic surgery.

Part IV provides a summary of this thesis and discusses future work in the field of optical pancreatic cancer imaging using exogenous and endogenous contrast agents in both diagnostics and intraoperative imaging.

Figure 1. Projected cancer deaths of the most prevalent malignancies in the USA. Reprinted from Rahib et al. [19]

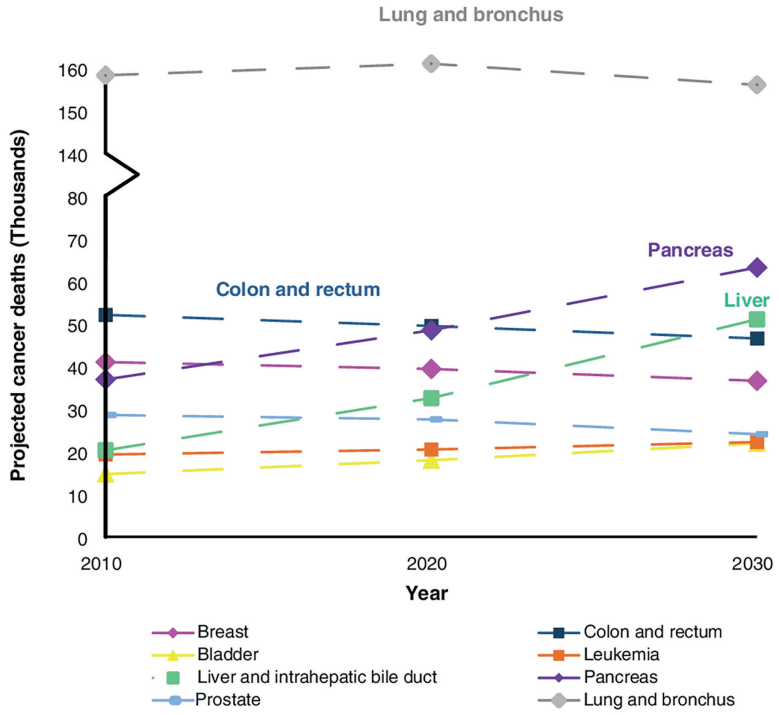

Figure 2. Overview on image-guided surgery modalities. Adapted from Stammes et al.[12] Abbreviations: (FF-)OCT: (full field-)optical coherence tomography; RS: raman spectroscopy; HSI: hyperspectral imaging; FGS: fluorescence-guided surgery; ioUS: intraoperative ultrasound; iCT: intraoperative computed tomography; iMRI: intraoperative magnetic resonance imaging.

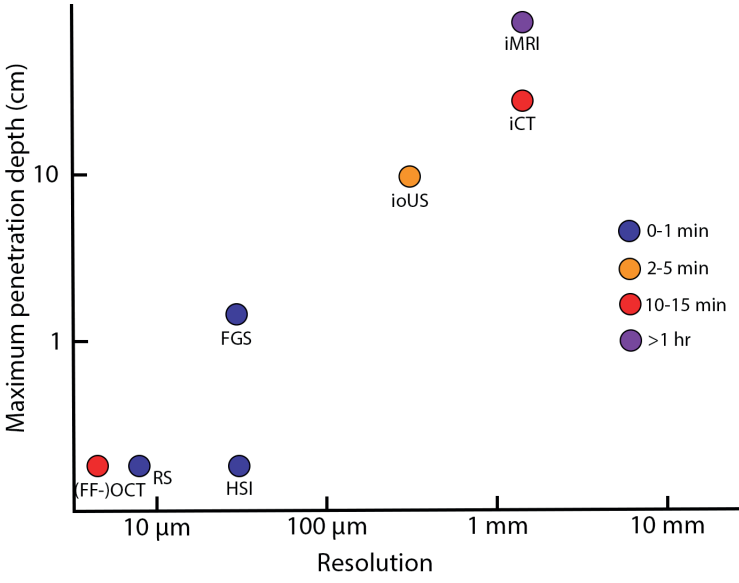

Figure 3. Optical imaging related to the electromagnetic spectrum. Reprinted from de Boer et al. [14]

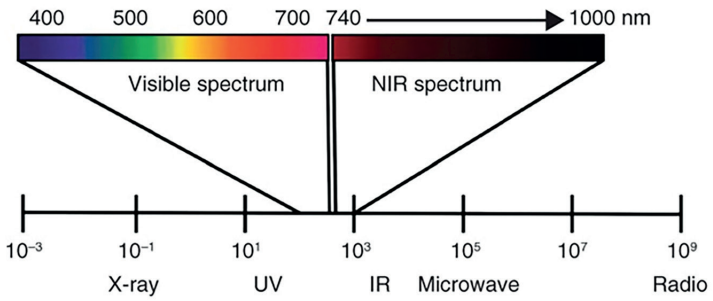

Figure 4. Thesis outline in brief.

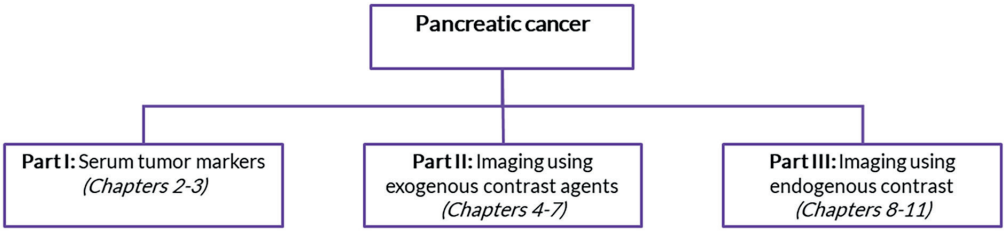

References

1. Ducreux M, Cuhna AS, Caramella C, et al. Cancer of the pancreas: ESMO Clinical Practice Guidelines for diagnosis, treatment and follow-up. Ann Oncol. 2015;26 Suppl 5:v56-68.
2. Versteijne E, van Dam JL, Suker M, et al. Neoadjuvant Chemoradiotherapy Versus Upfront Surgery for Resectable and Borderline Resectable Pancreatic Cancer: Long-Term Results of the Dutch Randomized PREOPANC Trial. J Clin Oncol. 2022;40(11):1220-1230.
3. Wood LD, Canto MI, Jaffee EM, Simeone DM. Pancreatic Cancer: Pathogenesis, Screening, Diagnosis and Treatment. Gastroenterology. 2022.
4. Rückert F, Pilarsky C, Grützmann R. Serum tumor markers in pancreatic cancer-recent discoveries. Cancers (Basel). 2010;2(2):1107-1124.
5. van Riet PA, Erler NS, Bruno MJ, Cahen DL. Comparison of fine-needle aspiration and fine-needle biopsy devices for endoscopic ultrasound-guided sampling of solid lesions: a systemic review and meta-analysis. Endoscopy. 2021;53(4):411-423.
6. Rimbaş M, Crino SF, Gasbarrini A, Costamagna G, Scarpa A, Larghi A. EUS-guided fine-needle tissue acquisition for solid pancreatic lesions: Finally moving from fine-needle aspiration to fine-needle biopsy? Endosc Ultrasound. 2018;7(3):137-140.
7. Grassia R, Imperatore N, Capone P, et al. EUS-guided tissue acquisition in chronic pancreatitis: Differential diagnosis between pancreatic cancer and pseudotumoral masses using EUS-FNA or core biopsy. Endosc Ultrasound. 2020;9(2):122-129.
8. Varadarajulu S, Tamhane A, Eloubeidi MA. Yield of EUS-guided FNA of pancreatic masses in the presence or the absence of chronic pancreatitis. Gastrointest Endosc. 2005;62(5):728-736; quiz 751, 753.
9. van Veldhuisen E, van den Oord C, Brada LJ, et al. Locally Advanced Pancreatic Cancer: Work-Up, Staging, and Local Intervention Strategies. Cancers (Basel). 2019;11(7).
10. Kim KS, Kwon J, Kim K, Chie EK. Impact of Resection Margin Distance on Survival of Pancreatic Cancer: A Systematic Review and Meta-Analysis. Cancer Res Treat. 2017;49(3):824-833.
11. Weissleder R, Pittet MJ. Imaging in the era of molecular oncology. Nature. 2008;452(7187):580-589.
12. Stammes MA, Bugby SL, Porta T, et al. Modalities for image- and molecular-guided cancer surgery. Br J Surg. 2018;105(2):e69-e83.
13. Rosenthal EL, Warram JM, Bland KI, Zinn KR. The status of contemporary image-guided modalities in oncologic surgery. Ann Surg. 2015;261(1):46-55.
14. de Boer E, Harlaar NJ, Taruttis A, et al. Optical innovations in surgery. Br J Surg. 2015;102(2):e56-72.
15. Vahrmeijer AL, Hutteman M, van der Vorst JR, van de Velde CJ, Frangioni JV. Image-guided cancer surgery using near-infrared fluorescence. Nat Rev Clin Oncol. 2013;10(9):507-518.
16. Huang D, Swanson EA, Lin CP, et al. Optical coherence tomography. Science. 1991;254(5035):1178-1181.
17. Middelburg TA, Hoy CL, Neumann HA, Amelink A, Robinson DJ. Correction for tissue optical properties enables quantitative skin fluorescence measurements using multi-diameter single fiber reflectance spectroscopy. J Dermatol Sci. 2015;79(1):64-73.
18. Lu G, Fei B. Medical hyperspectral imaging: a review. J Biomed Opt. 2014;19(1):10901.
19. Rahib L, Wehner MR, Matrisian LM, Nead KT. Estimated Projection of US Cancer Incidence and Death to 2040. JAMA Netw Open. 2021;4(4):e214708.

Part I

Chapter 2

Elevated CEA and CA19-9 serum levels independently predict advanced pancreatic cancer at diagnosis

L. van Manen, J.V. Groen, H. Putter, A.L. Vahrmeijer,
R.J. Swijnenburg, B.A. Bonsing, J.S.D. Mieog

Biomarkers. 2020 Feb 13:1-8.

Abstract

Purpose

It is suggested that tumor markers carcinoembryonic antigen (CEA) and carbohydrate antigen 19-9 (CA19-9) could be used to predict stage of pancreatic cancer. However, optimal cut-off values for CEA and CA19-9 are still disputable. This study aimed to assess the value of CEA and CA19-9 serum levels at diagnosis of pancreatic ductal adenocarcinoma (PDAC) as predictors for advanced stage of PDAC in patients discussed at pancreatic multidisciplinary team (MDT) meetings.

Methods

Patients with PDAC discussed at MDT meetings from 2013 through 2017 were reviewed, in order to determine optimal cut-off values of both CEA and CA19-9.

Results

In total, 375 patients were included. Optimal cut-off values for predicting advanced PDAC were 7.0 ng/ml for CEA and 305.0 U/ml for CA19-9, resulting in positive predictive values of 83.3%, 73.6%, and 91.4% for CEA, CA19-9 and combined, respectively. Both tumor markers were independent predictors of advanced PDAC, demonstrated by an odds ratio of 4.21 (95%CI: 1.85-9.56; P=0.001) for CEA and 2.58 for CA19-9 (95%CI: 1.30-5.14; P=0.007).

Conclusion

CEA appears to be a more robust predictor of advanced PDAC than CA19-9. Implementing CEA and CA19-9 serum levels during MDT meetings as additional tool for establishing tumor resectability is worthwhile for tailored diagnostics.

Introduction

Pancreatic ductal adenocarcinoma (PDAC) is one of the leading causes of cancer-related death.[1] Most patients present with metastatic disease, and a minority (20-25%) presents with localized disease eligible for curative-intended surgery.[2] Computed tomography (CT) is currently the predominant imaging modality for diagnosis and preoperative staging of PDAC. Additional diagnostics include Magnetic Resonance Imaging (MRI), Positron Emission Tomography, endoscopic ultrasound-guided fine needle aspiration and diagnostic laparoscopy.[3] However even with currently available predominant imaging modalities, in 12-18% of surgical explorations, a resection cannot be performed due to unexpected locally advanced disease or occult metastases. The high rate of this futile explorations, which have an associated morbidity up to 30% and a hospital mortality of 2% in open setting, highlights the importance of correct preoperative staging in PDAC.[4,5]

It is suggested that serum tumor markers could be used in clinical practice as an additional tool for screening, tumor staging, prediction of prognosis and even surveillance of treatment in several cancer types.[6-8] Carcinoembryonic antigen (CEA) and carbohydrate antigen 19-9 (CA19-9) are the most studied serum biomarkers for establishing both diagnosis and prognosis in pancreatic cancer patients.[9,10] The role of CEA and CA19-9 in predicting advanced PDAC, defined here as either metastatic or locally advanced PDAC, has scarcely been studied and only performed in patients undergoing surgical exploration.[11,12] To our knowledge, no reports are available about the role of CEA and CA19-9 in preoperative multidisciplinary decision making.

We hypothesized that CEA and CA19-9 serum levels at diagnosis are valuable tools for the prediction of advanced PDAC. This study aimed to assess the value of CEA and CA19-9 serum levels at diagnosis as predictors for advanced PDAC in patients discussed at the pancreatic multidisciplinary team (MDT) meetings in a tertiary referral center.

Patients and Methods

Patient selection

Four hundred twenty consecutive patients with PDAC were discussed at the pancreatic MDT meetings from January 2013 through December 2017 at the Leiden University Medical Center, a tertiary referral center for pancreatic cancer patients, were retrospectively reviewed. Patients with diagnoses other than primary PDAC were excluded from the analyses. The diagnosis of PDAC was confirmed either after analysing of tumor tissue acquired during endoscopic ultrasound-guided fine needle aspiration, endoscopic retrograde cholangiopancreatography, direct biopsy of a target lesion, the resected specimen or in case there was no suspicion of another pathology on preoperative imaging. Forty-five patients with resectable disease, who did not want to undergo surgery or were unfit for surgery (as decided by the MDT) were excluded from the analyses, because resectability could not be proven by surgical exploration. One hundred sixty-one patients were excluded from analyses involving CEA and CA19-9 serum levels (Figure 1). Approval of the local Medical Research and Ethical Committee was obtained for this retrospective cohort study.

Definitions

Laboratory findings (CEA, CA19-9, and total bilirubin) were defined as the last measured value before a MDT meeting. At MDT meetings at least one medical specialist of the following departments were present: Medical Oncology, Radiology, Hepatopancreaticobiliary Surgery, Gastroenterology and Pathology. All patients underwent CT or MRI scanning in order to assess the resectability of the tumor. Tumor size was determined as the largest diameter in the transversal direction on preoperative CT or MRI. Preoperative staging of PDAC was performed according to the American Joint Committee on Cancer (AJCC; 7th edition).[13] Advanced PDAC was defined as either locally advanced pancreatic cancer (LAPC) or presence of distant metastases (M+). According to the guidelines of the Dutch Pancreatic Cancer Group (DPCG, 2012), the following criteria were applicable for LAPC:

(1) Tumor abutment of the superior mesenteric artery, celiac axis or common hepatic artery >90° of the circumference of the vessel wall.

(2) Tumor involvement of the superior mesenteric vein/portal vein vessel wall resulting in occlusion or > 270° contact.

Overall survival was calculated from the date of the first suspicion of pancreatic cancer on CT or MRI to the date of death (event) or last follow-up (censored).

Statistical analysis

First, patient- and tumor characteristics were compared between the preoperatively advanced PDAC group (determined during MDT meetings), the intraoperatively advanced PDAC group (determined during explorative surgery) and the resected group (underwent resection). Continuous variables are presented as mean (standard deviation [SD]) in normal distributed data or median (interquartile range [IQR]) in non-normal distributed data. Categorical variables are presented as absolute numbers and percentages. Chi Squared test, One-Way ANOVA, and Kruskal-Wallis test were used to compare the patients -and tumor characteristics. A Kaplan-Meier curve was used to determine the median survival. Second, the predictive value of CEA and CA19-9 serum levels at diagnosis for advanced PDAC was evaluated by comparing the advanced PDAC group (preoperatively and intraoperatively) with the resected group. Subgroup analyses were performed to investigate if serum CEA and CA19-9 levels can differentiate between patients with LAPC, M+ or both (LAPC & M+). Receiver-operating characteristic (ROC) curve analyses and the Youden-Index were used to determine the optimal cut-off values for CEA and CA19-9, after which the sensitivity, specificity, positive predictive value (PPV), and negative predictive value (NPV) were calculated using the cut-off values. Lastly, a multivariable logistic regression analysis using clinically relevant parameters and the optimal cut-off values, was carried out to assess the independence of CEA and CA19-9 as predictors of advanced PDAC. Statistical analysis was performed using IBM SPSS Statistics for Windows, version 23.0 (IBM Corp., Armonk, N.Y., USA). A P-value below 0.05 (two-sided) was considered as statistically significant.

Results

Patient characteristics

Patient and tumor characteristics are summarized in Table 1. Out of the included 375 PDAC patients, 151 (40%) patients underwent resection, 68 (18%) patients were intraoperatively classified as advanced PDAC and 156 (42%) patients were classified as preoperatively advanced PDAC. The mean (SD) tumor size differed significantly (P<0.001) between the groups: 28.3 (12.8) mm in the resected group, 37.8 (17.5) mm in the intraoperative advanced PDAC group and 40.3 (17.5) mm in the preoperative advanced PDAC group. Overall survival differed significantly (P<0.001) between the three patient groups: median (95% CI) survival was 4.0 (3.3-4.8) months in the preoperative advanced PDAC group, 6.0 (4.5-7.5) months in the intraoperative advanced PDAC group and 20 (16.8-23.2) months in the resected group. The median (IQR) CEA serum level differed significantly (P<0.001) between the groups with the lowest level in the resected PDAC group (3.2; 2.0-4.8) compared to the intraoperative advanced (6.1; 3.2-21.7) and preoperative advanced PDAC group (5.1; 2.6-12.4). The median (IQR) CA19-9 serum level also differed significantly (P<0.001) between the resected group (153.0; 30.5-520.8), intraoperative advanced PDAC group (260.1; 71.3-819.7) and preoperative advanced PDAC group (458.0; 107.4-1948.0).

Determination of optimal cut-off value of CEA and CA19-9

No significant difference in CEA and CA19-9 serum levels were detected between the LAPC, M+ and LAPC & M+ group (CEA: P=0.562; CA19-9: P=0.177). Median (IQR) CEA and CA19-9 levels were 5.2 (2.7-12.0) and 367.1 (79.6-1149.0) for the LAPC group, 6.0 (3.2-24.7) and 320.4 (128.8-1215.0) for the M+ group and 5.6 (2.6-14.6) and 528.0 (180.0-3033.0) for LAPC & M+ group. Serum CEA and CA19-9 levels differed significantly between the resected and advanced PDAC patients, with an Area Under the Curve of 0.66 (95% CI: 0.59-0.74; P<0.001) for CEA and 0.68 (95% CI: 0.60-0.75; P<0.001) for CA19-9 (Figure 2). The optimal cut-off value, calculated using the Youden-Index, was 7.0 ng/ml for CEA and 305.0 U/ml for CA19-9. A CEA>7.0 ng/ml had a PPV of 83.3% and a CA19-9>305.0 U/ml had a PPV of 73.6% for presence of advanced PDAC (Table 2). The distribution of CEA and CA19-9 serum levels at diagnosis and the percentages of patients above and under the optimal cut-off values are illustrated in a boxplot (Figure 3). Diagnostic accuracy was calculated for other clinically relevant cut-off values for CEA and CA19-9 (Table S1). Furthermore, optimal cut-off values for CEA and CA19-9 serum levels were applied in the subgroups (LAPC, M+ and combined), of which the distribution per group is depicted in Figure S1.

Combined value of CEA and CA19-9 levels

Combining both optimal cut-off values yielded a 91.4% PPV for prediction of advanced PDAC (Table 2). Resection rates in the four groups were 7.9% (both elevated), 29.6% (solely elevated CEA), 36.8% (solely elevated CA19-9), and 62.0% (both not elevated). Other relevant combinations of cut-off values for CEA and CA19-9 are added in Table S1.

Multivariable analysis of predictive factors

At multivariable analysis, elevated CEA and CA19-9, female sex, age, tumor size increment were independent predictive factors for advanced PDAC (Table 3). CEA>7.0 ng/ml showed a higher odds ratio (OR) (OR: 4.18; 95% CI: 1.83-9.56; P=0.001) than CA19-9> 305.0 U/ml (OR: 2.66; 95%CI: 1.33-5.33; P=0.006).

Discussion

The aim of this study was to evaluate the value of CEA and CA19-9 serum levels in predicting advanced PDAC in patients discussed at MDT meetings. Median CEA and CA19-9 differed significantly between the resected, intraoperative advanced PDAC and preoperative advanced PDAC patient groups (P<0.001). The optimal cut-off values for predicting advanced PDAC were 7.0 ng/ml for CEA and 305.0 U/ml for CA19-9, resulting in a positive predictive value of 83.3%, 73.6%, and 91.4% for elevated CEA, CA19-9 and combined, respectively. Both tumor markers were independent predictors of advanced PDAC, however the numerical difference between CEA (OR: 4.18) and CA19-9 (OR: 2.66) could indicate that CEA appears to be a more robust factor.

Previous studies showed optimal cut-off values of CA19-9 varying between 92.77 U/ml and 353.15 U/ml, resulting in PPV varying from 79% to 95% for advanced PDAC during staging laparoscopy or laparotomy as recently reviewed by De Rosa et al.[11] Hartwig et al. reported the predictive value for resectability and survival of CA19-9 levels in 1543 patients.[14] They reported resection rates below 70% in case of preoperative CA19-9 levels >500 U/ml, which is therefore included in the definition of borderline resectable PDAC as a biological factor.[15]

Schlieman et al. valuated the role of CEA as a predictor of resectability and found no significant difference in preoperative CEA levels between the resected and non-resected group.[16] Most studies used a combination of CEA and CA19-9 levels to determine the prognosis [17-22], however, two studies evaluated a combination of those two tumor markers for prediction of resectability. [12,23] Fujioka et al. combined CEA and CA19-9 levels, yielding a NPV for resectability of 88% in 244 patients by using 5.5 ng/ml as optimal cut-off value for CEA and 157 U/ml for CA19-9.[12] Remarkably, CA19-9 was only associated with presence of metastases (both liver and peritoneal) and not significantly associated with LAPC, whereas CEA was associated with LAPC and presence of liver metastases. However, no comparison was made between median CEA and CA19-9 serum levels in LAPC and the metastasized patient group. Kim et al. demonstrated a 86.6% NPV for resectability after combining optimal cut-off values for CEA (2.47 ng/ml) and CA19-9 (92.77 U/ml) levels.[23] The large variety of optimal cut-off values could be explained by the difference in definition of (ir)resectability, the racial diversity and size of the study population. Our study included all patients discussed at MDT-meetings, which makes comparison with current literature somewhat complicated; but is clinically more relevant. Nevertheless, our cut-off values for CEA and CA19-9 were substantially higher, resulting in much higher prediction values and lower resection rates.

This study has several limitations. The tumor markers CEA and CA19-9 were not measured in all patients. In patients who did not undergo surgical exploration CEA and CA19-9 levels were less often measured. In addition, our study included all PDAC patients discussed at MDT meetings, were other studies included solely patient who underwent surgical exploration, which states the need for external validation of the optimal cut-off values in a prospective cohort study. Sixty percent of the patients discussed at our MDT meetings, underwent surgical exploration, which is significantly higher than the national average (27%).[24] This could be explained by the fact that our hospital is a tertiary referral center; patients diagnosed in other centers, who do not want further diagnostics or treatment are simply not referred to our center.

It has been shown that biliary obstruction could disturb the CA19-9 serum levels, however, after correction for biliary serum levels, CA19-9 remained an independent predictor. Another factor influencing the CA19-9 level, is the absence of a Lewis antigen, which is the case in approximately 4-7% of the population.[25,26] CA19-9 is not expressed in patients missing the Lewis antigen, even in the presence of tumors. Although we did not asses the Lewis antigen in our study, it exemplifies that CA19-9 serum levels should always be interpreted with caution. Moreover, CA19-9 is also associated with many other cancers, such as gastric or colorectal cancer.[27,28] We hypothesized that CEA is associated with tumor size because CEA is shedded into blood from tumor cells. However, in this study an increased CEA remains an independent predictor of advanced PDAC, even after correction for tumor size. Although, CEA serum levels can also be increased in colorectal cancer or metastases, lung cancer or metastases, and nicotine abuses, which illustrates its non-specificity for pancreatic tumors.[29]

Besides CEA and CA19-9, several other promising serum markers for PDAC have been reported the last years. Most studies focused on the capability of tumor marker to detect PDAC and therefore its potential for screening purposes.[30-32] For instance, carbohydrate antigen variants, such as CA242, showed good potential for early pancreatic cancer detection.[33] Moreover, it was shown that another variant, CA125, had superior detection rates for irresectable disease in a cohort of 212 patients[34], although its application is limited because a substantial proportion of patients with pancreatitis and jaundice also have increased serum CA125 levels.[32] During last years, more research is spent on microRNA detection in serum and exosomes in order to detect pancreatic tumors in early stage with promising results and high diagnostic accuracies.[35,36] Further studies should be performed to evaluate the most sensitive microRNA markers and role of these markers in prediction of advanced stage, i.e. irresectable, pancreatic cancer.

Clinical implications of our findings might be that specific patient groups need an intensified diagnostic multi-modality approach. In general, increased CEA and CA19-9 levels resulted in a high chance (91.4% PPV) of having advanced PDAC. Subgroup analysis showed that CEA and CA19-9 levels did not differ significantly between the LAPC, M+ and LAPC & M+ groups. This indicates that patients with increased CEA and CA19-9 levels should undergo meticulous preoperative staging focusing on both locoregional status and detection of distant metastases (Figure S1). MRI for example, could be used for preoperative detection of small (liver) metastases as it is more sensitive than CT, which is most commonly used.[37-40] Furthermore, diverse combinations of cut-off values and corresponding chances on having advanced disease are calculated based on our cohort, which could guide the MDT in the treatment process (Table S1). Although, it does not implicate that in case of elevated CEA and CA19-9 levels the MDT should not consider surgical treatment. In this situation we recommend a staging or diagnostic laparoscopy before performing laparotomy, which is cost-effective and therefore the current standard of care in our and some other centers.[41,42] Moreover, additional intraoperative imaging modalities (e.g. laparoscopic ultrasound or near-infrared fluorescence imaging) should also be considered in this patient category. Preliminary results showed that CEA-targeting near-infrared fluorescence imaging is promising for intraoperative evaluation of locoregional status and detection of distant metastases and further studies defining clinical benefit are ongoing.[43,44]

Conclusion

The results of this study showed that CEA and CA19-9 are independent prediction factors for presence of advanced PDAC at diagnosis. Although CEA appears to be a more robust factor for prediction of advanced PDAC in our study, combining CEA and CA19-9 cut-off values enhances the positive predictive value, which indicates that implementing these levels during MDT meetings could be worthwhile for tailored diagnostics.

Figure 1. Study flow chart of patient inclusion. *Abbreviations: CEA: carcinoembryonic antigen; CA19-9: carbohydrate antigen 19-9; PDAC: pancreatic ductal adenocarcinoma.*

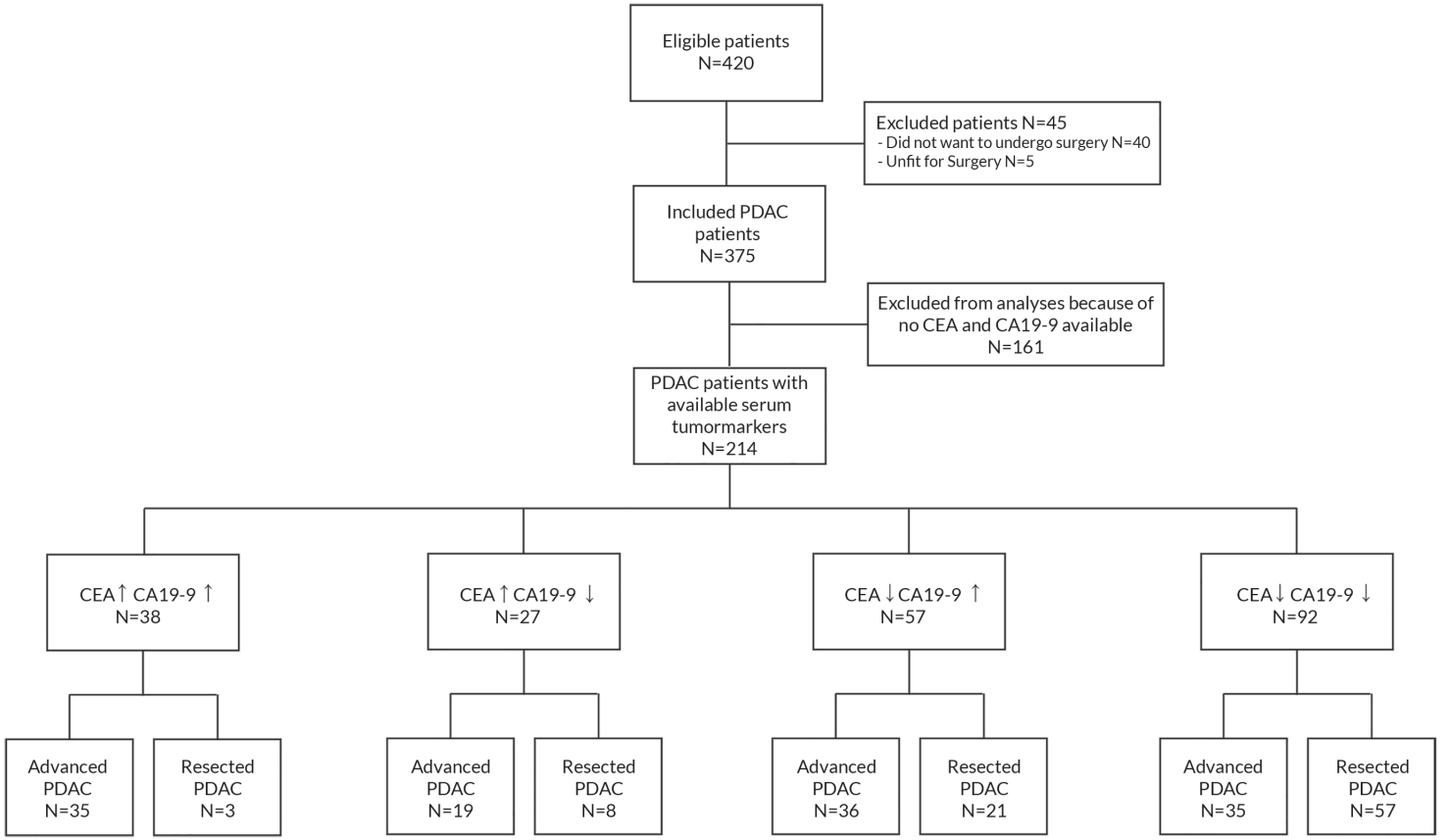

Table 1. Patient and tumor characteristics of patients discussed at the multidisciplinary team meetings.

	Resected (N=151)	Intraoperative advanced PDAC (N=68)	Preoperative advanced PDAC (N=156)	P
Age (y), *mean (SD)*	64.8 (9.6)	66.2 (9.6)	67.9 (9.8)	0.019
Sex, n (%)				0.328
Male	80 (53.0)	31 (45.6)	88 (56.1)	
Female	71 (47.0)	37 (54.4)	68 (43.6)	
ASA score, *n (%)*				0.374
1	21 (13.9)	8 (11.8)	33 (21.2)	
2	99 (65.6)	44 (64.7)	90 (57.7)	
≥3	31 (20.5)	16 (23.6)	33 (21.1)	
Bilirubin (µmol/L), *mean (SD)*	114.9 (129.8)	89.1 (120.2)	88.5 (130.5)	0.165
Tumor location, *n (%)*				0.088
Head	119 (78.8)	49 (72.1)	101 (64.7)	
Body	17 (11.3)	11 (16.2)	34 (21.8)	
Tail	15 (9.9)	8 (11.8)	21 (13.5)	
Tumor size (mm), *mean (SD)*	28.3 (12.8)	37.8 (17.5)	40.3 (17.5)	<0.001
Preoperative tumor stadium, *n* (%)				<0.001
Ia	23 (15.2)	4 (5.9)	0	
Ib	34 (22.5)	7 (10.3)	0	
IIa	75 (49.7)	34 (50.0)	9 (5.8)	
IIb	18 (11.9)	11 (16.2)	3 (1.9)	
III	1 (0.7)	9 (13.2) [1]	56 (35.9)	
IV	0	3 (4.4) [1]	88 (56.4)	
Diagnostic laparoscopy before surgery, *n* (%)	53 (35.1)	32 (47.1)	-	0.093
Reason why no resection, *n* (%)[2]				0.193
Locally advanced	-	27 (39.7)	77 (49.4)	
Involvement SMA	-	12	55	
Involvement CA	-	4	33	
Involvement CHA	-	11	61	
Involvement SMV/PV	-	21	114	
Other[3]	-	12	35	
Metastases	-	41 (60.3)	79 (50.6)	
Lung	-	0	14	
Liver	-	27	61	
Peritoneum	-	14	14	
Lymph nodes	-	8	31	
Other	-	1	3	
Median survival *(months, 95%CI)*	20.0 (16.8-23.2)	6.0 (4.5-7.5)	4.0 (3.3-4.8)	<0.001
Tumormarkers available, *n* (%)				
CEA	90 (59.6)	48 (70.6)	79 (50.6)	0.018
CA19-9	121 (80.1)	59 (86.8)	121 (77.6)	0.282
Tumormarkers, *median (IQR)*				
CEA (ng/ml)	3.2 (2.0-4.8)	6.1 (3.2-21.7)	5.1 (2.6-12.4)	<0.001
CA19-9 (U/ml)	153.0 (30.5-520.8)	260.1 (71.3-819.7)	458.0 (107.4-1948.0)	<0.001

PDAC: pancreatic ductal adenocarcinoma; CEA: carcinoembryonic antigen; CA19-9: carbohydrate antigen 19-9; SMA: superior mesenterial artery; CA: coeliac axis; CHA: common hepatic artery; SMV: superior mesenterial vein; PV: portal vein.

[1] These patients have advanced PDAC established by preoperative imaging, however they underwent either diagnostic laparoscopy for study inclusion or intentionally palliative bypass surgery.

[2] In general, more than one structures were involved in case of locally advanced and metastatic disease. In addition, if both metastases and locally advanced PDAC was found, we considered metastases as the reason of irresectability.

[3] Local ingrowth in other structures, such as duodenum, stomach, adrenal glands, inferior caval vein and aorta.

Figure 2. ROC curves CEA & CA19-9 for prediction of advanced PDAC. *Abbreviations: ROC: receiver operating characteristic; PDAC: pancreatic ductal adenocarcinoma; CEA: carcinoembryonic antigen; CA19-9: carbohydrate antigen 19-9; AUC: area under the curve.*

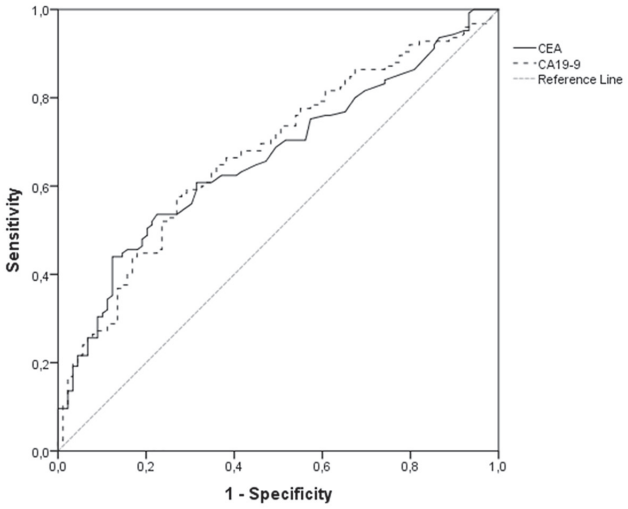

	AUC (95%CI)	Optimal cut-off value	Youden-Index	P
CEA	0.66 (0.59 - 0.74)	7.0	0.316	<0.001
CA19-9	0.68 (0.60 - 0.75)	305.0	0.306	<0.001

Figure 3. Boxplot presentation of the distribution of CEA & CA19-9 serum levels at diagnosis. Optimal cut-off values found by ROC analysis are illustrated as a horizontal dotted line. A logarithmic scale was used on the y-axis. The percentages indicate the proportion of patients per group above and below the optimal cut-off values. *Abbreviations: CEA: carcinoembryonic antigen; CA19-9: carbohydrate antigen 19-9; PDAC: pancreatic ductal adenocarcinoma.*

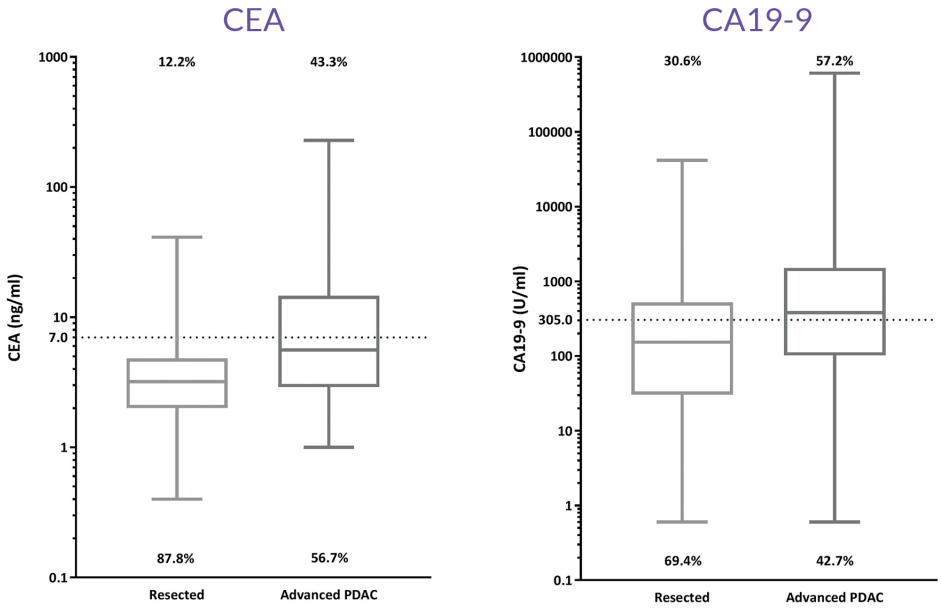

Table 2. Diagnostic value of optimal cut-off value of CEA and CA19-9 at diagnosis.

	CEA>7.0 (ng/ml)	CA19-9>305.0 (U/ml)	CEA >7.0 (ng/ml) and CA19-9>305.0 (U/ml)
Sensitivity (95% CI), (%)	43.3 (34.6 - 52.4)	57.2 (49.7 - 64.6)	27.1 (19.3 – 36.1)
Specificity (95% CI), (%)	87.8 (79.2 - 93.7)	69.4 (60.4 - 77.5)	96.4 (89.9 – 99.3)
PPV (95% CI), (%)	83.3 (73.5 - 90.0)	73.6 (67.4 - 78.9)	91.4 (77.2 – 97.1)
NPV (95% CI), (%)	52.3 (48.1 – 56.5)	52.2 (47.0 - 57.3)	48.5 (45.6 – 62.9)

CEA: carcinoembryonic antigen; CA19-9: carbohydrate antigen 19-9; PPV: positive predictive value; NPV: negative predictive value.

Table 3. Multivariable analysis of predictive factors for establishing advanced PDAC.

	Odds ratio	95% confidence interval	P
CEA>7.0 (ng/ml)	4.18	1.83 - 9.56	0.001
CA19-9>305.0 (U/ml)	2.66	1.33 - 5.33	0.006
Bilirubin> 17 (μmol/L)	0.61	0.30 - 1.22	0.159
Age	1.05	1.01 - 1.09	0.013
Female	2.15	1.08 - 4.30	0.029
Tumor size (mm)	1.07	1.04 - 1.10	<0.001

PDAC: pancreatic ductal adenocarcinoma; CEA: carcinoembryonic antigen; CA19-9: carbohydrate antigen 19-9.

Supplementary data

Figure S1. Boxplot presentation of the distribution of CEA & CA19-9 serum levels at diagnosis in patients with metastasized and/or locally advanced PDAC. Optimal cut-off values found by ROC analysis are illustrated as a horizontal dotted line. A logarithmic scale was used on the y-axis. The percentages indicate the proportion of patients per group above and below the optimal cut-off values. *Abbreviations: PDAC: pancreatic ductal adenocarcinoma; LAPC: locally advanced pancreatic cancer; M+: metastasized pancreatic cancer.*

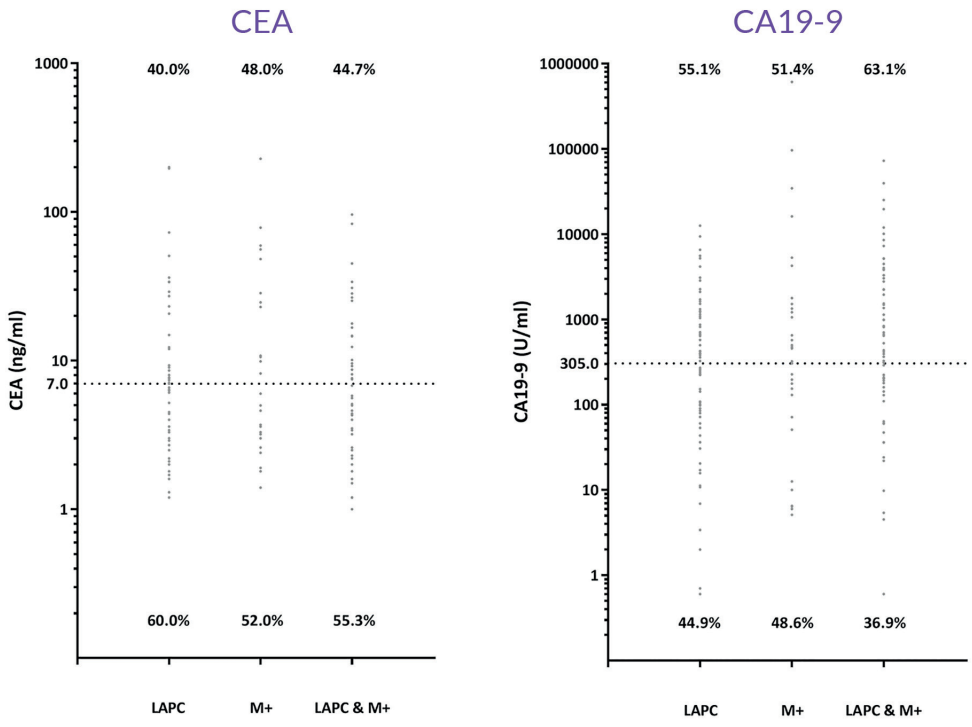

Table S1. Distribution of clinical test characteristics for different cut-off values for CEA and CA19-9.

		Number of patients (% of total)	Patients who underwent resection (resection rate [%])	Sensitivity (%)	Specificity (%)	PPV (%)	NPV (%)
CEA (N=217)	>3.0	139 (64.1)	50 (36.0)	70.1	44.4	64.0	51.3
	>5.0	85 (39.2)	19 (22.3)	52.0	78.9	77.6	53.8
	>7.0	***66 (30.4)***	***11 (16.7)***	***43.3***	***87.8***	***83.3***	***52.3***
	>10.0	47 (21.7)	8 (17.0)	30.7	91.1	83.0	48.2
	>15.0	35 (16.1)	6 (17.1)	22.8	93.3	82.9	46.2
	>20.0	31 (14.3)	4 (12.9)	21.3	95.6	87.1	46.2
	>25.0	26 (12.0)	3 (11.5)	18.1	96.7	88.5	45.6
	>30.0	20 (9.2)	3 (15.0)	13.4	96.7	85.0	44.2
	>50.0	10 (4.6)	0 (0.0)	7.9	100.0	100.0	43.5
CA19-9 (N=301)	>30.0	247 (82.1)	91 (36.8)	86.7	24.8	63.2	55.6
	>150.0	188 (62.5)	61 (32.4)	70.6	49.6	67.6	53.1
	>305.0	***140 (46.5)***	***37 (26.4)***	***57.2***	***69.4***	***73.6***	***52.2***
	>500.0	108 (35.9)	31 (28.7)	42.8	74.4	71.3	46.4
	>600.0	100 (33.2)	26 (26.0)	41.1	78.5	74.0	47.3
	>750.0	90 (29.9)	24 (26.7)	36.7	80.2	73.3	46.0
	>1000.0	78 (25.9)	19 (24.4)	32.8	84.3	75.6	45.7
	>2000.0	48 (15.9)	10 (20.8)	21.0	91.7	79.2	43.9
	>5000.0	23 (7.6)	3 (13.0)	11.1	97.5	87.0	42.5
	>10,000.0	13 (4.3)	2 (15.4)	6.1	98.4	84.6	41.3
Combined CEA and CA19-9 (N=214)	CEA >3.0 & CA19-9 >30.0	111 (51.9)	37 (33.3)	59.2	58.4	66.7	50.5
	CEA >5.0 & CA19-9 >150.0	57 (26.6)	11 (19.3)	36.8	87.6	80.7	49.7
	CEA >7.0 & CA19-9 >305.0	***38 (17.8)***	***3 (7.9)***	***28.0***	***96.6***	***92.1***	***48.9***
	CEA >10.0 & CA19-9 >500.0	21 (9.8)	2 (9.5)	15.2	97.8	90.5	45.1
	CEA >15.0 & CA19-9 >600.0	17 (7.9)	1 (5.9)	12.8	98.9	94.1	44.7
	CEA >20.0 & CA19-9 >750.0	14 (6.5)	1 (7.1)	10.4	98.9	92.9	44.0
	CEA >25.0 & CA19-9 >1000.0	11 (5.1)	0 (0.0)	8.8	100.0	100.0	43.8

CEA: carcinoembryonic antigen; CA19-9: carbohydrate antigen 19-9; PPV: positive predictive value; NPV: negative predictive value.

References

1. Siegel RL, Miller KD, Jemal A. Cancer Statistics, 2017. CA: a cancer journal for clinicians. 2017;67(1):7-30.
2. Alexakis N, Gomatos IP, Sbarounis S, et al. High serum CA 19-9 but not tumor size should select patients for staging laparoscopy in radiological resectable pancreas head and peri-ampullary cancer. European journal of surgical oncology : the journal of the European Society of Surgical Oncology and the British Association of Surgical Oncology. 2015;41(2):265-269.
3. Best LM, Rawji V, Pereira SP, Davidson BR, Gurusamy KS. Imaging modalities for characterising focal pancreatic lesions. The Cochrane database of systematic reviews. 2017;4:Cd010213.
4. Kim R, Prithviraj G, Kothari N, et al. PET/CT Fusion Scan Prevents Futile Laparotomy in Early Stage Pancreatic Cancer. Clin Nucl Med. 2015;40(11):e501-505.
5. Zamboni GA, Kruskal JB, Vollmer CM, Baptista J, Callery MP, Raptopoulos VD. Pancreatic adenocarcinoma: value of multidetector CT angiography in preoperative evaluation. Radiology. 2007;245(3):770-778.
6. Adamo MP, Boten JA, Coyle LM, et al. Validation of prostate-specific antigen laboratory values recorded in Surveillance, Epidemiology, and End Results registries. Cancer. 2017;123(4):697-703.
7. Lin JX, Wang W, Lin JP, et al. Preoperative Tumor Markers Independently Predict Survival in Stage III Gastric Cancer Patients: Should We Include Tumor Markers in AJCC Staging? Annals of surgical oncology. 2018.
8. Zhang Z, Yu Y, Xu F, et al. Combining multiple serum tumor markers improves detection of stage I epithelial ovarian cancer. Gynecologic oncology. 2007;107(3):526-531.
9. Goonetilleke KS, Siriwardena AK. Systematic review of carbohydrate antigen (CA 19-9) as a biochemical marker in the diagnosis of pancreatic cancer. European journal of surgical oncology : the journal of the European Society of Surgical Oncology and the British Association of Surgical Oncology. 2007;33(3):266-270.
10. Meng Q, Shi S, Liang C, et al. Diagnostic and prognostic value of carcinoembryonic antigen in pancreatic cancer: a systematic review and meta-analysis. OncoTargets and therapy. 2017;10:4591-4598.
11. De Rosa A, Cameron IC, Gomez D. Indications for staging laparoscopy in pancreatic cancer. HPB : the official journal of the International Hepato Pancreato Biliary Association. 2016;18(1):13-20.
12. Fujioka S, Misawa T, Okamoto T, et al. Preoperative serum carcinoembryonic antigen and carbohydrate antigen 19-9 levels for the evaluation of curability and resectability in patients with pancreatic adenocarcinoma. Journal of hepato-biliary-pancreatic surgery. 2007;14(6):539-544.
13. Edge SB, Compton CC. The American Joint Committee on Cancer: the 7th edition of the AJCC cancer staging manual and the future of TNM. Annals of surgical oncology. 2010;17(6):1471-1474.
14. Hartwig W, Strobel O, Hinz U, et al. CA19-9 in potentially resectable pancreatic cancer: perspective to adjust surgical and perioperative therapy. Annals of surgical oncology. 2013;20(7):2188-2196.
15. Isaji S, Mizuno S, Windsor JA, et al. International consensus on definition and criteria of borderline resectable pancreatic ductal adenocarcinoma 2017. Pancreatology : official journal of the International Association of Pancreatology (IAP) [et al]. 2018;18(1):2-11.
16. Schlieman MG, Ho HS, Bold RJ. Utility of tumor markers in determining resectability of pancreatic cancer. Archives of surgery (Chicago, Ill : 1960). 2003;138(9):951-955; discussion 955-956.
17. Kanda M, Fujii T, Takami H, et al. Combination of the serum carbohydrate antigen 19-9 and carcinoembryonic antigen is a simple and accurate predictor of mortality in pancreatic cancer patients. Surgery today. 2014;44(9):1692-1701.
18. Distler M, Pilarsky E, Kersting S, Grutzmann R. Preoperative CEA and CA 19-9 are prognostic markers for survival after curative resection for ductal adenocarcinoma of the pancreas - a retrospective tumor marker prognostic study. International journal of surgery (London, England). 2013;11(10):1067-1072.
19. Wu L, Huang P, Wang F, et al. Relationship between serum CA19-9 and CEA levels and prognosis of pancreatic cancer. Annals of translational medicine. 2015;3(21):328.
20. Tsavaris N, Kosmas C, Papadoniou N, et al. CEA and CA-19.9 serum tumor markers as prognostic factors in patients with locally advanced (unresectable) or metastatic pancreatic adenocarcinoma: a retrospective analysis. Journal of chemotherapy (Florence, Italy). 2009;21(6):673-680.
21. Reitz D, Gerger A, Seidel J, et al. Combination of tumour markers CEA and CA19-9 improves the prognostic prediction in patients with pancreatic cancer. Journal of clinical pathology. 2015;68(6):427-433.
22. Lee KJ, Yi SW, Chung MJ, et al. Serum CA 19-9 and CEA levels as a prognostic factor in pancreatic adenocarcinoma. Yonsei medical journal. 2013;54(3):643-649.
23. Kim YC, Kim HJ, Park JH, et al. Can preoperative CA19-9 and CEA levels predict the resectability of patients with pancreatic adenocarcinoma? Journal of gastroenterology and hepatology. 2009;24(12):1869-1875.
24. van der Geest LGM, Lemmens V, de Hingh I, et al. Nationwide outcomes in patients undergoing surgical exploration without resection for pancreatic cancer. The British journal of surgery. 2017;104(11):1568-1577.
25. Brockhaus M, Magnani JL, Blaszczyk M, et al. Monoclonal antibodies directed against the human Leb blood group antigen. The Journal of biological chemistry. 1981;256(24):13223-13225.
26. Tempero MA, Uchida E, Takasaki H, Burnett DA, Steplewski Z, Pour PM. Relationship of carbohydrate antigen 19-9 and Lewis antigens in pancreatic cancer. Cancer research. 1987;47(20):5501-5503.
27. Victorzon M, Haglund C, Lundin J, Roberts PJ. A prognostic value of CA 19-9 but not of CEA in patients with gastric cancer. European journal of surgical oncology : the journal of the European Society of Surgical Oncology and the British Association of Surgical Oncology. 1995;21(4):379-384.
28. Filella X, Molina R, Grau JJ, et al. Prognostic value of CA 19.9 levels in colorectal cancer. Annals of surgery. 1992;216(1):55-59.
29. Pezzuto A, Spoto C, Vincenzi B, Tonini G. Short-term effectiveness of smoking-cessation treatment on respiratory function and CEA level. Journal of comparative effectiveness research. 2013;2(3):335-343.
30. Petrushnko W, Gundara JS, De Reuver PR, O'Grady G, Samra JS, Mittal A. Systematic review of peri-operative prognostic biomarkers in pancreatic ductal adenocarcinoma. HPB : the official journal of the International Hepato Pancreato Biliary

Association. 2016;18(8):652-663.
31. Swords DS, Firpo MA, Scaife CL, Mulvihill SJ. Biomarkers in pancreatic adenocarcinoma: current perspectives. OncoTargets and therapy. 2016;9:7459-7467.
32. Ruckert F, Pilarsky C, Grutzmann R. Serum tumor markers in pancreatic cancer-recent discoveries. Cancers. 2010;2(2):1107-1124.
33. Dong D, Jia L, Zhang L, et al. Periostin and CA242 as potential diagnostic serum biomarkers complementing CA19.9 in detecting pancreatic cancer. Cancer science. 2018;109(9):2841-2851.
34. Luo G, Xiao Z, Long J, et al. CA125 is superior to CA19-9 in predicting the resectability of pancreatic cancer. Journal of gastrointestinal surgery : official journal of the Society for Surgery of the Alimentary Tract. 2013;17(12):2092-2098.
35. Liu R, Chen X, Du Y, et al. Serum microRNA expression profile as a biomarker in the diagnosis and prognosis of pancreatic cancer. Clinical chemistry. 2012;58(3):610-618.
36. Melo SA, Luecke LB, Kahlert C, et al. Glypican-1 identifies cancer exosomes and detects early pancreatic cancer. Nature. 2015;523(7559):177-182.
37. Holzapfel K, Reiser-Erkan C, Fingerle AA, et al. Comparison of diffusion-weighted MR imaging and multidetector-row CT in the detection of liver metastases in patients operated for pancreatic cancer. Abdominal imaging. 2011;36(2):179-184.
38. Kim HW, Lee JC, Paik KH, et al. Adjunctive role of preoperative liver magnetic resonance imaging for potentially resectable pancreatic cancer. Surgery. 2017;161(6):1579-1587.
39. Jeon SK, Lee JM, Joo I, et al. Magnetic resonance with diffusion-weighted imaging improves assessment of focal liver lesions in patients with potentially resectable pancreatic cancer on CT. European radiology. 2018.
40. Bipat S, Phoa SS, van Delden OM, et al. Ultrasonography, computed tomography and magnetic resonance imaging for diagnosis and determining resectability of pancreatic adenocarcinoma: a meta-analysis. Journal of computer assisted tomography. 2005;29(4):438-445.
41. Chang L, Stefanidis D, Richardson WS, Earle DB, Fanelli RD. The role of staging laparoscopy for intraabdominal cancers: an evidence-based review. Surgical endoscopy. 2009;23(2):231-241.
42. Morris S, Gurusamy KS, Sheringham J, Davidson BR. Cost-effectiveness of diagnostic laparoscopy for assessing resectability in pancreatic and periampullary cancer. BMC gastroenterology. 2015;15:44.
43. Gutowski M, Framery B, Boonstra MC, et al. SGM-101: An innovative near-infrared dye-antibody conjugate that targets CEA for fluorescence-guided surgery. Surgical oncology. 2017;26(2):153-162.
44. Hoogstins CES, Boogerd LSF, Sibinga Mulder BG, et al. Image-Guided Surgery in Patients with Pancreatic Cancer: First Results of a Clinical Trial Using SGM-101, a Novel Carcinoembryonic Antigen-Targeting, Near-Infrared Fluorescent Agent. Annals of surgical oncology. 2018.

Chapter 3

Stage-specific value of carbohydrate antigen 19-9 and carcinoembryonic antigen serum levels on survival and recurrence in pancreatic cancer: a single center study and meta-analysis

L. van Manen, J.V. Groen, H. Putter, M. Pichler,
A.L. Vahrmeijer, B.A. Bonsing, J.S.D. Mieog

Cancers (Basel). 2020 Oct 14;12(10).

Abstract

This study aimed to determine the stage-specific prognostic value of carbohydrate antigen 19-9 (CA19-9) and carcinoembryonic antigen (CEA) serum levels at diagnosis on overall survival (OS) and time to local recurrence or distant metastases in patients with pancreatic ductal adenocarcinoma (PDAC). Consecutive PDAC patients, discussed at multidisciplinary team meetings from 2013 through 2017, were reviewed. Prognostic factors were stage-specific (resection versus advanced PDAC) evaluated in Cox proportional hazard models. Additionally, a systematic literature search and meta-analysis was performed, as current literature is lacking a complete overview on used cut-off values and the added value of CEA as prognostic marker. In the retrospective cohort, elevated CA19-9 (>305 kU/L) level was independently associated with poor OS (Hazard ratio [HR]: 1.72[1.31-2.26]) and early recurrence (HR: 1.74[1.06-2.86]), whereas CEA was not significantly associated. The meta-analysis showed that both elevated CA19-9 and CEA serum levels were predictors for poor OS (pooled HR: 1.29[1.17-1.42] and HR: 1.51[1.33-1.73], respectively). In the resected cohort, elevated CA19-9 level was significantly associated with early recurrence (pooled HR: 2.41[1.77-3.29]), whereas CEA was not. Elevated CA19-9 serum level appear to be an independent prognostic factor for poor OS and early recurrence in PDAC patients, whereas the prognostic value of CEA is disputable.

Introduction

Pancreatic ductal adenocarcinoma (PDAC) is one of the most aggressive cancers with an overall 5-year survival rate up to 8%.[1] Only the minority of patients can be treated by extensive surgery.[2] As the diagnosis and treatment of PDAC is sometimes difficult to establish, patients are in general discussed during multidisciplinary team (MDT) meetings. Advances in neoadjuvant treatment have shown promising results in preoperative downstaging of locally advanced disease, resulting in improved survival after surgery.[3,4] Therefore, it could be helpful to identify which patients are at risk for early recurrence and associated poor survival after extensive surgery and consequently in which patients the MDT should favor neoadjuvant therapy. Moreover, tumor biology could be heterogenous in patients with similar tumor anatomy, and should be taken into consideration during the clinical work-up.[5,6] Additional tools, which should be readily available and easily implicated in the clinical workflow, to determine the optimal treatment strategy for the individual patient would add significant value to this multidisciplinary decision making process.

Serum tumor markers are such additional tools and their role as biological markers have been studied for several cancer types. Carbohydrate antigen 19-9 (CA19-9) and carcinoembryonic antigen (CEA) are the most studied tumor markers in pancreatic cancer and are both associated with disease stage and overall survival (OS) in patients who underwent pancreatic tumor resection. However, few studies reported on CA19-9 as marker for recurrence[7-9], whereas no studies evaluated CEA as a marker for recurrence. Moreover, little is known on the prognostic value of the combination of both tumor markers on OS and time to recurrence in unselected patients discussed at MDT meetings; thus not only in patients who underwent resection. Furthermore, current literature is lacking a complete overview on the prognostic value of both markers and the associated cut-off values, that can be incorporated in patient and treatment selection allocation.

The primary aim of this study was to determine the prognostic value of CA19-9 and CEA serum levels on OS and time to recurrence in PDAC patients, discussed in MDT meetings. The secondary aim was to pool existing data on the prognostic value of CA19-9 and CEA serum levels. Therefore, we performed a systematic literature search and meta-analysis, to compare our findings with the existing literature.

Methods

Patient selection

All consecutive patients discussed at MDT meetings from January 2013 through December 2017 at Leiden University Medical Center (Leiden, The Netherlands), were reviewed. Only patients diagnosed with PDAC, confirmed by pathological examination, or patients with a strong suspicion of PDAC, in case resection or biopsy could or was not performed, were included. Patients with resectable disease (as decided by the MDT), who did not want to undergo surgery or were deemed unfit for surgery were excluded from the analyses, because resectability, i.e. tumor stage, could not be proven by surgical exploration. Approval of the local Medical Research and Ethical Committee was obtained for this study (protocol number: G17.059) on 4 June 2018.

Definitions

Laboratory findings (CEA, CA19-9 and total bilirubin) were defined as the last measured value before a MDT meeting. Preoperative staging of PDAC was performed according to the American Joint Committee on Cancer (AJCC; 7th edition).[10] At MDT meetings at least one medical specialist of the following departments was present: Medical Oncology, Radiology, Hepatopancreaticobiliary Surgery, Gastroenterology and Pathology. All patients underwent radiological staging using Computed Tomography (CT) or Magnetic Resonance Imaging (MRI) or both in order to assess the resectability of the tumor. Tumor size was determined as the largest diameter in the transversal direction on CT or MRI.

Patients who did not undergo resection because of locally advanced (LAPC) or presence of metastases (M+), were categorized in the advanced PDAC group. LAPC was defined according to the Dutch Pancreatic Cancer Group (DPCG, 2012), as either tumor abutment of the superior mesenteric artery, celiac axis or common hepatic artery >90° of the circumference of the vessel wall or tumor involvement of the superior mesenteric vein/portal vein vessel wall resulting in occlusion or >270° contact.

R0 resection was defined as a free margin of >1mm on microscopic level, in accordance with the Royal College of Pathologists guidelines.[11] OS was calculated from the date of the first suspicion of pancreatic cancer on CT or MRI to the date of death (event) or last follow-up (censored). The overall time to recurrence was calculated as the interval between the date of surgery and time of recurrence. Disease recurrence (local or distant) was confirmed by imaging (CT, MRI, or PET-CT), which was performed in case of clinical symptoms suspected for disease recurrence.[12] In case a patient died without evidence of recurrence (censored), the date of last follow-up imaging or last follow-up without clinical signs of recurrent disease was used.

Statistical analysis

Continuous variables are presented as mean (standard deviation [SD]) in normal distributed data or median (interquartile range [IQR]) in non-normal distributed data. Categorical variables are presented as absolute numbers and percentages. Chi Squared test (for categorical variables), One-Way ANOVA (for normal distributed continuous variables), and Kruskal-Wallis test (for non-normal distributed continuous variables) were used to compare the patients and tumor characteristics between the resected PDAC, intraoperative PDAC and postoperative PDAC groups. Missing tumor marker values were imputed 50 times based on relevant prognostic factors, including sex, age, tumor size, survival, tumor stage, and resectability.[13] The Kaplan-Meier method was used to estimate median OS and time-to-recurrence. The curves were compared using the log-rank test.

CA19-9 and CEA were considered elevated if above 27 kU/L or 3 µg/L, respectively, according to the laboratory cut-off values commonly used in our center. Moreover, other clinically relevant cut-off values, CEA>7 µg/L and CA19-9>305 kU/L, as recently detected by our group, were also used in the analyses as well as combined cut-off values.[14]

Potential prognostic factors were first evaluated in an univariable Cox proportional hazard model. Variables with P-value below 0.200 were further evaluated in a multivariable Cox proportional

hazard model, except for CA19-9 and CEA, which were evaluated irrespective of statistical significance. For the tumor markers CA19-9 and CEA, the most significant cut-off values in the univariate analysis (standard Kaplan Meier curve) and preoperative bilirubin levels were used in the multivariable analysis.

A P-value below 0.05 (two-sided) was considered as statistically significant. Statistical analysis was performed using IBM SPSS Statistics for Windows, version 23.0 (IBM Corp., Armonk, N.Y., USA).

Systematic review of the literature

A systematic literature search was performed in PubMed for full-text articles reporting on the prognostic value of preoperative CA19-9 and CEA levels for OS and time to recurrence in PDAC patients. The search strategy consisted of the terms CA19-9, CEA, survival, recurrence, pancreatic cancer and/or synonyms. Screening of titles, abstract and subsequently full-text articles for eligibility and the data extraction was performed by two independent reviewers (L.M. and J.V.G). Only studies that report a hazard ratio (HR) in multivariable analysis were included in the pooled analysis. To asses heterogeneity between the studies the I^2 statistic was used. As the number of included studies was limited and cohort sizes varied, inverse-variance random-effect models were used to calculate pooled effects. Publication bias was assessed by funnel plots. All analyses were performed using Review Manager (RevMan 5; The Cochrane Collaboration, London, United Kingdom). The systematic review and meta-analysis was performed according to the PRISMA guidelines.[15]

Results

Patient and tumor characteristics

In total, 420 consecutive PDAC patients were discussed at our MDT meetings, of which 45 patients did not want to undergo further medical analysis or were deemed unfit for surgery. Three hundred seventy-five patients were available for analysis: 151 (40%) patients underwent resection and 224 (60%) patients did not undergo tumor resection because of either pre- or intraoperatively advanced PDAC (N=58 versus N=166, respectively; Table 1). The median CA19-9 and CEA serum levels differed significantly between the resected and (intra- and preoperative) advanced PDAC groups (CA19-9: 153.0 , 243.5 476.3 kU/L and CEA: 3.2, 5.2 and 5.7 µg/L, respectively; Table 1). The median survival was 24 (17-32) months for the patients who underwent resection, which was significantly longer compared to both advanced PDAC groups with a median survivals of 7 (6-8) and 5 (4-6) months, respectively.

CA19-9 versus CEA and overall survival

In the entire cohort, both CA19-9>27 kU/L and >305 kU/L were statistically significant associated with poor OS (median OS: 10 [8-11] versus 22 [6-37] months; 8 [6-10] versus 13 [8-18] months, respectively; Figure 1A). CEA>7 µg/L was statistically significant associated with poor OS (7 [6-9] versus 13 [10-16] months), whereas a cutoff value of 3 µg/L showed similar median OS (Figure 1B). In the resection cohort, CA19-9>27 kU/L and CA19-9>305 kU/L were statistically significant associated with poor OS (22 [17-27] versus 44 [35-53] months; 17 [14-20] versus 44 [28-60]

months, respectively), whereas elevated CEA levels were not associated with poor OS (Figure S1). In the pre- and intraoperatively advanced PDAC cohorts, both elevated CA19-9 and CEA levels were not statistically significant associated with poor OS (Figure S1). Combining elevated CA19-9 (>305 kU/L) and CEA (>7 µg/L) levels result in a median OS of 5 (3-6) months for the entire cohort, which was statistically significant worse compared to solely elevated CEA (10 [5-15] months), solely elevated CA19-9 (7 [5-10] months) or low serum levels for both markers (16 [11-21] months; Figure 1C).

At multivariate analysis, ASA score III-IV (HR: 1.74 [1.15-2.66]), CA19-9>305 kU/L (HR: 1.72 [1.31-2.26]) and tumor size >20 mm (HR: 2.36 [1.49-3.73]) were prognostic factors for poor OS in the entire cohort (Table 2). Combined elevated CA19-9 and CEA levels at multivariate analysis, showed that both elevated CA19-9 and CEA (HR: 1.71 [1.21-2.42]) and solely elevated CA19-9 (HR: 2.17 [1.46-3.23]) serum levels were independently associated with poor OS in the entire cohort (Table S1). In the resection cohort, CA19-9>305 kU/L was an independent prognostic factor for poor OS (HR: 2.59 [1.52-4.42]). As univariate analysis showed similar OS for pre- and intraoperatively advanced PDAC patients, both cohorts were combined at multivariate analysis. In this advanced PDAC cohort, CA19-9>305 kU/L was not an independent prognostic factor for poor OS (HR:0.89 [0.64-1.24]; Table 2).

CA19-9 and CEA and time-to-recurrence after resection

Median time to recurrence after resection was similar in patients with normal and elevated CEA (>3 µg/L; >7 µg/L) levels. CA19-9>27 kU/L was not statistically significant associated with early recurrence (15 [11-18] versus 22 [12-32] months), whereas CA19-9>305 kU/L was prognostic for early recurrence (11 [10-13] versus 21 [14-28] months), which was confirmed at multivariable analysis (Table 3). Combining elevated CA19-9 and CEA levels in multivariate analysis was not prognostic for early recurrence (Table S2). Furthermore, CA19-9>305 kU/L was statistically significant associated with both early locoregional recurrence and distant metastases (Figure S2), although this could not be confirmed at multivariate analysis (Table 3).

Systematic literature review and meta-analysis

A total of 113 studies was identified and screened for eligibility (Figure S3). Eighteen studies, including ours, reported on the prognostic value determined at diagnosis of either CEA, CA19-9 serum levels or both on survival in PDAC patients (Table S3).[7,16-29] Several cut-off values were used varying from 5–4000 kU/L for CA19-9 and 3–20 µg/L for CEA. Four studies did not perform multivariable analysis and were therefore not included in the meta-analysis.[18,19,24,25] The included studies demonstrated symmetric funnel plots (Figure S4). Pooled analysis showed a HR of 1.29 (1.17-1.42) and 1.51 (1.33-1.73) for elevated CA19-9 and CEA levels, respectively (Figure 3). Pooled analysis of two studies, that combined elevated CA19-9 and CEA levels, showed a HR of 1.35 (1.33–1.37; Table S4). Subgroup analysis showed similar results in both advanced (N=8 studies) and resected (N=10 studies) patients.

Four studies reported on the prognostic value for recurrence after pancreatic resections for PDAC patients of preoperative serum CA19-9 levels, whereas no studies evaluated the prognostic value

of CEA, except ours (Table S5).[7-9,21] In three studies, including ours, elevated CA19-9 levels (CA19-9>37 kU/L, CA19-9>100 kU/L and CA19-9>305 kU/L) were a prognostic factor for early recurrence (pooled HR: 2.63 [1.92-3.59]), whereas two studies did not perform a multivariable analysis (Figure 3).

Discussion

This study aimed to determine the stage-specific prognostic value of CA19-9 and CEA serum levels at diagnosis on OS and time to recurrence in PDAC patients discussed at MDT meetings. In the current cohort, both elevated CA19-9 (>305 kU/L) and CEA (>7 µg/L) levels were significantly associated with a poor median OS. Multivariable analysis showed that CA19-9 is an independent prognostic factor (HR: 1.72) for poor OS, whereas CEA did not yield a significant association anymore. Moreover, elevated CA19-9 levels (>305 kU/L) were independently associated with early recurrence (HR: 1.74). Our systematic literature search revealed that eighteen studies reported on either the prognostic value of both CEA and CA19-9 for OS, time to recurrence or both in PDAC patients, although none of them included consecutive PDAC patients discussed at the MDT meetings. Generally, the findings of these studies were in concordance with our analyses, as the meta-analysis revealed a prognostic role of elevated CA19-9 (pooled HR: 1.29) and CEA levels (pooled HR: 1.51) on OS. However, no optimal cut-off values for CA19-9 and CEA could be determined, as the included studies used a variety of cut-off values.

One of the limitations of our cohort study is its retrospective design. Because of missing values CEA and CA19-9 were imputed several times based on relevant prognostic factors. Moreover, elevated CEA levels could also be elevated in case of nicotine abuses or presence of other cancers, such as colon cancer or rare adenosquamous PDAC.[30-32] In patients missing the Lewis antigen, which is the case in 4-7% of the population, CA19-9 level will stay low, therefore both CA19-9 and CEA levels should be interpreted with caution.[33-35] Elevated bilirubin serum levels as result of biliary obstruction could also influence the serum CA19-9 levels, although in this study we corrected for this effect during the analyses.[36] Compared to the meta-analysis, elevated CEA levels were not associated with poor OS or early recurrence in our cohort. Publication bias and the use of different cut-off levels could be a possible explanation of the discrepancy between the outcomes of the studies included in the meta-analysis and our retrospective cohort, although the shape of the funnel plots, including only five studies (including ours), was symmetric.

Tailored treatment of the individual cancer patient is the future in surgical oncology. In the era of neoadjuvant treatment for pancreatic cancer, we do not know in advance which patient will benefit or not. It has been shown that a >30% decrease of CA19-9 levels is related with a response on neoadjuvant chemotherapy thereby improving the prediction rate for resectability of LAPC, illustrating that tumor biology, and not only tumor anatomy, plays an important role.[37] Furthermore, monitoring of disease recurrence after resection by testing biomarkers could be helpful in addition to imaging techniques such as CT, MRI or PET-CT.[38,39] CA 19-9 has been shown superior to CEA for monitoring of recurrence following radical resection of pancreatic

cancer.[40] The results of this study could implicate that the MDT should consider neoadjuvant therapy in patients with elevated CA19-9 levels to achieve local downstaging in order to prevent patients from early recurrence and therefore unnecessary and high impact surgeries with long recovery times. Moreover the results of the meta-analysis suggest that both elevated CA19-9 and CEA levels could indicate aggressive tumor growth in advanced stage PDAC, resulting in a poor OS.

Conclusions

In conclusion, elevated CA19-9 serum levels appear to be an independent prognostic factor for poor OS in PDAC patients, whereas the prognostic value of CEA is disputable. In patients who underwent resection, preoperative CA19-9 and not CEA levels are prognostic for early recurrence, which could be a plea to consider them as biologically (locally) advanced disease. Future trials should standardize and incorporate CA19-9 levels in their patient and treatment selection allocation.

Table 1. Patient and tumor characteristics.

Variable	Resected PDAC (*n* = 151)	Intraoperative Advanced PDAC (*n* = 58)	Preoperative Advanced PDAC (*n* = 166)	*p*-Value
Age (y), mean (SD)	64.8 (9.8)	66.1 (10.1)	67.8 (9.6)	0.021
Sex, *n* (%)				0.206
Male	80 (53.0)	25 (43.1)	94 (56.6)	
Female	71 (47.0)	33 (56.9)	72 (43.4)	
ASA score, *n* (%)				0.360
I	21 (13.9)	7 (12.1)	34 (20.5)	
II	99 (65.6)	39 (67.2)	95 (57.2)	
III-IV	31 (20.5)	12 (20.7)	37 (22.3)	
Bilirubin (µmol/L), mean (SD)	114.9 (129.8)	89.1 (120.2)	85.7 (127.5)	0.143
Tumormarkers, median (IQR)				
CA19-9 (kU/L)	153.0 (30.5–520.8)	243.5 (66.8–678.3)	476.3 (107.9–2145.3)	<0.001
CEA (µg/L)	3.2 (2.0–4.8)	5.2 (3.3–16.3)	5.7 (2.6–14.6)	<0.001
Tumormarkers available, *n* (%)				
CA19-9	121 (80.1)	50 (86.2)	130 (78.3)	0.431
CEA	90 (59.6)	41 (70.7)	86 (51.8)	0.037
Tumor location, *n* (%)				0.044
Head	119 (78.8)	44 (75.9)	106 (63.9)	
Body	17 (11.3)	9 (15.5)	36 (21.7)	
Tail	15 (9.9)	5 (8.6)	24 (14.5)	
Preoperative TNM stage, *n* (%)				<0.001
Ia	23 (15.2)	4 (6.9)	0	
Ib	34 (22.5)	7 (12.1)	0	
IIa	75 (49.7)	33 (56.9)	7 (4.2)	
IIb	18 (11.9)	12 (20.7)	2 (1.2)	
III	1 (0.7)	2 (3.4)	65 (39.2)	
IV	0	0	92 (55.4)	
Tumor size (mm), mean (SD)	27.9 (12.8)	37.8 (17.3)	40.3 (17.5)	<0.001
Chemotherapy, *n* (%)				<0.001
No or unknown	36 (23.8)	41 (70.6)	108 (65.1)	
Yes	115 (76.2)	17 (29.4)	58 (34.9)	
Neoadjuvant	7	-	6	
Adjuvant	115	-	-	
Palliative	-	17	52	
Survival (months), median (95%CI)	24 (17–32)	7 (6–8)	5 (4–6)	<0.001

Abbreviations: PDAC: pancreatic ductal adenocarcinoma; CA19-9: carbohydrate antigen 19-9; CEA: carcinoembryonic antigen.

Figure 1. Survival curves for CA19-9 and CEA serum levels.

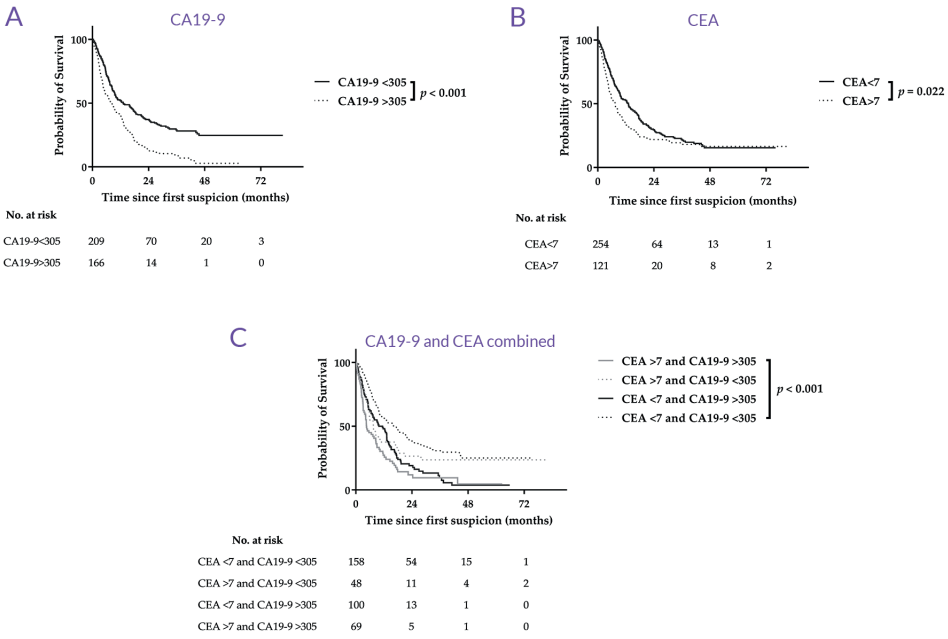

Table 2. Multivariable cox regression analysis for overall survival.

Parameter	Entire Cohort (*n* = 375)			Resected Cohort (*n* = 151)			Advanced PDAC Cohort (*n* = 224)		
	HR	95% CI	*p*-value	HR	95% CI	*p*-value	HR	95% CI	*p*-value
Tumormarkers									
CA19-9 >305 kU/L	1.72	1.31–2.26	<0.001	2.59	1.52–4.42	<0.001	0.89	0.64–1.24	0.494
CEA >7 µg/L	1.26	0.89–1.77	0.191	0.66	0.29–1.46	0.302	1.11	0.79–1.49	0.568
Age (yr)									
>65 yr	1.28	0.98–1.67	0.067	1.03	0.66–1.63	0.891	1.01	0.72–1.42	0.964
Sex, *n* (%)									
Female	0.84	0.65–1.08	0.170	1.01	0.64–1.60	0.960	0.65	0.47–0.88	0.006
ASA score, *n* (%)									
I	1.00	1.00–1.00	1.000	1.00	1.00–1.00	1.000	1.00	1.00–1.00	1.000
II	1.13	0.78–1.63	0.531	1.50	0.68–3.29	0.315	1.64	1.05–2.56	0.028
III-IV	1.74	1.15–2.66	0.010	3.44	1.45–8.13	0.005	2.28	1.34–3.86	0.002
Bilirubin									
>17 µmol/L	0.78	0.61–1.01	0.062	0.81	0.50–1.31	0.383	1.09	0.79–1.49	0.612
Tumor size									
>20 mm	2.36	1.49–3.73	<0.001	1.57	0.81–3.06	0.184	2.74	1.37–5.49	0.004

Abbreviations: CA19-9: carbohydrate antigen 19-9; CEA: carcinoembryonic antigen.

Figure 2. Recurrence patterns by CA19-9 and CEA serum levels.

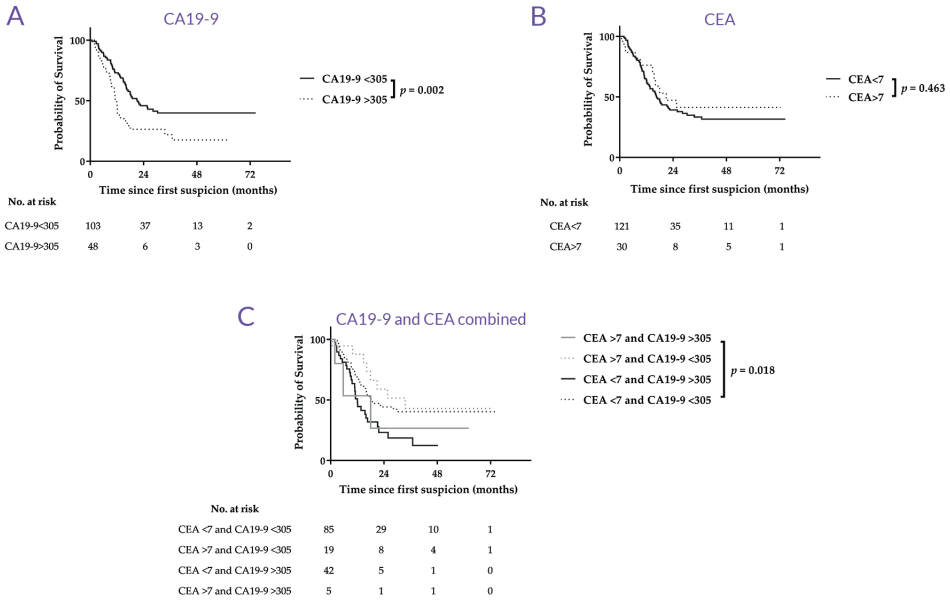

Table 3. Multivariable cox regression analysis for recurrence in resected PDAC cohort.

Parameter	General Recurrence (*n* = 84) *			Locoregional Recurrence (*n* = 55) *			Distant recurrence (*n* = 61) *		
	HR	95% CI	*p*-value	HR	95% CI	*p*-value	HR	95% CI	*p*-value
Tumormarkers									
CA19-9 > 305 kU/L	1.72	1.03–2.85	0.038	1.81	0.96–3.42	0.067	1.75	0.95–3.20	0.072
CEA > 7 µg/L	0.70	0.30–1.63	0.413	0.77	0.25–2.36	0.650	0.73	0.27–1.96	0.536
Tumor size									
>20 mm	1.95	1.02–3.72	0.043	1.76	0.83–3.77	0.144	1.76	0.83–3.71	0.140
Perineural invasion									
Present	1.24	0.77–2.02	0.376	1.12	0.62–2.02	0.715	1.38	0.78–2.46	0.273
Margin status									
R1	1.46	0.93–2.29	0.099	1.38	0.79–2.41	0.253	1.59	0.95–2.67	0.079
Differentiation grade									
Well	1.00	1.00–1.00	1.000	1.00	1.00–1.00	1.000	1.00	1.00–1.00	1.000
Moderate	1.88	0.91–3.86	0.087	1.61	0.74–3.52	0.233	2.04	0.82–5.07	0.124
Poorly	1.80	0.88–3.71	0.111	1.05	0.46–2.41	0.904	2.17	0.88–5.34	0.093
Undifferentiated or unknown	1.64	0.50–5.35	0.415	0.66	0.14–3.16	0.600	2.62	0.72–9.57	0.144

Abbreviations: PDAC: pancreatic ductal adenocarcinoma; HR: Hazard Ratio; CA19-9: carbohydrate antigen 19-9; CEA: carcinoembryonic antigen.
** Some patients had both locoregional recurrence and distant metastases.*

Figure 3. Forest plots of prognostic value of (A) CA19-9 and (B) CEA on overall survival in PDAC patients, including subgroup analysis. The prognostic value of CA19-9 on recurrence in resected PDAC patients was also shown (C). *Abbreviations: CA19-9: carbohydrate antigen 19-9; CEA: carcinoembryonic antigen; d.f.: degrees of freedom.*

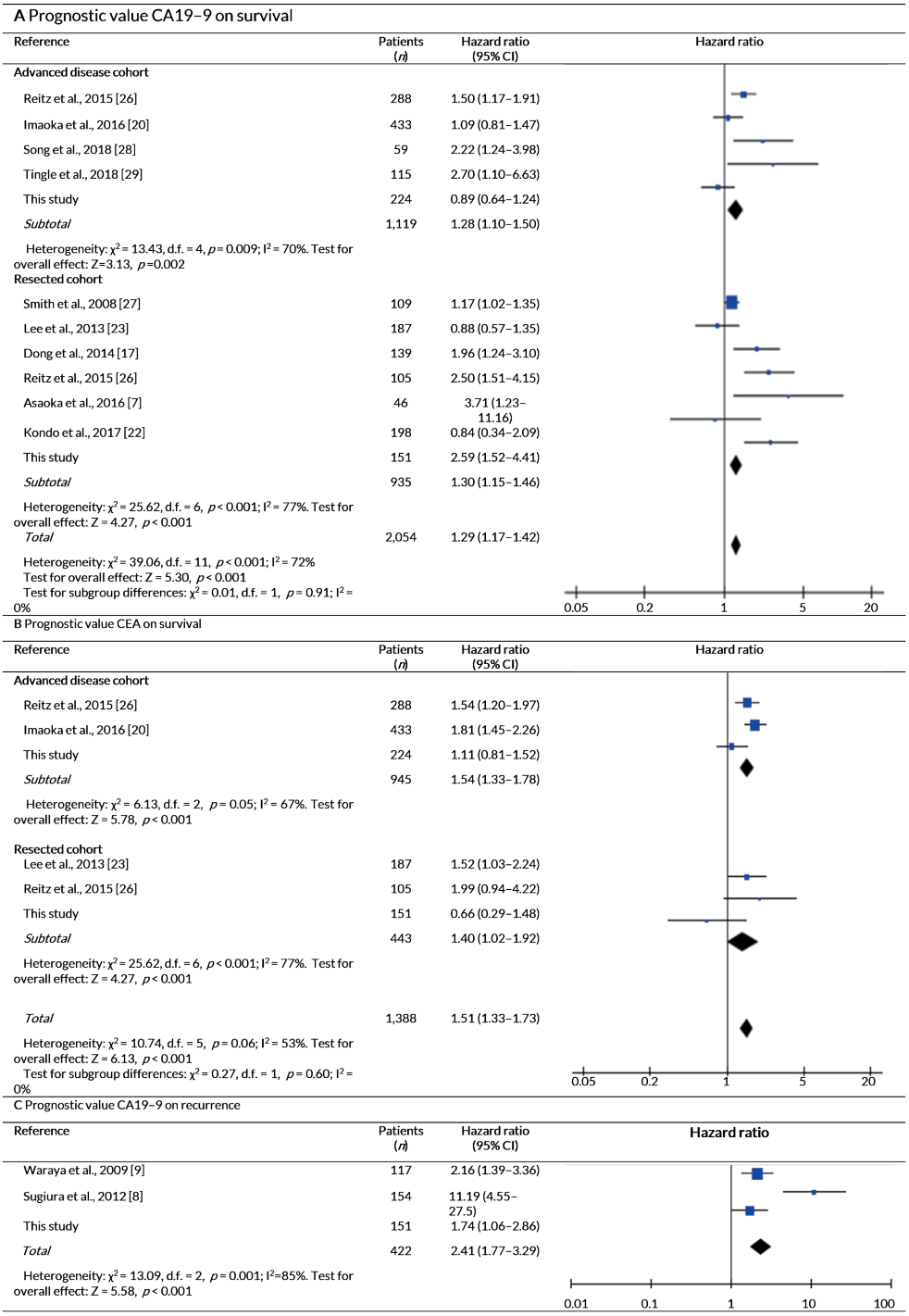

Supplementary data

Figure S1. Survival curves for CA19-9 and CEA serum levels stratified by resected PDAC (A–C), intraoperative advanced PDAC (D–F) and preoperative advanced PDAC (G–I) patients.

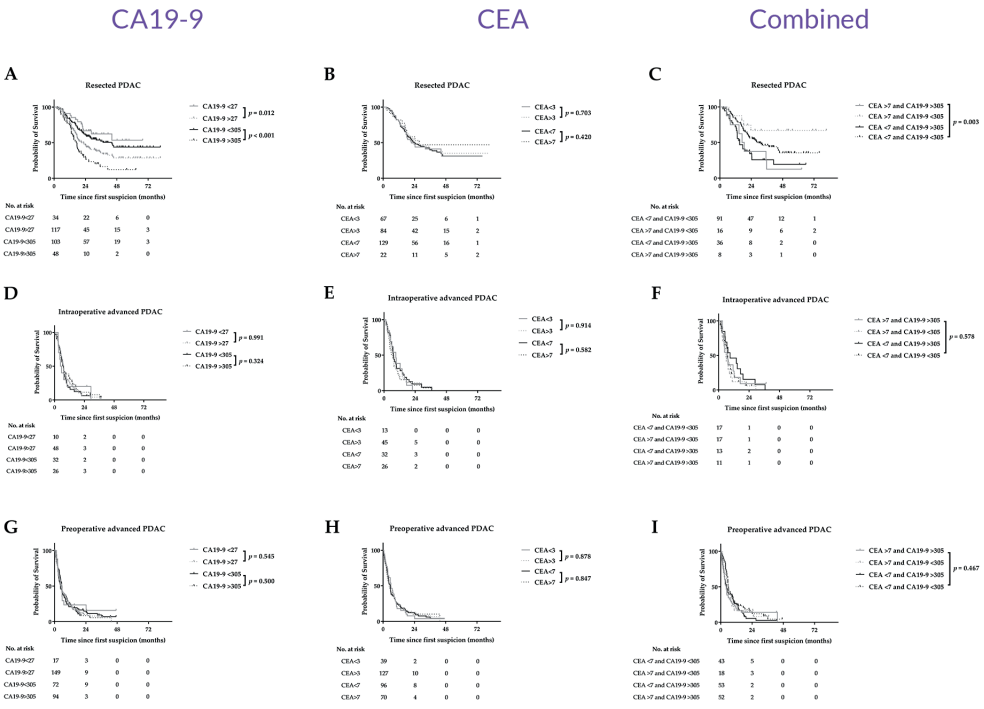

Table S1. Multivariable cox regression analysis for overall survival including combined CA19-9 and CEA levels.

Parameter	Entire Cohort (*n* = 375)			Resected Cohort (*n* = 151)			Advanced PDAC Cohort (*n* = 224)		
	HR	95% CI	*p*-value	HR	95% CI	*p*-value	HR	95% CI	*p*-value
Tumormarkers									
CA19-9 < 305 kU/L and CEA < 7 µg/L	1.00	1.00–1.00	1.000	1.00	1.00-1.00	1.000	1.00	1.00–1.00	1.000
CA19-9 < 305 kU/L and CEA >7 µg/L	1.24	0.72–2.12	0.439	0.40	0.11–1.38	0.145	1.30	0.76–2.21	0.337
CA19-9 > 305 kU/L and CEA < 7 µg/L	1.71	1.21–2.42	0.003	2.23	1.24–4.01	0.007	1.00	0.65–1.54	0.992
CA19-9 >305 kU/L and CEA > 7 µg/L	2.17	1.46–3.23	<0.001	2.74	0.86–8.70	0.088	0.99	0.62–1.58	0.967
Age (yr)									
>65 yr	1.28	0.98–1.67	0.070	1.03	0.65–1.64	0.889	1.02	0.72–1.44	0.917
Sex, n (%)									
Female	0.84	0.65–1.08	0.167	0.98	0.62–1.57	0.943	0.65	0.47–0.88	0.006
ASA score, n (%)									
I	1.00	1.00–1.00	1.000	1.00	1.00–1.00	1.000	1.00	1.00–1.00	1.000
II	1.13	0.78–1.65	0.526	1.69	0.73–3.91	0.224	1.61	1.03–2.52	0.038
III-IV	1.75	1.15–2.67	0.010	3.85	1.53–9.69	0.004	2.23	1.31–3.79	0.003
Bilirubin >17 µmol/L	0.78	0.61–1.01	0.063	0.79	0.48–1.30	0.351	1.09	0.80–1.51	0.581
Tumor size >20 mm	2.36	1.48–3.75	<0.001	1.60	0.82–3.13	0.170	2.73	1.36–5.50	0.005

Abbreviations: CA19-9: carbohydrate antigen 19-9; CEA: carcinoembryonic antigen.

Table S2. Multivariable cox regression analysis for recurrence in resected PDAC cohort including combined CA19-9 and CEA levels.

Parameter	General Recurrence (*n* = 84) *			Locoregional Recurrence (*n* = 55) *			Distant Recurrence (*n* = 61) *		
	HR	95% CI	*p*-value	HR	95% CI	*p*-value	HR	95% CI	*p*-value
Tumormarkers									
CA19-9 <305 kU/L and CEA<7 µg/L	1.00	1.00–1.00	1.000	1.00	1.00–1.00	1.000	1.00	1.00–1.00	1.000
CA19-9 <305 kU/L and CEA >7 µg/L	0.62	0.23–1.70	0.354	0.66	0.17–2.60	0.551	0.65	0.21–2.00	0.449
CA19-9 > 305 kU/L and CEA < 7 µg/L	1.63	0.93–2.86	0.091	1.70	0.83–3.48	0.149	1.65	0.85–3.21	0.140
CA19-9 >305 kU/L and CEA >7 µg/L	1.41	0.40–5.00	0.591	1.44	0.51–4.02	0.491	1.49	0.31–7.09	0.614
Tumor size									
>20 mm	1.97	1.03–3.76	0.041	1.79	0.83–3.83	0.136	1.77	0.84–3.74	0.135
Perineural invasion									
Present	1.26	0.77–2.07	0.353	1.13	0.62–2.06	0.692	1.41	0.78–2.53	0.257
Margin status									
R1	1.48	0.94–2.32	0.092	1.40	0.80–2.46	0.242	1.61	0.95–2.71	0.075
Differentiation grade									
Well	1.00	1.00–1.00	1.000	1.00	1.00–1.00	1.000	1.00	1.00–1.00	1.000
Moderate	1.88	0.91–3.86	0.088	1.61	0.73–3.53	0.234	2.04	0.82–5.08	0.125
Poorly	1.66	0.51–5.41	0.109	1.06	0.46–2.44	0.895	2.18	0.88–5.39	0.091
Undifferentiated or unknown	1.66	0.51–5.41	0.405	0.65	0.14–3.18	0.599	2.67	0.73–9.76	0.138

*Abbreviations: PDAC: pancreatic ductal adenocarcinoma; HR: Hazard Ratio; CA19-9: carbohydrate antigen 19-9; CEA: carcinoembryonic antigen. * Some patients had both locoregional recurrence and distant metastases.*

Figure S2. Recurrence patterns (locoregional (A–C) vs metastatic recurrence (D–F)) by CA19-9 and CEA serum levels.

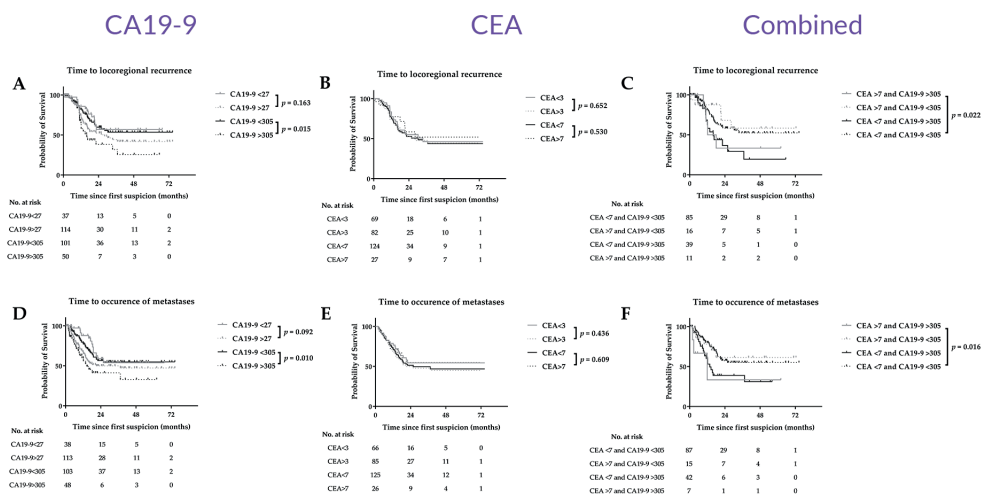

Figure S3. Flowchart of study selection.

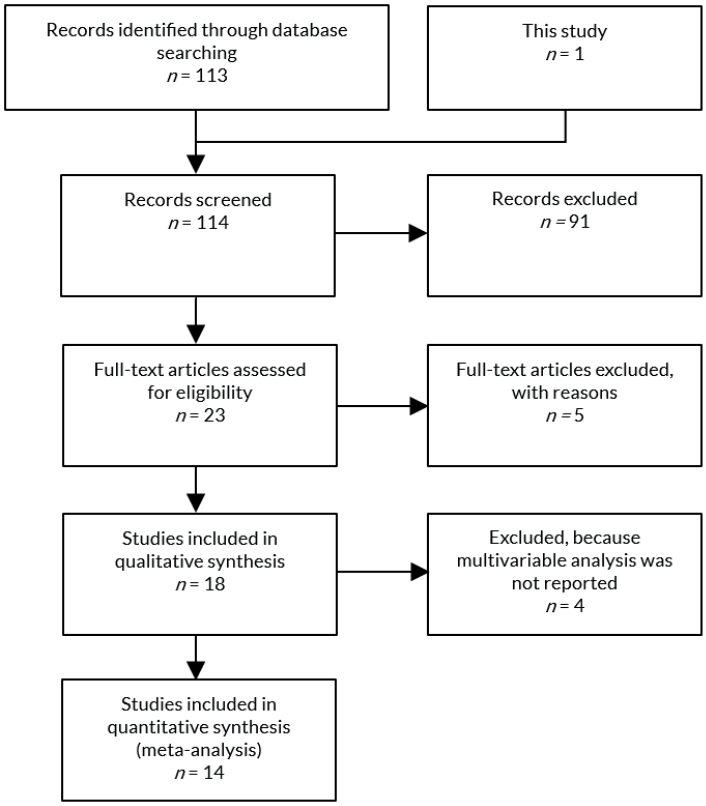

Table S3. Studies that report on prognostic value of serum CA19-9 and CEA on overall survival in PDAC patients.

Study	Country	Study Population (No. of Patients)	Cut-off Level (CEA: µg/L; CA19-9: kU/L)	Fraction above Cut-off (%)	Median OS (95% CI) below Cut-off (Months)	Median OS (95% CI) above Cut-off (Months)	Performance of Multivariable analysis
CA19-9							
Ni et al., 2005	China	Resected and advanced PDAC (*n* = 105)	1,000	37.8	9	6	No
Ferrone et al., 2006	United States	Resected PDAC (*n* = 111)	37 200 1000 2000	NR	28 28 28 22	19 14 12 13	No
Smith et al., 2008	United Kingdom	Resected PDAC (*n* = 109)	150	58.7	22.1	10.4	Yes
Martin et al., 2012	United States	Resected (n = 30) and advanced (*n* = 93) PDAC	37	Resected: 50 Advanced: 72	Resected: 36 Advanced: 32.3	Resected: 20 Advanced: 11.3	No
Hartwig et al., 2013	Germany	Resected PDAC (*n* = 1,543)	<5 5 - 37 37- 100 100 - 250 250 - 500 500 - 1,000 1000 - 2,000 2000 - 4,000 ≥4000	6.4 18.2 14.0 16.0 13.2 11.9 8.2 6.0 6.1	-	26.8 28.5 26.9 22.5 20.1 15.4 12 12.3 14.4	No
Lee et al., 2013	Korea	Resected PDAC (*n* = 187)	376	75.4	12.4	13.5	Yes
Dong et al., 2014	China	Resected PDAC (*n* = 139)	339	43.3	24.9	11.9	Yes
Reitz et al., 2015	Austria	Resected and advanced PDAC (*n* = 393)	931	47.1	10	5	Yes
Asaoka et al., 2016	Japan	Resected PDAC (*n* = 46)	230	30.4	NR	15.8	Yes
Imaoka et al., 2016 [	Japan	Resected PDAC (*n* = 119)	37	68.0	55.9	44.9	Yes
Imaoka et al., 2016	Japan	Metastatic PDAC (*n* = 433)	37	84.8	8.9	7.8	Yes
Kondo et al., 2017	Japan	Resected PDAC (*n* = 198)	300	32.2	18.8	46.7	Yes
Tingle et al., 2018	United Kingdom	Advanced PDAC (*n* = 115)	770	NR	15.1	7.7	Yes
Song et al., 2018	China	Metastatic PDAC (*n* = 59)	626	57.6	NR	NR	Yes
This study	The Netherlands	Resected and advanced PDAC (*n* = 375)	305	44.3	13	8	Yes
CEA							
Ni et al., 2005	China	Resected and advanced PDAC (*n* = 105)	5	47.6	11	6	No
Lee et al., 2013	Korea	Resected PDAC (*n* = 187)	5	39.0	16.1	10.2	Yes
Reitz et al., 2015	Austria	Resected and advanced PDAC (*n* = 393)	6.9	33.6	10	4	Yes
Asaoka et al., 2016	Japan	Resected PDAC (*n* = 46)	4	23.9	NR	NR	Yes
Imaoka et al., 2016	Japan	Metastatic PDAC (*n* = 433)	5 20	57.3 30.3	10.3 NR	6.8 6.1	Yes
This study	The Netherlands	Resected and advanced PDAC (*n* = 375)	7	32.3	13	7	Yes
CA19-9 and CEA combined							
Distler et al., 2013	Germany	Resected PDAC (*n* = 259)	75 (CA19-9) 3 (CEA)	35.1	33.3	23.9	Yes
This study	The Netherlands	Resected and advanced PDAC (*n* = 375)	305 (CA19-9) 7 (CEA)	18.4	7	5	Yes

Abbreviations: CA 19-9: cancer antigen 19-9, CEA: carcinoembryonic antigen, OS: overall survival,

*PDAC: pancreatic ductal adenocarcinoma, HR: Hazard Ratio, NR: not reported. * Multiple cut-off values have been used.*

Figure S4. Funnel plots of included studies in meta-analysis, determining the prognostic value of CA19-9 on overall survival (A) CEA on overall survival (B) both CA19-9 and CEA on overall survival (C) and CA19-9 on recurrence (D) in PDAC patients.

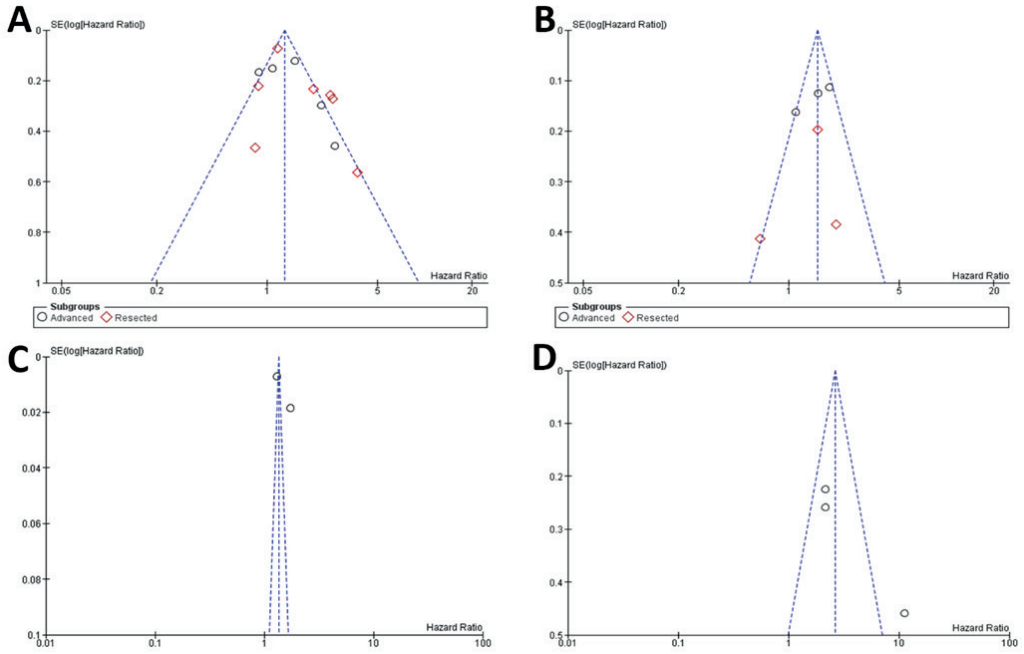

Table S4. Forest plot of prognostic value of CA19-9 and CEA combined on overall survival in PDAC patients.

Prognostic value CA19-9 and CEA combined			
Reference	**Patients (*n*)**	**Hazard ratio (95% CI)**	**Hazard ratio**
Distler et al., 2013	259	1.30 (1.13–1.50)	
This study	375	1.73 (1.20–2.48)	
Total	634	1.35 (1.33–1.37)	
Heterogeneity: χ^2 = 206.50, d.f. = 1, p < 0.001; I^2 = 100%			
Test for overall effect: Z = 44.58, p < 0.001			

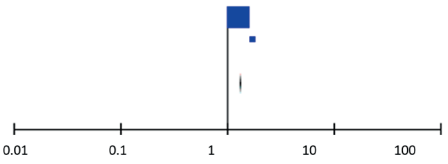

Abbreviations: CA 19-9: cancer antigen 19-9; CEA: carcinoembryonic antigen; d.f.: degrees of freedom.

Table S5. Studies that report on prognostic value of preoperative serum CA19-9 and CEA for early recurrence in resected PDAC patients.

Study	Country	Marker	Study Population (No. of Patients)	Cut-off Level	Fraction above Cut-off (%)	Median OS (95% CI) below Cut-off (Months)	Median OS (95% CI) above Cut-off (Months)	Performance of Multivariable analysis
Waraya et al., 2009	Japan	CA19-9	Resected PDAC (*n* = 117)	37	56.4	30.6	12.7	Yes
Sugiura et al., 2012	Japan	CA19-9	Resected PDAC (*n* = 154)	100	47.4	22	6	Yes
Asaoka et al., 2016	Japan	CA19-9	Resected PDAC (*n* = 46)	230	30.4	12.7	5.8	No
Imaoka et al., 2016	Japan	CA19-9	Resected PDAC (*n* = 119)	37	68.0	24.8	17.9	No
This study	The Netherlands	CA19-9	Resected PDAC (*n* = 151)	27 305	76.8 31.8	22 21	15 11	Yes
		CEA	Resected PDAC (*n* = 151)	3 7	53.0 19.9	18 21	15 16	No

Abbreviations: CA 19-9: cancer antigen 19-9, CEA: carcinoembryonic antigen, PDAC: pancreatic ductal adenocarcinoma.

References

1. Siegel RL, Miller KD, Jemal A. Cancer statistics, 2018. CA: a cancer journal for clinicians. 2018;68(1):7-30.
2. Ryan DP, Hong TS, Bardeesy N. Pancreatic adenocarcinoma. The New England journal of medicine. 2014;371(22):2140-2141.
3. Conroy T, Desseigne F, Ychou M, et al. FOLFIRINOX versus gemcitabine for metastatic pancreatic cancer. The New England journal of medicine. 2011;364(19):1817-1825.
4. Suker M, Beumer BR, Sadot E, et al. FOLFIRINOX for locally advanced pancreatic cancer: a systematic review and patient-level meta-analysis. The Lancet Oncology. 2016;17(6):801-810.
5. Isaji S, Mizuno S, Windsor JA, et al. International consensus on definition and criteria of borderline resectable pancreatic ductal adenocarcinoma 2017. Pancreatology : official journal of the International Association of Pancreatology (IAP) [et al]. 2018;18(1):2-11.
6. Tzeng CW, Fleming JB, Lee JE, et al. Defined clinical classifications are associated with outcome of patients with anatomically resectable pancreatic adenocarcinoma treated with neoadjuvant therapy. Annals of surgical oncology. 2012;19(6):2045-2053.
7. Asaoka T, Miyamoto A, Maeda S, et al. Prognostic impact of preoperative NLR and CA19-9 in pancreatic cancer. Pancreatology : official journal of the International Association of Pancreatology (IAP) [et al]. 2016;16(3):434-440.
8. Sugiura T, Uesaka K, Kanemoto H, et al. Serum CA19-9 is a significant predictor among preoperative parameters for early recurrence after resection of pancreatic adenocarcinoma. Journal of gastrointestinal surgery : official journal of the Society for Surgery of the Alimentary Tract. 2012;16(5):977-985.
9. Waraya M, Yamashita K, Katagiri H, et al. Preoperative serum CA19-9 and dissected peripancreatic tissue margin as determiners of long-term survival in pancreatic cancer. Annals of surgical oncology. 2009;16(5):1231-1240.
10. Edge SB, Compton CC. The American Joint Committee on Cancer: the 7th edition of the AJCC cancer staging manual and the future of TNM. Annals of surgical oncology. 2010;17(6):1471-1474.
11. Campbell F, Smith RA, Whelan P, et al. Classification of R1 resections for pancreatic cancer: the prognostic relevance of tumour involvement within 1 mm of a resection margin. Histopathology. 2009;55(3):277-283.
12. Tummers WS, Groen JV, Sibinga Mulder BG, et al. Impact of resection margin status on recurrence and survival in pancreatic cancer surgery. The British journal of surgery. 2019;106(8):1055-1065.
13. Azur MJ, Stuart EA, Frangakis C, Leaf PJ. Multiple imputation by chained equations: what is it and how does it work? International journal of methods in psychiatric research. 2011;20(1):40-49.
14. van Manen L, Groen JV, Putter H, et al. Elevated CEA and CA19-9 serum levels independently predict advanced pancreatic cancer at diagnosis. Biomarkers : biochemical indicators of exposure, response, and susceptibility to chemicals. 2020:1-8.
15. Liberati A, Altman DG, Tetzlaff J, et al. The PRISMA statement for reporting systematic reviews and meta-analyses of studies that evaluate healthcare interventions: explanation and elaboration. BMJ (Clinical research ed). 2009;339:b2700.
16. Distler M, Pilarsky E, Kersting S, Grutzmann R. Preoperative CEA and CA 19-9 are prognostic markers for survival after curative resection for ductal adenocarcinoma of the pancreas - a retrospective tumor marker prognostic study. International journal of surgery (London, England). 2013;11(10):1067-1072.
17. Dong Q, Yang XH, Zhang Y, et al. Elevated serum CA19-9 level is a promising predictor for poor prognosis in patients with resectable pancreatic ductal adenocarcinoma: a pilot study. World journal of surgical oncology. 2014;12:171.
18. Ferrone CR, Finkelstein DM, Thayer SP, Muzikansky A, Fernandez-delCastillo C, Warshaw AL. Perioperative CA19-9 levels can predict stage and survival in patients with resectable pancreatic adenocarcinoma. Journal of clinical oncology : official journal of the American Society of Clinical Oncology. 2006;24(18):2897-2902.
19. Hartwig W, Strobel O, Hinz U, et al. CA19-9 in potentially resectable pancreatic cancer: perspective to adjust surgical and perioperative therapy. Annals of surgical oncology. 2013;20(7):2188-2196.
20. Imaoka H, Mizuno N, Hara K, et al. Prognostic impact of carcinoembryonic antigen (CEA) on patients with metastatic pancreatic cancer: A retrospective cohort study. Pancreatology : official journal of the International Association of Pancreatology (IAP) [et al]. 2016;16(5):859-864.
21. Imaoka H, Shimizu Y, Senda Y, et al. Post-adjuvant chemotherapy CA19-9 levels predict prognosis in patients with pancreatic ductal adenocarcinoma: A retrospective cohort study. Pancreatology : official journal of the International Association of Pancreatology (IAP) [et al]. 2016;16(4):658-664.
22. Kondo N, Murakami Y, Uemura K, et al. Comparison of the prognostic impact of pre- and post-operative CA19-9, SPan-1, and DUPAN-II levels in patients with pancreatic carcinoma. Pancreatology : official journal of the International Association of Pancreatology (IAP) [et al]. 2017;17(1):95-102.
23. Lee KJ, Yi SW, Chung MJ, et al. Serum CA 19-9 and CEA levels as a prognostic factor in pancreatic adenocarcinoma. Yonsei medical journal. 2013;54(3):643-649.
24. Martin LK, Wei L, Trolli E, Bekaii-Saab T. Elevated baseline CA19-9 levels correlate with adverse prognosis in patients with early- or advanced-stage pancreas cancer. Medical oncology (Northwood, London, England). 2012;29(5):3101-3107.
25. Ni XG, Bai XF, Mao YL, et al. The clinical value of serum CEA, CA19-9, and CA242 in the diagnosis and prognosis of pancreatic cancer. European journal of surgical oncology : the journal of the European Society of Surgical Oncology and the British Association of Surgical Oncology. 2005;31(2):164-169.
26. Reitz D, Gerger A, Seidel J, et al. Combination of tumour markers CEA and CA19-9 improves the prognostic prediction in patients with pancreatic cancer. Journal of clinical pathology. 2015;68(6):427-433.
27. Smith RA, Bosonnet L, Ghaneh P, et al. Preoperative CA19-9 levels and lymph node ratio are independent predictors of survival in patients with resected pancreatic ductal adenocarcinoma. Digestive surgery. 2008;25(3):226-232.
28. Song JY, Chen MQ, Guo JH, Lian SF, Xu BH. Combined pretreatment serum CA19-9 and neutrophil-to-lymphocyte ratio as a potential prognostic factor in metastatic pancreatic cancer patients. Medicine. 2018;97(4):e9707.
29. Tingle SJ, Severs GR, Goodfellow M, Moir JA, White SA. NARCA: A novel prognostic scoring system using neutrophil-

albumin ratio and Ca19-9 to predict overall survival in palliative pancreatic cancer. Journal of surgical oncology. 2018;118(4):680-686.

30. Pezzuto A, Spoto C, Vincenzi B, Tonini G. Short-term effectiveness of smoking-cessation treatment on respiratory function and CEA level. Journal of comparative effectiveness research. 2013;2(3):335-343.
31. Victorzon M, Haglund C, Lundin J, Roberts PJ. A prognostic value of CA 19-9 but not of CEA in patients with gastric cancer. European journal of surgical oncology : the journal of the European Society of Surgical Oncology and the British Association of Surgical Oncology. 1995;21(4):379-384.
32. Simone CG, Zuluaga Toro T, Chan E, Feely MM, Trevino JG, George TJ, Jr. Characteristics and outcomes of adenosquamous carcinoma of the pancreas. Gastrointestinal cancer research : GCR. 2013;6(3):75-79.
33. Brockhaus M, Magnani JL, Blaszczyk M, et al. Monoclonal antibodies directed against the human Leb blood group antigen. The Journal of biological chemistry. 1981;256(24):13223-13225.
34. Tempero MA, Uchida E, Takasaki H, Burnett DA, Steplewski Z, Pour PM. Relationship of carbohydrate antigen 19-9 and Lewis antigens in pancreatic cancer. Cancer research. 1987;47(20):5501-5503.
35. Luo G, Liu C, Guo M, et al. Potential Biomarkers in Lewis Negative Patients With Pancreatic Cancer. Annals of surgery. 2017;265(4):800-805.
36. Mann DV, Edwards R, Ho S, Lau WY, Glazer G. Elevated tumour marker CA19-9: clinical interpretation and influence of obstructive jaundice. European journal of surgical oncology : the journal of the European Society of Surgical Oncology and the British Association of Surgical Oncology. 2000;26(5):474-479.
37. van Veldhuisen E, Vogel JA, Klompmaker S, et al. Added value of CA19-9 response in predicting resectability of locally advanced pancreatic cancer following induction chemotherapy. HPB : the official journal of the International Hepato Pancreato Biliary Association. 2018;20(7):605-611.
38. Motoi F, Murakami Y, Okada KI, et al. Sustained Elevation of Postoperative Serum Level of Carbohydrate Antigen 19-9 is High-Risk Stigmata for Primary Hepatic Recurrence in Patients with Curatively Resected Pancreatic Adenocarcinoma. World journal of surgery. 2019;43(2):634-641.
39. Motoi F, Rikiyama T, Katayose Y, Egawa S, Unno M. Retrospective evaluation of the influence of postoperative tumor marker status on survival and patterns of recurrence after surgery for pancreatic cancer based on RECIST guidelines. Annals of surgical oncology. 2011;18(2):371-379.
40. Daamen LA, Groot VP, Heerkens HD, Intven MPW, van Santvoort HC, Molenaar IQ. Systematic review on the role of serum tumor markers in the detection of recurrent pancreatic cancer. HPB : the official journal of the International Hepato Pancreato Biliary Association. 2018;20(4):297-304.

Part II

Chapter 4

A practical guide for the use of indocyanine green and methylene blue in fluorescence-guided abdominal surgery

L. van Manen, H.J.M. Handgraaf, M. Diana, J. Dijkstra,
T. Ishizawa, A.L. Vahrmeijer, J.S.D. Mieog

Journal of Surgical Oncology. 2018 Aug;118(2):283-300.

Abstract

Near-infrared (NIR) fluorescence imaging is gaining clinical acceptance over the last years and has been used for detection of lymph nodes, several tumor types, vital structures and tissue perfusion. This review focuses on NIR fluorescence imaging with indocyanine green and methylene blue for different clinical applications in abdominal surgery with an emphasis on oncology, based on a systematic literature search. Furthermore, practical information on doses, injection times and intraoperative use are provided.

Introduction

Cancer is one of the leading causes of death worldwide, resulting in 8.2 million deaths annually.[1] Treatments for cancer include surgery, radiation therapy, chemotherapy and targeted therapies. Surgery is often the cornerstone in the treatment of solid cancers in the abdominal cavity. Especially during oncologic surgery, it is pivotal to remove as much tumor as possible and simultaneously to prevent unnecessary damage to surrounding healthy tissue. Despite that the quality of preoperative imaging modalities, such as MRI and CT, has been improved during the last decades, intraoperative navigation using CT or MRI is only performed in specialised hospitals, mostly confined to the field of neurosurgery, due to the complexity, high costs, tissue deformation and long acquisition times.[2] Today, for intraoperative navigation, the surgeon has to rely in the majority of the cases only on visual and tactile feedback to distinguish between different kind of tissue structures. Additionally, (laparoscopic) intraoperative ultrasound or sometimes a gamma probe can be used during oncologic surgery. However, this is not always sufficient. Tumor-positive (R1 or R2) resection margins in colorectal cancer, for example, occur in approximately 10% of the operated patients.[3,4] Together with the increasing rate of minimal invasive (laparoscopic and robotic) surgery and therefore the lack of tactile feedback, there is a demand of improving visibility of different kind of tissue types, especially for distinguishing malignant and benign structures.

In the past years, new intraoperative imaging systems that exploit the near-infrared (NIR) light spectrum, have been evaluated (pre)clinically for different applications.[5-8] For intraoperative purposes, NIR light (700 - 900 nm) is more advantageous than visible light due to its capability to penetrate deeper into tissue, up to 10 mm. In addition, in the NIR spectrum tissue exhibits almost no autofluorescence. NIR fluorescent contrast agents lead therefore to maximized signal-to-background ratios and enhance the contrast of different tissue types.[9,10] NIR fluorescence imaging requires a NIR fluorescent agent (i.e. fluorophore) combined with an imaging system that is able to both excite and detect the fluorophore. The fluorescence signal can be visualized after milliseconds, which is advantageous above other emerging imaging techniques, such as Raman spectroscopy or Optical Coherence Tomography, which require more time to visualize the same field of view.[11] Moreover, most systems are capable of merging fluorescence signals with normal RGB color videos, allowing direct anatomical orientation.

Different fluorophores have been evaluated (pre)clinically in NIR fluorescence imaging. These fluorophores have to be injected locally or systematically before surgery. Today, only two of them, indocyanine green (ICG) and methylene blue (MB), are approved for clinical use by the Food and Drug Administration and the European Medicines Agency. 5-aminolevulinic acid (5-ALA) is also clinically used as a fluorophore, especially in the field of neurosurgery field. However, this dye is fluorescent at 510 nm, which is outside the NIR spectrum.[12] Consequently, the penetration capacity of 5-ALA is negligible. ICG and MB are nonspecific contrast agents in the near-infrared region and they do not bind to tumor ligands. ICG has a half-time of 150-180 seconds and is solely cleared by the liver.[13] Its excitation peaks around 800 nm. ICG is very safe; adverse events are reported in less than 1 in 40,000 patients and mostly comprise hypersensitivity reactions.[14] MB in low doses (<2mg/kg) is safe, however it can induce severe adverse effects such as arrhythmias, coronary vasoconstriction and haemolytic anaemia in patients with renal insufficiency or after administration of higher doses.[15] MB is partially renal cleared and has an excitation peak of approximately 700 nm. Therefore it has a less tissue penetration capacity

and background tissue shows more autofluorescence. Due to their differences in clearance patterns ICG and MB have been used for various applications. In short, the indications can be used for lymph node mapping, detection of vital structures (e.g. ureters, bile ducts), identification of tumors, and assessment of tissue perfusion. This review provides a practical approach for NIR fluorescence imaging with ICG and MB for different clinical applications in abdominal surgery, with an emphasis on oncology.

Methods

We searched in PubMed for in human (*in vivo*) trials using ICG and MB in NIR fluorescence guided abdominal surgery, published before January 2018. The search was based on the following search items: "Indocyanine green" or "ICG", "Methylene Blue" or "MB", "Near-infrared" or "NIR", and "Fluorescence" or "fluorescent". More specific search terms were added per application (SLN mapping, tumor detection, tissue perfusion, detection of vital structures). Only articles written in English were included. Case reports and (systematic) reviews were excluded from the analysis. After selection of relevant articles, clinically relevant information focussing on how to perform NIR fluorescence imaging in daily practice was extracted from the articles to set-up a review. In this article, the different applications of NIR fluorescence in abdominal surgery, SLN mapping, tumor detection, visualization of vital structures and tissue perfusion, are discussed separately.

Results

Our search revealed a total of 891 articles, which are reported in a flow diagram (Figure 1). After exclusion of 720 articles, who did not meet our eligibility criteria, a total of 171 original articles remained, which formed the basis of this review.

Sentinel lymph node mapping

Sentinel lymph node mapping is only part of standard care in melanoma and breast cancer.[16,17] Current standard-of-care is a combination of blue dye and gamma probe for Technetium-99m (Tc-99m) detection, which has certain disadvantages. Blue dye has no penetration capacity whatsoever and a gamma probe does not allow visual identification. SLN mapping is not part of standard clinical care in abdominal oncological surgery.[18,19] Today, NIR fluorescence imaging of SLN(s) as a new and additional modality was evaluated for SLN mapping in malignancies of the oesophagus, stomach, colon, bladder, prostate, cervix, endometrium and ovarium.

CLINICAL APPLICATIONS

Oesophageal cancer

Oesophageal cancer is a disease with a dismal prognosis, showing an overall 5-year survival rate around 14%.[20] Extensive lymphadenectomy improves the prognosis, especially at early stages.[21-23] To visualise the sentinel lymph nodes, ICG was evaluated as a NIR fluorescent marker in three clinical studies. All studies were feasibility studies and therefore using a small study population: 1-20 patients.[24-26] Ninety-five percent of the sentinel lymph nodes could be

detected in the cohort of 20 patients, as shown by Yuasa et al.[25] However, further research is necessary before introduction into clinical practice.

Gastric cancer

Gastric cancer is one of the most common cancers in the world, especially in Eastern Asia with an incidence of 24 and 9.8 per 100,000 in men and women, respectively. We found ten clinical studies using ICG during NIR fluorescence imaging during laparoscopic or open gastric surgery.[27-36] The SLN identification rates ranges from 90 to 100%, however it decreases to 0% for T4 tumors.[35] It also has to be mentioned that most studies did not include these higher stages in their study, which could explain the high resection rates. In Japan and Korea, T1N0M0 tumors are standard treated with endoscopic resection, which creates new opportunities for clinical use of NIRF for SLN mapping in selected cases, as demonstrated by Bok et al., who showed that a combination of endoscopic submucosal dissection and sentinel node navigation surgery (laparoscopic) was feasible in 12 out of 13 patients.[37]

Colorectal cancer

SLN mapping in colorectal cancer is still a controversial procedure, due to the relatively low visibility of the lymphatic system after injection of blue dye.[38] In the past years NIR fluorescent imaging with other available dyes, such as ICG, was used in nine clinical studies during surgery.[29,39-46] All studies were performed in a small population, ranges from 5 to 30 patients, who underwent laparoscopic or open surgery due to colorectal cancer. The SLN detection rates by NIR fluorescence imaging vary between 65.5% and 100%, which could probably explained by the experience in the participating centers.

Bladder cancer

A cystectomy with pelvic lymphadenectomy is the treatment of choice for patients with bladder cancer. However, accurate intraoperative detection of SLNs is difficult and lacks sensitivity.[47] Moreover, there is a great inter-patient variability in lymph drainage patterns, which makes the location of the SLN unpredictable. Recently, NIR fluorescence imaging using ICG could detect a sentinel lymph node in at least 90%, which indicated that this technique could contribute to improved intraoperative staging of bladder cancer.[48-50]

Prostate cancer

Prostate cancer is one of the most common cancers in men and treatment consists of diverse interventions, including surgical resection.[51] (Extended) lymph node dissection is sometimes performed during radical prostatectomy, depending on the preoperative risk assessment.[52,53] Ten studies evaluated the use of ICG during prostatectomy, which showed a high detection rate of SLNs, however due to the low prevalence of SLN metastases a low positive predictive value was found. [54-64] This supports the findings that NIR fluorescence imaging could be useful in high risk groups.

Cervical cancer

Early stage cervical cancer, which is often detected by screening, is normally treated with radical hysterectomy and pelvic lymph node dissection.[65] Lymph node status is one of the independent prognostic factors for the patient's survival.[66] However, if the resected lymph nodes were not

involved, which is often the case in early stage cervical cancer, patients underwent unnecessarily lymphadenectomy. This could be prevented by performing SLN mapping, for instance with NIR fluorescence imaging, as shown in different studies.[67-83] These studies, performed in early stage cervical cancer, showed detection rates varying from 60 to 100%. Recently, three studies compared ICG to the current golden standard for SLN mapping, blue dye and Tc-99m, in study populations varying from 58 to 144 patients.[73,74,76] It was concluded, that detection rates did not differ significantly between blue dye with Tc-99m and ICG. However, all studies showed significantly higher rates of bilateral lymph node detection, especially in larger tumor sizes (>2 cm). Hence, it indicates that intraoperative lymph node mapping with fluorescence imaging using ICG is at least comparable to the current golden standard.

Endometrial cancer

Endometrial cancer is one of the most common cancers in women and patients often presents with an early stage disease.[51,84] Currently, there is no agreement about performing SLN mapping to avoid extensive lymphadenectomy during surgery in early stage endometrial cancer.[19] However, in some centers fluorescence imaging is used for SLN mapping and incorporated in standard care.[85] Nineteen studies showed that fluorescence imaging is useful, indicating high detection rates of lymph nodes, varying from 68 to 100 %.[69,71-73,78,80,83,86-97] Laios et al. showed the lowest detection rate (68%), which was probably caused by the learning process as visualized by a learning curve.[69] Rossi et al. showed that cervical stromal injection of ICG is preferable over hysteroscopic endometrial injection for SLN detection, as illustrated by the significant difference in detection rates (82% vs. 33% respectively, p=0.027).[87] These results indicate that SLN mapping with NIR fluorescence imaging is feasible and may be worth considering for use in clinical practice.

Ovarian cancer

One study evaluated the implementation of NIR fluorescence imaging of SLNs during laparoscopic surgery in 7 patients with early-stage ovarian cancer.[98] In all patients, at least one SLN was detected after intraoperatively injection with ICG in both sides of the proper ovarian and suspensory ligament. Nevertheless, more studies have to be performed to determine the added value of fluorescence imaging for intraoperative lymph node staging, which is essential before implementation into clinical practice.

SUMMARY OF FINDINGS

Sentinel lymph node mapping using ICG has been evaluated for several applications in abdominal surgery (gastroenterology, urology and gynaecology) with different imaging systems.[24-36,39-46,48-50,54-64,67-83,86-98] In these studies a high diversity in doses has been used, varying from 100 µg to 25 mg. In general, based on the evaluated clinical studies a dose of (at least) 2.5 mg is recommended for good visualization of sentinel lymph nodes.

It was shown, that ICG bound to human serum albumin (ICG:HSA) could also be used for SLN mapping.[26,79] Moreover, Hachey et al. showed that ICG:HSA is preferable above using ICG alone in oesophageal cancer, which could probably be explained by the rapid lymphatic clearance and poor retention of ICG alone.[26] However, due to the limited evidence we prefer an injection of ICG alone. As part of standard care, which consists of peritumoral blue dye injection, ICG could also be injected

around the tumor. Most of the studies used a four quadrant injection in the submucosa around the tumor. The timing of the injection is also an important issue. One study in gastric cancer prefers injection (endoscopically) one day before surgery.[36] They showed lower false negative results than intraoperatively subserosal injection, probably because of frequent leakage from damaged lymphatic vessels, caused by mobilising the stomach. On the other hand, most studies showed good results by performing injection, just after applying general anaesthesia.[25,29,31,33,41,46,48-50,54,57,68-74,76,78,80,81,83,87-89,92,93,95,96] For good visibility of the tumor and consequently a good injection place, a minimal-invasive (endoscopic, cystoscopic) approach is recommended, which also prevents damaging of lymphatic vessels. For cervical and endometrial cancer a cervical stromal injection of ICG is preferable above a hysteroscopic injection.[87] As shown in Figure 2, approximately 15-30 minutes after injection, the sentinel lymph nodes will be visualised.[33,39,43,50,62,89] In the mean-time the surgical procedure can be started, and the surgeon will therefore lose minimal time. After identification of the SLN(s) the additional oncological resection can be performed.

HOW TO USE IT

Taken together, optimal use of ICG for SLN mapping could be achieved by peritumorally injection of 2.5 mg ICG. Intraoperative injection, just after applying anesthesia, in a minimal invasive manner seems optimal. The SLNs could be visualized 15-30 minutes after injection (Table 1).

Tumor imaging

ICG has been used as a contrast agent for intraoperative detection of diverse tumor types, which is based on two characteristics of ICG: hepatic clearance and the enhanced permeability and retention (EPR) effect. Solid tumors (other than hepatobiliary tract) could be visualised by the EPR effect, which is based on the visualization with ICG of the increased permeability and reduced drainage in tumor tissue after tumor-induced angiogenesis.[99,100]

CLINICAL APPLICATIONS

Liver tumors (primary & secondary)

Due to its hepatic clearance, ICG can be used for imaging of hepatobiliary tumors, both metastases and primary liver cancers (cholangiocarcinoma and hepatocellular carcinoma). Healthy liver tissue clears ICG within a couple of hours, whereas tumor tissue retains ICG by compression of bile ducts. However, recent studies suggested also a molecular mechanism.[101,102] Immature hepatocytes, which are located in the transition zone between the tumor and normal liver parenchyma, were not able to excrete ICG into the biliary ducts due to down-regulation of anion transporters. This results in a fluorescent rim around the tumor or metastasis, making it easy to identify them. Furthermore, ICG accumulates into well-differentiated hepatocellular carcinoma (HCC), resulting in complete fluorescence signal rather than a dark center. In a retrospective cohort study in our institute it was shown that NIR fluorescence imaging of colorectal liver metastases was able to identify more and smaller tumors, resulting in reduced recurrences in a subset of patients.[103] Twenty-one studies evaluated the use of NIR fluorescence imaging with ICG for liver tumor detection, both primary tumors as metastatic spread of colorectal, uveal, breast and pancreatic cancer.[101,102,104-122]

Summary of findings

To establish the optimal dose and injection time our group performed a comparison study with 10 mg and 20 mg ICG injection. However, no significant difference in optimal tumor-to-background contrast between respectively a 24h or 48h administration and 10 mg or 20 mg injection was found.[122] Therefore, we recommend a bolus of 10 mg of injected intravenously 24 hours before surgery based on clinical and logistical preferences. Tumor tissue compresses small bile ducts and consequently causes local inflammation. In these bile ducts and inflamed liver tissue ICG is retained for some days. Therefore, other groups showed also good results with ICG injection up to 14 days before surgery, although using much higher doses of ICG, up to 0.5 mg/kg.[101,106,108,109,111-113,117-120] Today, no randomised trial has been performed to compare these high differences in dosing and injection timing. After administering ICG, a fluorescent rim can be identified around tumors during surgery, as illustrated in Figure 3. Several studies showed that this technique not only identifies known tumors, but also occult, otherwise undetectable submillimeter tumors. However, only subcapsular lesions up to around 1 cm from the liver surface are expected to be visible, due to the limited penetration depth of NIR fluorescence.[123] Nevertheless, it could therefore be used as a complementary intraoperative tool, as CT/MRI and intraoperative ultrasound still showed relatively high rates of false negatives for superficially located (subcapsular) lesions.[124,125]

Peritoneal metastases

Preoperative detection of peritoneal metastases is often difficult with the current image modalities.[126] Adequate pre- and intraoperative staging is therefore an important issue for offering the best treatment. In the last years, more evidence is coming up, which showed that hyperthermic intraperitoneal chemotherapy (HIPEC) combined with cytoreductive surgery gave a better survival in patients with limited peritoneal metastases from colorectal or ovarian cancer.[127,128] Four (pilot) studies evaluated the intraoperative visibility of peritoneal spread in liver, colorectal and ovarian cancer with NIR fluorescence imaging.[129-132] All studies showed a good visibility of peritoneal metastases, however in patients with ovarian cancer treated with HIPEC, distinguishing benign scars and malignant lesions was difficult.[131] Moreover, Tummers et al. showed a high false positive rate, which could be explained by the EPR effect, which underscores the need for tumor-selective targets.[132] Since HCC tissues often retain bile juice productivity even in metastatic sites, fluorescence imaging following preoperative intravenous injection of ICG can also be applied to identification of extrahepatic metastases of HCC.[130]

Summary of findings

All studies started with ICG injection 24h before surgery. Unfortunately, no fluorescence signal was visible during exploration. However, intraoperative injection was feasible and showed good results. Hence, we recommend intravenously injection of ICG after abdominal exposition. A dose of 0.25 mg/kg of ICG could therefore be used. As shown above, detection of peritoneal metastases could be useful during intraoperative staging and cytoreductive surgery (combined with HIPEC). Clinical application of NIRF imaging during cytoreductive surgery should be reserved for patients with limited peritoneal spread (peritoneal cancer index < 8).[129,133] If advanced peritoneal spread has been established preoperatively, the added value of fluorescence imaging with ICG is limited. After injection of ICG, peritoneal nodules become fluorescent from at least 5 minutes.[129] Tumor positive nodules become hyperfluorescent. Due to physiological accumulation of ICG, detection of small peritoneal metastases is hampered in some abdominal regions (such as in the liver and visceral peritoneum).

Adrenal tumors

Adrenal masses are often resected by performing minimal invasive surgery (laparoscopic or robotic).[134,135] Identification of the adrenal glands and determining the resection margins could be difficult, especially when it is surrounded by retroperitoneal fat. The added value of NIR fluorescence imaging using ICG during minimal invasive (partial) adrenalectomy has been determined in four studies.[136-139] Based on the difference in perfusion between the adrenals and the surrounding tissues, the adrenal glands and different types of adrenal tumors could be detected. Colvin et al. showed that NIR fluorescence imaging was superior and equivalent in 46.5% and 25.6% respectively, to conventional robotic view in determining the borders of the adrenal glands in 40 patients.[139] Other mentioned studies showed similar results in determining the adrenal gland borders, however they were performed in much smaller populations.

Summary of findings

Three out of four studies used a 5 mg dose of ICG, which turned out to be the optimal dose for visibility of the adrenal glands.[136,138,139] After exposure of the retroperitoneum and acquiring a good view on the adrenal glands and its surrounding tissue, ICG could be intravenously injected. One minute after injection of ICG, the fluorescence signal could be detected.[139] First of all, the arterial vasculature of the adrenal glands and kidneys became fluorescent. After a few seconds, the fluorescence signal highlights the adrenal parenchyma, however it is slightly less fluorescent as the adjacent kidneys.[138] Adrenocortical tumors could be easily recognized by the hyperfluorescent signal, although medullary tumors (such as pheochromocytomas) were hypofluorescent during NIRF imaging.[138,139] In the background, the liver could show more intense fluorescence, in case of right adrenal surgery. The optimal tumor-to-background contrast is achieved after 5 min.[139] If the fluorescent signal washes out (>20 min after injection), a new injection of 5 mg ICG could be administered.

Other solid tumors

ICG has also been evaluated in other solid tumors in the abdominal region, although the added value has not been proven. Our group studied the role of ICG for intraoperative visualization of pancreatic tumors during pancreaticoduodenectomy in eight patients.[140] After injection of ICG,

only in one patients a clear tumor-to-pancreas contrast was observed. The use NIR fluorescence imaging during nephrectomy has also been a topic of research, as reviewed by Bjurlin et al.[141] Based on the angiographic properties of ICG, it could play a role in determining vascular clamping during nephrectomy.[142,143] However, for tumor imaging NIR fluorescence imaging with ICG showed inconsistent results. One study compared the fluorescent signal with histologic findings in 100 patients undergoing partial nephrectomies, and showed that the ICG pattern (hypofluorescent, isofluorescent, or afluorescent) was insufficient to distinguish benign from malignant renal lesions.[144]

HOW TO USE IT

As summarised in Table 1, we recommend 10 mg, 5 mg and 0.25 mg/kg ICG injection intravenously for good intraoperative visibility of liver tumors, adrenal tumors and peritoneal metastases, respectively. Intraoperative injection is optimal for detection of peritoneal metastases and adrenal tumors, although for detection of liver tumors it is preferable to inject ICG 24 hours before surgery.

Visualization of vital structures

Currently, no good intraoperative imaging techniques are available for both biliary duct and ureter visualization. Intraoperative cholangiography is sometimes used for enhanced bile duct identification. Two disadvantages of this technique are the exposition of radiation to the patients and health care personnel and the chance of causing bile duct injuries by bile duct cannulation. [145,146] Other techniques such as ureteral stenting is sometimes performed to visualize the ureter. However, the benefit is currently questionable and it is also associated with a risk of ureteral injury.[147,148] NIR fluorescence imaging with ICG and MB is used for both biliary and ureter mapping, based on their clearance characteristics.[7]

CLINICAL APPLICATIONS

Biliary duct

During laparoscopic cholecystectomy, nowadays one of the most performed surgeries, it is important to visualize the so-called critical view of safety. This ensures that the cystic duct has been identified correctly. Still, due to anatomical variations, the cystic duct could be misidentified by the common hepatic duct or the common bile duct. Misidentification, with a reported incidence ranging from 0.08% to 1.5%, is accomplished with a morbidity up to 21% and high healthcare costs.[149-152] The use of intravenously ICG injection for identification of the bile ducts with NIR fluorescence cholangiography was evaluated in 30 studies, which showed a pooled cystic duct identification in 1,019/1,050 (97%) patients.[140,153-181] Although, the biliary ducts could be very well visualized, the diminished visualization of the bile ducts in minority of the patients, could be caused by inflammatory tissue or fatty peritoneum (in obese patients) covering the biliary ducts, which hampered the penetration of NIR light.[174,176] In a pilot study it was recently discovered that directly injection of ICG into the gallbladder shows low fluorescence signals in the liver and seems also feasible, especially in case of severe cholecystitis.[182]

Summary of findings

Before starting with NIR fluorescence cholangiography, 5 mg ICG should be prepared according to a recent optimal dose study of our group.[183] Administering ICG directly prior to surgery results in highly fluorescent liver tissue, which may hamper identification of bile ducts. Therefore, ICG has to be injected intravenously 3 to 7 hours before surgery for optimal bile duct to liver contrast, resulting in a better bile duct discrimination. For elective cholecystectomy, which is sometimes part of oncologic surgery (in case of cholangio- or pancreatic carcinoma), this approach is feasible. Five studies showed that with this dose the cystic duct beginning to became fluorescent around 30 to 40 minutes after intravenous ICG injection.[158,159,169,170,176]

In general, during cholecystectomy it is important to obtain the critical view of safety: visibility of the cystic duct and cystic artery entering the gallbladder. After preparation of the gallbladder hilum both medially and laterally, critical view could be achieved by retracting the gallbladder caudo-medially and exposing the triangle of Calot (Figure 4). If the cystic duct was detected, ICG could also be administrated again to visualize the cystic artery. It is important to realize that after a second ICG administration, the liver will become again highly fluorescent. After detection of both the cystic duct and cystic artery, these structures could be transected and the gallbladder could be removed.

Ureter

Ureter injuries were seen in minority of the cases during colorectal surgery, with a reported incidence varying from 0.15 % to 0.66% for open and laparoscopic procedures, respectively.[184] Although the incidence seems low, ureteral injuries are associated with a significant morbidity. The use of intraoperative ureter visualization with NIR fluorescence imaging was evaluated in six studies, of which four studies used ICG and two used MB as contrast agents.[185-190] ICG was used in 3 studies during robotic surgery to detect the level of the ureteral stenosis in a population varying from 7 to 25 patients. In these studies ICG was injected both through the ureteral catheter, of which only the tip was inserted into the ureteral orifice, or in the renal pelvis.

Summary of findings

We prefer MB above ICG as a NIR fluorescent contrast agent for detection of the ureter, because MB is cleared via the kidneys and could therefore intravenously injected easily. Verbeek et al. showed that in 12 patients both ureters could be detected 10 minutes after infusion of MB, whereas Al Taher et al. detected both ureters in only a half of the patients (5 out of 10).[185,190] Verbeek et al. injected MB intraoperatively after visualization of the ureters. However, this approach is not comparable to clinical practice. Therefore we recommend to inject MB intravenously after first incision was made (open surgery) or after introduction of the first trocars (laparoscopic surgery). Based on both studies, 0.25 mg/kg MB could be injected, after which the ureters will become visible from 10 up to 60 minutes, as illustrated in Figure 5. A disadvantage of MB is that it is fluorescent at approximately 700 nm, which is subject to higher absorption and more nonspecific background fluorescence. A novel dye, ZW800-1, was therefore developed. This dye is fluorescent at 800 nm, exclusively cleared via the kidneys and has already shown to be safe in a Phase 1 study. [K.S. de Valk et al., unpublished data]

HOW TO USE IT

To summarize, ICG could be used for biliary duct imaging, whereas MB is preferable for ureter mapping. Optimal doses and injection times are 5 mg 3-7 hours before surgery, and 0.25 mg/kg intraoperatively, respectively (Table 1).

Tissue perfusion

Restoring normal functioning and tissue healing after surgical intervention is, among others, critically dependent on tissue perfusion. Insufficient perfusion with oxygenated blood could result in ischemia and subsequent tissue damage. An important clinical problem is anastomotic leakage, which is one of the most serious complication after gastrointestinal surgery.[191,192] Large retrospective cohort studies showed leakage rates up to 19% in case of colorectal surgery.[192] Today, surgeons have to evaluate the anastomotic perfusion by inspection, which is a subjective method and difficult to quantify.[193] Different techniques have been used to evaluate the anastomotic perfusion, however none of them are currently common used in clinical practice, due to their disadvantages.[194]

Intraoperative evaluation of liver perfusion is also a clinical relevant issue, especially for determining the effect of the resection on the liver function, however currently no good intraoperative tools are available. Some studies suggests the use of contrast enhanced ultrasound, as an additional tool for resection planning.[195,196] Due to the characteristic of ICG binding to plasma proteins, it will mainly remain intravascular after intravenously injection, which makes it a perfect candidate for perfusion imaging.

CLINICAL APPLICATIONS

Anastomotic bowel perfusion

Since the introduction of NIR fluorescence imaging, 11 clinical studies reported the use of ICG as a NIR fluorescent agent in evaluation of the esophagogastric anastomosis.[24,194,197-205] One study compared the anastomotic leakage (AL) rate in perfusion detection both with and without the use of ICG fluorescence imaging, which resulted in reducing the rate from 20% to 0%.[205] Twenty-one clinical trials reported the use of ICG as a NIR fluorescence agent with different imaging systems in intraoperative evaluation of colorectal anastomoses.[180,206-225] ICG was often injected after anastomotic site selection to evaluate the effect of ICG in selecting the correct anastomotic site. This resulted in the change of surgical plan between 3.7% and 40%. Some studies also evaluated the rate of the AL with using ICG and it was shown in a recent systematic review that the rate of AL decreases from 8.5 to 3.3 % in the group which used ICG.[226] On the other hand, a case-matched retrospective study in 346 patients did not show a significant decline in AL (7.5% vs 6.4%), although the anastomotic site was changed in 5% of the patients.[214]

Summary of findings

Based on the above mentioned studies we recommend the following approach. First of all, normal surgical procedure could be started according to standard of care. Before performing the anastomosis, 2.5 mg of ICG dye can be injected intravenously, which is based on the doses used in most of the clinical trials.[197-200,202,203] However, most studies in colorectal surgery used ICG injection doses varying from 0.2 to 0.5 mg/kg.[206,213,221,223,224] Nevertheless, it was shown that the colorectal anastomotic perfusion could also be visualized by using a much lower and less toxic dose (2.5 mg), which is in concordance with the optimal dose used for evaluation gastroesophageal anastomotic perfusion.[210,212] Hence, we recommend an intravenously injection of 2.5 mg ICG for both types of anastomoses. Within 60 seconds the vasculature will be visible and the anastomotic site can be visualized with NIR fluorescence imaging.[209,210,212,215,223] If the fluorescence signal starts to fade, another bolus of 2.5 mg ICG can be injected to evaluate the perfusion for a second look (>15 minutes after first injection). If a good perfusion was detected with NIR fluorescence imaging, the procedure could be finished as usual.

Hepatic perfusion during liver segmentectomy

Due to the complex liver anatomy, liver surgery is only performed in high volume centers. Especially, during oncologic surgery, it is difficult to determine the resection margins and to estimate the remnant liver volume in order to achieve the optimal balance between cancer curability and postoperative hepatic function. The portal and hepatic veins are the important anatomical landmarks used for resection planning. Seven studies evaluated the use of ICG for determining the resection planes during liver surgery.[104,110,117,164,227-229] In 89% to 100% of the performed surgeries, the resection lines could be easily visualized.

Summary of findings

After clamping of the selected portal branch, ICG could be injected, resulting in highlighted liver, except of the less-perfused part of the liver. Two methods of injection (portal vein and peripheral vein) were evaluated. The used doses of ICG varied from 1.25 mg to 0.5 mg/kg.[104,110,117,164,227-229] However, Inoue et al. showed comparable results of portal vein and peripheral vein injection with 2.5 mg ICG, which we therefore recommend as the optimal dose.[228] Intraportal ICG injection could be performed under ultrasonic guidance after clamping the proximal portal pedicle. An alternative for portal injection is an intravenously (in a peripheral vein) ICG injection after clamping of the selected portal vein, which we prefer during laparoscopic surgery, due to the technical difficulties with portal injection. A disadvantage of intravenously ICG injection is the lower concentration of ICG available than using the intraportal injection method.[228] The liver segments become fluorescent after one to two minutes.[104,227]

HOW TO USE IT

For optimal evaluation of anastomotic bowel and liver segment perfusion a 2.5 mg intravenously injection of ICG is recommended. After intraoperative injection, the vasculature becomes visible after approximately one to two minutes (Table 1).

Discussion and future perspectives

NIR fluorescence imaging has been widely evaluated during the past decades. Several clinical studies have been performed with different conditions and therapeutic doses of contrast agents. Hence, it may be difficult for surgeons to directly apply these new techniques in daily practice, although the technique itself is fairly straightforward and has a limited learning curve. This review focussed on its application with the currently only available contrast agents, ICG and MB, during oncologic abdominal surgery, of which a summary was given in Table 1. We evaluated the timing of the injection, the injection locations, and the dose of contrast agents, which could guide the surgeon for intraoperative use of the different applications of NIR fluorescence imaging in abdominal oncologic surgery.

The use of ICG, contributes to a better visibility of sentinel lymph nodes, biliary ducts and tissue perfusion, than current image modalities or surgeons visual/tactical feedback. Furthermore, liver tumors could be easily identified with ICG, because of its clearing by the liver, whereas it is not specific for other types of solid abdominal tumors in the abdomen, such as pancreatic and renal tumors.[140,144] Moreover, we have shown that intraoperative visualization of peritoneal metastases and adrenal tumors using ICG is feasible and could therefore be used as an additional intraoperative image modality until specific tumor targets are available. Today, no evidence is available for intraoperative visualization of nerves, which is important during colorectal surgery, using ICG due to its non-specificity.[230-232] Therefore, diverse other nerve specific contrast agents are currently being investigated.[233-237]

MB was evaluated for ureter detection, however its clinical use during abdominal surgery, would be limited subject due to higher absorption and more nonspecific background fluorescence. Hence, a specific antibody binding to a fluorophore, ZW800-1, has been evaluated and showed better ureter visibility than MB in preclinically testing.[238] Moreover, it was also described that MB could be useful in abdominal surgery for detection of neuroendocrine tumors. However, the evidence is limited to one preclinical mice study and a case report of a patient with a paraganglioma, and should therefore be further validated in new studies.[239,240]

To improve the tumor visibility during oncologic surgery, (new) NIR fluorophores, such as IRDye-800CW, were combined with tumor-specific targets as described by Haque et al.[241] Diverse specific tumor-specific fluorophores have been investigated during the last years, for instance in patients with colorectal cancer (during endoscopy), ovarian cancer, renal cell carcinoma, and peritonitis carcinomatosa.[242-246] Currently, more clinical trials in patients with pancreatic, colorectal and renal cancer are underway.[NCT02743975, NCT02317705, NCT01778933, NCT02973672]

Although we have shown the great progress made using NIR fluorescence imaging, it also has his limitations. The most important drawback is the lack of quantitative comparison of fluorescence signals in the currently published studies. Especially, for evaluation of anastomotic bowel perfusion, most of them did not take into account the over-time diffusion of the used NIR fluorophore, resulting in an overestimation of the fluorescence signal in vascularized areas. Diana et al. developed

a quantitative software based analysis which calculates the stiffness of the slope of the fluorescence signal to reach the peak intensity, given the fact this is the most important perfusion marker.[247-250] Based on those parameters, a virtual bowel perfusion cartography is created, which could be superimposed on the white light images, resulting in a nearly real-time quantitative perfusion image, as shown in Figure 6.

Today, NIR fluorescence imaging is performed in the classic first NIR window, between 650 and 950 nm. The penetration depth of NIR light in the first NIR window is up to 1 cm and therefore limited for detection of superficial lesions, however it could even be useful for intraoperative margin assessment.[123] NIR fluorescence imaging systems, capable of imaging in the second NIR or shortwave infrared window (1000-1700 nm), will allow more in depth visibility of structures.

In conclusion, ICG and MB are relatively safe and sensitive non-specific fluorophores, which have been widely evaluated in NIR fluorescence imaging. In the nearby future, more specific tumor targets will be evaluated and used in clinical practice, which will provide new opportunities in the field of abdominal surgery.

Table 1. Summary of known clinical applications of near-infrared fluorescence imaging in abdominal surgery and recommendations for intraoperative use.

Application	Tissue type	Imaging system used in different studies	Preferred contrast agent	Recommended dose (mg)	Preferred injection	Timing of injection	Time to visualize structures (minutes)
SLN mapping	Oesophagus	laparoscopic	Indocyanine green	2.5	Endoscopic: 4 quadrants injection	Just before surgery	15-30
	Gastric	laparoscopic, open	Indocyanine green	2.5	Endoscopic: 4 quadrants injection	Just before surgery	15-30
	Colorectal	laparoscopic, open	Indocyanine green	2.5	Subserosal: 4 quadrants injection	Intraoperatively	15-30
	Bladder	Robotic, open	Indocyanine green	2.5	Cystoscopic: bladder mucosa	Intraoperatively	15-30
	Prostate	Robotic, laparoscopic	Indocyanine green	2.5	Transrectal: under US guidance into prostate lobes	Intraoperatively	15-30
	Cervix	Laparoscopic, robotic	Indocyanine green	2.5	Transvaginal: Submucosa cervix 4 quadrants injection	Intraoperatively	15-30
	Endometrium	Laparoscopic, robotic	Indocyanine green	2.5	Transvaginal: submucosa cervix 4 quadrants injection	Intraoperatively	15-30
	Ovarium	Laparoscopic	Indocyanine green	2.5	Laparoscopic: dorsal and ventral side of proper ovarian and the suspensory ligament	Intraoperatively	15-30
Tumor imaging	Liver	Open, laparoscopic	Indocyanine green	10	Intravenously	24 hours before surgery	Directly
	Adrenal	Laparoscopic, robotic	Indocyanine green	5	Intravenously	Intraoperatively	1
	Peritoneal metastases	Open	Indocyanine green	0.25 (mg/kg)	Intravenously	Intraoperatively	>5
Vital structures	Bile duct	laparoscopic	Indocyanine green	5	Intravenously	3 to 7 hours before surgery	Directly
					Into gallbladder	Intraoperatively	Directly
	Ureter	Open, laparoscopic, robotic	Methylene blue	0.25 (mg/kg)	Intravenously	Intraoperatively	>10
Perfusion	Esophagogastric anastomoses	laparoscopic, robotic	Indocyanine green	2.5	Intravenously	After mobilization and selecting of anastomotic site	1
	Colorectal anastomoses	Open, laparoscopic, robotic	Indocyanine green	2.5	Intravenously	After mobilization and selecting of anastomotic site	1
	Liver segments	Open	Indocyanine green	2.5	Portal vein	During surgery	2
		Laparoscopic	Indocyanine green	2.5	Intravenously	During surgery	2

Figure 1. Flow-chart of the literature search strategy.

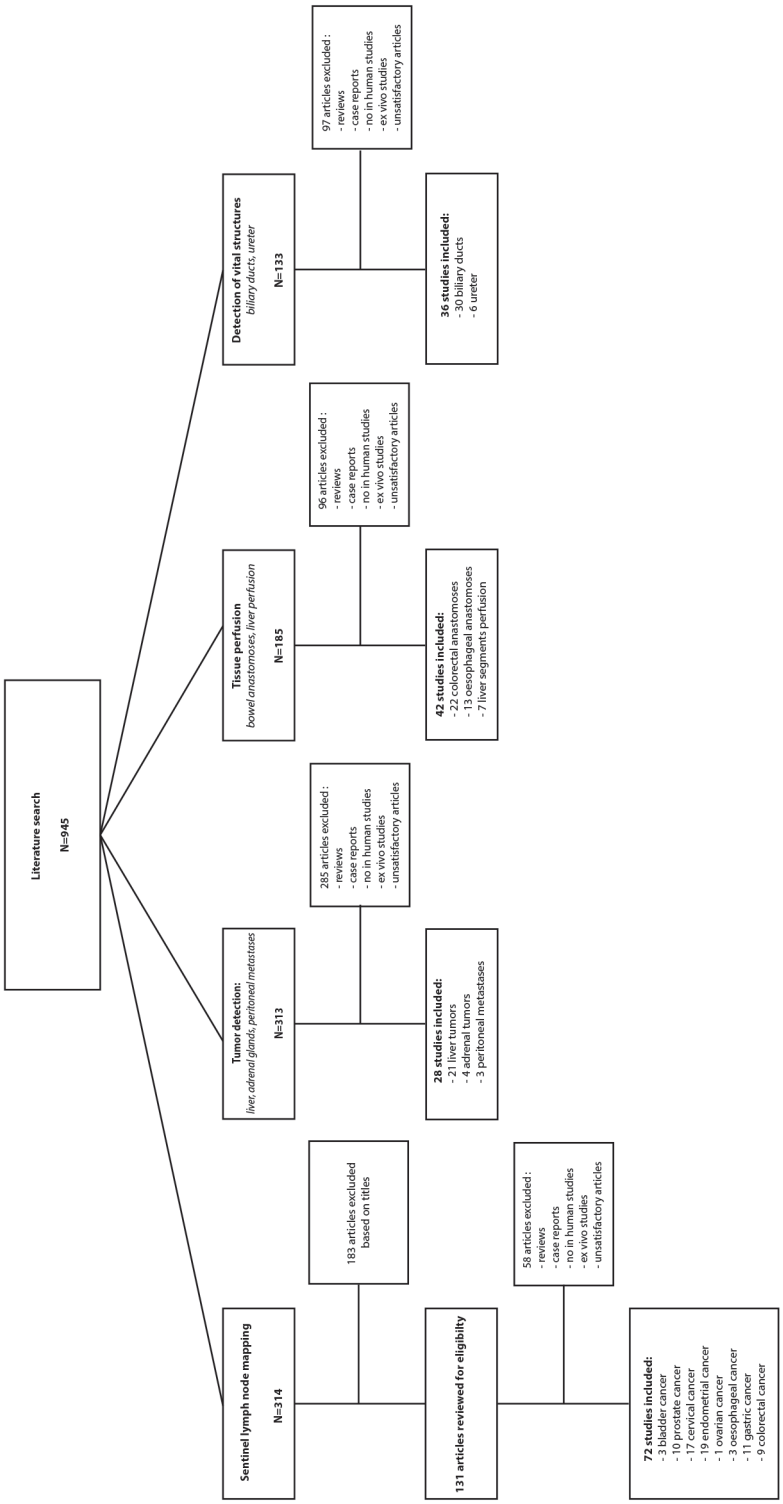

Figure 2. Example of lymph node mapping in bladder cancer during surgery and *ex vivo*. *Upper panel:* arrowheads indicate the NIR fluorescent lymph nodes along the left external iliac vein during surgery. *Lower panel:* Fluorescent lymph nodes after excision. Reprinted by permission from John Wiley and Sons: Journal of Surgical Oncology [49] © 2014.

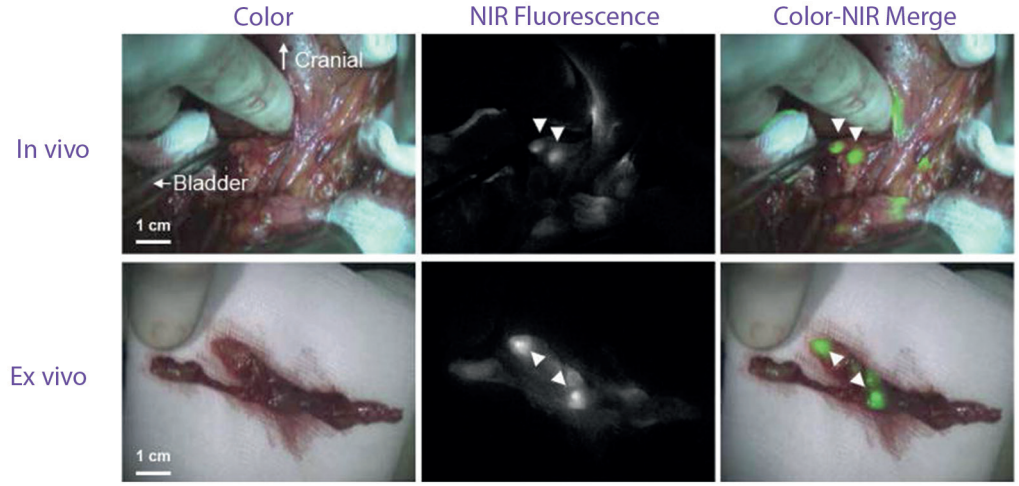

Figure 3. Example of two colorectal liver metastases detected by NIRF imaging. *White arrow:* a fluorescent lesion, which was not detected by preoperative imaging. *Dashed arrow:* a preoperative suspected lesion could be recognised by its characterizing fluorescent rim. Reprinted by permission from Elsevier: European Journal of Surgical Oncology [103]. © 2017.

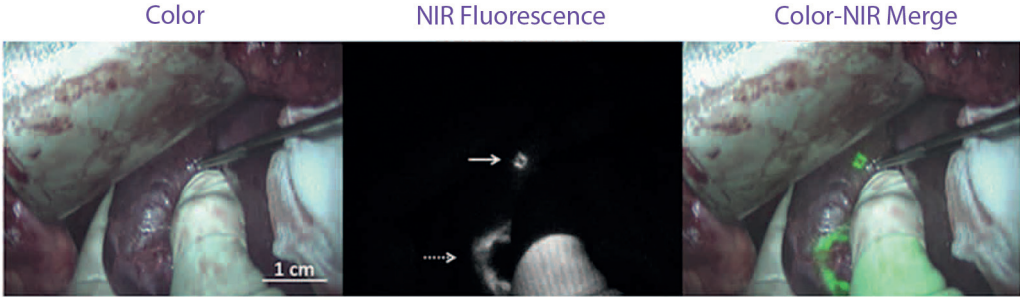

Figure 4. Example of bile duct imaging using ICG 24 h after injection. The position of the common bile duct was indicated by the arrow; the liver by L; and surrounding adipose tissue by Ad. Adapted and reprinted by permission from Springer Nature: Surgical Endoscopy [171]. © 2014.

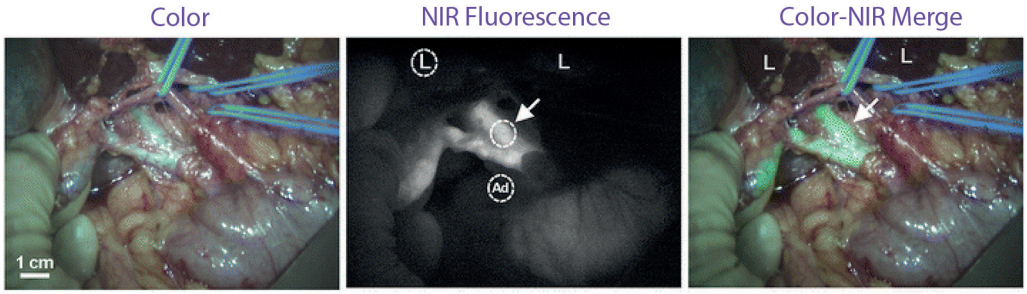

Figure 5. Example of ureter imaging using MB. *Upper panel:* NIRF image of right ureter, 45 minutes after MB administration. *Lower panel:* NIRF image of right ureter, covered by blood and tissue. Reprinted by permission from Elsevier: The Journal of Urology [190]. © 2013.

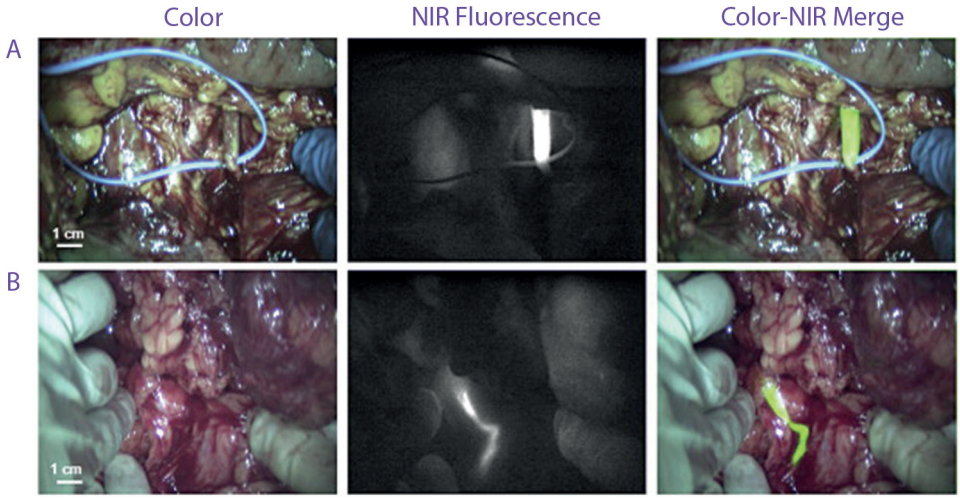

Figure 6. The concept of quantitative fluorescence measurements (Fluorescence-based Enhanced Reality=FLER) for determining the bowel perfusion. *Upper panel:* The fluorescence signal is analysed during 40 seconds after intravenous administration of ICG. Using specific software (VR-PERFUSION, IRCAD; France) the slope of the fluorescence time-to-peak is computed and converted to color codes, resulting in a virtual perfusion cartography. *Lower panel:* The white light image is combined with the perfusion cartography, creating an augmented reality view of the bowel perfusion at the resection site.

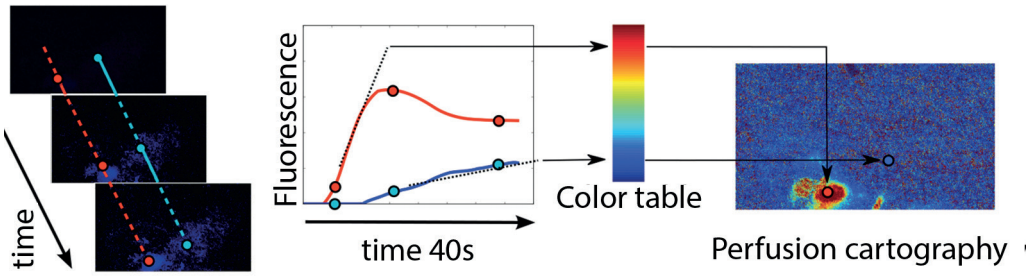

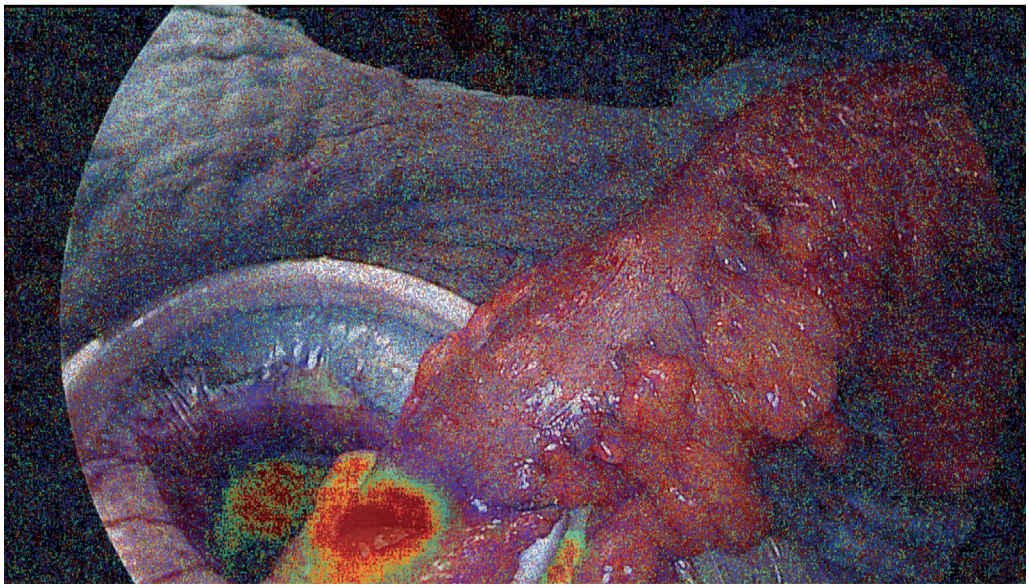

References

1. Steward, B., and Christopher P. Wild. Worldcancerreport World Health Organization (2016).
2. Kubben PL, ter Meulen KJ, Schijns OE, et al.: Intraoperative MRI-guided resection of glioblastoma multiforme: a systematic review. The Lancet Oncology 2011;12:1062-1070.
3. Tilly C, Lefevre JH, Svrcek M, et al.: R1 rectal resection: look up and don't look down. Annals of surgery 2014;260:794-799; discussion 799-800.
4. Khan MA, Hakeem AR, Scott N, Saunders RN: Significance of R1 resection margin in colon cancer resections in the modern era. Colorectal disease : the official journal of the Association of Coloproctology of Great Britain and Ireland 2015;17:943-953.
5. Mondal SB, Gao S, Zhu N, et al.: Real-time fluorescence image-guided oncologic surgery. Advances in cancer research 2014;124:171-211.
6. AV DS, Lin H, Henderson ER, et al.: Review of fluorescence guided surgery systems: identification of key performance capabilities beyond indocyanine green imaging. Journal of Biomedical Optics 2016;21.
7. Gioux S, Choi HS, Frangioni JV: Image-guided surgery using invisible near-infrared light: fundamentals of clinical translation. Molecular imaging 2010;9:237-255.
8. Handgraaf HJ, Verbeek FP, Tummers QR, et al.: Real-time near-infrared fluorescence guided surgery in gynecologic oncology: a review of the current state of the art. Gynecologic oncology 2014;135:606-613.
9. Chance B: Near-infrared images using continuous, phase-modulated, and pulsed light with quantitation of blood and blood oxygenation. Annals of the New York Academy of Sciences 1998;838:29-45.
10. Frangioni JV: In vivo near-infrared fluorescence imaging. Current opinion in chemical biology 2003;7:626-634.
11. Stammes MA, Bugby SL, Porta T, et al.: Modalities for image- and molecular-guided cancer surgery. The British journal of surgery 2018;105:e69-e83.
12. Stummer W, Pichlmeier U, Meinel T, et al.: Fluorescence-guided surgery with 5-aminolevulinic acid for resection of malignant glioma: a randomised controlled multicentre phase III trial. The Lancet Oncology 2006;7:392-401.
13. Shimizu S, Kamiike W, Hatanaka N, et al.: New method for measuring ICG Rmax with a clearance meter. World journal of surgery 1995;19:113-118; discussion 118.
14. Benya R, Quintana J, Brundage B: Adverse reactions to indocyanine green: a case report and a review of the literature. Catheterization and cardiovascular diagnosis 1989;17:231-233.
15. Ginimuge PR, Jyothi SD: Methylene blue: revisited. Journal of anaesthesiology, clinical pharmacology 2010;26:517-520.
16. Valsecchi ME, Silbermins D, de Rosa N, et al.: Lymphatic mapping and sentinel lymph node biopsy in patients with melanoma: a meta-analysis. Journal of clinical oncology : official journal of the American Society of Clinical Oncology 2011;29:1479-1487.
17. He PS, Li F, Li GH, et al.: The combination of blue dye and radioisotope versus radioisotope alone during sentinel lymph node biopsy for breast cancer: a systematic review. BMC cancer 2016;16:107.
18. Hayashi H, Ochiai T, Mori M, et al.: Sentinel lymph node mapping for gastric cancer using a dual procedure with dye- and gamma probe-guided techniques. Journal of the American College of Surgeons 2003;196:68-74.
19. Levenback CF, van der Zee AG, Rob L, et al.: Sentinel lymph node biopsy in patients with gynecologic cancers Expert panel statement from the International Sentinel Node Society Meeting, February 21, 2008. Gynecologic oncology 2009;114:151-156.
20. Dubecz A, Gall I, Solymosi N, et al.: Temporal trends in long-term survival and cure rates in esophageal cancer: a SEER database analysis. Journal of thoracic oncology : official publication of the International Association for the Study of Lung Cancer 2012;7:443-447.
21. Lerut T, Nafteux P, Moons J, et al.: Three-field lymphadenectomy for carcinoma of the esophagus and gastroesophageal junction in 174 R0 resections: impact on staging, disease-free survival, and outcome: a plea for adaptation of TNM classification in upper-half esophageal carcinoma. Annals of surgery 2004;240:962-972; discussion 972-964.
22. Nishihira T, Hirayama K, Mori S: A prospective randomized trial of extended cervical and superior mediastinal lymphadenectomy for carcinoma of the thoracic esophagus. American journal of surgery 1998;175:47-51.
23. Peyre CG, Hagen JA, DeMeester SR, et al.: The number of lymph nodes removed predicts survival in esophageal cancer: an international study on the impact of extent of surgical resection. Annals of surgery 2008;248:549-556.
24. Kubota K, Yoshida M, Kuroda J, et al.: Application of the HyperEye Medical System for esophageal cancer surgery: a preliminary report. Surgery today 2013;43:215-220.
25. Yuasa Y, Seike J, Yoshida T, et al.: Sentinel lymph node biopsy using intraoperative indocyanine green fluorescence imaging navigated with preoperative CT lymphography for superficial esophageal cancer. Annals of surgical oncology 2012;19:486-493.
26. Hachey KJ, Gilmore DM, Armstrong KW, et al.: Safety and feasibility of near-infrared image-guided lymphatic mapping of regional lymph nodes in esophageal cancer. The Journal of thoracic and cardiovascular surgery 2016;152:546-554.
27. Fujita T, Seshimo A, Kameoka S: Detection of sentinel nodes in gastric cancer by indocyanine green fluorescence imaging. Hepato-gastroenterology 2012;59:2213-2216.
28. Kinami S, Oonishi T, Fujita J, et al.: Optimal settings and accuracy of indocyanine green fluorescence imaging for sentinel node biopsy in early gastric cancer. Oncology letters 2016;11:4055-4062.
29. Kusano M, Tajima Y, Yamazaki K, et al.: Sentinel node mapping guided by indocyanine green fluorescence imaging: a new method for sentinel node navigation surgery in gastrointestinal cancer. Digestive surgery 2008;25:103-108.
30. Miyashiro I, Miyoshi N, Hiratsuka M, et al.: Detection of sentinel node in gastric cancer surgery by indocyanine green fluorescence imaging: comparison with infrared imaging. Annals of surgical oncology 2008;15:1640-1643.
31. Miyashiro I, Kishi K, Yano M, et al.: Laparoscopic detection of sentinel node in gastric cancer surgery by indocyanine green fluorescence imaging. Surgical endoscopy 2011;25:1672-1676.
32. Tajima Y, Murakami M, Yamazaki K, et al.: Sentinel node mapping guided by indocyanine green fluorescence imaging during laparoscopic surgery in gastric cancer. Annals of surgical oncology 2010;17:1787-1793.

33. Takahashi N, Nimura H, Fujita T, et al.: Laparoscopic sentinel node navigation surgery for early gastric cancer: a prospective multicenter trial. Langenbeck's archives of surgery 2017;402:27-32.
34. Yoshida M, Kubota K, Kuroda J, et al.: Indocyanine green injection for detecting sentinel nodes using color fluorescence camera in the laparoscopy-assisted gastrectomy. Journal of gastroenterology and hepatology 2012;27 Suppl 3:29-33.
35. Tummers QR, Boogerd LS, de Steur WO, et al.: Near-infrared fluorescence sentinel lymph node detection in gastric cancer: A pilot study. World journal of gastroenterology 2016;22:3644-3651.
36. Tajima Y, Yamazaki K, Masuda Y, et al.: Sentinel node mapping guided by indocyanine green fluorescence imaging in gastric cancer. Annals of surgery 2009;249:58-62.
37. Bok GH, Kim YJ, Jin SY, et al.: Endoscopic submucosal dissection with sentinel node navigation surgery for early gastric cancer. Endoscopy 2012;44:953-956.
38. Bembenek AE, Rosenberg R, Wagler E, et al.: Sentinel lymph node biopsy in colon cancer: a prospective multicenter trial. Annals of surgery 2007;245:858-863.
39. Andersen HS, Bennedsen ALB, Burgdorf SK, et al.: In vivo and ex vivo sentinel node mapping does not identify the same lymph nodes in colon cancer. International journal of colorectal disease 2017;32:983-990.
40. Ankersmit M, van der Pas MH, van Dam DA, Meijerink WJ: Near infrared fluorescence lymphatic laparoscopy of the colon and mesocolon. Colorectal disease : the official journal of the Association of Coloproctology of Great Britain and Ireland 2011;13 Suppl 7:70-73.
41. Cahill RA, Anderson M, Wang LM, et al.: Near-infrared (NIR) laparoscopy for intraoperative lymphatic road-mapping and sentinel node identification during definitive surgical resection of early-stage colorectal neoplasia. Surgical endoscopy 2012;26:197-204.
42. Hirche C, Mohr Z, Kneif S, et al.: Ultrastaging of colon cancer by sentinel node biopsy using fluorescence navigation with indocyanine green. International journal of colorectal disease 2012;27:319-324.
43. van der Pas MH, Ankersmit M, Stockmann HB, et al.: Laparoscopic sentinel lymph node identification in patients with colon carcinoma using a near-infrared dye: description of a new technique and feasibility study. Journal of laparoendoscopic & advanced surgical techniques Part A 2013;23:367-371.
44. Noura S, Ohue M, Seki Y, et al.: Feasibility of a lateral region sentinel node biopsy of lower rectal cancer guided by indocyanine green using a near-infrared camera system. Annals of surgical oncology 2010;17:144-151.
45. Currie AC, Brigic A, Thomas-Gibson S, et al.: A pilot study to assess near infrared laparoscopy with indocyanine green (ICG) for intraoperative sentinel lymph node mapping in early colon cancer. European journal of surgical oncology : the journal of the European Society of Surgical Oncology and the British Association of Surgical Oncology 2017.
46. Handgraaf HJ, Boogerd LS, Verbeek FP, et al.: Intraoperative fluorescence imaging to localize tumors and sentinel lymph nodes in rectal cancer. Minimally invasive therapy & allied technologies : MITAT : official journal of the Society for Minimally Invasive Therapy 2016;25:48-53.
47. Hurle R, Naspro R: Pelvic lymphadenectomy during radical cystectomy: a review of the literature. Surgical oncology 2010;19:208-220.
48. Polom W, Markuszewski M, Cytawa W, et al.: Fluorescent Versus Radioguided Lymph Node Mapping in Bladder Cancer. Clinical genitourinary cancer 2017;15:e405-e409.
49. Schaafsma BE, Verbeek FP, Elzevier HW, et al.: Optimization of sentinel lymph node mapping in bladder cancer using near-infrared fluorescence imaging. Journal of surgical oncology 2014;110:845-850.
50. Manny TB, Hemal AK: Fluorescence-enhanced robotic radical cystectomy using unconjugated indocyanine green for pelvic lymphangiography, tumor marking, and mesenteric angiography: the initial clinical experience. Urology 2014;83:824-829.
51. Siegel RL, Miller KD, Jemal A: Cancer Statistics, 2017. CA: a cancer journal for clinicians 2017;67:7-30.
52. Cagiannos I, Karakiewicz P, Eastham JA, et al.: A preoperative nomogram identifying decreased risk of positive pelvic lymph nodes in patients with prostate cancer. The Journal of urology 2003;170:1798-1803.
53. Hansen J, Rink M, Bianchi M, et al.: External validation of the updated Briganti nomogram to predict lymph node invasion in prostate cancer patients undergoing extended lymph node dissection. The Prostate 2013;73:211-218.
54. Chennamsetty A, Zhumkhawala A, Tobis SB, et al.: Lymph Node Fluorescence During Robot-Assisted Radical Prostatectomy With Indocyanine Green: Prospective Dosing Analysis. Clinical genitourinary cancer 2017;15:e529-e534.
55. Morozov AO, Alyaev YG, Rapoport LM, et al.: Near-infrared fluorescence with indocyanine green for diagnostics in urology: initial experience. Urologia 2017;84:197-202.
56. Nguyen DP, Huber PM, Metzger TA, et al.: A Specific Mapping Study Using Fluorescence Sentinel Lymph Node Detection in Patients with Intermediate- and High-risk Prostate Cancer Undergoing Extended Pelvic Lymph Node Dissection. European urology 2016;70:734-737.
57. Hruby S, Englberger C, Lusuardi L, et al.: Fluorescence Guided Targeted Pelvic Lymph Node Dissection for Intermediate and High Risk Prostate Cancer. The Journal of urology 2015;194:357-363.
58. Ramirez-Backhaus M, Mira Moreno A, Gomez Ferrer A, et al.: Indocyanine Green Guided Pelvic Lymph Node Dissection: An Efficient Technique to Classify the Lymph Node Status of Patients with Prostate Cancer Who Underwent Radical Prostatectomy. The Journal of urology 2016;196:1429-1435.
59. van den Berg NS, Buckle T, KleinJan GH, et al.: Multispectral Fluorescence Imaging During Robot-assisted Laparoscopic Sentinel Node Biopsy: A First Step Towards a Fluorescence-based Anatomic Roadmap. European urology 2017;72:110-117.
60. KleinJan GH, van den Berg NS, de Jong J, et al.: Multimodal hybrid imaging agents for sentinel node mapping as a means to (re)connect nuclear medicine to advances made in robot-assisted surgery. European journal of nuclear medicine and molecular imaging 2016;43:1278-1287.
61. Yuen K, Miura T, Sakai I, et al.: Intraoperative Fluorescence Imaging for Detection of Sentinel Lymph Nodes and Lymphatic Vessels during Open Prostatectomy using Indocyanine Green. The Journal of urology 2015;194:371-377.
62. Manny TB, Patel M, Hemal AK: Fluorescence-enhanced robotic radical prostatectomy using real-time lymphangiography and tissue marking with percutaneous injection of unconjugated indocyanine green: the initial clinical experience in 50 patients. European urology

2014;65:1162-1168.
63. Jeschke S, Lusuardi L, Myatt A, et al.: Visualisation of the lymph node pathway in real time by laparoscopic radioisotope- and fluorescence-guided sentinel lymph node dissection in prostate cancer staging. Urology 2012;80:1080-1086.
64. van der Poel HG, Buckle T, Brouwer OR, et al.: Intraoperative laparoscopic fluorescence guidance to the sentinel lymph node in prostate cancer patients: clinical proof of concept of an integrated functional imaging approach using a multimodal tracer. European urology 2011;60:826-833.
65. Averette HE, Nguyen HN, Donato DM, et al.: Radical hysterectomy for invasive cervical cancer. A 25-year prospective experience with the Miami technique. Cancer 1993;71:1422-1437.
66. Di Stefano AB, Acquaviva G, Garozzo G, et al.: Lymph node mapping and sentinel node detection in patients with cervical carcinoma: a 2-year experience. Gynecologic oncology 2005;99:671-679.
67. Crane LM, Themelis G, Pleijhuis RG, et al.: Intraoperative multispectral fluorescence imaging for the detection of the sentinel lymph node in cervical cancer: a novel concept. Molecular imaging and biology : MIB : the official publication of the Academy of Molecular Imaging 2011;13:1043-1049.
68. Buda A, Bussi B, Di Martino G, et al.: Sentinel Lymph Node Mapping With Near-Infrared Fluorescent Imaging Using Indocyanine Green: A New Tool for Laparoscopic Platform in Patients With Endometrial and Cervical Cancer. Journal of minimally invasive gynecology 2016;23:265-269.
69. Laios A, Volpi D, Tullis ID, et al.: A prospective pilot study of detection of sentinel lymph nodes in gynaecological cancers using a novel near infrared fluorescence imaging system. BMC research notes 2015;8:608.
70. Beavis AL, Salazar-Marioni S, Sinno AK, et al.: Sentinel lymph node detection rates using indocyanine green in women with early-stage cervical cancer. Gynecologic oncology 2016;143:302-306.
71. Buda A, Di Martino G, Vecchione F, et al.: Optimizing Strategies for Sentinel Lymph Node Mapping in Early-Stage Cervical and Endometrial Cancer: Comparison of Real-Time Fluorescence With Indocyanine Green and Methylene Blue. International journal of gynecological cancer : official journal of the International Gynecological Cancer Society 2015;25:1513-1518.
72. Buda A, Dell'Anna T, Vecchione F, et al.: Near-Infrared Sentinel Lymph Node Mapping With Indocyanine Green Using the VITOM II ICG Exoscope for Open Surgery for Gynecologic Malignancies. Journal of minimally invasive gynecology 2016;23:628-632.
73. Buda A, Papadia A, Zapardiel I, et al.: From Conventional Radiotracer Tc-99(m) with Blue Dye to Indocyanine Green Fluorescence: A Comparison of Methods Towards Optimization of Sentinel Lymph Node Mapping in Early Stage Cervical Cancer for a Laparoscopic Approach. Annals of surgical oncology 2016;23:2959-2965.
74. Imboden S, Papadia A, Nauwerk M, et al.: A Comparison of Radiocolloid and Indocyanine Green Fluorescence Imaging, Sentinel Lymph Node Mapping in Patients with Cervical Cancer Undergoing Laparoscopic Surgery. Annals of surgical oncology 2015;22:4198-4203.
75. Paredes P, Vidal-Sicart S, Campos F, et al.: Role of ICG-99mTc-nanocolloid for sentinel lymph node detection in cervical cancer: a pilot study. European journal of nuclear medicine and molecular imaging 2017.
76. Di Martino G, Crivellaro C, De Ponti E, et al.: Indocyanine Green versus Radiotracer with or without Blue Dye for Sentinel Lymph Node Mapping in Stage >IB1 Cervical Cancer (>2 cm). Journal of minimally invasive gynecology 2017;24:954-959.
77. Lopez Labrousse MI, Frumovitz M, Guadalupe Patrono M, Ramirez PT: Sentinel lymph node mapping in minimally invasive surgery: Role of imaging with color-segmented fluorescence (CSF). Gynecologic oncology 2017;146:676-677.
78. Jewell EL, Huang JJ, Abu-Rustum NR, et al.: Detection of sentinel lymph nodes in minimally invasive surgery using indocyanine green and near-infrared fluorescence imaging for uterine and cervical malignancies. Gynecologic oncology 2014;133:274-277.
79. Schaafsma BE, van der Vorst JR, Gaarenstroom KN, et al.: Randomized comparison of near-infrared fluorescence lymphatic tracers for sentinel lymph node mapping of cervical cancer. Gynecologic oncology 2012;127:126-130.
80. Rossi EC, Ivanova A, Boggess JF: Robotically assisted fluorescence-guided lymph node mapping with ICG for gynecologic malignancies: a feasibility study. Gynecologic oncology 2012;124:78-82.
81. van der Vorst JR, Hutteman M, Gaarenstroom KN, et al.: Optimization of near-infrared fluorescent sentinel lymph node mapping in cervical cancer patients. International journal of gynecological cancer : official journal of the International Gynecological Cancer Society 2011;21:1472-1478.
82. Furukawa N, Oi H, Yoshida S, et al.: The usefulness of photodynamic eye for sentinel lymph node identification in patients with cervical cancer. Tumori 2010;96:936-940.
83. Buda A, Di Martino G, De Ponti E, et al.: Laparoscopic Sentinel Node Mapping in Cervical and Endometrial Malignancies: A Case-Control Study Comparing Two Near-Infrared Fluorescence Systems. Journal of minimally invasive gynecology 2017.
84. Orr JW, Jr., Holloway RW, Orr PF, Holimon JL: Surgical staging of uterine cancer: an analysis of perioperative morbidity. Gynecologic oncology 1991;42:209-216.
85. Abu-Rustum NR: Sentinel lymph node mapping for endometrial cancer: a modern approach to surgical staging. Journal of the National Comprehensive Cancer Network : JNCCN 2014;12:288-297.
86. Yamagami W, Susumu N, Kataoka F, et al.: A Comparison of Dye Versus Fluorescence Methods for Sentinel Lymph Node Mapping in Endometrial Cancer. International journal of gynecological cancer : official journal of the International Gynecological Cancer Society 2017;27:1517-1524.
87. Rossi EC, Jackson A, Ivanova A, Boggess JF: Detection of sentinel nodes for endometrial cancer with robotic assisted fluorescence imaging: cervical versus hysteroscopic injection. International journal of gynecological cancer : official journal of the International Gynecological Cancer Society 2013;23:1704-1711.
88. Papadia A, Zapardiel I, Bussi B, et al.: Sentinel lymph node mapping in patients with stage I endometrial carcinoma: a focus on bilateral mapping identification by comparing radiotracer Tc99m with blue dye versus indocyanine green fluorescent dye. Journal of cancer research and clinical oncology 2017;143:475-480.
89. Paley PJ, Veljovich DS, Press JZ, et al.: A prospective investigation of fluorescence imaging to detect sentinel lymph nodes at robotic-assisted endometrial cancer staging.

American journal of obstetrics and gynecology 2016;215:117.e111-117.
90. Martinelli F, Ditto A, Bogani G, et al.: Laparoscopic Sentinel Node Mapping in Endometrial Cancer After Hysteroscopic Injection of Indocyanine Green. Journal of minimally invasive gynecology 2017;24:89-93.
91. Holloway RW, Ahmad S, Kendrick JE, et al.: A Prospective Cohort Study Comparing Colorimetric and Fluorescent Imaging for Sentinel Lymph Node Mapping in Endometrial Cancer. Annals of surgical oncology 2017;24:1972-1979.
92. Holloway RW, Bravo RA, Rakowski JA, et al.: Detection of sentinel lymph nodes in patients with endometrial cancer undergoing robotic-assisted staging: a comparison of colorimetric and fluorescence imaging. Gynecologic oncology 2012;126:25-29.
93. Hagen B, Valla M, Aune G, et al.: Indocyanine green fluorescence imaging of lymph nodes during robotic-assisted laparoscopic operation for endometrial cancer. A prospective validation study using a sentinel lymph node surgical algorithm. Gynecologic oncology 2016;143:479-483.
94. Geppert B, Lonnerfors C, Bollino M, et al.: A study on uterine lymphatic anatomy for standardization of pelvic sentinel lymph node detection in endometrial cancer. Gynecologic oncology 2017;145:256-261.
95. Eriksson AG, Beavis A, Soslow RA, et al.: A Comparison of the Detection of Sentinel Lymph Nodes Using Indocyanine Green and Near-Infrared Fluorescence Imaging Versus Blue Dye During Robotic Surgery in Uterine Cancer. International journal of gynecological cancer : official journal of the International Gynecological Cancer Society 2017;27:743-747.
96. Eriksson AG, Montovano M, Beavis A, et al.: Impact of Obesity on Sentinel Lymph Node Mapping in Patients with Newly Diagnosed Uterine Cancer Undergoing Robotic Surgery. Annals of surgical oncology 2016;23:2522-2528.
97. Taskin S, Sukur YE, Altin D, et al.: Laparoscopic near-infrared fluorescent imaging as an alternative option for sentinel lymph node mapping in endometrial cancer: A prospective study. International journal of surgery (London, England) 2017;47:13-17.
98. Buda A, Passoni P, Corrado G, et al.: Near-infrared Fluorescence-guided Sentinel Node Mapping of the Ovary With Indocyanine Green in a Minimally Invasive Setting: A Feasible Study. Journal of minimally invasive gynecology 2017;24:165-170.
99. Matsumura Y, Maeda H: A new concept for macromolecular therapeutics in cancer chemotherapy: mechanism of tumoritropic accumulation of proteins and the antitumor agent smancs. Cancer research 1986;46:6387-6392.
100. Maeda H, Wu J, Sawa T, et al.: Tumor vascular permeability and the EPR effect in macromolecular therapeutics: a review. Journal of controlled release : official journal of the Controlled Release Society 2000;65:271-284.
101. Ishizawa T, Masuda K, Urano Y, et al.: Mechanistic background and clinical applications of indocyanine green fluorescence imaging of hepatocellular carcinoma. Annals of surgical oncology 2014;21:440-448.
102. Boogerd LS, Handgraaf HJ, Lam HD, et al.: Laparoscopic detection and resection of occult liver tumors of multiple cancer types using real-time near-infrared fluorescence guidance. Surgical endoscopy 2017;31:952-961.
103. Handgraaf HJM, Boogerd LSF, Hoppener DJ, et al.: Long-term follow-up after near-infrared fluorescence-guided resection of colorectal liver metastases: A retrospective multicenter analysis. European journal of surgical oncology : the journal of the European Society of Surgical Oncology and the British Association of Surgical Oncology 2017;43:1463-1471.
104. Aoki T, Yasuda D, Shimizu Y, et al.: Image-guided liver mapping using fluorescence navigation system with indocyanine green for anatomical hepatic resection. World journal of surgery 2008;32:1763-1767.
105. Yokoyama N, Otani T, Hashidate H, et al.: Real-time detection of hepatic micrometastases from pancreatic cancer by intraoperative fluorescence imaging: preliminary results of a prospective study. Cancer 2012;118:2813-2819.
106. Morita Y, Sakaguchi T, Unno N, et al.: Detection of hepatocellular carcinomas with near-infrared fluorescence imaging using indocyanine green: its usefulness and limitation. International journal of clinical oncology 2013;18:232-241.
107. Ishizuka M, Kubota K, Kita J, et al.: Intraoperative observation using a fluorescence imaging instrument during hepatic resection for liver metastasis from colorectal cancer. Hepato-gastroenterology 2012;59:90-92.
108. Peloso A, Franchi E, Canepa MC, et al.: Combined use of intraoperative ultrasound and indocyanine green fluorescence imaging to detect liver metastases from colorectal cancer. HPB : the official journal of the International Hepato Pancreato Biliary Association 2013;15:928-934.
109. Kudo H, Ishizawa T, Tani K, et al.: Visualization of subcapsular hepatic malignancy by indocyanine-green fluorescence imaging during laparoscopic hepatectomy. Surgical endoscopy 2014;28:2504-2508.
110. Abo T, Nanashima A, Tobinaga S, et al.: Usefulness of intraoperative diagnosis of hepatic tumors located at the liver surface and hepatic segmental visualization using indocyanine green-photodynamic eye imaging. European journal of surgical oncology : the journal of the European Society of Surgical Oncology and the British Association of Surgical Oncology 2015;41:257-264.
111. Shimada S, Ohtsubo S, Ogasawara K, Kusano M: Macro- and microscopic findings of ICG fluorescence in liver tumors. World journal of surgical oncology 2015;13:198.
112. Kawaguchi Y, Nagai M, Nomura Y, et al.: Usefulness of indocyanine green-fluorescence imaging during laparoscopic hepatectomy to visualize subcapsular hard-to-identify hepatic malignancy. Journal of surgical oncology 2015;112:514-516.
113. Kaibori M, Matsui K, Ishizaki M, et al.: Intraoperative Detection of Superficial Liver Tumors by Fluorescence Imaging Using Indocyanine Green and 5-aminolevulinic Acid. Anticancer research 2016;36:1841-1849.
114. Zhang YM, Shi R, Hou JC, et al.: Liver tumor boundaries identified intraoperatively using real-time indocyanine green fluorescence imaging. Journal of cancer research and clinical oncology 2017;143:51-58.
115. Takahashi H, Zaidi N, Berber E: An initial report on the intraoperative use of indocyanine green fluorescence imaging in the surgical management of liver tumorss. Journal of surgical oncology 2016;114:625-629.
116. Masuda K, Kaneko J, Kawaguchi Y, et al.: Diagnostic accuracy of indocyanine green fluorescence imaging and multidetector row computed tomography for identifying hepatocellular carcinoma with liver explant correlation. Hepatology research : the official journal of the Japan Society of Hepatology 2017.
117. Terasawa M, Ishizawa T, Mise Y, et al.: Applications of fusion-fluorescence imaging using indocyanine green in laparoscopic hepatectomy. Surgical endoscopy 2017.
118. Gotoh K, Yamada T, Ishikawa O, et al.: A novel image-guided

surgery of hepatocellular carcinoma by indocyanine green fluorescence imaging navigation. Journal of surgical oncology 2009;100:75-79.
119. Uchiyama K, Ueno M, Ozawa S, et al.: Combined use of contrast-enhanced intraoperative ultrasonography and a fluorescence navigation system for identifying hepatic metastases. World journal of surgery 2010;34:2953-2959.
120. Ishizawa T, Fukushima N, Shibahara J, et al.: Real-time identification of liver cancers by using indocyanine green fluorescent imaging. Cancer 2009;115:2491-2504.
121. Tummers QR, Verbeek FP, Prevoo HA, et al.: First experience on laparoscopic near-infrared fluorescence imaging of hepatic uveal melanoma metastases using indocyanine green. Surgical innovation 2015;22:20-25.
122. van der Vorst JR, Schaafsma BE, Hutteman M, et al.: Near-infrared fluorescence-guided resection of colorectal liver metastases. Cancer 2013;119:3411-3418.
123. Vahrmeijer AL, Hutteman M, van der Vorst JR, et al.: Image-guided cancer surgery using near-infrared fluorescence. Nature reviews Clinical oncology 2013;10:507-518.
124. Holzapfel K, Reiser-Erkan C, Fingerle AA, et al.: Comparison of diffusion-weighted MR imaging and multidetector-row CT in the detection of liver metastases in patients operated for pancreatic cancer. Abdominal imaging 2011;36:179-184.
125. Hariharan D, Constantinides VA, Froeling FE, et al.: The role of laparoscopy and laparoscopic ultrasound in the preoperative staging of pancreatico-biliary cancers--A meta-analysis. European journal of surgical oncology : the journal of the European Society of Surgical Oncology and the British Association of Surgical Oncology 2010;36:941-948.
126. de Bree E, Koops W, Kroger R, et al.: Peritoneal carcinomatosis from colorectal or appendiceal origin: correlation of preoperative CT with intraoperative findings and evaluation of interobserver agreement. Journal of surgical oncology 2004;86:64-73.
127. Kuijpers AM, Mirck B, Aalbers AG, et al.: Cytoreduction and HIPEC in the Netherlands: nationwide long-term outcome following the Dutch protocol. Annals of surgical oncology 2013;20:4224-4230.
128. Al Rawahi T, Lopes AD, Bristow RE, et al.: Surgical cytoreduction for recurrent epithelial ovarian cancer. The Cochrane database of systematic reviews 2013:Cd008765.
129. Liberale G, Vankerckhove S, Caldon MG, et al.: Fluorescence Imaging After Indocyanine Green Injection for Detection of Peritoneal Metastases in Patients Undergoing Cytoreductive Surgery for Peritoneal Carcinomatosis From Colorectal Cancer: A Pilot Study. Annals of surgery 2016;264:1110-1115.
130. Satou S, Ishizawa T, Masuda K, et al.: Indocyanine green fluorescent imaging for detecting extrahepatic metastasis of hepatocellular carcinoma. Journal of gastroenterology 2013;48:1136-1143.
131. Veys I, Pop FC, Vankerckhove S, et al.: ICG-fluorescence imaging for detection of peritoneal metastases and residual tumoral scars in locally advanced ovarian cancer: A pilot study. Journal of surgical oncology 2017.
132. Tummers QR, Hoogstins CE, Peters AA, et al.: The Value of Intraoperative Near-Infrared Fluorescence Imaging Based on Enhanced Permeability and Retention of Indocyanine Green: Feasibility and False-Positives in Ovarian Cancer. PloS one 2015;10:e0129766.
133. Gilly FN, Cotte E, Brigand C, et al.: Quantitative prognostic indices in peritoneal carcinomatosis. European journal of surgical oncology : the journal of the European Society of Surgical Oncology and the British Association of Surgical Oncology 2006;32:597-601.
134. Janetschek G, Finkenstedt G, Gasser R, et al.: Laparoscopic surgery for pheochromocytoma: adrenalectomy, partial resection, excision of paragangliomas. The Journal of urology 1998;160:330-334.
135. Kumar A, Hyams ES, Stifelman MD: Robot-assisted partial adrenalectomy for isolated adrenal metastasis. Journal of endourology 2009;23:651-654.
136. DeLong JC, Chakedis JM, Hosseini A, et al.: Indocyanine green (ICG) fluorescence-guided laparoscopic adrenalectomy. Journal of surgical oncology 2015;112:650-653.
137. Sound S, Okoh AK, Bucak E, et al.: Intraoperative tumor localization and tissue distinction during robotic adrenalectomy using indocyanine green fluorescence imaging: a feasibility study. Surgical endoscopy 2016;30:657-662.
138. Manny TB, Pompeo AS, Hemal AK: Robotic partial adrenalectomy using indocyanine green dye with near-infrared imaging: the initial clinical experience. Urology 2013;82:738-742.
139. Colvin J, Zaidi N, Berber E: The utility of indocyanine green fluorescence imaging during robotic adrenalectomy. Journal of surgical oncology 2016;114:153-156.
140. Hutteman M, van der Vorst JR, Mieog JS, et al.: Near-infrared fluorescence imaging in patients undergoing pancreaticoduodenectomy. European surgical research Europaische chirurgische Forschung Recherches chirurgicales europeennes 2011;47:90-97.
141. Bjurlin MA, McClintock TR, Stifelman MD: Near-infrared fluorescence imaging with intraoperative administration of indocyanine green for robotic partial nephrectomy. Current urology reports 2015;16:20.
142. McClintock TR, Bjurlin MA, Wysock JS, et al.: Can selective arterial clamping with fluorescence imaging preserve kidney function during robotic partial nephrectomy? Urology 2014;84:327-332.
143. Bjurlin MA, Gan M, McClintock TR, et al.: Near-infrared fluorescence imaging: emerging applications in robotic upper urinary tract surgery. European urology 2014;65:793-801.
144. Manny TB, Krane LS, Hemal AK: Indocyanine green cannot predict malignancy in partial nephrectomy: histopathologic correlation with fluorescence pattern in 100 patients. Journal of endourology 2013;27:918-921.
145. Way LW, Stewart L, Gantert W, et al.: Causes and prevention of laparoscopic bile duct injuries: analysis of 252 cases from a human factors and cognitive psychology perspective. Annals of surgery 2003;237:460-469.
146. Halawani HM, Tamim H, Khalifeh F, et al.: Impact of intraoperative cholangiography on postoperative morbidity and readmission: analysis of the NSQIP database. Surgical endoscopy 2016;30:5395-5403.
147. Speicher PJ, Goldsmith ZG, Nussbaum DP, et al.: Ureteral stenting in laparoscopic colorectal surgery. The Journal of surgical research 2014;190:98-103.
148. Beraldo S, Neubeck K, Von Friderici E, Steinmuller L: The prophylactic use of a ureteral stent in laparoscopic colorectal surgery. Scandinavian journal of surgery : SJS : official organ for the Finnish Surgical Society and the Scandinavian Surgical Society 2013;102:87-89.
149. Halbert C, Altieri MS, Yang J, et al.: Long-term outcomes of patients with common bile duct injury following laparoscopic cholecystectomy. Surgical endoscopy 2016;30:4294-4299.

150. Halbert C, Pagkratis S, Yang J, et al.: Beyond the learning curve: incidence of bile duct injuries following laparoscopic cholecystectomy normalize to open in the modern era. Surgical endoscopy 2016;30:2239-2243.
151. Tornqvist B, Stromberg C, Persson G, Nilsson M: Effect of intended intraoperative cholangiography and early detection of bile duct injury on survival after cholecystectomy: population based cohort study. BMJ (Clinical research ed) 2012;345:e6457.
152. Nuzzo G, Giuliante F, Giovannini I, et al.: Bile duct injury during laparoscopic cholecystectomy: results of an Italian national survey on 56 591 cholecystectomies. Archives of surgery (Chicago, Ill : 1960) 2005;140:986-992.
153. Dip F, Roy M, Lo Menzo E, et al.: Routine use of fluorescent incisionless cholangiography as a new imaging modality during laparoscopic cholecystectomy. Surgical endoscopy 2015;29:1621-1626.
154. Dip FD, Asbun D, Rosales-Velderrain A, et al.: Cost analysis and effectiveness comparing the routine use of intraoperative fluorescent cholangiography with fluoroscopic cholangiogram in patients undergoing laparoscopic cholecystectomy. Surgical endoscopy 2014;28:1838-1843.
155. Larsen SS, Schulze S, Bisgaard T: Non-radiographic intraoperative fluorescent cholangiography is feasible. Danish medical journal 2014;61:A4891.
156. Prevot F, Rebibo L, Cosse C, et al.: Effectiveness of intraoperative cholangiography using indocyanine green (versus contrast fluid) for the correct assessment of extrahepatic bile ducts during day-case laparoscopic cholecystectomy. Journal of gastrointestinal surgery : official journal of the Society for Surgery of the Alimentary Tract 2014;18:1462-1468.
157. Spinoglio G, Priora F, Bianchi PP, et al.: Real-time near-infrared (NIR) fluorescent cholangiography in single-site robotic cholecystectomy (SSRC): a single-institutional prospective study. Surgical endoscopy 2013;27:2156-2162.
158. Schols RM, Bouvy ND, van Dam RM, et al.: Combined vascular and biliary fluorescence imaging in laparoscopic cholecystectomy. Surgical endoscopy 2013;27:4511-4517.
159. Schols RM, Bouvy ND, Masclee AA, et al.: Fluorescence cholangiography during laparoscopic cholecystectomy: a feasibility study on early biliary tract delineation. Surgical endoscopy 2013;27:1530-1536.
160. Buchs NC, Pugin F, Azagury DE, et al.: Real-time near-infrared fluorescent cholangiography could shorten operative time during robotic single-site cholecystectomy. Surgical endoscopy 2013;27:3897-3901.
161. Kaneko J, Ishizawa T, Masuda K, et al.: Indocyanine green reinjection technique for use in fluorescent angiography concomitant with cholangiography during laparoscopic cholecystectomy. Surgical laparoscopy, endoscopy & percutaneous techniques 2012;22:341-344.
162. Tagaya N, Shimoda M, Kato M, et al.: Intraoperative exploration of biliary anatomy using fluorescence imaging of indocyanine green in experimental and clinical cholecystectomies. Journal of hepato-biliary-pancreatic sciences 2010;17:595-600.
163. Ishizawa T, Bandai Y, Ijichi M, et al.: Fluorescent cholangiography illuminating the biliary tree during laparoscopic cholecystectomy. The British journal of surgery 2010;97:1369-1377.
164. Aoki T, Murakami M, Yasuda D, et al.: Intraoperative fluorescent imaging using indocyanine green for liver mapping and cholangiography. Journal of hepato-biliary-pancreatic sciences 2010;17:590-594.
165. Ishizawa T, Tamura S, Masuda K, et al.: Intraoperative fluorescent cholangiography using indocyanine green: a biliary road map for safe surgery. Journal of the American College of Surgeons 2009;208:e1-4.
166. Zarrinpar A, Dutson EP, Mobley C, et al.: Intraoperative Laparoscopic Near-Infrared Fluorescence Cholangiography to Facilitate Anatomical Identification: When to Give Indocyanine Green and How Much. Surgical innovation 2016;23:360-365.
167. Kono Y, Ishizawa T, Tani K, et al.: Techniques of Fluorescence Cholangiography During Laparoscopic Cholecystectomy for Better Delineation of the Bile Duct Anatomy. Medicine 2015;94:e1005.
168. Daskalaki D, Fernandes E, Wang X, et al.: Indocyanine green (ICG) fluorescent cholangiography during robotic cholecystectomy: results of 184 consecutive cases in a single institution. Surgical innovation 2014;21:615-621.
169. Ishizawa T, Kaneko J, Inoue Y, et al.: Application of fluorescent cholangiography to single-incision laparoscopic cholecystectomy. Surgical endoscopy 2011;25:2631-2636.
170. Buchs NC, Hagen ME, Pugin F, et al.: Intra-operative fluorescent cholangiography using indocyanin green during robotic single site cholecystectomy. The international journal of medical robotics + computer assisted surgery : MRCAS 2012;8:436-440.
171. Verbeek FP, Schaafsma BE, Tummers QR, et al.: Optimization of near-infrared fluorescence cholangiography for open and laparoscopic surgery. Surgical endoscopy 2014;28:1076-1082.
172. Mitsuhashi N, Kimura F, Shimizu H, et al.: Usefulness of intraoperative fluorescence imaging to evaluate local anatomy in hepatobiliary surgery. Journal of hepato-biliary-pancreatic surgery 2008;15:508-514.
173. Zroback C, Chow G, Meneghetti A, et al.: Fluorescent cholangiography in laparoscopic cholecystectomy: the initial Canadian experience. American journal of surgery 2016;211:933-937.
174. Ankersmit M, van Dam DA, van Rijswijk AS, et al.: Fluorescent Imaging With Indocyanine Green During Laparoscopic Cholecystectomy in Patients at Increased Risk of Bile Duct Injury. Surgical innovation 2017;24:245-252.
175. Graves C, Ely S, Idowu O, et al.: Direct Gallbladder Indocyanine Green Injection Fluorescence Cholangiography During Laparoscopic Cholecystectomy. Journal of laparoendoscopic & advanced surgical techniques Part A 2017.
176. Igami T, Nojiri M, Shinohara K, et al.: Clinical value and pitfalls of fluorescent cholangiography during single-incision laparoscopic cholecystectomy. Surgery today 2016;46:1443-1450.
177. van Dam DA, Ankersmit M, van de Ven P, et al.: Comparing Near-Infrared Imaging with Indocyanine Green to Conventional Imaging During Laparoscopic Cholecystectomy: A Prospective Crossover Study. Journal of laparoendoscopic & advanced surgical techniques Part A 2015;25:486-492.
178. Osayi SN, Wendling MR, Drosdeck JM, et al.: Near-infrared fluorescent cholangiography facilitates identification of biliary anatomy during laparoscopic cholecystectomy. Surgical endoscopy 2015;29:368-375.
179. Kawaguchi Y, Velayutham V, Fuks D, et al.: Usefulness of Indocyanine Green-Fluorescence Imaging for Visualization of

the Bile Duct During Laparoscopic Liver Resection. Journal of the American College of Surgeons 2015;221:e113-117.
180. Boni L, David G, Mangano A, et al.: Clinical applications of indocyanine green (ICG) enhanced fluorescence in laparoscopic surgery. Surgical endoscopy 2015;29:2046-2055.
181. Dip F, Nguyen D, Montorfano L, et al.: Accuracy of Near Infrared-Guided Surgery in Morbidly Obese Subjects Undergoing Laparoscopic Cholecystectomy. Obesity surgery 2016;26:525-530.
182. Liu YY, Liao CH, Diana M, et al.: Near-infrared cholecystocholangiography with direct intragallbladder indocyanine green injection: preliminary clinical results. Surgical endoscopy 2017.
183. Boogerd LSF, Handgraaf HJM, Huurman VAL, et al.: The Best Approach for Laparoscopic Fluorescence Cholangiography: Overview of the Literature and Optimization of Dose and Dosing Time. Surgical innovation 2017;24:386-396.
184. Palaniappa NC, Telem DA, Ranasinghe NE, Divino CM: Incidence of iatrogenic ureteral injury after laparoscopic colectomy. Archives of surgery (Chicago, Ill : 1960) 2012;147:267-271.
185. Al-Taher M, van den Bos J, Schols RM, et al.: Fluorescence Ureteral Visualization in Human Laparoscopic Colorectal Surgery Using Methylene Blue. Journal of laparoendoscopic & advanced surgical techniques Part A 2016;26:870-875.
186. Lee Z, Simhan J, Parker DC, et al.: Novel use of indocyanine green for intraoperative, real-time localization of ureteral stenosis during robot-assisted ureteroureterostomy. Urology 2013;82:729-733.
187. Lee Z, Moore B, Giusto L, Eun DD: Use of indocyanine green during robot-assisted ureteral reconstructions. European urology 2015;67:291-298.
188. Morozov AO, Alyaev YG, Rapoport LM, et al.: Near-infrared fluorescence with indocyanine green for diagnostics in urology: initial experience. Urologia 2017:0.
189. Siddighi S, Yune JJ, Hardesty J: Indocyanine green for intraoperative localization of ureter. American journal of obstetrics and gynecology 2014;211:436.e431-432.
190. Verbeek FP, van der Vorst JR, Schaafsma BE, et al.: Intraoperative near infrared fluorescence guided identification of the ureters using low dose methylene blue: a first in human experience. The Journal of urology 2013;190:574-579.
191. Kassis ES, Kosinski AS, Ross P, Jr., et al.: Predictors of anastomotic leak after esophagectomy: an analysis of the society of thoracic surgeons general thoracic database. The Annals of thoracic surgery 2013;96:1919-1926.
192. McDermott FD, Heeney A, Kelly ME, et al.: Systematic review of preoperative, intraoperative and postoperative risk factors for colorectal anastomotic leaks. The British journal of surgery 2015;102:462-479.
193. Karliczek A, Harlaar NJ, Zeebregts CJ, et al.: Surgeons lack predictive accuracy for anastomotic leakage in gastrointestinal surgery. International journal of colorectal disease 2009;24:569-576.
194. Pacheco PE, Hill SM, Henriques SM, et al.: The novel use of intraoperative laser-induced fluorescence of indocyanine green tissue angiography for evaluation of the gastric conduit in esophageal reconstructive surgery. American journal of surgery 2013;205:349-352; discussion 352-343.
195. Park YS, Lee CH, Park PJ, et al.: Intraoperative contrast-enhanced sonographic portography combined with indigo carmine dye injection for anatomic liver resection in hepatocellular carcinoma: a new technique. Journal of ultrasound in medicine : official journal of the American Institute of Ultrasound in Medicine 2014;33:1287-1291.
196. Shindoh J, Seyama Y, Umekita N: Three-dimensional staining of liver segments with an ultrasound contrast agent as an aid to anatomic liver resection. Journal of the American College of Surgeons 2012;215:e5-10.
197. Zehetner J, DeMeester SR, Alicuben ET, et al.: Intraoperative Assessment of Perfusion of the Gastric Graft and Correlation With Anastomotic Leaks After Esophagectomy. Annals of surgery 2015;262:74-78.
198. Shimada Y, Okumura T, Nagata T, et al.: Usefulness of blood supply visualization by indocyanine green fluorescence for reconstruction during esophagectomy. Esophagus : official journal of the Japan Esophageal Society 2011;8:259-266.
199. Saito T, Yano M, Motoori M, et al.: Subtotal gastrectomy for gastric tube cancer after esophagectomy: a safe procedure preserving the proximal part of gastric tube based on intraoperative ICG blood flow evaluation. Journal of surgical oncology 2012;106:107-110.
200. Rino Y, Yukawa N, Sato T, et al.: Visualization of blood supply route to the reconstructed stomach by indocyanine green fluorescence imaging during esophagectomy. BMC medical imaging 2014;14:18.
201. Murawa D, Hunerbein M, Spychala A, et al.: Indocyanine green angiography for evaluation of gastric conduit perfusion during esophagectomy--first experience. Acta chirurgica Belgica 2012;112:275-280.
202. Kumagai Y, Ishiguro T, Haga N, et al.: Hemodynamics of the reconstructed gastric tube during esophagectomy: assessment of outcomes with indocyanine green fluorescence. World journal of surgery 2014;38:138-143.
203. Koyanagi K, Ozawa S, Oguma J, et al.: Blood flow speed of the gastric conduit assessed by indocyanine green fluorescence: New predictive evaluation of anastomotic leakage after esophagectomy. Medicine 2016;95:e4386.
204. Kamiya K, Unno N, Miyazaki S, et al.: Quantitative assessment of the free jejunal graft perfusion. The Journal of surgical research 2015;194:394-399.
205. Campbell C, Reames MK, Robinson M, et al.: Conduit Vascular Evaluation is Associated with Reduction in Anastomotic Leak After Esophagectomy. Journal of gastrointestinal surgery : official journal of the Society for Surgery of the Alimentary Tract 2015;19:806-812.
206. Watanabe J, Ota M, Suwa Y, et al.: Evaluation of the intestinal blood flow near the rectosigmoid junction using the indocyanine green fluorescence method in a colorectal cancer surgery. International journal of colorectal disease 2015;30:329-335.
207. Wada T, Kawada K, Takahashi R, et al.: ICG fluorescence imaging for quantitative evaluation of colonic perfusion in laparoscopic colorectal surgery. Surgical endoscopy 2017.
208. Sherwinter DA, Gallagher J, Donkar T: Intra-operative transanal near infrared imaging of colorectal anastomotic perfusion: a feasibility study. Colorectal disease : the official journal of the Association of Coloproctology of Great Britain and Ireland 2013;15:91-96.
209. Sherwinter DA: Transanal near-infrared imaging of colorectal anastomotic perfusion. Surgical laparoscopy, endoscopy & percutaneous techniques 2012;22:433-436.
210. Ris F, Hompes R, Cunningham C, et al.: Near-infrared (NIR) perfusion angiography in minimally invasive colorectal surgery. Surgical endoscopy 2014;28:2221-2226.

211. Protyniak B, Dinallo AM, Boyan WP, Jr., et al.: Intraoperative indocyanine green fluorescence angiography--an objective evaluation of anastomotic perfusion in colorectal surgery. The American surgeon 2015;81:580-584.
212. Nishigori N, Koyama F, Nakagawa T, et al.: Visualization of Lymph/Blood Flow in Laparoscopic Colorectal Cancer Surgery by ICG Fluorescence Imaging (Lap-IGFI). Annals of surgical oncology 2016;23 Suppl 2:S266-274.
213. Kudszus S, Roesel C, Schachtrupp A, Hoer JJ: Intraoperative laser fluorescence angiography in colorectal surgery: a noninvasive analysis to reduce the rate of anastomotic leakage. Langenbeck's archives of surgery 2010;395:1025-1030.
214. Kin C, Vo H, Welton L, Welton M: Equivocal effect of intraoperative fluorescence angiography on colorectal anastomotic leaks. Diseases of the colon and rectum 2015;58:582-587.
215. Kim JC, Lee JL, Yoon YS, et al.: Utility of indocyanine-green fluorescent imaging during robot-assisted sphincter-saving surgery on rectal cancer patients. The international journal of medical robotics + computer assisted surgery : MRCAS 2016;12:710-717.
216. Kawada K, Hasegawa S, Wada T, et al.: Evaluation of intestinal perfusion by ICG fluorescence imaging in laparoscopic colorectal surgery with DST anastomosis. Surgical endoscopy 2017;31:1061-1069.
217. Jafari MD, Wexner SD, Martz JE, et al.: Perfusion assessment in laparoscopic left-sided/anterior resection (PILLAR II): a multi-institutional study. Journal of the American College of Surgeons 2015;220:82-92.e81.
218. Jafari MD, Lee KH, Halabi WJ, et al.: The use of indocyanine green fluorescence to assess anastomotic perfusion during robotic assisted laparoscopic rectal surgery. Surgical endoscopy 2013;27:3003-3008.
219. Hellan M, Spinoglio G, Pigazzi A, Lagares-Garcia JA: The influence of fluorescence imaging on the location of bowel transection during robotic left-sided colorectal surgery. Surgical endoscopy 2014;28:1695-1702.
220. Grone J, Koch D, Kreis ME: Impact of intraoperative microperfusion assessment with Pinpoint Perfusion Imaging on surgical management of laparoscopic low rectal and anorectal anastomoses. Colorectal disease : the official journal of the Association of Coloproctology of Great Britain and Ireland 2015;17 Suppl 3:22-28.
221. Foppa C, Denoya PI, Tarta C, Bergamaschi R: Indocyanine green fluorescent dye during bowel surgery: are the blood supply "guessing days" over? Techniques in coloproctology 2014;18:753-758.
222. Carus T, Dammer R: Laparoscop fluorescence angiography with indocyanine green to control the perfusion of gastrointestinal anastomoses intraoperatively. Surgical technology international 2012;22:27-32.
223. Boni L, Fingerhut A, Marzorati A, et al.: Indocyanine green fluorescence angiography during laparoscopic low anterior resection: results of a case-matched study. Surgical endoscopy 2017;31:1836-1840.
224. Boni L, David G, Dionigi G, et al.: Indocyanine green-enhanced fluorescence to assess bowel perfusion during laparoscopic colorectal resection. Surgical endoscopy 2016;30:2736-2742.
225. Bae SU, Baek SJ, Hur H, et al.: Intraoperative near infrared fluorescence imaging in robotic low anterior resection: three case reports. Yonsei medical journal 2013;54:1066-1069.
226. Degett TH, Andersen HS, Gogenur I: Indocyanine green fluorescence angiography for intraoperative assessment of gastrointestinal anastomotic perfusion: a systematic review of clinical trials. Langenbeck's archives of surgery 2016;401:767-775.
227. Uchiyama K, Ueno M, Ozawa S, et al.: Combined intraoperative use of contrast-enhanced ultrasonography imaging using a sonazoid and fluorescence navigation system with indocyanine green during anatomical hepatectomy. Langenbeck's archives of surgery 2011;396:1101-1107.
228. Inoue Y, Arita J, Sakamoto T, et al.: Anatomical Liver Resections Guided by 3-Dimensional Parenchymal Staining Using Fusion Indocyanine Green Fluorescence Imaging. Annals of surgery 2015;262:105-111.
229. Kawaguchi Y, Nomura Y, Nagai M, et al.: Liver transection using indocyanine green fluorescence imaging and hepatic vein clamping. The British journal of surgery 2017;104:898-906.
230. Wagner OJ, Louie BE, Vallieres E, et al.: Near-infrared fluorescence imaging can help identify the contralateral phrenic nerve during robotic thymectomy. The Annals of thoracic surgery 2012;94:622-625.
231. Mangano MS, De Gobbi A, Beniamin F, et al.: Robot-assisted nerve-sparing radical prostatectomy using near-infrared fluorescence technology and indocyanine green: initial experience. Urologia 2017:0.
232. Chen SC, Wang MC, Wang WH, et al.: Fluorescence-assisted visualization of facial nerve during mastoidectomy: A novel technique for preventing iatrogenic facial paralysis. Auris, nasus, larynx 2015;42:113-118.
233. Whitney MA, Crisp JL, Nguyen LT, et al.: Fluorescent peptides highlight peripheral nerves during surgery in mice. Nature biotechnology 2011;29:352-356.
234. Gibbs-Strauss SL, Nasr KA, Fish KM, et al.: Nerve-highlighting fluorescent contrast agents for image-guided surgery. Molecular imaging 2011;10:91-101.
235. Barth CW, Gibbs SL: Direct Administration of Nerve-Specific Contrast to Improve Nerve Sparing Radical Prostatectomy. Theranostics 2017;7:573-593.
236. Gray D, Kim E, Cotero V, et al.: Compact Fluorescence and White Light Imaging System for Intraoperative Visualization of Nerves. Proceedings of SPIE--the International Society for Optical Engineering 2012;8207.
237. Park MH, Hyun H, Ashitate Y, et al.: Prototype nerve-specific near-infrared fluorophores. Theranostics 2014;4:823-833.
238. Verbeek FP, van der Vorst JR, Tummers QR, et al.: Near-infrared fluorescence imaging of both colorectal cancer and ureters using a low-dose integrin targeted probe. Annals of surgical oncology 2014;21 Suppl 4:S528-537.
239. Tummers QR, Boonstra MC, Frangioni JV, et al.: Intraoperative near-infrared fluorescence imaging of a paraganglioma using methylene blue: A case report. International journal of surgery case reports 2015;6c:150-153.
240. Winer JH, Choi HS, Gibbs-Strauss SL, et al.: Intraoperative localization of insulinoma and normal pancreas using invisible near-infrared fluorescent light. Annals of surgical oncology 2010;17:1094-1100.
241. Haque A, Faizi MS, Rather JA, Khan MS: Next generation NIR fluorophores for tumor imaging and fluorescence-guided surgery: A review. Bioorganic & medicinal chemistry 2017;25:2017-2034.
242. Guzzo TJ, Jiang J, Keating J, et al.: Intraoperative Molecular Diagnostic Imaging Can Identify Renal Cell Carcinoma. The Journal of urology 2016;195:748-755.

243. van Dam GM, Themelis G, Crane LM, et al.: Intraoperative tumor-specific fluorescence imaging in ovarian cancer by folate receptor-alpha targeting: first in-human results. Nature medicine 2011;17:1315-1319.
244. Shum CF, Bahler CD, Low PS, et al.: Novel Use of Folate-Targeted Intraoperative Fluorescence, OTL38, in Robot-Assisted Laparoscopic Partial Nephrectomy: Report of the First Three Cases. Journal of endourology case reports 2016;2:189-197.
245. Hoogstins CE, Tummers QR, Gaarenstroom KN, et al.: A Novel Tumor-Specific Agent for Intraoperative Near-Infrared Fluorescence Imaging: A Translational Study in Healthy Volunteers and Patients with Ovarian Cancer. Clinical cancer research : an official journal of the American Association for Cancer Research 2016;22:2929-2938.
246. Burggraaf J, Kamerling IM, Gordon PB, et al.: Detection of colorectal polyps in humans using an intravenously administered fluorescent peptide targeted against c-Met. Nature medicine 2015;21:955-961.
247. Diana M, Halvax P, Dallemagne B, et al.: Real-time navigation by fluorescence-based enhanced reality for precise estimation of future anastomotic site in digestive surgery. Surgical endoscopy 2014;28:3108-3118.
248. Diana M, Dallemagne B, Chung H, et al.: Probe-based confocal laser endomicroscopy and fluorescence-based enhanced reality for real-time assessment of intestinal microcirculation in a porcine model of sigmoid ischemia. Surgical endoscopy 2014;28:3224-3233.
249. Diana M, Agnus V, Halvax P, et al.: Intraoperative fluorescence-based enhanced reality laparoscopic real-time imaging to assess bowel perfusion at the anastomotic site in an experimental model. The British journal of surgery 2015;102:e169-176.
250. Diana M, Noll E, Diemunsch P, et al.: Enhanced-reality video fluorescence: a real-time assessment of intestinal viability. Annals of surgery 2014;259:700-707.

Chapter 5

Intraoperative detection of the remnant cystic duct during robot-assisted surgery using near-infrared fluorescence imaging: a case report

L. van Manen, Q.R.J.G. Tummers, A. Inderson, A. Bhalla,
A.L. Vahrmeijer, B.A. Bonsing, J.S.D. Mieog

BMC Surgery 19, 104 (2019).

Abstract

Background

Post cholecystectomy syndrome is characterized as recurrence of symptoms as experienced before cholecystectomy. In rare cases, a remnant cystic duct is causing these symptoms and occasionally surgical resection is performed. During surgery, visualization of the biliary ducts could be difficult due to inflammation and dense adhesions.

Case presentation

In this article, we presented a 36-year old woman with post-cholecystectomy syndrome in which we evaluated the feasibility of near-infrared (NIR) fluorescence imaging using indocyanine green (ICG) for visualization of the remnant cystic and common bile duct during robot-assisted surgery. Intraoperative visualization of the remnant biliary duct and other important structures was feasible, and resection of the remnant cystic duct was successfully performed under fluorescence guidance, without any complications.

Conclusions

NIR fluorescence imaging of the biliary ducts using ICG does not prolong the operating time, and could potentially decrease the operation time in difficult procedures, because of easy and fast detection of the biliary tract. Furthermore, it is a non-hazardous and non-invasive technique, as it does not require use of radiation and cannot cause bile duct injury. This case illustrated that ICG NIR fluorescence imaging during difficult robot-assisted surgical procedures of the bile ducts is effective and therefore highly recommended.

Background

Cholecystectomy is the most common surgical procedure for patients with symptomatic cholecystolithiasis. Currently, minimally invasive surgery, either laparoscopic or robot-assisted, is the standard approach. Unfortunately, in some patients symptoms, such as abdominal pain and dyspepsia might persist after surgery, which has been defined as the post cholecystectomy syndrome (PCS).[1] A remnant cystic duct, defined as a residual duct longer than 1cm, could be one of the causes of PCS, although the true incidence is uncertain.[2] Treatment depends on the severity of symptoms and a resection of the remnant cystic duct is occasionally performed. Especially during laparoscopic or robot-assisted surgery, inflammation and dense adhesions hamper good visualization of the remnant cystic duct. This could result in serious complications, such as bile duct injury (BDI).[3,4] Today, no well-established, non-invasive and non-hazardous imaging techniques are available to guide the surgeon intraoperatively during such interventions. Intraoperative radiographic cholangiography (IOC) is sometimes used for bile duct visualization. However, especially in case of post cholecystectomy syndrome, it is difficult to navigate and to cannulate the common bile duct (CBD). Near-infrared (NIR) fluorescence imaging, is a new technique that has recently been evaluated during open and minimally invasive surgery.[5] In general, a fluorophore is excited and detected by specialized NIR fluorescence camera systems, in order to visualize the tissue of interest. The fluorophore indocyanine green (ICG), which is rapidly cleared by the liver after intravenous (IV) injection, has been extensively used for visualization of the bile ducts and many other applications.[6]

In this case report, we describe the feasibility of NIR fluorescence imaging using ICG for visualization of the remnant cystic duct during robot-assisted surgery. This case report was described according to the SCARE guidelines.[7]

Case presentation

A 36-year old woman presented with an acute biliary pancreatitis at a peripheral hospital, after which a laparoscopic cholecystectomy was performed. One year later, she developed several episodes of acute onsets of abdominal pain, which were caused by biliary pancreatitis. Endoscopic ultrasound (EUS) revealed a high suspicion on presence of small bile stones in the remnant cystic duct. Although, Magnetic resonance cholangiopancreaticography (MRCP) did not show either an evident remnant biliary duct or presence of bile stones in either the remnant cystic duct or CBD, which could be explained by the limited image quality due to artefacts. Moreover, it has been shown that MRCP has a 93% sensitivity for detection of bile stones.[8] The a priori probability on presence of CBD stones was assessed as low, as no biochemical evidence of post hepatic obstruction (elevated bilirubin) was present. Based on this, patient was referred to an university hospital to investigate the possibility to remove the bile stones in the remnant cystic duct either endoscopically or surgically., Given the clinical symptoms, the findings at EUS (length of remnant cystic duct and suspicion on small bile stones in remnant cystic duct) and MRCP, the patient opted for a definitive therapeutic approach (surgical resection of remnant cystic duct) instead of another diagnostic modality (endoscopic retrograde cholangio-pancreatography), although this could have

had therapeutic implications. Consequently, the case was discussed at the hepatopancreaticobiliary (HPB) multidisciplinary team meeting and a robot-assisted surgical resection of the remnant cystic duct under NIR fluorescence guidance using ICG was proposed. After screening for contraindications for the use of ICG (impaired kidney function, hypo/hyperthyroidism, pregnancy, and allergy for iodine), the patients provided informed consent for the use of ICG NIR fluorescence imaging.

After induction of general anaesthesia, 5 mg (2.5 mg/ml) of ICG was injected IV in order to visualize the biliary ducts. The patient was positioned in reverse Trendelenburg, and a small incision was made for introduction of 12 mm trocar at the umbilicus. Consequently, four additional robot trocars (8 mm) were placed under direct visualization. After docking, one experienced HPB surgeon and one surgical resident started the surgical procedure with exploration of the hepatoduodenal ligament until the liver hilum (Figure 1). Using the Da Vinci Xi (Intuitive Surgical Inc., Sunnyvale, USA) fluorescence camera (Firefly™), the liver and CBD could be easily visualized, around 30 min. after IV injection of ICG. After adhesiolysis, the fluorescent remnant cystic duct and the non-fluorescent cystic artery were identified, also confirmed by the placed metal clips during the previous operation (Figure 2). Using an additional IV injection of 2.5 mg ICG, the right hepatic artery and remnant cystic artery were confirmed with the Firefly™ (Figure 3; Supplementary Video). Resection of both the remnant cystic duct and artery was performed under fluorescence guidance. During resection of the cystic duct, some pus was relieved, indicating an infected state of the duct. The stump was controlled by double hemoclips. No gallstones were seen during surgery, which was confirmed *ex vivo*. Final pathology revealed presence of chronic and fibrosing inflammation in the remnant cystic duct. There were no complications during the procedure, which lasted 1 hour and 35 minutes. The patient was checked postoperatively for jaundice, colic pain, and biochemically and none was present in the recovery period. The patient was discharged the same day and has not experienced similar symptoms as before during the first month of the follow-up.

Discussion and conclusions

A case report of a patient with a symptomatic remnant cystic duct, who underwent robot-assisted resection under fluorescence guidance, is presented. Good visualization of the remnant cystic duct and CBD was achieved by NIR fluorescence imaging using ICG, which helped to identify both structures and thereby resulting in an easier and safer surgical procedure. Intraoperative identification of a symptomatic cystic remnant duct can be challenging. Adhesions and inflammation could hamper visualization during surgery. As a consequence, BDI could occur, which is a complication with high mortality.[9] During surgery, no bile stones were visualized, although the resected specimen showed presence of chronic inflammation, which could indicate that a obstructing bile stone could have been located in the remnant cystic duct for a certain period of time.

Intraoperative assessment of the biliary ducts can be performed by different imaging techniques, of which IOC has been studied the most. However, the benefit of using IOC has not been proven in randomized clinical trials (RCTs), as level 1 evidence is low and all trials were insufficiently powered.[10,11] Moreover, IOC is an invasive and time-consuming technique, and also involves

the use of ionizing radiation.[11,12] It could also cause BDI by itself, as insertion of a cannula for injection of contrast agents is necessary.[13] Compared to IOC, NIR fluorescence imaging of the biliary ducts using ICG does not prolong the operating time significantly, and could potentially decrease the operation time in difficult procedures, because of easy and fast detection of the biliary tract.[14] Currently, an ongoing international RCT is comparing the operation time of the procedure with and without the use of ICG fluorescence.[15] Furthermore, it is a non-hazardous and non-invasive technique, as it does not require use of radiation and cannot cause BDI.[16] Recently, a randomized controlled trial showed superiority of NIR fluorescence imaging with respect to standard white light conditions for detection of extrahepatic bile ducts during laparoscopic surgery.[17] Moreover, they showed encouraging results in their patient cohort of 639 patients (2 BDI in white light conditions vs. no BDI in de NIR fluorescence patient group) although due to low incidence of BDI, it is difficult to prove statistically significant differences between the two conditions. However, there are some limitations of this technique, such as the inability to detect bile stones and the limited penetration depth of NIR light up to 10 mm.[5,18]

Optimal injection times of ICG are still under discussion, although a systematic review showed that most studies used a preoperative administration, which was therefore recommended.[18,19] We have shown, that injection of ICG after anesthesia, which was also the procedure in two recent RCTs, was also sufficient to visualize the biliary ducts during the whole procedure (30 min. – 125 min. post injection) and could be easily implemented in clinical practice as the preparation phase of robotic surgery takes more time than conventional laparoscopy or laparotomy.[15,17] As shown, the arterial vasculature could also be visualized by an extra IV injection of ICG, to confirm identification before resection.

In conclusion, this case demonstrates the use of NIR fluorescence imaging as a valuable tool for surgical guidance during a robot-assisted procedure of resection of the remnant cystic duct. This technique is safe and can easily be implemented in the surgical procedure. Therefore, we recommend to use ICG NIR fluorescence imaging during difficult robotic surgical procedures of the biliary tract, such as resection of a remnant cystic duct and gallbladder surgery in which inflamed surrounding tissue is expected. Nevertheless, a less invasive approach by using ERCP, remains the first line of treatment for patient with a symptomatic remnant cystic duct and therefore robotic surgery should only be performed in difficult cases.

Figure 1. Representative color and fluorescence image with an overview of the liver hilum after some adhesiolysis. Insets showed more detailed view of the remnant cystic and common bile duct, which was folded up in the liver hilum.

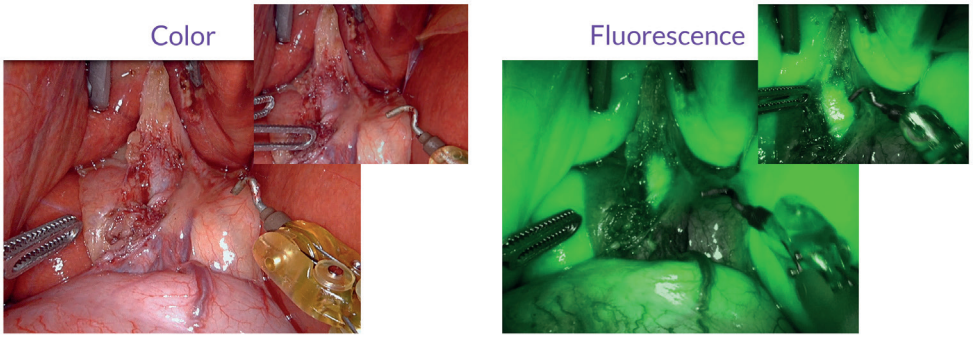

Figure 2. Color and fluorescence image of the remnant cystic duct and artery after dissection and detaching of the adhesions. *Abbreviations: CA: cystic artery; CD: (remnant) cystic duct; CBD: common bile duct*

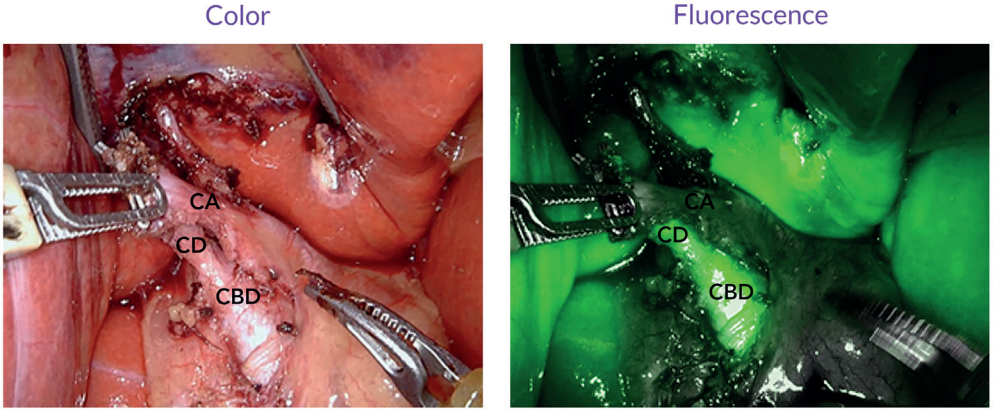

Figure 3. Confirmation of the arterial vasculature (remnant cystic artery and right hepatic artery) after injection of an extra bolus indocyanine green. *Abbreviations: CA: cystic artery; CD: (remnant) cystic duct; CBD: common bile duct; RHA: right hepatic artery.*

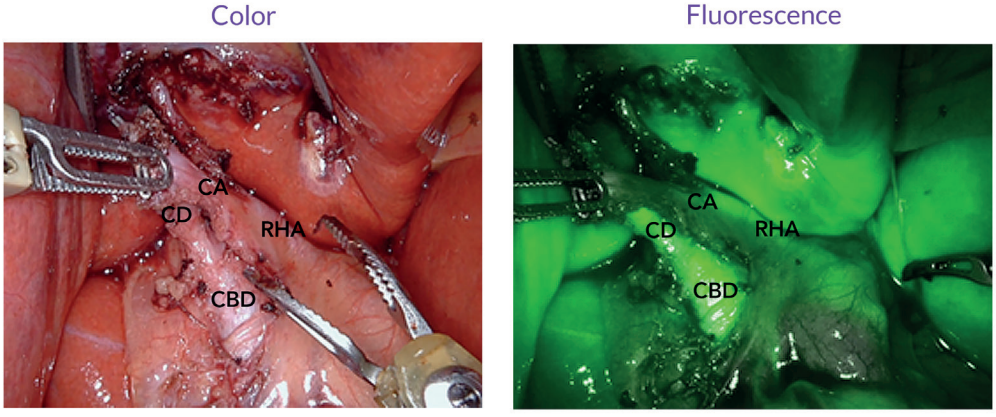

References

1. Kim JY, Kim KW, Ahn CS, et al. Spectrum of biliary and nonbiliary complications after laparoscopic cholecystectomy: radiologic findings. AJR Am J Roentgenol. 2008;191(3):783-789.
2. Pernice LM, Andreoli F. Laparoscopic treatment of stone recurrence in a gallbladder remnant: report of an additional case and literature review. J Gastrointest Surg. 2009;13(11):2084-2091.
3. Demetriades H, Pramateftakis MG, Kanellos I, Angelopoulos S, Mantzoros I, Betsis D. Retained gallbladder remnant after laparoscopic cholecystectomy. J Laparoendosc Adv Surg Tech A. 2008;18(2):276-279.
4. Walsh RM, Ponsky JL, Dumot J. Retained gallbladder/cystic duct remnant calculi as a cause of postcholecystectomy pain. Surg Endosc. 2002;16(6):981-984.
5. Vahrmeijer AL, Hutteman M, van der Vorst JR, van de Velde CJ, Frangioni JV. Image-guided cancer surgery using near-infrared fluorescence. Nat Rev Clin Oncol. 2013;10(9):507-518.
6. van Manen L, Handgraaf HJM, Diana M, et al. A practical guide for the use of indocyanine green and methylene blue in fluorescence-guided abdominal surgery. J Surg Oncol. 2018;118(2):283-300.
7. Agha RA, Borrelli MR, Farwana R, Koshy K, Fowler AJ, Orgill DP. The SCARE 2018 statement: Updating consensus Surgical CAse REport (SCARE) guidelines. Int J Surg. 2018;60:132-136.
8. Giljaca V, Gurusamy KS, Takwoingi Y, et al. Endoscopic ultrasound versus magnetic resonance cholangiopancreatography for common bile duct stones. Cochrane Database Syst Rev. 2015(2):Cd011549.
9. Halbert C, Altieri MS, Yang J, et al. Long-term outcomes of patients with common bile duct injury following laparoscopic cholecystectomy. Surg Endosc. 2016;30(10):4294-4299.
10. Buddingh KT, Nieuwenhuijs VB, van Buuren L, Hulscher JB, de Jong JS, van Dam GM. Intraoperative assessment of biliary anatomy for prevention of bile duct injury: a review of current and future patient safety interventions. Surg Endosc. 2011;25(8):2449-2461.
11. Ford JA, Soop M, Du J, Loveday BP, Rodgers M. Systematic review of intraoperative cholangiography in cholecystectomy. Br J Surg. 2012;99(2):160-167.
12. Buddingh KT, Weersma RK, Savenije RA, van Dam GM, Nieuwenhuijs VB. Lower rate of major bile duct injury and increased intraoperative management of common bile duct stones after implementation of routine intraoperative cholangiography. J Am Coll Surg. 2011;213(2):267-274.
13. Ishizawa T, Bandai Y, Ijichi M, Kaneko J, Hasegawa K, Kokudo N. Fluorescent cholangiography illuminating the biliary tree during laparoscopic cholecystectomy. Br J Surg. 2010;97(9):1369-1377.
14. Dip F, Roy M, Lo Menzo E, Simpfendorfer C, Szomstein S, Rosenthal RJ. Routine use of fluorescent incisionless cholangiography as a new imaging modality during laparoscopic cholecystectomy. Surg Endosc. 2015;29(6):1621-1626.
15. van den Bos J, Schols RM, Luyer MD, et al. Near-infrared fluorescence cholangiography assisted laparoscopic cholecystectomy versus conventional laparoscopic cholecystectomy (FALCON trial): study protocol for a multicentre randomised controlled trial. BMJ Open. 2016;6(8):e011668.
16. Dip FD, Asbun D, Rosales-Velderrain A, et al. Cost analysis and effectiveness comparing the routine use of intraoperative fluorescent cholangiography with fluoroscopic cholangiogram in patients undergoing laparoscopic cholecystectomy. Surg Endosc. 2014;28(6):1838-1843.
17. Dip F, LoMenzo E, Sarotto L, et al. Randomized Trial of Near-infrared Incisionless Fluorescent Cholangiography. Ann Surg. 2019.
18. Boogerd LSF, Handgraaf HJM, Huurman VAL, et al. The Best Approach for Laparoscopic Fluorescence Cholangiography: Overview of the Literature and Optimization of Dose and Dosing Time. Surg Innov. 2017;24(4):386-396.
19. Vlek SL, van Dam DA, Rubinstein SM, et al. Biliary tract visualization using near-infrared imaging with indocyanine green during laparoscopic cholecystectomy: results of a systematic review. Surg Endosc. 2017;31(7):2731-2742.

Chapter 6

Latest developments in molecular tracers for fluorescence image-guided cancer surgery

S. Hernot, L. van Manen, P. Debie, J.S.D. Mieog, A.L. Vahrmeijer

Lancet Oncology. 2019 Jul;20(7).

Abstract

Real-time intraoperative guidance is essential during oncological surgery for complete and safe tumour resection. Fluorescence imaging in the near-infrared spectrum has shown potential for guiding surgeons during complex interventions. Recently, there has been a shift towards the use of fluorescence contrast agents for molecular imaging. The first targeted fluorescent agents, of which most consist of approved therapeutic antibodies conjugated to a fluorescent dye, have been evaluated in several early-phase clinical trials. Moreover, advances in protein engineering and drug design have led to the development of a variety of tracers suitable for molecular fluorescence image-guided surgery. In this Review, we discuss preclinical and clinical evidence, ongoing clinical trials, and the latest developments in the field of molecular near-infrared tracers for fluorescence-guided cancer surgery.

Introduction

Surgery is pivotal in the treatment of solid cancers. Unfortunately, tumour-positive resection margins occur in 8-70% of the cases depending on the cancer type.[1-4] Because complete removal of tumour tissue is mandatory for prolonged survival and to preserve as much healthy tissue as possible, intraoperative guidance is essential to surgeons. Besides using visual (based on white light reflectance) and tactile feedback, surgeons can use ultrasound imaging as an additional tool for intraoperative guidance in selected cases, but this tool alone is often insufficient.[5] Other imaging techniques, such as x-ray, CT, or MRI are mainly used for surgical planning or interim assessment because they do not provide real-time intraoperative guidance. Recently, surgeons have started to use fluorescent light for surgical navigation.

Fluorescence imaging uses a specialised camera to capture light emitted by a fluorescent contrast agent after excitation with an appropriate light source. All imaging equipment can be integrated into a compact open-field device or within laparoscopic or robotic instruments for contact-free and real-time interrogation (Figure 1). The fluorescent contrast agent is administered to visualise the organ or tissue of interest with sufficient sensitivity and contrast. For medical applications, fluorescent agents that emit at wavelengths in the near-infrared region, between 650 and 800 nm, are more advantageous than those emitting visual light. Near infrared light can penetrate deeper into tissue (up to several mm) with less scattering than visual light and there is less autofluorescence.[6]

Indocyanine green and methylene blue are the only available near-infrared fluorophores that are approved by the US Food and Drug Administration. Indocyanine green is mainly used for the evaluation of blood flow, sentinel lymph node mapping, and liver tumour imaging.[7] Methylene blue has been evaluated for ureter, thyroid nodule, and neuroendocrine tumour visualisation; however, it is currently not used in regular surgical care due to its non-specificity and limited quantum yield. Besides indocyanine green and methylene blue, 5-aminolevulinic acid and its derivate 5-aminolevulinic acid hexyl ester, are two non-fluorescent prodrugs that are both clinically approved for imaging of malignant gliomas and bladder cancer, respectively. These prodrugs elicit the synthesis of fluorescent protoporphyrin IX (maximal emission peak around 634 nm, thus just outside the near-infrared region), which accumulates in malignant tumour tissue. Two randomised controlled phase 3 trials [8,9] have shown improved resection margins and also increased progression-free survival for patients with malignant gliomas and bladder cancer. However, drawbacks of fluorescence imaging with 5-aminolevulinic acid include inhomogeneous signals that are dependent on the tumour grade, absence of penetration depth, and photobleaching.[10]

Over recent years there has been a shift from structural and functional fluorescence imaging to molecular fluorescence imaging using more specific fluorescent agents (Figure 2). Molecular fluorescence imaging could be used for many applications relevant to oncological surgery such as the detection of occult tumour lesions, assessment of tumour margins and locoregional invasion, and emphasis on vital structures (Figure 1).[11] In this Review, we focus on the clinical evidence in molecular near-infrared fluorescence-guided cancer surgery and latest developments regarding molecular probes in the field.

Targeted fluorescent agents under evaluation in clinical trials

The specific accumulation of a fluorescent contrast agent in a tissue of interest requires stable conjugation of a fluorophore to a targeting molecule. The targeted cells, most often cancer cells, will thus literally light up, whereas the background is expected to be significantly less fluorescent once the unbound tracer has cleared. Several tumour-specific ligands, recognising diverse molecular biomarkers, have been evaluated for molecular fluorescence imaging applications in the clinic. An overview of published and ongoing clinical trials is provided in Table 1.

In 2011, van Dam and colleagues[12] did the first targeted fluorescence molecular imaging trial by using the contrast agent EC-17, which consists of folic acid conjugated with fluorescein isothiocyanate (emission: 520 nm), in patients with ovarian cancer during cytoreductive surgery. In three patients, folate receptor-alpha expressing malignant tumour deposits could be clearly identified intraoperatively and distinguished from benign structures. Similar results were found for lung, breast and renal tumours. [13-16] However, the limited penetration of light and relatively high autofluorescence signal arising from collagen-rich tissues in this wavelength range turned out to be suboptimal. Consequently, the analogous fluorescent tracer OTL-38, also targeting folate receptor, but emitting at 796 nm, was developed and tested in several cancer types including ovarian, lung, renal and endometrial tumours, as well as mengingioma.[17-26] Hoogstins and colleagues [17] showed in 12 patients with ovarian cancer that surgeons were able to detect 29% additional malignant lesions during debulking surgery, which were not detected using visual inspection. Other pilot studies showed that pulmonary adenocarcinomas could be detected with a sensitivity up to 100% [23] and squamous cell carcinomas with up to 70%.[21] Furthermore, in situ fluorescence imaging even appeared to be superior to 18F-FDG-PET for the detection of malignant pulmonary nodules.[19] A larger multicenter international phase 2 trial (NCT02872701) determining the clinical efficacy in terms of detection of additional tumour-positive nodules, synchronous lesions, and tumour-positive margins during lung surgery in 110 patients has been completed, but results are not published yet. In another trial, [26] endometrial cancer, including omental and lymph node metastases, could also be detected using OTL-38 in four patients. Nevertheless, a high rate of false-positive signals (34%) was recorded, which was caused by the non-specific targeting of OTL-38 to folate receptor-β in non-metastatic lymph nodes.

Alternatively, tozuleristide is a naturally occurring knotted peptide conjugated to indocyanine green. This tracer has known affinities for matrix metalloproteinase-2 and annexin A2, which are expressed in a variety of solid tumours. Dintzis and colleagues [43] showed that tozuleristide, when administered between 1 to 26 h before surgery, enabled detection of tumour tissue in freshly resected pathology specimens of 23 patients with breast cancer. Phase 1 studies (NCT02234297; NCT02462629) in paediatric and adult subjects with CNS tumours have been completed and a randomised phase 2/3 trial (NCT03579602) has started recruiting patients.

With the introduction of the commercially available near-infrared fluorophore IRDye800CW, existing therapeutic monoclonal antibodies could quite easily be repurposed after fluorescence labelling. For example, bevacizumab-IRDye800CW has been used in various clinical feasibility trials targeting tumours that overexpress vascular endothelial growth factor. Harlaar and colleagues [27] studied seven patients with peritoneal carcinomatosis of colorectal origin undergoing cytoreductive surgery and

showed that fluorescence imaging with bevacizumab-IRDye800CW enabled in-situ detection of additional malignant lesions while fluorescence uptake was absent in clinically suspicious but benign lesions. Contrarily, for breast cancer surgery, a dose of 4.5 mg of bevacizumab-IRDye800CW, which falls under the microdosing regimen, was too low to enable in-situ margin assessment.[28] Tumour-positive margins could nevertheless be detected *ex vivo* after bread-loaf slicing (a common method of processing surgical specimens for histopathology) on the back table.[28] These results demonstrate the relevance of developing fluorescence-guided intraoperative pathology that could provide fast feedback to the surgeon on excised specimens (Figure 1). However, detection of lymph node metastases was difficult. Additional studies with bevacizumab-IRDye800CW are planned in endometriosis (NCT02975219), pancreatic cancer (NCT02743975) and perihilar cholangiocarcinoma (NCT03620292).

According to an analogous strategy, the human-mouse chimeric monoclonal antibody cetuximab, which targets the epidermal growth factor receptor (EGFR), was conjugated to IRDye800CW.[29] Rosenthal and colleagues [30] reported no grade 2 or higher adverse events after administration of cetuximab-IRDye800CW in a dose-escalation study with doses up to 62.5 mg/m^2 which corresponds to 25% of the therapeutic dose of cetuximab, preceded by an injection of 100 mg of unlabelled cetuximab. Furthermore, in-situ mean target-to-background ratio values up to 5.2 were found between head and neck tumours and surrounding tissue. This study [30] also showed the ability of *ex vivo* back-table fluorescence imaging to identify positive tumour margins, as well as over resected lesions. Cetuximab-IRDye800CW yielded high sensitivity (97%) and specificity (93%) for the *ex vivo* detection of lymph node metastases compared with standard histopathology.[31] This finding suggests that unnecessary neck lymph node dissections could potentially be avoided, eventually resulting in decreased morbidity. A Phase 2 clinical trial has been launched in 70 patients with the aim to determine the fluorescent threshold level needed to distinguish tumour tissue from normal tissue (NCT03134846). Tummers and colleagues [33] evaluated the accuracy of the same tracer during pancreatic surgery in seven patients. A sensitivity of 96% and a specificity of 67% were achieved for primary tumour detection, with a mean in-situ target to background ratio value of 2.3. Tumour positive lymph nodes could also be identified intraoperatively (mean target to background ratio of 6.3). *Ex vivo* fluorescence analysis showed a sensitivity of 100% and specificity 78% macroscopically, and a sensitivity of 91% and specificity of 66% microscopically for detection of metastatic lymph nodes in the optimal dose cohort (50 mg).[34] Cetuximab-IRDye800CW has also been tested in three patients with glioblastoma, of which the two contrast-enhancing tumours on preoperative CT imaging showed fluorescence signal accumulation with a mean *ex vivo* TBR of 4.0, whereas the non-contrast-enhancing tumour did not show a clear fluorescence signal (ratio of 1.2).[35]

IRDye800CW-labeled panitumumab, which is a fully humanised monoclonal antibody with improved EGFR binding characteristics compared with cetuximab-IRDye800CW, was clinically evaluated in a dose escalation study [32] using a loading dose of 100 mg unlabelled panitumumab before surgery to saturate EGFR receptors in normal tissue and therefore optimize tissue contrast. Doses of 0.5 and 1 mg/kg allowed in-situ imaging of head and neck tumours with mean target to background ratios between 2.4 and 2.6. Fluorescence imaging was able to detect tumour tissue in the resected specimens with a high sensitivity of 91% and negative predicting value of 93%.[36] Further analysis of the back-table fluorescence imaging data yielded a 100% sensitivity for the

detection of tumour-positive resection margins (<2 mm) and 95% sensitivity for close resection margins (<5mm).[37] Furthermore van Keulen and colleagues [38] showed that fluorescence imaging using panitumumab-IRDye800CW could improve the surgical decision-making in three (21%) of 14 patients with head and neck cancer through the identification of close margins and unanticipated regions of primary disease. In-situ margin assessment has not yet been investigated, although this would be more beneficial for the surgeon to plan and perform the resection during the procedure under fluorescence guidance.

Finally, a 700 nm fluorophore conjugated to an anti-carcinoembryonic antigen (CEA) targeting antibody, SGM-101, was recently evaluated in two pilot studies for 26 patients needing colorectal cancer surgery and 12 patients who needed pancreatic cancer surgery. Tumour-specific fluorescence signals, with the highest target to background ratios (*in vivo* 1.8 and *ex vivo* 6.1) found in the 10 mg dose group, could be observed during surgery with a diagnostic accuracy of 84% in colorectal tumours.[40] In the expansion cohort comprising 17 patients, fluorescence imaging yielded 19 (43%) extra lesions compared with the surgeon's clinical evaluation, resulting in a change of treatment plan in 32% of the patients. In patients with pancreatic adenocarcinoma, fluorescence imaging using SGM-101 was able to detect 21 lesions in total, of which one was a false-positive.[39] However, because of the presence of dense desmoplastic stromal tissue surrounding tumour ducts, fluorescence signals and associated target to background ratios were more modest compared with the colorectal cancer group (*in vivo* 1.6 and *ex vivo* 3.2). Two lesions detected by visual inspection were not fluorescent. The use of SGM-101 could have resulted in a change of the treatment plan in one patient, as illustrated in Figure 3.

Hybrid fluorescent and radioactive targeted tracers

To overcome the main limitation of near-infrared fluorescence image guidance in terms of the sensitive detection of deeper-lying lesions, use of multimodality imaging has been advocated. Nuclear techniques have been found to be particularly complementary with fluorescence navigation because gamma rays are scarcely attenuated by overlying tissue. In addition to the superficial fluorescent signal, contrast agents featuring both a radioactive label and a fluorescent dye can offer preoperative information for surgical planning via single photon emission computed tomography or PET imaging and acoustic guidance for the surgeon via gamma-probe tracing. ^{99m}Tc-Nanocolloid in complex with indocyanine green was the first hybrid tracer tested in humans for refinement of the sentinel lymph node procedure. A prospective trial of 495 patients with head and neck cancer, skin, penile, prostate or vulva cancer, showed the benefit of indocyanine green-^{99m}Tc-Nanocolloid in terms of precise visual guidance, depth estimation and detection of sentinel lymph nodes close to the injection site.[49] However, the intraoperative detection of (lymph node) metastases or occult tumour lesions requires targeted agents.

The monoclonal antibody girentuximab-IRDye800CW co-labelled with ^{111}In was used for the visualisation of clear-cell renal-cell carcinomas, in which carbonic anhydrase IX is overexpressed. [41] Fluorescence imaging was feasible in 12 patients, with high fluorescence in the tumour (mean

target to background ratio of 2.5). The added-value of the radioguidance consisted in tracing lesions covered with perinephric fat and endophytic lesions. Bombesin, co-labelled with IRDye800CW and ^{68}Ga was used in 14 patients for detection of glioblastoma multiforma in which the gastrin-releasing peptide receptor is overexpressed. Good correlation between PET signals and intraoperative fluorescence signal was shown. During surgery, most of the tumours showed fluorescence (mean target to background ratio of 4.9), resulting in a sensitivity of 94% and specificity of 100%.[42] With the recent success of radiolabelled prostate-specific membrane antigen (PSMA)-targeted tracers for PET/CT imaging and targeted radionuclide therapy, efforts have also been made towards the design and preclinical validation of hybrid nuclear and fluorescent PSMA-tracers for use as surgical navigation tools in prostate cancer.[50]

Activatable fluorescent agents evaluated in clinical trials

A different strategy to actively trace tumour tissue is by using activatable fluorescent tracers. The fluorescent agent is optically silent until activated, often through enzymatic cleavage of the backbone structure (Figure 2). Two activatable fluorescent probes, LUM015 and AVB-620, have been evaluated clinically. Whitney and colleagues [44] described the use of LUM015, which is a cathepsin-activated fluorescent probe, in a phase 1 study in 15 patients with sarcoma or breast cancer. LUM015 was well-tolerated in the three dose groups (0.5 mg/kg, 1.0 mg/kg and 1.5 mg/kg) and showed tumour-specific fluorescence during *ex vivo* imaging with a mean target to background ratio of 4.1 in 13 (87%) patients. Another research group showed the feasibility of LUM015 for intraoperative detection of residual breast cancer in 15 patients.[45] In this cohort, elevated fluorescent signals were noticed in *ex vivo* resected breast tumours, resulting in mean target to background ratios of 4.7 in the 0.5 mg/kg group, and 4.2 in the 1.0 mg/kg dose group. Furthermore, for five patients, residual positive margins could be detected in the lumpectomy wall. Currently, a phase 2 study (NCT03321929) is recruiting patients with breast cancer to determine the efficacy of LUM015 in a larger patient cohort (n=250) and a phase 3 trial (NCT03686215) will start soon afterwards. Next to this, LUM015 is also being evaluated for detection of other cancer types such as gastrointestinal cancers (NCT02584244), peritoneal metastasis (NCT03834272), brain cancer (NCT03717142), or prostate cancer (NCT03441464).

The first clinical use of AVB-620, in breast cancer was described by Unkart and colleagues.[46] This tracer consists of a cell-penetrating peptide bearing a Cy5 fluorophore and a neutralising peptide bearing a Cy7 fluorophore. After proteolytic cleavage, the two peptides are separated, and the Cy5 bearing cell-penetrating peptide will become functional, increasing Cy5 fluorescence intensity and decreasing Cy7 emission. The Cy5/Cy7 fluorescence ratio was used for the analysis of fluorescence signals on resected tumour specimens. 15 patients were included in a dose-escalation cohort and 12 patients in the expansion cohort. Depending on injection time, either 1 day before surgery or on the day of surgery, mean fluorescence ratios of *ex vivo* tumour specimens obtained were 1.1 or 1.9 for cancerous breast tissue, and 0.6 or 1.2 for adjacent normal breast tissue. Based on these results a phase 2 trial (NCT03113825) has been launched to determine the accuracy of AVB-620 for distinguishing malignant and nonmalignant breast tissue.

Emerging targeted fluorescent molecular tracers with improved pharmacokinetics and specificity

The inherent capacity of antibodies to effectively recognise specific cell-surface expressed antigens and the relatively easy process through which new antibodies can be generated, makes them the biggest class of readily available targeted agents. Therefore, many groups are currently evaluating preclinically novel near-infrared fluorescence-labelled antibodies targeting alternative biomarkers for distinct intraoperative imaging applications, all showing the feasibility of the antibodies to highlight tumour lesions.[51-54] The long blood retention of antibodies due to their large size and neonatal Fc receptor-mediated recycling, in combination with the enhanced permeability and retention effect has been associated with long delayed imaging times (several days between the moment of injection and the surgery) and non-specific tissue accumulation resulting in false positive signals.[33,40,55] Furthermore, antibodies are known to show poor tissue penetration at microscopic level (Table 2).[56]

Advances in protein-engineering have led to the development of antibody-fragments (minibodies, Fab-fragments, diabodies,[57] and single chain variable fragments) (Figure 2, Table 2) that retain similar binding characteristics, but show better tumour penetration and more rapid clearance from non-targeted tissues. For example, Zhang and colleagues [58] showed that the IRDye800CW-labelled minibody that is specific to the prostate stem-cell antigen facilitated complete resection of invasive tumours and detection of tumour-infiltrated lymph nodes in mice. A clinical trial with the minibody IAB2M-IRDye800CW that is specific to prostate specific membrane antigen has been launched with the aim of evaluating the safety, feasibility, and optimal dose of the contrast agent to visualise cancer invasion in 20 patients. In a second stage, the effect of fluorescence imaging guidance on the completeness of tumour resection, urinary and sexual function outcome, disease recurrence, and survival will also be assessed in 50 men who are scheduled for robot-assisted laparoscopic radical prostatectomy (ISRCTN10046036).

Antibody-fragments with a low molecular weight (<60 kDa in size) that are rapidly eliminated from the blood via renal excretion have especially been researched as tools for molecular imaging applications because they enable highly specific and high-contrast imaging at early timepoints after injection.[59] However, the conjugation of near-infrared fluorescent dyes (such as IRDye800CW) can cause increased albumin binding and hepatic clearance of the tracers, and that can possibly influence their typical pharmacokinetic profile.[60] The Fab-fragment VB6–845-IRDye800CW, which targets the epithelial cell adhesion molecule highly overexpressed on most epithelial cancers, showed high target to background ratios between 8 and 24 h after injection in orthotopic breast and colorectal tumour mouse models.[61] This tracer has been produced for clinical use and a phase 1 trial (NL7363) is planned in patients with oesophageal, gastric, or rectosigmoid cancer who will have laparoscopic surgery. Researchers have also been interested in single- domain antibodies, better known as nanobodies™, which are derived from heavy-chain antibodies found in camelids. Several fluorescently-labelled nanobodies, targeting tumour markers such as carbonic anhydrase IX or HER2 have been successfully evaluated in preclinical models, with noteworthy tumour to background ratios reached within 1 to 3 h after injection.[62,63]

Another class of targeted agents that have elicited interest are non-immunoglobulin protein scaffolds, which include centyrins, affibodies, or cystine knottins (Figure 2).[64–66] These scaffolds exhibit similar pharmacokinetics as the small antibody fragments, but are generated through random mutagenesis or rational design of the antigen-binding regions, instead of via immunisation in which the affinity of molecules for their antigen is matured naturally in an animal. For example, the IRDye800CW-labelled anti-EGFR affibody molecule ABY-029 showed high-uptake and high-contrast values on *ex vivo* slices compared with normal brain tissue in an intracranial glioma rat model within 1 h after injection.[67] ABY-029 is under investigation in three phase 1 clinical trials; one for recurrent glioma (NCT02901925), another for primary sarcoma (NCT03154411), and one in head and neck cancer surgery (NCT03282461). In addition to the clinically tested tozuleristide, Tummers and colleagues [65] validated another cystine knottin peptide binding specifically to integrin $\alpha_v\beta_6$ in orthotopic and spontaneous transgenic pancreatic tumour models.

Peptides and small molecules are even smaller in size than the compounds above; however, the pharmacokinetic profile of each tracer becomes dependent on their individual physicochemical characteristics. In comparison with platform technologies such as antibodies, antibody fragments, and protein scaffolds high throughput generation of novel peptides and small molecules with adequate properties for *in vivo* imaging is more difficult and unpredictable. However, once a lead compound against a specific biomarker has been identified, it can be routinely produced according to current good manufacturing protocols for clinical use at a much lower cost than biologicals, which require production through fermentation (Table 2). Bombesin-antagonists [68] and RGD peptides [69] are often subject to preclinical investigation. Besides IRdye800CW and Cy5, cRGD has also been conjugated with zwitterionic fluorophore ZW800–1. cRGD-ZW800–1 exhibits substantially less non-specific binding in normal organs and tissues than does IRDye800CW-labelled cRGD, and is cleared exclusively through the kidneys.[70] A drawback of ZW800–1 is its instability over time in serum, although it appears that this limitation can be overcome by rapid internalisation.[71] Using cRGD-ZW800–1, Handgraaf and colleagues [69] showed the feasibility to image integrin overexpression on malignant and neoangiogenic cells in various tumour models, including pancreas, colorectal, oral, and breast cancer with high tumour signals and tumour to background ratios at 4 h after injection. Moreover, tumour signals were still clearly distinguishable after 24 and even after 48 h. Because of the easy production procedure and low cost, this probe is undergoing clinical translation and the first human data are expected in the near future (NL7724; Table 1).

Challenges and considerations towards clinical translations of novel tracers

A wide variety of molecular tracers have shown potential to specifically highlight tumour lesions in animal models and are awaiting clinical translation. The field of PET imaging, which is considerably more advanced regarding the development of targeted tracers, favours the use of highly specific agents with fast pharmacokinetics, both from a safety and practical point of view. Analogously, for fluorescence imaging applications, the timing of administration of the contrast agent (e.g., just before surgery would be highly convenient) and the clearing pattern of the agent need to be considered. For example, renally cleared agents would permit improved visualisation of liver lesions in comparison with fluorescent agents cleared via the hepatobiliary route.[59] However, because the minimal signal level that must be reached for sensitive detection with fluorescence imaging devices is higher than for PET, slower blood clearance rates could enhance signal intensities at the target. Dose optimisation studies are therefore essential to obtain superior image quality in terms of both signal intensity and tumour to background ratios. Yet, the use of highly sensitive imaging instruments and the design of brighter fluorescent dyes are probably more advisable approaches towards clinical translation than increasing the injected dose of rapidly cleared targeted contrast agents to improve detection's sensitivity because of potential toxicity.

Despite all preclinical evidence, the real assessment of the value of fluorescent contrast agents for intra-operative imaging can only be performed in humans. Hereto, promising compounds have to undergo a translational process before clinical trials can be initiated. Current good manufacturing practice and toxicity studies remain the main bottlenecks of development because of their cost and time-consuming administrative burden. Because targeted fluorescent contrast agents often require doses above the microdosing level, a simplified regulation with less extensive toxicity studies as for radiopharmaceuticals is unfortunately not possible. Fast clearing tracers with predictable biodistributions could eventually have an advantage regarding documentation of the intended use because they are less likely to elicit unpredictable toxicity issues. Furthermore, the choice for a targeting moiety will have to be balanced between the ease of generation (derived from a generic platform technology) and the cost for routine production (relatively cheap chemical synthesis *vs* expensive fermentation process). For the field of intraoperative fluorescence imaging, this is even more important because the financial added value is probably less than for cancer therapeutics or companion diagnostic PET tracers.

The effectiveness of a molecular tracer will not only be determined by its general pharmacokinetic profile but will also be highly dependent on the biomarker it is intended to recognise and its expression pattern. Unfortunately, so far, no clear consensus exists on the most optimal biomarkers for the field. Yet, many prerequisites have been defined; these include: the biomarker should be highly overexpressed on tumour cells or stroma, while presenting no or low expression on normal tissue or after chemotherapy or radiotherapy to ensure high-contrast and specific imaging of only the tissue of interest; biomarkers are preferred to be extracellularly expressed to permit targeting by molecules that do not penetrate cells, but should ideally also internalise after binding for a long-lasting signal; the biomarker should show specificity across at least different types and subtypes of cancers to avoid preoperative screening of patients (unlike nuclear medicine applications for which

lately targeting of highly specific biomarkers is most often warranted to enable patient stratification for personalised therapies); and within one tumour type, homogeneous expression throughout the cancerous tissue is warranted, independently of tumour stage. However, most human tumours are known to exhibit substantial spatial and temporal intratumour heterogeneity, and this aspect is particularly difficult to mimic in preclinical models. Therefore, *in vivo* efficacy shown in preclinical research can often not be directly extrapolated to the clinical setting. From a regulatory and economic point of view, the feasibility of administrating a cocktail of fluorescent molecular tracers to overcome tumour heterogeneity has been suggested but is unlikely.

Future perspectives

Intraoperative fluorescence molecular imaging is still in its infancy. Clinical studies completed so far mainly consist of early-phase trials aimed at evaluating the safety of fluorescent contrast agents, estimating the optimal dose, showing feasibility of intraoperative lesion detection, and assessing exploratory data on sensitivity and specificity. It has been shown that near-infrared fluorescence imaging can improve the detection of peritoneal lesions during cytoreductive surgery, which is associated with improved survival. However, the primary solid tumour types for which surgical margin assessment and intraoperative staging (i.e., detection of lymph node or distant metastases) would be most beneficial, is not yet established. On the one hand, depending on the desired distance of the resection margin, in-situ molecular fluorescence imaging could be supportive to plan surgical dissection planes or to visualise remnant tumour cells after resection. On the other hand, surgical specimen imaging could be complementary and could provide precise information about both the extent of the tumour and the resection margins. When close resection margins are encountered, an additional resection could be considered and performed.

Large, multicentre, randomised controlled trials are thus mandatory to find out the diagnostic accuracy of fluorescence molecular imaging and to show the value of this technique on surgical outcomes and benefits to the patient. To convince regulatory authorities and reimbursement agencies, it is essential to identify clinically meaningful endpoints and surrogates of clinical benefit that are acceptable to authorities. A phase 3 multicentre, randomised controlled trial (NCT03659448) has been launched in patients with metastastic colorectal cancer to prove the added value of imaging with SGM-101 targeting anti-carcinoembryonic antigen in terms of resection margins. Furthermore, a phase 3 trial (NCT03180307) with OTL-38 is underway and includes patients with ovarian cancer who are scheduled to have open debulking surgery. In this study, the efficacy, which has been defined as the proportion of patients in which fluorescence imaging yields at least one additional tumour-positive lesion compared with normal conditions, will be assessed, as well as the diagnostic accuracy of OTL-38 at the patient level.

Nevertheless, the absence of a general consensus on standardised protocols for the clinical evaluation of new molecular fluorescent agents makes the conduction of multicentre trials and the comparison between clinical studies difficult. For example, tumour to background ratio is an important determinant for evaluating the efficacy of a fluorescent tracer; however, calculating

tumour to background ratios could be influenced by selection bias of relevant regions of interest, and studies report tumour to background ratios measured in different circumstances (e.g., *in vivo* or *ex vivo*). Furthermore, detected signal intensities not only depend on the chemical, photo- chemical, and biological characteristics of the fluorescent agent being investigated; but are also affected by tissue optical factors, depth of signal, as well as by the technical specifications and performance of the chosen imaging instrument. Importantly, the fluorescence imaging system should match the fluorescent contrast agent for optimal detection. Despite considerable efforts towards the development of a universal tool for calibration, quality control, and benchmarking of imaging devices, its development remains challenging because of the diversity of parameters influencing imaging.[72] Alternatively, advances in methods and models supporting accurate quantification of fluorophore concentrations in tissue would enable more objective distinction between tumour or non-tumour tissue. Improved image processing and interpretation would be desirable for the determination of clinically relevant cut off values for resection margins and exclusion of false-positive signals.[73] Meanwhile, guidelines regarding experimental workflow, data collection, image analysis, and reporting have emerged.[74–76] These are intended to obtain reliable, reproducible, and comparable data that will eventually ensure clinical implementation and approval of the technique.

Besides adequate open-surgery fluorescent imaging devices currently available, many laparoscopic and robotic surgical systems are already equipped with fluorescence cameras. It is to be expected that, in the future, more and more complex surgeries will be performed in a minimally invasive way, because they have already shown substantial benefits and led to a reduction in hospital costs.[77] With minimally invasive surgeries, it is even more important to guide the surgeon because of the limited field of view, associated risk of missing hidden lesions, and the absence of tactile feedback. However, it is also important to simultaneously highlight vital structures such as ureters or nerves, in addition to tumour tissue. During such procedures, the combination of fluorophores would be beneficial (e.g., one for tumour detection and one for detection of other important structures or tissue perfusion). This can be achieved by using fluorescence camera systems that are equipped with two or more fluorescent channels.

Conclusions

Fluorescence molecular imaging has so far shown its potential to support surgical procedures and the feasibility to improve clinical outcomes. Although there is much enthusiasm about these first results, intraoperative fluorescence molecular imaging is now at a crucial turning point in which unequivocal efficacy studies are needed to move the field beyond current proof of concept studies to produce a real change in clinical practice. Once this step has been taken, more extensive investments are to be expected towards novel tracers with improved characteristics pertaining to pharmacokinetics and specificity, as well as more sophisticated image analysis software. An important asset of fluorescence imaging is the relative ease by which the technology can be integrated within the routine of many different surgical and interventional cases, hence the necessity for centres of expertise to train users, as well as to create wide-spread awareness of the technique.

Figure 1. Principle of intraoperative molecular near infrared (NIR) fluorescence imaging. Top: Schematic illustration of (potential) applications of molecular targeted NIR fluorescence imaging. Bottom: Implementation of fluorescence guidance during both open and laparoscopic surgery. After intravenous injection of the tracer (one hour up to several days before surgery depending on the tracer), the tumour and/or other tissues-of-interest can be visualized with a specialized NIR camera, thereby guiding the surgeon in real-time during the resection. Immediately after resection, the specimen(s) can be sliced and imaged with a back-table fluorescence camera and microscope. The pathologist can thus rapidly check the resection margins on the presence of fluorescence and provide rapid feedback to the surgeon.

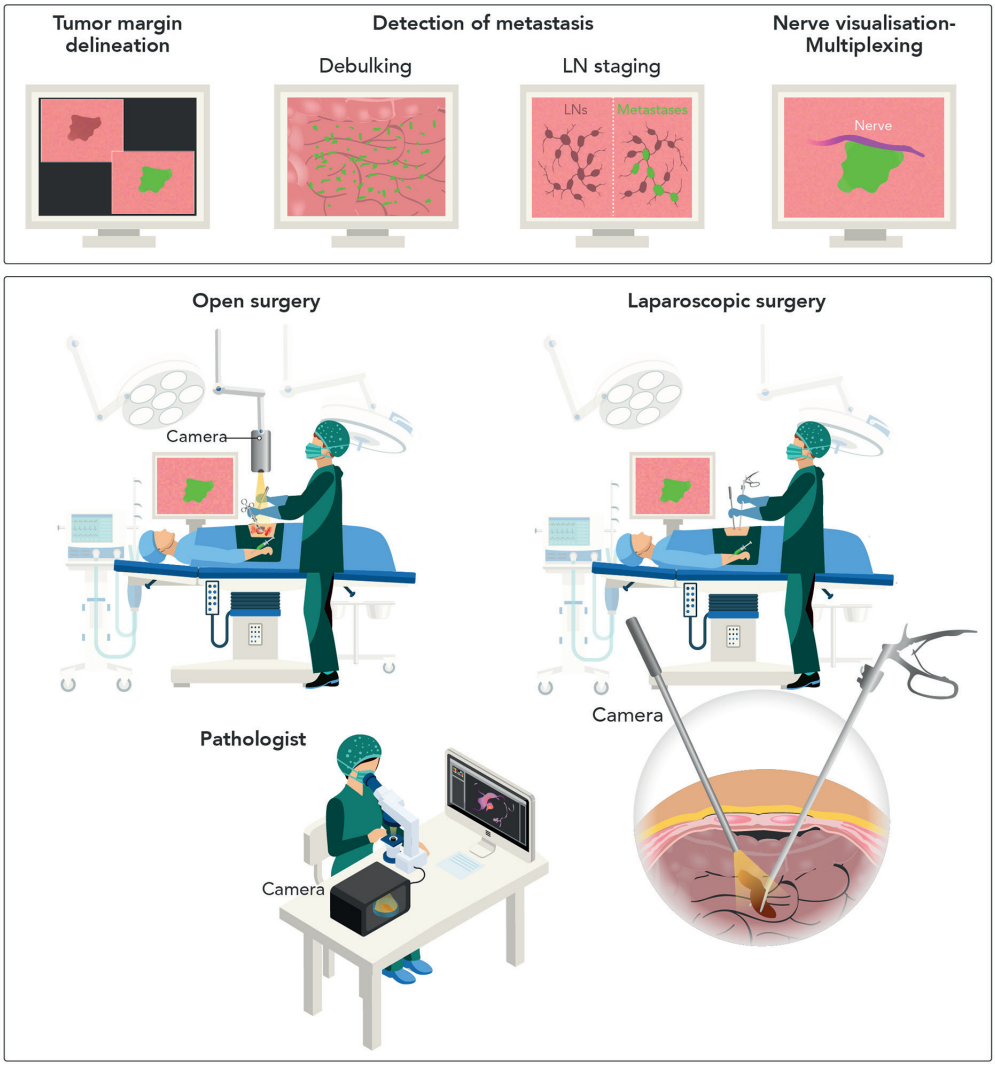

Figure 2. Molecular fluorescent contrast agents and targeting moieties used for intraoperative imaging during cancer surgery. Top: Schematic representation of the mode of action of the different types of fluorescent contrast agents. Non-targeted fluorescent contrast agents such as ICG aggregate to serum proteins in the circulation and passively accumulate in tumour tissue via the enhanced permeability and retention (EPR) effect. Targeted fluorescent contrast agents, consisting of a fluorescent dye conjugated to a targeting moiety, actively accumulate in tumour tissue by recognition of a specific biomarker expressed by tumour cells or tumour-associated stromal cells. Imaging is performed once unbound tracers have been cleared sufficiently. Activatable fluorescent contrast agents remain optically silent until fluorescent dyes are released by enzymatic digestion of their backbone. Bottom: Schematic representation of the different (sub-) classes of targeting moieties used for the design of targeted fluorescent contrast agents: Antibodies, antibody-fragments, protein scaffolds, peptides and small molecules. Representative space-filling images of an Antibody (1IGT), Fab (6B9Z), Diabody (1MOE), scFv (1P4I), Nanobody (5MY6), Centyrin (5L2H), Affibody (2KZJ) and Knottin (2N8B) were obtained from the RCSB protein bank and prepared using PyMOL. The space-filling Minibody model is an interpretation created using PyMOL, Antigen-binding regions are highlighted in orange.

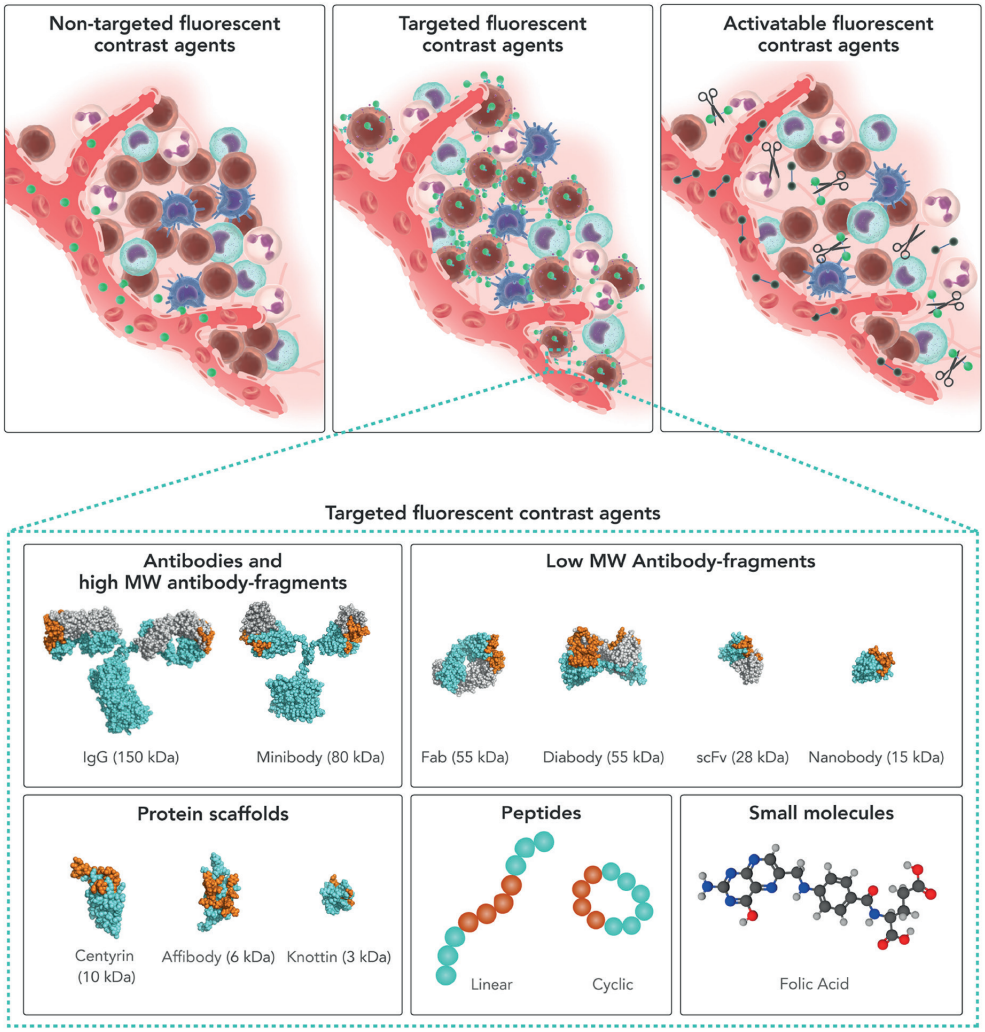

Table 1. Overview of ongoing and published clinical trials in molecular fluorescence-guided cancer surgery. Some studies share (partially) the same patient population. *VATS=video-assisted thoracoscopic surgery. VEGF=vascular endothelial growth factor. EGFR=epidermal growth factor receptor. CEA=carcinoembryonic antigen. CAIX=carbonic anhydrase IX. GRPR=gastrin-releasing peptide receptor. EpCam=epithelial cell adhesion molecule. PSMA=prostate-specific membrane antigen. HER2=human epidermal growth factor receptor 2. MMP=matrix metalloproteinase. HSP=heat shock protein. SPECT= single photon emission computed tomography. PEGylated=attachment of polyethylene glycol.*

Agent	Target	Ref or Study	Target tissue	Study type	Study population (n)	Incorporation	Interval between injection and surgery	Other(s)
EC17	Folate receptor	[12]	Ovarian cancer	Phase 1	10	Open (cytoreductive) surgery	2-8 h	..
		[13]	Lung cancer	Phase 1	30	Open surgery/ VATS	4 h	..
		[14]	Lung cancer	Phase 1	50	Open surgery	4 h	..
		[16]	Renal cell carcinoma	Case report	4	Open surgery	4 h	..
		[15]	Breast and ovarian cancer	Phase 1	15 (12 ovarian, 3 breast cancer)	Open surgery	2-3 h	..
		NCT01778933	Renal cell carcinoma	Phase 1	10	Open / laparoscopic surgery	2-4 h	..
OTL38	Folate receptor	[17]	Ovarian cancer	Phase 1a/Ib	42	Open (debulking) surgery	2-3 h	Phase 1a: 30 healthy volunteers Phase 1b: 12 patients
		NCT03180307	Ovarian cancer	Phase 3	147	Open (debulking) surgery	N.S.	..
		[18]	Renal cancer	Case report	3	Robotic surgery	2 h	..
		NCT02645409	Renal cancer	Phase 2	20	N.S.	2 h	..
		[19]	Pulmonary adenocarcinoma	Phase 1	50	VATS, robotic surgery	3-6 h	Combined with PET-CT
		[20]	Pulmonary adenocarcinoma	Case report	1	VATS	3-6 h	..
		[21]	Pulmonary squamous cell carcinoma	Phase 1	12	VATS	3-6 h	..
		[22]	Pulmonary adenocarcinoma	Phase 1	20	VATS	3-6 h	..
		[23]	Pulmonary adenocarcinoma	Phase 1	10	VATS	3-6 h	..
		[24]	Pulmonary ground glass opacities	Phase 1	20	VATS	3-6 h	..
		NCT02872701	Pulmonary adenocarcinoma	Phase 2 (multicenter)	110	VATS	2-3 h	..
		[25]	Meningioma	Case report	1	Open surgery	N.S.	..
		[26]	Endometrium	Phase 1	4	Open surgery	2-3 h	..

Agent	Target	Ref or Study	Target tissue	Study type	Study population (n)	Incorporation	Interval between injection and surgery	Other(s)
Bevacizumab-IRDye800CW	VEGF	[27]	Colorectal peritoneal metastases	Phase 1	7	Open surgery	2 days	..
		[28]	Breast cancer	Phase 1	20	Open surgery	3 days	..
		NCT02975219	Endometriosis	Phase 1	10	N.S.	3 days	..
		NCT02743975	Pancreatic cancer	Phase 1/2	26	Open surgery	3 days	..
		NCT03620292	Perihilar cholangio-carcinoma	Phase 1/2	12	Open surgery	3 days	Including *ex vivo* endoscopic fluorescence imaging of resected specimen
Cetuximab-IRDye800CW	EGFR	[29]	Head and neck cancer	Phase 1	9	Open surgery	3-7 days	Dose escalation study
		[30]	Head and neck cancer	Phase 1	12	Open surgery	3-7 days	Dose escalation study
		[31]	Head and neck cancer	Phase 1	12	Open surgery	3-7 days	Dose escalation study
		[32]	Head and neck cancer	Phase 1a	12	Open surgery	1-5 days	Dose escalation study evaluating both cetuximab-IRDye800CW and panitumum-ab-IRDye800
		NCT03134846	Head and neck cancer	Phase 1/2	79	Open surgery	4 days	Part I: dose escalation in 9 patients
		[33]	Pancreatic cancer	Phase 1	7	Open and laparoscopic surgery	2-5 days	Part 2: expansion cohort in 70 patients
		[34]	Pancreatic cancer	Phase 1	7	Open surgery	2-5 days	Photoacoustic imaging was also performed
		[35]	Glioblastoma	Case reports	3	Open surgery	2 days	..
Panitumum-ab-IRDye800CW	EGFR	[32]	Head and neck cancer	Phase 1a	15	Open surgery	1-5 days	Dose escalation study evaluating both cetuxi-mab-IRDYe800CW and panitumum-ab-IRDye800
		[36]	Head and neck cancer	Phase 1	21	Open surgery	1-5 days	..
		[37]	Oral squamous cell carcinoma	Phase 2	8	Open surgery	1-4 days	..
		[38]	Head and neck cancer	Phase 1	14	Open surgery	1-5 days	..
		NCT03384238	Pancreatic cancer	Phase 1/2	24	Open/ laparo-scopic surgery	2-5 days	..
		NCT03510208	Malignant glioma	Phase 1/2	22	Open surgery	1-5 days	..
		NCT03582124	Lung carcinoma	Phase 1/2	30	N.S.	1-5 days	..
		NCT03405142	Head and neck cancer	Phase 2	20	Open surgery	2-5 days	Focussing on lymph node detection by comparing near infrared fluores-cence with lymphoscintigra-phy and SPECT/CT after injection of 99mTc-labeled Tilmanocept

Agent	Target	Ref or Study	Target tissue	Study type	Study population (n)	Incorporation	Interval between injection and surgery	Other(s)
SGM-101	CEA	[39]	Pancreatic cancer	Phase 1	12	Open surgery	2-4 days	..
		[40]	Colorectal cancer	Phase 1/2	26	Open and laparoscopic surgery	2-4 days	..
		NCT03659448	Colorectal cancer	Phase 3 (Randomized controlled trial)	300	Open and laparoscopic surgery	2-4 days	..
^{111}In-DOTA-Labetuzumab-IRDye800CW	CEA	NCT03699332	Colorectal peritoneal metastases	Phase 1/2	29	Open surgery	6-7 days	Dual modality imaging
^{111}In-DOTA-Girentuximab-IRDye800CW	CAIX	[41]	Renal cancer	Phase 1	15	Open surgery	7 days	Dual modality imaging
^{68}Ga-NOTA-IRDye-800CW-BBN	GRPR	[42]	Glioblastoma	Phase 1	14	Open surgery	2 h	Dual modality imaging
Tozuleristide (BLZ-100)	Cell-surface chlorotoxin binding proteins	[43]	Breast cancer	Phase 1	23	Open surgery	1-26 h	Fluorescence imaging was only conducted ex vivo on resected specimens
		NCT02234297	Glioma	Phase 1	17	Open surgery	2 h	..
		NCT02462629	CNS tumours	Phase 1	32	Open surgery	1 h	Dose escalation and expansion cohort in pediatric subjects
		NCT03579602	CNS tumours	Phase 2/3 (randomized controlled trial)	114	Open surgery	1-36 h	Subjects will be randomized 1:10 to 1 of 2 study arms. Study arm 1: no BLZ-100 injection, although imaging will be performed. Study arm 2: BLZ-100 injection and imaging will be done.
VB5-845D-800CW	EpCam	NTR7570	Esophageal/gastric- or rectosigmoid cancer	Phase 1	34	Laparoscopic surgery	Optimal injection time will be based on the results of part Ia	Part Ia: dose escalation in human volunteers (N=16)
ABY029	EGFR	NCT02901925	Recurrent glioma	Phase 1a	12	Open surgery	1-3 h	..
		NCT03154411	Sarcoma	Phase 1a	18	Open surgery	1-3 h	..
		NCT03282461	Head and neck cancer	Phase 1a	12	Open surgery	1-3 h	..
IR800 IAb2M	PSMA	ISRCTN 10046036	Prostate cancer	Phase 1	120	Robot-assisted laparoscopic surgery	1-2 days	Part I: dose escalation in 20 patients Part 2: randomized allocation of IR800 IAb2M in 100 patients
cRGD-ZW800-1	Integrins (associated with tumor angiogenesis)	NL7724	Colorectal cancer	Phase 2	12	Laparoscopic surgery	<24 h	Ureter could also be visualized simultaneously, due to characteristics of ZW800-1

Agent	Target	Ref or Study	Target tissue	Study type	Study population (n)	Incorporation	Interval between injection and surgery	Other(s)
HS-196	HSP-90 inhibitor	NCT03333031	Breast cancer	Phase 1	120	Open surgery	24 h	Part I: dose escalation Part 2: expansion cohort
KSP-910638G	HER2	NCT03161418	N.S.	Phase 1a	26	N.S.	N.S.	Orally administration of tracer; safety trial in human volunteers
LS301	$\alpha_v\beta_3$ integrins	NCT02807597	Breast cancer	Phase 1	22	Open surgery	4-24 h	Including evaluation of feasibility for sentinel lymph node detection
LUM015	Cathepsins	[44]	Sarcoma and breast cancer	Phase 1	15	Open surgery	2-6 h	Activatable tracer: PEGylated protease-activated
		[45]	Breast cancer	Phase 2	15	Open surgery	2-6 h	Activatable tracer: PEGylated protease-activated
		NCT03321929	Breast cancer	Phase 2	250	Open surgery	2-6 h	Activatable tracer: PEGylated protease-activated
		NCT03686215	Breast cancer	Phase 3	250	Open surgery	2-6 h	Activatable tracer: PEGylated protease-activated
		NCT02584244	Colorectal, pancreatic, and esophageal cancers	Phase 1/2	21	Open surgery	2-6 h	Activatable tracer: PEGylated protease-activated; Fluorescence imaging will only be conducted ex-vivo on resected specimens
		NCT03834272	Peritoneal metastases	Phase 1	18	Open surgery	2-6 h	Activatable tracer: PEGylated protease-activated
		NCT03717142	Brain cancer	Phase 1	36	Open surgery	2-6 h	Activatable tracer: PEGylated protease-activated
		NCT03441464	Prostate cancer	Phase 1	12	Open surgery	2-6 h	Activatable tracer: PEGylated protease-activated; Fluorescence imaging will only be conducted ex-vivo on resected specimens
AVB-620	MMPs	[46]	Breast cancer	Phase 1	27	Open surgery	2-20 h	Activatable tracer: ratiometric activatable cell-penetrating peptide; Part I: dose escalation in 15 patients Part 2: expansion cohort of 12 patients
		NCT02901925	Breast cancer	Phase 2	110	Open surgery	< 24 h	Activatable tracer: ratiometric activatable cell-penetrating peptide

Growth Factor; EGFR: Epidermal Growth Factor Receptor, CEA: CarcinoEmbryonic Antigen, CAIX: Carbonic Anhydrase IX; GRPR: Gastrin-Releasing Peptide Receptor; EpCam: Epithelial Cell Adhesion Molecule; PSMA: Prostate-Specific Membrane Antigen, HER2: Human Epidermal Growth Factor Receptor 2; MMP: Matrix Metalloproteinase.

Figure 3. Example of intraoperative molecular fluorescence imaging during pancreatic surgery. A: Intraoperative fluorescence imaging of a pancreatic tumour (asterisk: tumour bulk), which could be visualized using a monoclonal antibody for carcinoembryonic antigen (CEA) conjugated to a 700 nm fluorophore (SGM-101). Based on the fluorescence image, the surgeons initially decided to move the planned resection line (black dashed line: proposed resection line based on visual inspection/palpation; blue dashed line: proposed resection line based on fluorescence). B: *Ex vivo* analysis of a resected pancreatic tumour. C: Histopathological analysis of a tumour slice of a primary pancreatic tumour showing fluorescence, CEA expression, and microscopically localisation of tumour cells. Adapted and reprinted by permission from Springer Nature: Annals of Surgical Oncology © 201839.

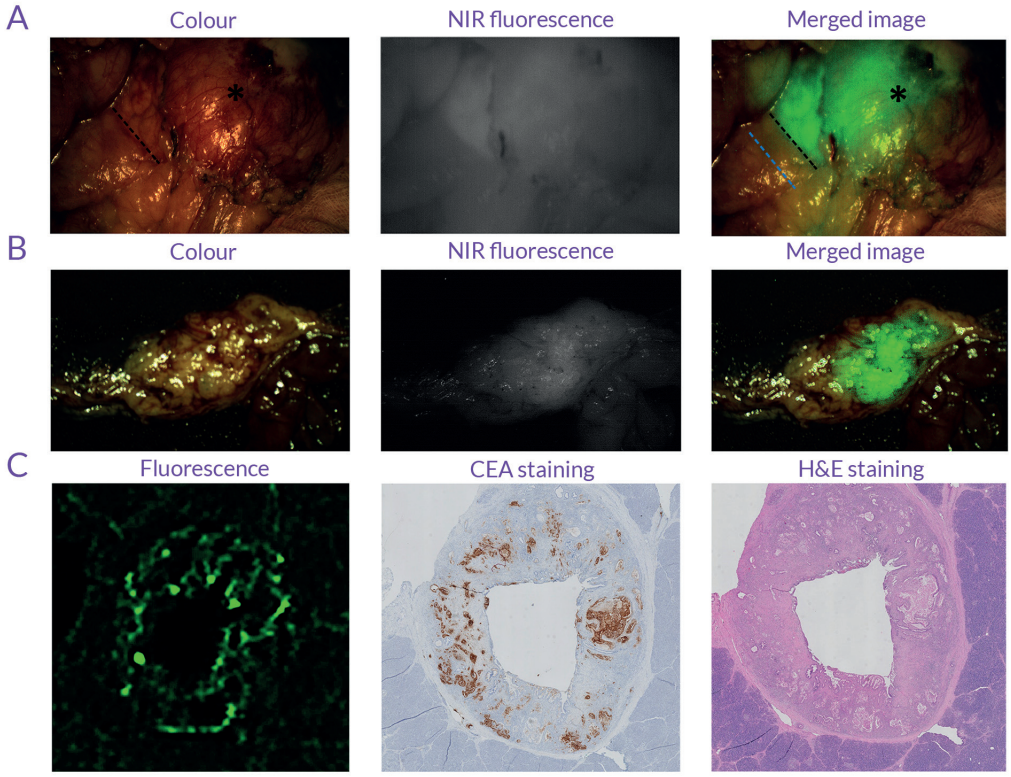

Table 2: Overview of the different (sub-) classes of targeting moieties used for the design of targeted fluorescent contrast agents and key-elements to consider towards clinical application and implementation.

	mAbs	Ab-Fragments		Protein Scaffolds	Peptides	Small Molecules
		High MW	Low MW			
Size	150 kDa	80 kDa	15 - 55 kDa	3 – 10 kDa	0.5 - 2 kDa	0.5 – 1 kDa
Delayed scanning time	Several days	One to several days	One to several hours	1 – 3 h	1 – 24 h	1 – 24 h
Tissue penetration	+/-	+	+/++	++	+++	+++
Platform technology	Yes	Yes	Yes	Yes	No	No
Generation strategy	Immunization	Immunization	Immunization	Random mutagenesis - Rational design	Rational design	Rational design
Routine production method	Fermentation	Fermentation	Fermentation	Fermentation/ Chemical Synthesis	Chemical Synthesis	Chemical Synthesis
(cGMP) Production Cost	€€€	€€€	€€€	€€€/€	€	€
Subclasses applied in fluorescence-guided surgery		Minibody	Fab, Diabody, scFv, Nanobody	Affibody, Centyrin, Knottin	Linear, Cyclic	

References

1. Tilly C, Lefevre JH, Svrcek M, et al. R1 rectal resection: look up and don't look down. Ann Surg 2014; 260(5): 794-9; discussion 9-800.
2. Wong LS, McMahon J, Devine J, et al. Influence of close resection margins on local recurrence and disease-specific survival in oral and oropharyngeal carcinoma. Br J Oral Maxillofac Surg 2012; 50(2): 102-8.
3. Esposito I, Kleeff J, Bergmann F, et al. Most pancreatic cancer resections are R1 resections. Ann Surg Oncol 2008; 15(6): 1651-60.
4. Vos EL, Gaal J, Verhoef C, Brouwer K, van Deurzen CHM, Koppert LB. Focally positive margins in breast conserving surgery: Predictors, residual disease, and local recurrence. Eur J Surg Oncol 2017; 43(10): 1846-54.
5. Stammes MA, Bugby SL, Porta T, et al. Modalities for image- and molecular-guided cancer surgery. Br J Surg 2018; 105(2): e69-e83.
6. Gioux S, Choi HS, Frangioni JV. Image-guided surgery using invisible near-infrared light: fundamentals of clinical translation. Mol Imaging 2010; 9(5): 237-55.
7. van Manen L, Handgraaf HJM, Diana M, et al. A practical guide for the use of indocyanine green and methylene blue in fluorescence-guided abdominal surgery. J Surg Oncol 2018; 118(2): 283-300.
8. Stummer W, Pichlmeier U, Meinel T, et al. Fluorescence-guided surgery with 5-aminolevulinic acid for resection of malignant glioma: a randomised controlled multicentre phase III trial. Lancet Oncol 2006; 7(5): 392-401.
9. Grossman HB, Stenzl A, Fradet Y, et al. Long-term decrease in bladder cancer recurrence with hexaminolevulinate enabled fluorescence cystoscopy. J Urol 2012; 188(1): 58-62.
10. Hadjipanayis CG, Widhalm G, Stummer W. What is the Surgical Benefit of Utilizing 5-Aminolevulinic Acid for Fluorescence-Guided Surgery of Malignant Gliomas? Neurosurgery 2015; 77(5): 663-73.
11. Vahrmeijer AL, Hutteman M, van der Vorst JR, van de Velde CJ, Frangioni JV. Image-guided cancer surgery using near-infrared fluorescence. Nat Rev Clin Oncol 2013; 10(9): 507-18.
12. van Dam GM, Themelis G, Crane LM, et al. Intraoperative tumour-specific fluorescence imaging in ovarian cancer by folate receptor-alpha targeting: first in-human results. Nat Med 2011; 17(10): 1315-9.
13. Kennedy GT, Okusanya OT, Keating JJ, et al. The Optical Biopsy: A Novel Technique for Rapid Intraoperative Diagnosis of Primary Pulmonary Adenocarcinomas. Ann Surg 2015; 262(4): 602-9.
14. Okusanya OT, DeJesus EM, Jiang JX, et al. Intraoperative molecular imaging can identify lung adenocarcinomas during pulmonary resection. J Thorac Cardiovasc Surg 2015; 150(1): 28-35 e1.
15. Tummers QR, Hoogstins CE, Gaarenstroom KN, et al. Intraoperative imaging of folate receptor alpha positive ovarian and breast cancer using the tumour specific agent EC17. Oncotarget 2016; 7(22): 32144-55.
16. Guzzo TJ, Jiang J, Keating J, et al. Intraoperative Molecular Diagnostic Imaging Can Identify Renal Cell Carcinoma. J Urol 2016; 195(3): 748-55.
17. Hoogstins CE, Tummers QR, Gaarenstroom KN, et al. A Novel Tumour-Specific Agent for Intraoperative Near-Infrared Fluorescence Imaging: A Translational Study in Healthy Volunteers and Patients with Ovarian Cancer. Clin Cancer Res 2016; 22(12): 2929-38.
18. Shum CF, Bahler CD, Low PS, et al. Novel Use of Folate-Targeted Intraoperative Fluorescence, OTL38, in Robot-Assisted Laparoscopic Partial Nephrectomy: Report of the First Three Cases. J Endourol Case Rep 2016; 2(1): 189-97.
19. Predina JD, Newton AD, Keating J, et al. Intraoperative Molecular Imaging Combined With Positron Emission Tomography Improves Surgical Management of Peripheral Malignant Pulmonary Nodules. Ann Surg 2017; 266(3): 479-88.
20. Predina JD, Newton A, Connolly C, Singhal S. Folate receptor-targeted molecular imaging improves identification of malignancy during pulmonary resection: a case report. J Cardiothorac Surg 2017; 12(1): 110.
21. Predina JD, Newton AD, Xia L, et al. An open label trial of folate receptor-targeted intraoperative molecular imaging to localize pulmonary squamous cell carcinomas. Oncotarget 2018; 9(17): 13517-29.
22. Predina JD, Newton AD, Keating J, et al. A Phase I Clinical Trial of Targeted Intraoperative Molecular Imaging for Pulmonary Adenocarcinomas. Ann Thorac Surg 2018; 105(3): 901-8.
23. Predina JD, Newton AD, Connolly C, et al. Identification of a Folate Receptor-Targeted Near-Infrared Molecular Contrast Agent to Localize Pulmonary Adenocarcinomas. Mol Ther 2018; 26(2): 390-403.
24. Predina JD, Newton A, Corbett C, et al. Localization of Pulmonary Ground-Glass Opacities with Folate Receptor-Targeted Intraoperative Molecular Imaging. J Thorac Oncol 2018; 13(7): 1028-36.
25. Pierce JT, Cho SS, Nag S, et al. Folate Receptor Overexpression in Human and Canine Meningiomas-Immunohistochemistry and Case Report of Intraoperative Molecular Imaging. Neurosurgery 2018.
26. Boogerd LSF, Hoogstins CES, Gaarenstroom KN, et al. Folate receptor-alpha targeted near-infrared fluorescence imaging in high-risk endometrial cancer patients: a tissue microarray and clinical feasibility study. Oncotarget 2018; 9(1): 791-801.
27. Harlaar NJ, Koller M, de Jongh SJ, et al. Molecular fluorescence-guided surgery of peritoneal carcinomatosis of colorectal origin: a single-centre feasibility study. The Lancet Gastroenterology & Hepatology 2016; 1(4): 283-90.
28. Lamberts LE, Koch M, de Jong JS, et al. Tumour-Specific Uptake of Fluorescent Bevacizumab-IRDye800CW Microdosing in Patients with Primary Breast Cancer: A Phase I Feasibility Study. Clin Cancer Res 2017; 23(11): 2730-41.
29. de Boer E, Warram JM, Tucker MD, et al. In Vivo Fluorescence Immunohistochemistry: Localization of Fluorescently Labeled Cetuximab in Squamous Cell Carcinomas. Sci Rep 2015; 5: 10169.
30. Rosenthal EL, Warram JM, de Boer E, et al. Safety and Tumour Specificity of Cetuximab-IRDye800 for Surgical Navigation in Head and Neck Cancer. Clin Cancer Res 2015; 21(16): 3658-66.
31. Rosenthal EL, Moore LS, Tipirneni K, et al. Sensitivity and Specificity of Cetuximab-IRDye800CW to Identify Regional Metastatic Disease in Head and Neck Cancer. Clin Cancer Res 2017; 23(16): 4744-52.
32. Gao RW, Teraphongphom N, de Boer E, et al. Safety of panitumumab-IRDye800CW and cetuximab-IRDye800CW for

fluorescence-guided surgical navigation in head and neck cancers. Theranostics 2018; 8(9): 2488-95.
33. Tummers WS, Miller SE, Teraphongphom NT, et al. Intraoperative Pancreatic Cancer Detection using Tumour-Specific Multimodality Molecular Imaging. Ann Surg Oncol 2018; 25(7): 1880-8.
34. Tummers WS, Miller SE, Teraphongphom NT, et al. Detection of visually occult metastatic lymph nodes using molecularly targeted fluorescent imaging during surgical resection of pancreatic cancer. HPB (Oxford) 2019.
35. Miller SE, Tummers WS, Teraphongphom N, et al. First-in-human intraoperative near-infrared fluorescence imaging of glioblastoma using cetuximab-IRDye800. J Neurooncol 2018; 139(1): 135-43.
36. Gao RW, Teraphongphom NT, van den Berg NS, et al. Determination of Tumour Margins with Surgical Specimen Mapping Using Near-Infrared Fluorescence. Cancer Res 2018; 78(17): 5144-54.
37. van Keulen S, van den Berg NS, Nishio N, et al. Rapid, non-invasive fluorescence margin assessment: Optical specimen mapping in oral squamous cell carcinoma. Oral Oncol 2019; 88: 58-65.
38. van Keulen S, Nishio N, Fakurnejad S, et al. The clinical application of fluorescence-guided surgery in head and neck cancer. J Nucl Med 2019; publised online Feb 7. DOI:10.2967/jnumed.118.222810.
39. Boogerd LSF, Hoogstins CES, Schaap DP, et al. Safety and effectiveness of SGM-101, a fluorescent antibody targeting carcinoembryonic antigen, for intraoperative detection of colorectal cancer: a dose-escalation pilot study. The Lancet Gastroenterology & Hepatology 2018; 3(3): 181-91.
40. Hoogstins CES, Boogerd LSF, Sibinga Mulder BG, et al. Image-Guided Surgery in Patients with Pancreatic Cancer: First Results of a Clinical Trial Using SGM-101, a Novel Carcinoembryonic Antigen-Targeting, Near-Infrared Fluorescent Agent. Ann Surg Oncol 2018; 25(11): 3350-7.
41. Hekman MC, Rijpkema M, Muselaers CH, et al. Tumour-targeted Dual-modality Imaging to Improve Intraoperative Visualization of Clear Cell Renal Cell Carcinoma: A First in Man Study. Theranostics 2018; 8(8): 2161-70.
42. Li D, Zhang J, Chi C, et al. First-in-human study of PET and optical dual-modality image-guided surgery in glioblastoma using (68)Ga-IRDye800CW-BBN. Theranostics 2018; 8(9): 2508-20.
43. Dintzis SM, Hansen S, Harrington KM, et al. Real-time Visualization of Breast Carcinoma in Pathology Specimens From Patients Receiving Fluorescent Tumour-Marking Agent Tozuleristide. Arch Pathol Lab Med 2018.
44. Whitley MJ, Cardona DM, Lazarides AL, et al. A mouse-human phase 1 co-clinical trial of a protease-activated fluorescent probe for imaging cancer. Sci Transl Med 2016; 8(320): 320ra4.
45. Smith BL, Gadd MA, Lanahan CR, et al. Real-time, intraoperative detection of residual breast cancer in lumpectomy cavity walls using a novel cathepsin-activated fluorescent imaging system. Breast Cancer Res Treat 2018; 171(2): 413-20.
46. Unkart JT, Chen SL, Wapnir IL, Gonzalez JE, Harootunian A, Wallace AM. Intraoperative Tumour Detection Using a Ratiometric Activatable Fluorescent Peptide: A First-in-Human Phase 1 Study. Ann Surg Oncol 2017; 24(11): 3167-73.
47. van Leeuwen FW, Valdés-Olmos R, Buckle T, Vidal-Sicart S. Hybrid surgical guidance based on the integration of radionuclear and optical technologies. Br J Radiol 2016; 89: 20150797
48. Brouwer OR, Buckle T, Vermeeren L, et al. Comparing the hybrid fluorescent-radioactive tracer indocyanine green-99mTc-nanocolloid with 99mTc-nanocolloid for sentinel node identification: a validation study using lymphoscintigraphy and SPECT/CT. J Nucl Med 2012; 53(7): 1034-40.
49. KleinJan GH, van Werkhoven E, van den Berg NS, et al. The best of both worlds: a hybrid approach for optimal pre- and intraoperative identification of sentinel lymph nodes. Eur J Nucl Med Mol Imaging 2018; 45(11): 1915-25.
50. Schottelius M, Wurzer A, Wissmiller K, et al. Synthesis and Preclinical Characterization of the PSMA-Targeted Hybrid Tracer PSMA-I&F for Nuclear and Fluorescence Imaging of Prostate Cancer. J Nucl Med 2019; 60(1): 71-8.
51. Odenthal J, Rijpkema M, Bos D, et al. Targeting CD44v6 for fluorescence-guided surgery in head and neck squamous cell carcinoma. Sci Rep 2018; 8(1): 10467.
52. Boonstra MC, Van Driel PB, Keereweer S, et al. Preclinical uPAR-targeted multimodal imaging of locoregional oral cancer. Oral Oncol 2017; 66: 1-8.
53. Lwin TM, Miyake K, Murakami T, et al. Fluorescent humanized anti-CEA antibody specifically labels metastatic pancreatic cancer in a patient-derived orthotopic xenograft (PDOX) mouse model. Oncotarget 2018; 9(99): 37333-42.
54. van Driel PB, Boonstra MC, Prevoo HA, et al. EpCAM as multi-tumour target for near-infrared fluorescence guided surgery. BMC Cancer 2016; 16(1): 884.
55. Warram JM, de Boer E, Moore LS, et al. A ratiometric threshold for determining presence of cancer during fluorescence-guided surgery. J Surg Oncol 2015; 112(1): 2-8.
56. Xenataki KT, Oliveira S, van Bergen en Henegouwen PM. Antibody or Antibody Fragments- Implications for Molecular Imaging and Targeted Therapy of Solid Tumours. Frontiers in Immunology 2017; doi: 10.3389/ mmu.2017.01287.
57. Sonn GA, Behesnilian AS, Jiang ZK, et al. Fluorescent Image-Guided Surgery with an Anti-Prostate Stem Cell Antigen (PSCA) Diabody Enables Targeted Resection of Mouse Prostate Cancer Xenografts in Real Time. Clin Cancer Res 2016; 22(6): 1403-12.
58. Zhang M, Kobayashi N, Zettlitz KA, et al. Near-Infrared Dye-Labeled Anti-Prostate Stem Cell Antigen Minibody Enables Real-Time Fluorescence Imaging and Targeted Surgery in Translational Mouse Models. Clinical Cancer Research 2019; 25(1): 188-200.
59. Krasniqi A, D'Huyvetter M, Devoogdt N, et al. Same-Day Imaging Using Small Proteins: Clinical Experience and Translational Prospects in Oncology. J Nucl Med 2018; 59(6): 885-91.
60. Debie P, Van Quathem J, Hansen I, et al. Effect of Dye and Conjugation Chemistry on the Biodistribution Profile of Near-Infrared-Labeled Nanobodies as Tracers for Image-Guided Surgery. Mol Pharm 2017; 14(4): 1145-53.
61. Boogerd LSF, Boonstra MC, Prevoo HAJM, et al. Fluorescence-guided tumour detection with a novel anti-EpCAM targeted antibody fragment: Preclinical validation. Surgical Oncology 2019; 28: 1-8.
62. Debie P, Vanhoeij M, Poortmans N, et al. Improved Debulking of Peritoneal Tumour Implants by Near-Infrared Fluorescent Nanobody Image Guidance in an Experimental Mouse Model. Mol Imaging Biol 2018; 20(3): 361-7.

63. van Brussel AS, Adams A, Oliveira S, et al. Hypoxia-Targeting Fluorescent Nanobodies for Optical Molecular Imaging of Pre-Invasive Breast Cancer. Mol Imaging Biol 2016; 18(4): 535-44.
64. Mahalingam SM, Dudkin VY, Goldberg S, et al. Evaluation of a Centyrin-Based Near-Infrared Probe for Fluorescence-Guided Surgery of Epidermal Growth Factor Receptor Positive Tumours. Bioconjug Chem 2017; 28(11): 2865-73.
65. Tummers WS, Kimura RH, Abou-Elkacem L, et al. Development and Preclinical Validation of a Cysteine Knottin Peptide Targeting Integrin alphavbeta6 for Near-infrared Fluorescent-guided Surgery in Pancreatic Cancer. Clin Cancer Res 2018; 24(7): 1667-76.
66. Samkoe KS, Gunn JR, Marra K, et al. Toxicity and Pharmacokinetic Profile for Single-Dose Injection of ABY-029: a Fluorescent Anti-EGFR Synthetic Affibody Molecule for Human Use. Mol Imaging Biol 2017; 19(4): 512-21.
67. de Souza AL, Marra K, Gunn J, et al. Fluorescent Affibody Molecule Administered In Vivo at a Microdose Level Labels EGFR Expressing Glioma Tumour Regions. Mol Imaging Biol 2017; 19(1): 41-8.
68. Xu H, Bandari RP, Lee L, et al. Design, Synthesis, and in Vitro and in Vivo Evaluation of High Affinity and Specificity Near-Infrared Fluorescent Bombesin Antagonists for Tumour Imaging. J Med Chem 2018; 61(17): 7657-70.
69. Handgraaf HJM, Boonstra MC, Prevoo H, et al. Real-time near-infrared fluorescence imaging using cRGD-ZW800-1 for intraoperative visualization of multiple cancer types. Oncotarget 2017; 8(13): 21054-66.
70. Choi HS, Gibbs SL, Lee JH, et al. Targeted zwitterionic near-infrared fluorophores for improved optical imaging. Nat Biotechnol 2013; 31(2): 148-53.
71. Hyun H, Owens EA, Narayana L, et al. Central C-C Bonding Increases Optical and Chemical Stability of NIR Fluorophores. RSC Adv 2014; 4(102): 58762-8.
72. Koch M, Symvoulidis P, Ntziachristos V. Tackling standardization in fluorescence molecular imaging. Nature Photonics 2018; 12(9): 505-15.
73. Valdes PA, Angelo JP, Choi HS, Gioux S. qF-SSOP: real-time optical property corrected fluorescence imaging. Biomed Opt Express 2017; 8(8): 3597-605.
74. Koller M, Qiu SQ, Linssen MD, et al. Implementation and benchmarking of a novel analytical framework to clinically evaluate tumour-specific fluorescent tracers. Nat Commun 2018; 9(1): 3739.
75. Tummers WS, Warram JM, van den Berg NS, et al. Recommendations for reporting on emerging optical imaging agents to promote clinical approval. Theranostics 2018; 8(19): 5336-47.
76. Pogue BW, Zhu TC, Ntziachristos V, et al. Fluorescence-guided surgery and intervention - An AAPM emerging technology blue paper. Med Phys 2018; 45(6): 2681-8.
77. Braga M, Vignali A, Zuliani W, Frasson M, Di Serio C, Di Carlo V. Laparoscopic versus open colorectal surgery: cost-benefit analysis in a single-center randomized trial. Ann Surg 2005; 242(6): 890-5, discussion 5-6.

Chapter 7

Near-infrared fluorescence imaging of pancreatic cancer using a fluorescently labelled anti-CEA nanobody probe: a preclinical study

L. van Manen, L.D.A.N. de Muynck, V.M. Baart, S. Bhairosingh, P. Debie, A.L. Vahrmeijer, S. Hernot, J.S.D. Mieog

Biomolecules. 2023; 13(4):618.

Abstract

Molecular fluorescence-guided surgery using near-infrared light has the potential to improve the rate of complete resection of cancer. Typically, monoclonal antibodies are being used as targeting moieties, however smaller fragments, such as single-domain antibodies (i.e., Nanobodies®) improve tumor specificity and enable tracer injection on the same day as surgery. In this study, the feasibility of a carcinoembryonic antigen-targeting Nanobody (NbCEA5) conjugated to two zwitterionic dyes (ZW800-1 Forte [ZW800F] and ZW800-1) for visualization of pancreatic ductal adenocarcinoma (PDAC) was investigated. After site-specific conjugation of NbCEA5 to the zwitterionic dyes, binding specificity was evaluated on human PDAC cell lines with flow cytometry. A dose escalation study was performed for both NbCEA5-ZW800F and NbCEA5-ZW800-1 in mice with subcutaneously implanted pancreatic tumors. Fluorescence imaging was performed up to 24 h after intravenous injection. Furthermore, the optimal dose for NbCEA5-ZW800-1 was injected in mice with orthotopically implanted pancreatic tumors. A dose-escalation study showed superior mean fluorescence intensities for NbCEA5-ZW800-1 compared to NbCEA5-ZW800F. In the orthotopic tumor models, NbCEA5-ZW800-1 accumulated specifically in pancreatic tumors with a mean *in vivo* tumor-to-background ratio of 2.4 (SD = 0.23). This study demonstrated the feasibility and potential advantages of using a CEA-targeted Nanobody conjugated to ZW800-1 for intraoperative PDAC imaging.

Introduction

Molecular fluorescence-guided cancer surgery using near-infrared (NIR) light is an innovative and promising optical imaging technique that entered the surgical theatre in the past years.[1] It needs a camera system that is able to excite an (intravenously injected) fluorophore conjugated to a tumor-specific targeting molecule and detect its emitted fluorescence.[2] The technique is thought to be of significant added value to improve intraoperative navigation, which could be especially relevant during pancreatic cancer surgery. Pancreatic cancer has a dismal prognosis as most of the patients (around 80% [3]) have either locally advanced or metastasized disease at diagnosis. During surgery, margin assessment is of utmost importance since tumor-positive resection margins are encountered in up to 70% of the cases.[4,5] Distinguishing tumor tissue from benign surrounding tissues using an imaging technique that is easy to use, such as NIR fluorescence imaging, is one of the key elements to improve the quality of pancreatic surgery.[6] One of the most commonly targeted and studied biomarkers for pancreatic cancer is the carcinoembryonic antigen (CEA), which is a glycoprotein involved in cell adhesion and is overexpressed in more than 90% of pancreatic cancers.[7-9] CEA is still overexpressed in tumor tissue after neoadjuvant therapy, which makes this an excellent target moiety, and therefore an interesting candidate for targeted fluorescence imaging, since more patients are being treated with neoadjuvant therapy followed by surgery and/or adjuvant chemotherapy.[10] It has already been demonstrated that an anti-CEA monoclonal antibody conjugated to a 700 nm fluorophore (SGM-101) could clearly visualize pancreatic tumors during surgery.[11] Nonetheless, monoclonal antibodies typically limit NIR fluorescence imaging due to restricted tumor penetration and long blood circulation time, resulting in suboptimal pharmacokinetics, low signal-to-noise ratios, and extended time between injection and surgery (3–5 days). Single domain antibodies or Nanobodies®, which are the smallest (15 kDa) intact antigen-binding fragments derived from camelid heavy-chain only antibodies, are excellent candidates for molecular imaging as they show rapid target recognition and clearing from the circulation via renal excretion.[12] This results in lower background fluorescence, improved tumor specificity, and enables tracer injection just prior to surgery.[13-16]

In addition to Methylene Blue and Indocyanine Green, during the past years, many NIR fluorophores have become available for conjugation to target moieties, of which IRDye800CW is the most commonly used NIR fluorophore.[17] A fundamental problem of these conventional NIR fluorophores for tumor targeting is that they are polysulfonatic and highly anionic, resulting in non-specific uptake in tissue and organs, leading to higher background fluorescence, which could be clinically relevant for the implementation of fluorescence-guided pancreatic surgery since both the pancreatic head is anatomically closely related to the liver and pancreatic tumors often metastasize to the liver. To overcome this limitation, a new chemical class of fluorophores, so-called zwitterionic dyes, was developed. Having strong charges (sulfonates and quaternary amines) that are balanced electrically and geometrically over the surface of the molecule, zwitterionic NIR fluorophores are self-shielding and exhibit extremely low non-specific binding and tissue uptake *in vivo* after intravenous injection.[18]

In this study, the main goal was to assess the feasibility of a CEA-targeted Nanobody conjugated to two zwitterionic dyes, ZW800-Forte and ZW800-1, to facilitate the visualization of pancreatic cancer and characterize the results with respect to tumor specificity, mean fluorescence intensity and tumor-to-background ratio.

Material and methods

Fluorescent tracers

Two fluorescent zwitterionic dyes (ZW800-1 Forte (ZW800F) and ZW800-1), activated with maleimide for thiol-linkage, were conjugated site-specifically to either a CEA-targeted Nanobody (NbCEA5) or a control Nanobody (R3B23).**[15,19]** Both Nanobodies were generated in the context of previous studies and produced as described previously.[14] ZW800-F has two absorption peaks, at 685 nm and 754 nm, respectively, and an emission peak of 772 nm in phosphate-buffered saline (PBS).[20] ZW800-1-Maleimide has an absorption peak of approximately 772 nm and an emission peak of 788 nm in PBS.[20]

In brief, the Nanobodies were genetically engineered to carry a carboxy-terminal tag consisting of a hexahistidine-tag, a 14 amino acid linker, and a cysteine-tag, and were subsequently expressed in Escherichia coli cultures.[19] Purification of the Nanobodies from periplasmic extracts was performed by immobilized metal affinity chromatography, after which size-exclusion chromatography (SEC) was applied.[21] Prior to conjugation to the dyes, Nanobodies were reduced by incubation at 37 °C with 180× molar excess of 2-MEA (ACROS organics, Thermo Fisher Scientific, Rockford, IL, USA). After 90 min, 2-MEA was removed by buffer exchange on a PD-10 desalting column (GE Healthcare, Chicago, IL, USA) using PBS (pH 7.4) as an elution buffer. The reduced Nanobody was then incubated with a 5-fold molar excess of either ZW800F or ZW800-1, dissolved at 20 mg/mL in Dimethyl sulfoxide. SEC was used to purify the fluorescently labeled Nanobodies (Superdex 75 10/300 GL, PBS as running buffer at 1.0 mL/min) as well as to assess purity afterwards. The concentration of the conjugated Nanobodies was determined via spectrophotometry (NanoDropTM 2000, Thermo Fisher Scientific, Rockford, IL, USA) and the degree of labeling, calculated as the ratio of the dye concentration and protein concentration, taking a correction factor of 3% into account for the absorbance of the dye at 280 nm.[22]

Human cancer cell lines

Two pancreatic cancer cell lines were used for this experiment. BxPC3-luc2 cells were bought by Perkin Elmer (Waltham, MA, USA) and PANC-1 were obtained from ATCC. BxPC-3-luc2 cells were cultured in RPMI 1640 cell culture medium (Gibco, Invitrogen, Carlsbad, CA, USA) and PANC-1 cells were cultured in Dulbecco's Modified Eagle Medium (DMEM) + GlutaMAX™ cell culture medium (Gibco, Invitrogen, Carlsbad, CA, USA). l-glutamine, 25 mM HEPES, 10% fetal bovine serum (FBS; Hyclone, Thermo Scientific, Rockford, IL, USA), and penicillin/streptomycin (both 100 IU/mL; Invitrogen) were added as supplements.[23] All cell lines were cultured in absence of mycoplasma, which was confirmed using a polymerase chain reaction. The cells were grown in a humidified incubator (37 °C, 5% CO_2) to 90% confluence, and were detached afterwards with trypsin/EDTA.[23] Viability was assessed using Trypan Blue staining in 0.4% solution (Gibco, Invitrogen).

Flow cytometry

After detachment and assessment of the viability of the cell lines, 0.5 × 10^6 cells were resuspended per tube in ice cold PBS. Hereafter, cells were washed twice in ice-cold PBS supplemented with 0.5% bovine serum albumin (BSA) and incubated with the anti-CEA monoclonal antibody labeled by APC (FAB41281A-APC; R&D Systems, Minneapolis, MN, USA), NbCEA5-ZW800F, NbCEA5-ZW800-1 or R3B23-ZW800-1 for 30 min on ice (concentrations: 10 nM, 100 nM, and 1000 nM). After washing twice, cells were resuspended in 400 µL PBS/0.5%BSA and analyzed on an LSRII flow cytometer (Biosciences, Franklin Lanes, Evansville, IN, USA) using the 670/14 laser for measuring APC signals and 780/60 laser for measuring ZW800-1 or ZW800F signals.**[23,24]** All steps were performed to avoid exposure to light. Histograms were generated using FlowJo software (TreeStar, Ashland, OR, USA, version 10.6.2).

Animal procedures

The Animal Welfare Committee of Leiden University Medical Center approved all animal experiments for animal health, ethics, and research. Six-week-old athymic female mice (CD1-Foxn1nu, Charles River Laboratories, Wilmington, MA, USA) weighing between 20 and 35 g were housed in ventilated cages. Normal pellet food (as NIR fluorescence imaging was performed in the 800 nm range) and sterilized water were provided ad libitum. Throughout tumor inoculation and imaging procedures, animals were anesthetized with 4% isoflurane for induction and 2% isoflurane for maintenance. To induce subcutaneous tumors, BxPC3-luc2 cells (Perkin Elmer, Waltham, MA, USA) were injected at either one or two sites on the back of the mice (500,000 cells per spot). The pancreatic orthotopic models were performed according to Moreno et al.[25] In brief, after performing a lateral incision in the left flank, the pancreas was exposed, and consequently, 500,000 BxPC3-luc2 cells (resuspended in 50 µL PBS) were injected into the body of the pancreas. All mice undergoing orthotopic tumor implantation received painkilling (0.1 mg/kg buprenorphine subcutaneously, every 8 h) during and after the surgical procedure as needed. Following imaging, the mice were euthanized using carbon dioxide, and organs were collected and imaged for fluorescence to evaluate the biodistribution pattern of the tracers.

Camera systems

The Pearl Impulse whole animal imaging system (LI-COR Biosciences, Lincoln, NE, USA) and the Quest Artemis (Quest Medical Imaging, Middenmeer, The Netherlands) open fluorescence camera system were used for fluorescence measurements. The excitation wavelengths for the Pearl Impulse imager and Quest Artemis imaging systems are 685/785 nm and 680/793 nm, respectively, and the collected emission wavelengths were 720/820 nm and 700–800/805–850 nm, respectively.

Experimental and imaging procedure

The subcutaneously implanted tumors were monitored using a digital caliper and mice were considered for imaging if the tumor size was above 5 by 5 mm. A dose escalation study was performed for both tracers, varying from 0.5, 1, 2, and 4 nmol based on the fluorophore concentration (N = 3 mice/group, except for the 4 nmol group: N = 2). For the subcutaneous models imaging was performed 1, 2, 4, 8, and 24 h after intravenous injection. The orthotopic implanted tumor models (N = 2) were imaged 2 h after intravenous injection. Biodistribution was performed in the orthotopic tumor models immediately after the euthanasia of the animals.

Ex vivo analysis

After imaging, the excised tumors were fixed in 4% formalin and embedded in paraffin (FFPE) blocks. All tissues were sectioned, and consequently, fluorescence imaging at 800 nm was performed on the slides using the Odyssey imager (LI-COR Biosciences, Lincoln, NE, USA) and AxioZ1 scanner (Carl Zeiss AG, Oberkochen, Germany). Additionally, hematoxylin-eosin (HE) staining, CEA-specific staining, DAPI for routine nuclear staining, and staining with a negative mouse antibody was performed as previously described [24], and consequently, these images were digitalized using the 3D HISTECH Confocal imager (Sysmex, Etten-Leur, The Netherlands).

Statistical analysis

Statistical analysis and generation of graphs were performed using GraphPad Prism software (version 8, GraphPad Software Inc., La Jolla, CA, USA). Tumor-to-background ratios (TBRs) were calculated by dividing the mean fluorescence intensity (MFI) of the tumor (in arbitrary units (AU)) by the signal from the surrounding tissue (orthotopic model: adjacent normal pancreas; subcutaneous model: adjacent abdominal background signal in donut shape surrounding the tumor) and were reported as mean plus standard deviation. The main outcomes (MFI and TBR) were compared using an independent sample T-test and one-way ANOVA taking multiple comparisons into account. The *p*-values of < 0.05 were considered to be statistically significant.

Results

Conjugation and binding specificity

NbCEA5 and R3B23 were successfully conjugated with ZW800F and ZW800-1 and eluted as a single peak on analytical SEC. The degree of labeling ranged between 0.8 and 1.0. NbCEA5-ZW800F binding to living tumor cells was evaluated using flow cytometry in BxPC3-luc2 cells. A right shift was noticed for NbCEA5-ZW800F compared to R3B23-ZW800F (negative control Nanobody).

Furthermore, NbCEA5-ZW800-1 was evaluated in the high CEA positive BxPC3-luc2 and the modest CEA positive PANC-1 cell line, demonstrating a larger right shift for the BxPC3-luc2 cells and thereby confirming specific binding (Supplementary data Figure S1).

In vivo NIR fluorescence imaging of pancreatic tumors

In vivo NIR fluorescence imaging using NbCEA5-ZW800F was performed over a 24 h period, resulting in a maximal TBR at 2 h after injection. The mean TBRs of 1.5 (SD = 0.17), 1.7 (SD = 0.18), and 1.8 (SD = 0.34) were observed for the 0.5, 1, and 2 nmol dose groups, respectively. MFIs for all time points in all dose groups were below 0.10 AU, and therefore the intrinsic fluorescence uptake of NbCEA5-ZW800F was considered to be not sufficient to proceed in further experiments. A dose-escalation study using NbCEA5-ZW800-1 was then performed in 4 dose groups (0.5 nmol; 1 nmol; 2 nmol; 4 nmol) demonstrating a significantly higher TBR for the 4 nmol dose group at 4 h after injection compared to the lower dose groups (mean TBR 2.1.[SD = 0.09]; p = 0.009). Furthermore, MFIs of the 4 nmol dose group were above or around 0.10 AU for all imaging time points (Figure 1).

Next, NIR fluorescence imaging of subcutaneous tumors after injection of both NbCEA5-ZW800-1 (N = 6) and R3B23-ZW800-1 (N = 3) was performed using the Quest Artemis clinical camera system. At 8 h after injection, the mean TBR was 1.8 (SD = 0.19) for the NbCEA5-ZW800-1 and 1.5 (SD = 0.16) for R3B23-ZW800-1, which was, however, not statistically significantly different (p = 0.09; Figure 2). In the orthotopic tumor models (N = 2), fluorescence clearly accumulated 2 h after injection of NbCEA5-ZW800-1 in the pancreatic tumors with a mean TBR of 2.4 (SD = 0.23; Figure 3). In one mouse, two splenic metastases could also be visualized with a mean TBR of 1.8 (SD = 0.42).

Biodistribution and histologic analysis

The presence of tumor cells for all detected fluorescent lesions was histologically confirmed. *Ex vivo* histological analysis showed that NbCEA5-ZW800-1 is fully penetrating the tumors and selectively targeting the CEA-positive tumor cells, whereas R3B23-ZW800-1 is not. The microscopic fluorescence signals of the NbCEA5-ZW800-1 are correlated with the CEACAM5 expression. (Figure 4). Biodistribution values for the relevant organs showed an MFI of 4.63 (SD = 0.47) for the kidney, 0.13 (SD = 0.03) for the tumor, 0.11 (SD = 0.04) for the liver, 0.05 (SD = 0.005) for the pancreas, and 0.02 (SD = 0.003) for muscle. Relevant tumor-to-organ ratios were 1.2 (tumor-to-liver); 7.9 (tumor-to-muscle), 2.6 (tumor-to-pancreas), and 0.03 (tumor-to-kidney, Supplementary data Figure S2).

Discussion

In this preclinical study, a CEA-targeted Nanobody, conjugated to zwitterionic dyes from the ZW800 family, was evaluated for intraoperative visualization of pancreatic tumors. Maleimide conjugation of this Nanobody to the zwitterionic dye ZW800-1 (NbCEA5-ZW800-1) showed superior tumor accumulation in terms of MFI and TBR compared to conjugation to the zwitterionic dye ZW800F. Furthermore, by using NbCEA5-ZW800-1, both subcutaneously and orthotopically implanted tumors could be visualized early (from 2 h) after tracer injection. Tumor-specific uptake was confirmed histologically. The results could indicate that the designed tracer has the potential of being translated for in-human use.

This CEA-targeting Nanobody was designed previously for clinical utility in both nuclear and fluorescence imaging. However, until now it has not been clinically translated.[19] Recently, this Nanobody has been demonstrated to visualize colorectal and pancreatic cancer in preclinical studies, although it was conjugated with another fluorescent dye, i.e., IRDye800CW.[14-16] For the pancreatic orthotopic model, it showed similar results concerning TBR values compared to our results (2.7 vs. 2.4), however, biodistribution patterns were not described in these studies.[14] Furthermore, the TBR values of these studies were difficult to compare as the TBR was determined on images taken from a different camera system (Maestro CRI imaging system) with different excitation and emission filters.

The designed tracer NbCEA5-ZW800-1 has the advantage of being mainly renally cleared and also demonstrated early tumor visualization after intravenous injection. An advantage of using Nanobodies compared to monoclonal antibodies is shorter imaging times although with lower TBRs and MFIs, which was in concordance with the results of Baart et al.[26] In that study, uPAR-targeted Fab- (50–55 kDa) and Fab 2 (100–110 kDa) fragments were compared to their humanized parental antibody, thereby showing a greatly improved time-to-imaging, while the antibody itself demonstrated a superior peak fluorescence.

The strong kidney accumulation is one of the drawbacks of Nanobody-based tracers in general, however, it has to be expected that the kidney signal will not overwhelm the tumor signal in humans, since the kidneys are located retroperitoneally and are surrounded by perinephric fat. Future studies can directly compare this Nanobody construct to either a ZW800-1 labeled monoclonal anti-CEA antibody or conjugation of this Nanobody to other NIR fluorophores, or both, with respect to the tumor specificity and biodistribution patterns. Biodistribution studies have been performed for an anti-CEA targeted monoclonal antibody labeled to a 700-nm fluorophore, SGM-101, although only using Single Photon Emission Computed Tomography-Computed Tomography (SPECT-CT) imaging, making a fair comparison of our results to their tumor to organ ratios difficult, however, tracer accumulation in the kidneys seemed to be much higher for the monoclonal antibody compared to the Nanobody.[27] Future studies should therefore focus on biodistribution patterns of a monoclonal antibody versus a Nanobody labeled to ZW800-1 to evaluate the tumor-to-organ ratios (especially liver tissue), which would be clinically relevant since both the pancreatic head is anatomically close to the liver and pancreatic tumors often metastasize to the liver.

The results of this study could implicate that this novel anti-CEA Nanobody, NbCEA5-ZW800-1, has the potential to be translated into the clinic. As CEA is also overexpressed in other cancers, such as colorectal cancer, this tracer could also be used for intraoperative fluorescence imaging or endoscopic fluorescence imaging of other cancers.[28] It would also be useful to perform nuclear labeling, enabling nuclear imaging using for instance Positron Emission Tomography-Computed Tomography (PET-CT). An advantage of using CEA as a targeting moiety is that the CEA expression in PDAC is minimally affected by neoadjuvant chemoradiotherapy, making this tracer suitable for both intraoperative optical imaging and preoperative staging using PET-CT.[10,29] Patient selection could be performed based on elevated CEA levels as these are correlated to CEA expression profiles.[30] Future studies should focus on the optical characteristics and the effect on biodistribution of conjugation of this Nanobody to other NIR fluorophores. Based on these results the design of this CEA-targeted Nanobody tracer could be further optimized. Furthermore, the search for NIR fluorophores should not be limited to NIR-I fluorophores, as recently also organic fluorophores that can be used for conjugation and able to be detected in the NIR-II window (1000–1400 nm) have been developed.[31] The advantages of imaging in the NIR-II window are weaker autofluorescence, lower absorption, and reduced scattering, thereby improving the penetration depth and image quality, which has recently been demonstrated in humans during liver surgery.[32]

Conclusions

In conclusion, this study demonstrates the feasibility of a novel fluorescent tracer, NbCEA5-ZW800-1, for intraoperative pancreatic cancer imaging in a preclinical animal study, as it showed tumor-specific fluorescence uptake and a short time to image. It could indicate that the designed tracer has the potential of being translated for clinical implementation in order to reduce the percentage of tumor-positive resection margins during pancreatic cancer surgery, although future studies should focus on the comparison of conjugation strategies to other NIR fluorophores, thereby optimizing the design of this CEA targeted Nanobody tracer.

Figure 1. *Left panel:* Average tumor-to-background ratios (A), mean fluorescence intensities in the tumor (B) and representative images of the optimal doses based on the TBR acquired by the Pearl Imager (C) for NbCEA5-ZW800F. *Right panel:* Average tumor-to-background ratios (D), mean fluorescence intensities in the tumor (E) and representative images of the optimal doses based on the TBR acquired by the Pearl Imager (F) for NbCEA5-ZW800-1. Scale bars are 10 mm. *Abbreviations: T=tumor; Ki=kidneys.*

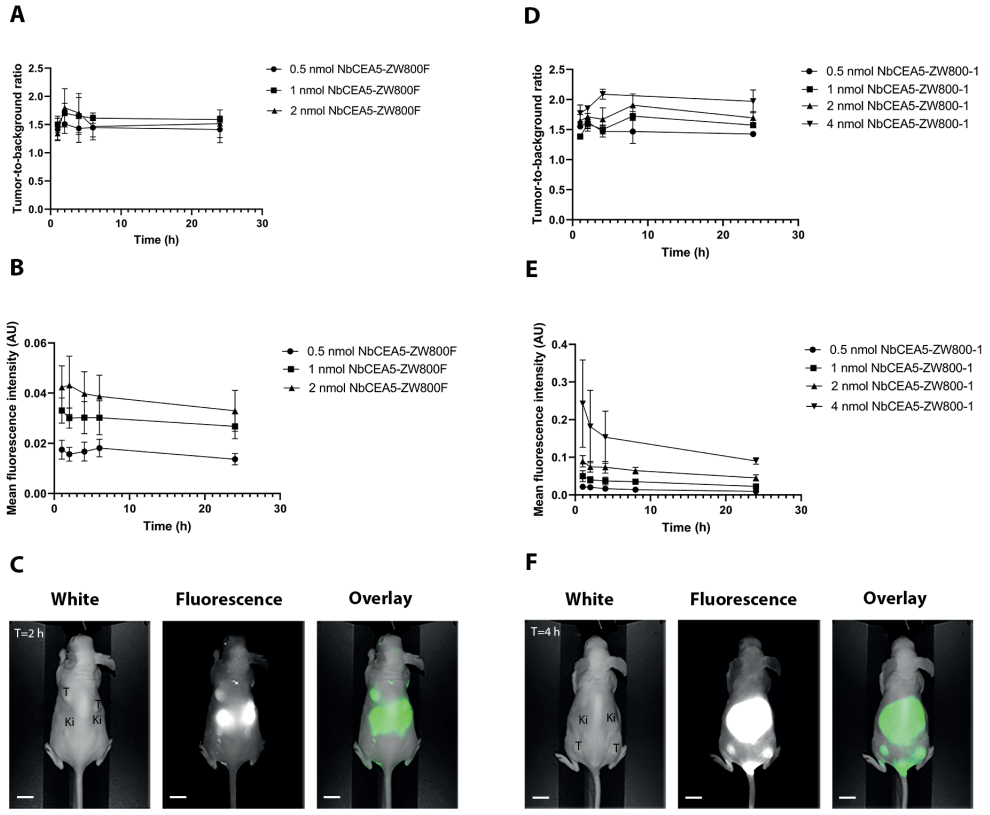

Figure 2. Comparison of tumor-to-background ratios over time for both NbCEA5-ZW800-1 and NbR3B23-ZW800-1 (control nanobody) (A). Representative fluorescence overlay image acquired by the Quest Imaging system for NbCEA5-ZW800-1 (B) and NbR3B23-ZW800-1 (C) at the optimal imaging timepoint (8h). Scale bars are 10 mm. *Abbreviations: T=tumor; Ki=kidneys.*

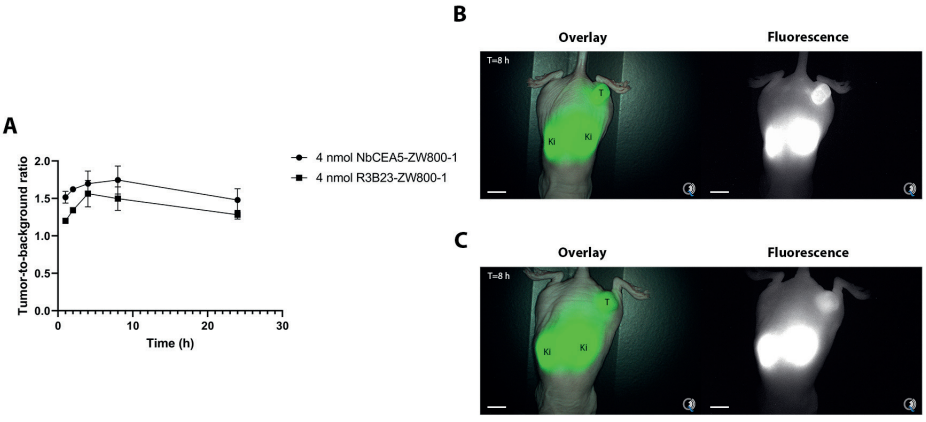

Figure 3. Fluorescence overlay image of an orthotopic implanted pancreatic tumor model including splenic metastases 4 after injection of 4 nmol NbCEA5-ZW800-1 (A). Scale bars are 10 mm. Note: the kidneys were removed. Presence of tumor cells was histologically confirmed (B and C). Scale bars are 1000 µm. *Abbreviations: T=tumor; Sp: spleen; M=metastasis; P=normal pancreas.*

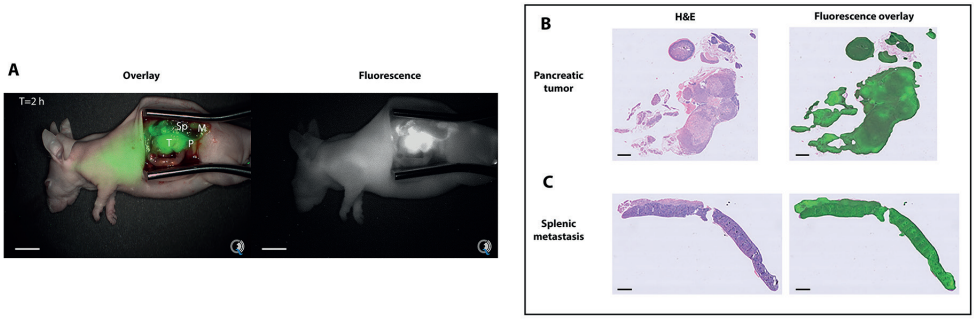

Figure 4. Representative examples of hematoxylin-eosin (HE) staining, CEACAM5 staining, and combined DAPI staining with NIR fluorescence (800 nm) on *ex vivo* tumor tissue sections of mice injected with NbCEA5-ZW800-1. (A) Representative examples of hematoxylin-eosin (HE) staining, CEACAM5 staining, and combined DAPI staining with NIR fluorescence (800 nm) on *ex vivo* tumor tissue sections of mice injected with NbR3B23-ZW800-1. (B). Scale bars are 1000 μm.

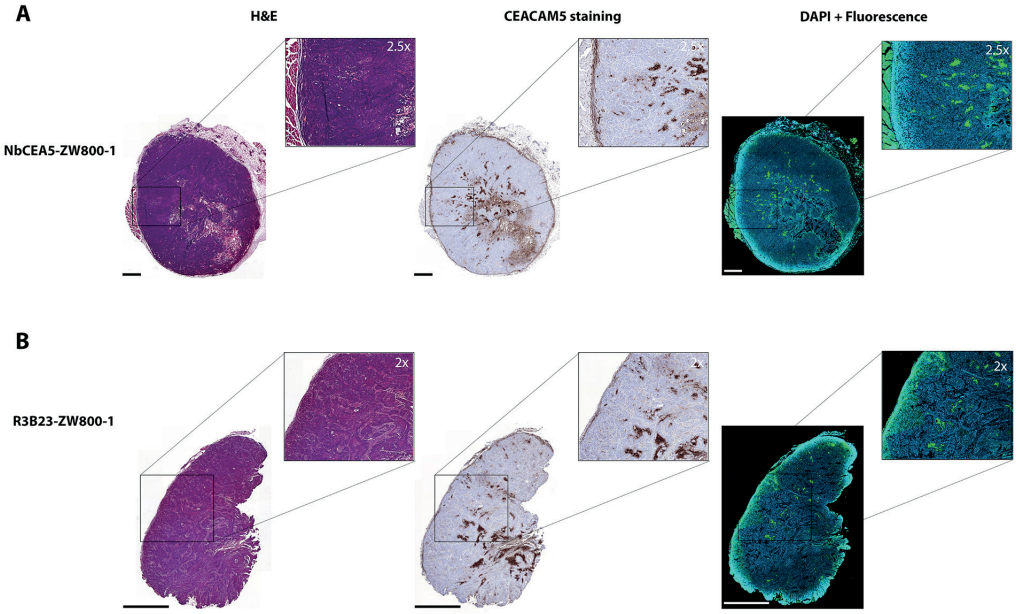

Supplementary data

Figure S1. Overview on flowcytometry results.

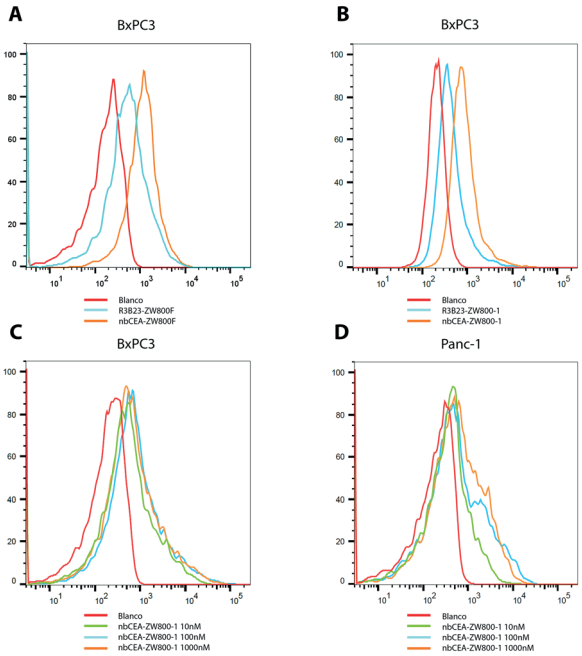

Figure S2. Biodistribution data of NbCEA5-ZW800-1 in the pancreatic orthotopic models (N=2). Scale bar is 10 mm. *Abbreviations: Lu=lungs; Ht=heart; Li=liver; Tu=tumor; Pa=pancreas; Sp=spleen; Int=small intestines; St=stomach; Ki=kidneys; Co=colon; Sk=skin; Mu=muscle.*

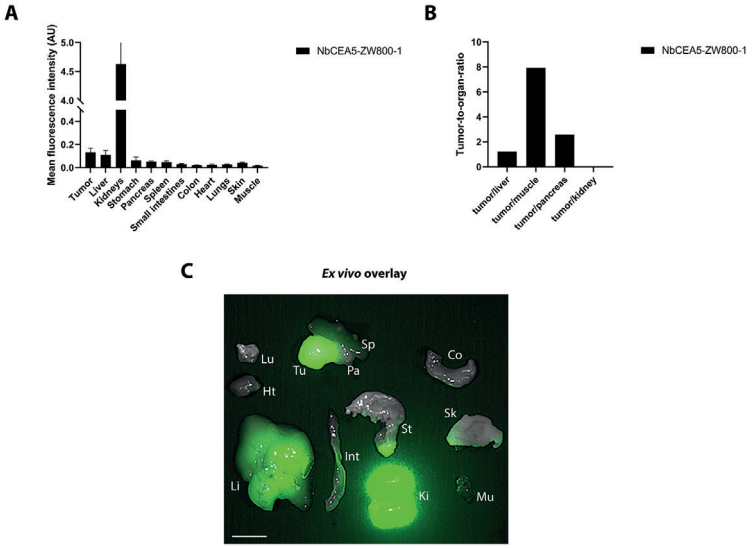

References

1. Hernot S, van Manen L, Debie P, Mieog JSD, Vahrmeijer AL. Latest developments in molecular tracers for fluorescence image-guided cancer surgery. Lancet Oncol. 2019;20(7):e354-e367.
2. Mieog JSD, Achterberg FB, Zlitni A, et al. Fundamentals and developments in fluorescence-guided cancer surgery. Nature reviews Clinical oncology. 2022;19(1):9-22.
3. Ducreux M, Cuhna AS, Caramella C, et al. Cancer of the pancreas: ESMO Clinical Practice Guidelines for diagnosis, treatment and follow-up. Annals of oncology : official journal of the European Society for Medical Oncology. 2015;26 Suppl 5:v56-68.
4. Esposito I, Kleeff J, Bergmann F, et al. Most pancreatic cancer resections are R1 resections. Ann Surg Oncol. 2008;15(6):1651-1660.
5. Jamieson NB, Foulis AK, Oien KA, et al. Positive mobilization margins alone do not influence survival following pancreatico-duodenectomy for pancreatic ductal adenocarcinoma. Annals of surgery. 2010;251(6):1003-1010.
6. de Muynck L, White KP, Alseidi A, et al. Consensus Statement on the Use of Near-Infrared Fluorescence Imaging during Pancreatic Cancer Surgery Based on a Delphi Study: Surgeons' Perspectives on Current Use and Future Recommendations. Cancers. 2023;15(3).
7. de Geus SW, Boogerd LS, Swijnenburg RJ, et al. Selecting Tumor-Specific Molecular Targets in Pancreatic Adenocarcinoma: Paving the Way for Image-Guided Pancreatic Surgery. Mol Imaging Biol. 2016;18(6):807-819.
8. van Manen L, Groen JV, Putter H, et al. Stage-Specific Value of Carbohydrate Antigen 19-9 and Carcinoembryonic Antigen Serum Levels on Survival and Recurrence in Pancreatic Cancer: A Single Center Study and Meta-Analysis. Cancers. 2020;12(10).
9. van Manen L, Groen JV, Putter H, et al. Elevated CEA and CA19-9 serum levels independently predict advanced pancreatic cancer at diagnosis. Biomarkers : biochemical indicators of exposure, response, and susceptibility to chemicals. 2020;25(2):186-193.
10. Vuijk FA, de Muynck L, Franken LC, et al. Molecular targets for diagnostic and intraoperative imaging of pancreatic ductal adenocarcinoma after neoadjuvant FOLFIRINOX treatment. Sci Rep. 2020;10(1):16211.
11. Hoogstins CES, Boogerd LSF, Sibinga Mulder BG, et al. Image-Guided Surgery in Patients with Pancreatic Cancer: First Results of a Clinical Trial Using SGM-101, a Novel Carcinoembryonic Antigen-Targeting, Near-Infrared Fluorescent Agent. Ann Surg Oncol. 2018;25(11):3350-3357.
12. Debie P, Devoogdt N, Hernot S. Targeted Nanobody-Based Molecular Tracers for Nuclear Imaging and Image-Guided Surgery. Antibodies (Basel). 2019;8(1).
13. Debie P, Vanhoeij M, Poortmans N, et al. Improved Debulking of Peritoneal Tumor Implants by Near-Infrared Fluorescent Nanobody Image Guidance in an Experimental Mouse Model. Mol Imaging Biol. 2018;20(3):361-367.
14. Lwin TM, Hernot S, Hollandsworth H, et al. Tumor-specific near-infrared nanobody probe rapidly labels tumors in an orthotopic mouse model of pancreatic cancer. Surgery. 2020;168(1):85-91.
15. Lwin TM, Turner MA, Amirfakhri S, et al. Rapid tumor-labeling kinetics with a site-specific near-infrared anti-CEA nanobody in a patient-derived orthotopic xenograft mouse model of colon cancer. Journal of surgical oncology. 2021;124(7):1121-1127.
16. Lwin TM, Turner MA, Nishino H, et al. Fluorescent Anti-CEA Nanobody for Rapid Tumor-Targeting and Imaging in Mouse Models of Pancreatic Cancer. Biomolecules. 2022;12(5).
17. van Manen L, Handgraaf HJM, Diana M, et al. A practical guide for the use of indocyanine green and methylene blue in fluorescence-guided abdominal surgery. Journal of surgical oncology. 2018;118(2):283-300.
18. Choi HS, Gibbs SL, Lee JH, et al. Targeted zwitterionic near-infrared fluorophores for improved optical imaging. Nature biotechnology. 2013;31(2):148-153.
19. Vaneycken I, Govaert J, Vincke C, et al. In vitro analysis and in vivo tumor targeting of a humanized, grafted nanobody in mice using pinhole SPECT/micro-CT. Journal of nuclear medicine : official publication, Society of Nuclear Medicine. 2010;51(7):1099-1106.
20. Curadel, LLC. available online: https://www.curadel.com/contrast-agents/ (accessed on 22 February 2023).
21. Debie P, Van Quathem J, Hansen I, et al. Effect of Dye and Conjugation Chemistry on the Biodistribution Profile of Near-Infrared-Labeled Nanobodies as Tracers for Image-Guided Surgery. Molecular pharmaceutics. 2017;14(4):1145-1153.
22. Massa S, Xavier C, De Vos J, et al. Site-specific labeling of cysteine-tagged camelid single-domain antibody-fragments for use in molecular imaging. Bioconjugate chemistry. 2014;25(5):979-988.
23. Houvast RD, Baart VM, Bhairosingh SS, et al. Glycan-Based Near-infrared Fluorescent (NIRF) Imaging of Gastrointestinal Tumors: a Preclinical Proof-of-Concept In Vivo Study. Mol Imaging Biol. 2020;22(6):1511-1522.
24. Boonstra MC, Tolner B, Schaafsma BE, et al. Preclinical evaluation of a novel CEA-targeting near-infrared fluorescent tracer delineating colorectal and pancreatic tumors. International journal of cancer. 2015;137(8):1910-1920.
25. Moreno JA, Sanchez A, Hoffman RM, Nur S, Lambros MP. Fluorescent Orthotopic Mouse Model of Pancreatic Cancer. Journal of visualized experiments : JoVE. 2016(115).
26. Baart VM, van Manen L, Bhairosingh SS, et al. Side-by-Side Comparison of uPAR-Targeting Optical Imaging Antibodies and Antibody Fragments for Fluorescence-Guided Surgery of Solid Tumors. Mol Imaging Biol. 2021.
27. Gutowski M, Framery B, Boonstra MC, et al. SGM-101: An innovative near-infrared dye-antibody conjugate that targets CEA for fluorescence-guided surgery. Surg Oncol. 2017;26(2):153-162.
28. Boogerd LSF, Hoogstins CES, Schaap DP, et al. Safety and effectiveness of SGM-101, a fluorescent antibody targeting carcinoembryonic antigen, for intraoperative detection of colorectal cancer: a dose-escalation pilot study. Lancet Gastroenterol Hepatol. 2018;3(3):181-191.
29. van Dam MA, Vuijk FA, Stibbe JA, et al. Overview and Future Perspectives on Tumor-Targeted Positron Emission Tomography and Fluorescence Imaging of Pancreatic Cancer in the Era of Neoadjuvant Therapy. Cancers. 2021;13(23).
30. Boogerd LSF, Vuijk FA, Hoogstins CES, et al. Correlation Between Preoperative Serum Carcinoembryonic Antigen Levels and Expression on Pancreatic and Rectal Cancer Tissue. Biomark Cancer. 2017;9:1179299x17710016.
31. Zhu S, Tian R, Antaris AL, Chen X, Dai H. Near-Infrared-II Molecular Dyes for Cancer Imaging and Surgery. Advanced materials (Deerfield Beach, Fla). 2019;31(24):e1900321.
32. Hu Z, Fang C, Li B, et al. First-in-human liver-tumour surgery guided by multispectral fluorescence imaging in the visible and near-infrared-I/II windows. Nature biomedical engineering. 2020;4(3):259-271.

Part III

Chapter 8

The clinical usefulness of optical coherence tomography during cancer interventions

L. van Manen, J. Dijkstra, C. Boccara, E. Benoit, A.L. Vahrmeijer, M.J. Gora, J.S.D. Mieog

Journal of Cancer Research and Clinical Oncology. 2018 Oct;144(10):1967-1990.

Abstract

Introduction

Tumor detection and visualization plays a key role in the clinical workflow of a patient with suspected cancer, both in the diagnosis and treatment. Several optical imaging techniques have been evaluated for guidance during oncological interventions. Optical coherence tomography (OCT) is a technique which has been widely evaluated during the past decades. This review aims to determine the clinical usefulness of OCT during cancer interventions focussing on qualitative features, quantitative features and the diagnostic value of OCT.

Methods

A systematic literature search was performed for articles published before May 2018 using OCT in the field of surgical oncology. Based on these articles an overview of the clinical usefulness of OCT was provided per tumor type.

Results

A total of 785 articles were revealed by our search, of which a total of 136 original articles were available for analysis, which formed the basis of this review. OCT is currently utilised for both preoperative diagnosis and intraoperative detection of skin, oral, lung, breast, hepatobiliary, gastrointestinal, urological and gynaecological malignancies. It showed promising results in tumor detection on a microscopic level, especially by using higher resolution imaging techniques, such as high definition OCT and full-field OCT.

Conclusion

In the nearby future, OCT could be used as an additional tool during bronchoscopic or endoscopic interventions and could also be implemented in margin assessment during (laparoscopic) cancer surgery if a laparoscopic or handheld OCT device will be further developed to make routine clinical use possible.

Introduction

Tumor detection and visualization plays a key role in the clinical workflow of a patient with suspected cancer, both in the diagnosis and treatment. During the last decades, numerous imaging modalities, such as ultrasound (US), computed tomography (CT), magnetic resonance imaging (MRI), have proven additional value in establishing the diagnosis of an oncologic patient. Nevertheless, pathologic analysis of representative tumor biopsies is often necessary for establishing the correct diagnosis.

Furthermore, intraoperative detection of the tumor margins is difficult, as surgeons currently mainly rely on visualization and palpation. Pathological techniques to examine the margins intraoperatively, such as frozen section analysis and imprint cytology have been extensively researched for the purpose of reducing the percentage of positive margins in breast cancer surgery for instance. However, all these methods have drawbacks, such as time-consuming and resource-intensive nature, difficulty in visualizing high-grade carcinomas, and imprecision, due to sampling errors and poor resolution.[1-3] With their ability to image molecular and physiological changes that are associated with cancer sensitively and non-invasively, optical imaging devices, such as optical coherence tomography (OCT), have the potential to improve intraoperative tumor detection.[4,5]

OCT is a technique that uses the interference of light to generate 2-dimensional cross-sectional images. It was first described in 1991 and is often denoted as the optical analog of ultrasound; it detects back-reflected light, instead of sound, from tissues.[6] In the field of cardiology and ophthalmology it is already used as part of standard clinical care.[7] OCT is, in contrast to other optical image modalities, able to image non-invasively and without the need for tissue preparation. The technique produces images, which are comparable to low-resolution histology. The resolution in comparison to US is 10-50 times better, and usually lies in the range of 1-20 µm in axial and transverse direction, depending on the modality used. This technique could be applied both for *ex vivo* and *in vivo* use. Moreover, in the last years OCT was used during endoscopy or bronchoscopy, by incorporating OCT into flexible fiberoptic probes, which could be inserted in the accessory channel of the majority of standard of care scopes.[8,9] For imaging with higher resolution and more cellular detail, high definition OCT (HD-OCT) and full-field OCT (FF-OCT) have been developed. HD-OCT is a commercially available system dedicated to skin imaging (Skintell®, Agfa Healthcare Mortsel, Belgium and München, Germany) providing axial and transversal resolution of 3 µm over 1.8 x 1.5 mm field of view, however with penetration depth limited to 570 µm. The penetration depth is also limited to first few hundred microns in FF-OCT that directly acquires 2D en face images (without beam scanning) by illuminating the full field of view with a white-light source, such as a halogen lamp.[10,11] In FF-OCT three-dimensional imaging can be performed, by stepping the reference mirror and recording successive en face images resulting in a stack of images.[12] With a speed limitation, which is caused by the long acquisition times, higher resolution OCT imaging can be only applied for *ex vivo* imaging.

The aim of this review is to determine the clinical usefulness of OCT and its variants during cancer interventions for both preoperative diagnosis and intraoperative tumor detection, with a focus on qualitative features, quantitative features and the diagnostic value of OCT, which are described per tumor type.

Methods

A literature search in PubMed was performed for articles using OCT in the field of surgical oncology, published before May 2018. The search consisted of different keywords: "optical coherence tomography" or "OCT" combined with general terms ("oncology", "oncologic", "tumor", "tumors", "malignancy", "malignancies", "cancer") and more tumor-specific MeSH terms ("skin neoplasms", "oral neoplasms", "lung neoplasms", "breast neoplasms", "pancreatic neoplasms", "liver neoplasms", "bile duct neoplasms", "esophageal neoplasms", "stomach neoplasms", "colorectal neoplasms", "prostate neoplasms", "kidney neoplasms", "urinary bladder neoplasms", and "ovarian neoplasms"). Case reports, (systematic) reviews, non-human studies and articles not written in English were excluded from the analysis.

Results

A total of 785 articles were revealed by our search, of which two were found by manual search on the SPIE digital library. After exclusion of 649 articles, that did not meet our eligibility criteria, a total of 136 original articles remained, of which an overview is given in Figure 1. The included articles, which form the basis of this review, are discussed separately per cancer type. An overview of the diagnostic value of OCT for tumor detection, including relevant study characteristics, is provided in Table 1.

Skin cancer

Skin tumors are usually divided into melanoma and non-melanoma cancer. Because of its aggressive character, the only curative treatment for local melanomas is surgical resection in combination with sentinel lymph node mapping. However, in the last years novel target therapies were developed which showed great potential in patients with unresectable or metastatic melanoma.[13] For basal cell carcinoma (BCC), which is a non-melanoma cancer and the most common type of cancer in caucasians worldwide, many treatment options are available and applied, dependent on the tumor characteristics and patient's preference.[14] Mohs micrographic surgery is currently performed in many clinics, to obtain free resection margins. Nevertheless, it would be preferable for both the patient and surgeon to obtain real-time feedback of the margin involvement during surgery. Many studies have determined the capacity of OCT for visualization of different types of skin cancer.

MALIGNANT MELANOMA

OCT images of a malignant melanoma showed irregular structures in the lower epidermis, which corresponded to histology. The basement membrane zone was also not visible, which made these characteristics specific for malignant melanoma.[15] Moreover, other characteristics have been investigated. In general, two characteristics were often visible: 1) the presence of horizontal highly reflective cords in the epidermis and dermis, which probably correspond to dense collagen cords of encapsulated tumor lobules; 2) the presence of large vertical icicle-shaped structures reaching the reticular dermis with the peak aspect, which corresponded to tumor cells and lymphocytes infiltration on histology (Figure 2).[16-18]

BASAL CELL CARCINOMA

Several specific features for BCC were suggested, of which disruption of layering, hyporeflective rounded areas surrounded by a hyperreflective halo (honeycomb structure), peripheral palisading and dilated vessels, well circumscribed black/signal poor areas were the most common and characteristic.[10,16,17,19-34] Two studies evaluated the diagnostic accuracy of OCT in detecting basal cell carcinomas *in vivo*, showing good results with sensitivity and specificity ranging from 79-94% and 85-96%, respectively.[19,23] Ulrich et al. evaluated the diagnostic value of OCT combined with clinical and dermoscopic assessment with sensitivity and specificity of 96% and 75%, respectively, which resulted in a higher diagnostic accuracy compared to clinical and dermoscopic information.[35] However, even for experienced observers it was difficult to distinguish BCC from actinic keratosis, which was illustrated by the 50% error rate.[19] Differentiation between the several BCC subtypes was difficult, however variants of OCT like HD-OCT and multi-beam swept source OCT (MSS-OCT) showed potential for clinical use.[10,16,34] Moreover, many studies were performed to assess the surgical margins during Mohs surgery.[27,32,36-42] Conventional OCT yielded to a sensitivity of 19% and specificity of 56%, whereas HD-OCT showed an improved sensitivity of 75% and a specificity of 64%.[36,37]

CONCLUSION

Diverse specific tumor characteristics for both melanoma and BCC were composed. In case of melanoma, no diagnostic studies were performed with OCT. OCT showed good results in BCC detection, however margin assessment, which is clinically most relevant, was much more difficult even with higher resolution OCT.

Oral cancer

Oral cancer, of which squamous cell carcinoma accounts for 90% of the cases, is often treated by a combination of surgery and radiotherapy.[43] Due to the difficult location and the surrounding vital structures, it is of outmost important to achieve complete tumor removal. OCT was utilised in 10 studies to evaluate its potential use.

ORAL (PRE-)CANCEROUS LESIONS

Several parameters were important to distinguish between benign and (pre)malignant oral lesions, such as disorganization of epithelial stratification (irregular collagen vessels), epithelial and/or keratin thickening, micro-structure invasion, heterogeneous cell distribution, and disorganization of the basement membrane.[44-46] Four studies in 19 to 125 patients showed that dysplasia detection was possible both after training of independent reviewers and using quantitative analysis.[47-50] Computer analysis, using a 70% standard deviation of the epithelial thickness, yielded a sensitivity of 82% and a 90% specificity, which indicated that epithelial thickness is one of the most characterizing features of oral dysplasia.[50,51] Squamous cell carcinoma was very well identified, resulting in a sensitivity of 82% and 93% and a specificity of 87% and 93%, as demonstrated by Wilder-Smith et al. and Hamdoon et al.[44,45] De Leeuw et al. evaluated 57 FF-OCT images for presence of cancerous lesions, yielding a 85% accuracy for reviewer 1 and a 89% accuracy for reviewer 2.[46] In both studies image assessment was performed by two independent reviewers, who used the main features of malignancy on OCT images. Using a variant of OCT, Swept Source

OCT (SS-OCT), Tsai et al. performed quantitative analysis and showed that in premalignant tissue, the epithelium became significantly thicker and the standard deviation became larger, due to epithelial disorganization.[52,53]

CONCLUSION

Several characteristics for (pre)malignant oral tissue were proposed, all showing good diagnostic accuracies. These morphological characteristics were confirmed by quantitative analysis, nevertheless no intraoperative studies were yet performed for real-time evaluation of the surgical resection margins.

Lung cancer

The diagnosis of lung cancer, which is the most common cancer in men worldwide, is often made by CT and flexible bronchoscopy. However, bronchoscopy lacks sensitivity, especially for early stage malignancies.[54] Five studies utilized OCT as an additional imaging tool for visualization of lung cancer both during bronchoscopy and after surgery on resected specimens.

OCT DURING BRONCHOSCOPY

Bronchial malignancies were generally characterized on OCT images by a thickened epithelium wall and loss of subepithelial identifiable microstructures. Tumor invasion was visible as a disappearance and/or disturbed architecture of the basement membrane.[55-57] In normal lung tissue, the basement membrane and the lamina propria were visualized as highly reflective layers, due to the presence of collagen vessels. Deeper layers containing seromucinous glands, connective tissue and cartilage, were characterized by polymorphic light and dark areas.[55,56] Hariri et al. composed specific OCT criteria for the different tumor types: adenocarcinoma, squamous cell carcinoma and poorly differentiated carcinoma.[58] Adenocarcinomas were characterized by round or angulated signal-poor to signal void structures, which were typically small and secondly by lack of signal-intense (bright) nests. Squamous cell carcinoma could be recognized by the presence of signal intense nest (brighter than surrounding tissue), which were round or irregularly shaped. These nests may have variably sizes and sometimes also areas of necrosis were visible as signal-poor areas. Lack of round/angulated signal-poor structures and lack of signal-intense nests were specific for poorly differentiated carcinomas.

These criteria were applied by Hariri et al. in a prospective validation cohort, in which three readers evaluated 153 OCT images acquired from five patients, divided over two assessments (separated by 7 months) preceded by a training session.[58] The overall accuracy improved from 81.8% to 83.3% after the second assessment.

SURGICAL RESECTED SPECIMENS

FF-OCT provided high resolution images of both normal and malignant resected lung specimens up to a depth of 5-15 µm. Normal lung tissue was recognized by the typical leace-like pattern, which was formed by the alveoli and their septal walls, visible as signal-void dark areas and bright areas respectively. Other lung components could also be identified, such as the pleura (bright signal), blood vessels and bronchi (dull grey signal). Adenocarcinomas, characterized by their

predominant lepidic growth pattern, could be really well identified. Tumor cells were also larger than normal cells, although they appeared to have a similar signal (dull grey) as normal cells.[59]

CONCLUSION

Although, the diagnostic accuracy was fairly high and OCT during bronchoscopy seems feasible in above mentioned studies, OCT is yet not adequate as a complete replacement for tissue biopsy. However, it has the potential to be implemented in bronchoscopy procedures for diagnosis of lung tumors. Intraoperative use for margin assessment of tumor detection is yet not evaluated.

Breast cancer

Breast cancer, which is the most common type of cancer in women, is responsible for 14% of the cancer-related deaths annually.[60] In breast cancer surgery, it is extremely important that borders of the excised specimen do not contain any tumor cells, since these positive margins are associated with a higher risk of local recurrence of the primary tumor.[61] Not only margin assessment, but also intraoperative staging by sentinel lymph node mapping is often performed in breast cancer patients.[62] Eight studies evaluated the use of OCT in resected surgical specimens and five studies evaluated the use of OCT for lymph node analysis.

TUMOR DETECTION SURGICAL SPECIMENS

Diverse tumor-specific criteria were developed based on histological features. Invasive ductal adenocarcinomas, which showed infiltrating tumor cells in surrounding tissue and surrounding fibrous tumor stroma were clearly visible.[63-65] Mucinous carcinomas could be recognized by mucin with floating tumor cells, which were reflected in the OCT image. Assayag et al. proposed three FF-OCT specific criteria for malignancy in addition to macroscopic characteristics, such as absence of normal breast tissue structures and presence of stellate lesions: 1) Presence of adipocytes with irregular size (fat infiltration); 2) Highly scattering trabecula aspect of fibrous tissue; 3) Presence of dark grey areas surrounded by white fibrous structures; 3).[63] Especially white fibrous structures were suspect for tumor stroma, whereas grey fibrous structures were associated with scar fibrous tissue in benign breast lobules. Furthermore, *ex vivo* analysis of resection margins was performed by Nguyen et al.[66] Thirty-seven breast cancer specimens were used for analysis, divided into a training set and a study data set. Of each specimen, 5 to 10 images were taken, resulting in 210 images used for the study data set and pathologic analysis by one researcher. Analysis showed a sensitivity and specificity of 100% and 82%, respectively, in tumor detection compared to histology, which is the current golden standard. Feasibility of multimodal imaging, by combining OCT with ultrasound and dye-enhanced wide-field polarization imaging, was demonstrated by Patel et al. and Curatolo. et al.[67,68]

Recently, a handheld OCT camera has been developed, which has been used in two studies, that evaluated the diagnostic accuracy of the camera after obtaining the *ex vivo* final margins in 46 and 35 patients, respectively.[69,70] *In vivo* imaging was feasible, although *ex vivo* images of the margins could be directly correlated to the histology slices, which consequently were used in both cohorts (Figure 3). After comparison of histology with readers interpretation, they showed a diagnostic accuracy in tumor detection at the surgical margins varying between 58% and 88%. The

authors stated that this variability could be explained by the minimal training preceded by image evaluation and by the experience in studying OCT images of the reader.

LYMPH NODES DETECTION

Normal lymph nodes were characterized by a distinct capsule that was highly scattering, in comparison to the lower scattering cortex. The lymphoid follicles, which were visible as a circular texture on the OCT image, could also be clearly observed in the cortex.[71,72] Lymph node invasion was characterized by loss of normal tissue architecture, presence of highly heterogeneous tendril-like structures and the presence of areas with highly backscattering areas, possibly due to changes in size and texture of the cell nuclei. One study compared the diagnostic accuracy of OCT to histology, after training of three reviewers, which resulted in an overall sensitivity and specificity of 58.8% and 81.4%, respectively.[73]

In order to improve the capability to distinguish benign and malignant invasion of lymph nodes, parametric imaging of the local attenuation coefficient was applied in OCT images and showed promising results in two feasibility studies.[72,74] FF-OCT showed a more detailed view of the lymph nodes, of which the strong stromal reaction, caused by tumor invasion, was one of the most characterizing morphological features for lymph node invasion on FF-OCT images. FF-OCT showed an improved sensitivity of 89% and specificity of 87% compared to regular OCT after training of two independent reviewers.[75]

CONCLUSION

OCT was used for both tumor detection and sentinel lymph node detection in breast cancer patients. Diverse specific criteria were applied and showed high diagnostic accuracy in margin assessment compared to histology. A handheld OCT camera, which could be used intraoperatively, was also applied for margin assessment and showed promising results. This indicates that with more training and further development, OCT could be used as an additional tool for intraoperatively tumor detection. For lymph node detection, especially FF-OCT was able to distinguish malignant invasion of lymph nodes from benign lymph nodes with high sensitivity and specificity.

Hepatopancreaticobiliary (HPB) tumors

The diagnosis of pancreaticobiliary cancers is often made by taking biopsies during endoscopic intervention. However, the current diagnostic accuracy for both pancreatic and biliary malignancies lacks sensitivity.[76,77] Moreover, in liver and pancreatic surgery, tumor positive resection margins defined as ≤1 mm tumor-to-margin distance, are found up to 24% and 75%, respectively.[78,79] Consequently, some progress in diagnostic accuracy of HPB tumors could be made. Nine studies evaluated the use of OCT both during endoscopy and in resected specimen.

OCT DURING ENDOSCOPY

OCT was used to distinguish malignant and benign pancreatic duct strictures both *in vivo* and *ex vivo* during routine endoscopic retrograde cholangiopancreatography (ERCP) procedures.[80-83] By using disturbance of normal three-layer architecture with heterogenous backscattering as marker for presence of tumor, *ex vivo* analysis of 100 OCT images of 10 patients showed an overall

sensitivity and specificity for tumor detection of 78.6% and 88.9%, respectively.[80] Moreover, a concordance between OCT and histology for detection of a pancreatic adenocarcinoma was seen in 97.6% of the 126 images.[80]

In vivo analysis resulted in a 100% accuracy for detection of neoplastic pancreatic ductal strictures.[82] Two criteria for malignant strictures were used: 1) unrecognizable layer architecture; 2) heterogeneous backscattering of signal.

Biliary duct imaging using OCT was performed in 2009 by Arvanitakis et al.[84] They used the above mentioned criteria for detecting of malignant biliary strictures, which was accurate in 84% of the included 37 patients. OCT seemed favorable in preoperative detection of unknown biliary strictures compared to randomly taken biopsies, which resulted in a 67% accuracy in the same cohort.

Besides ERCP, endoscopic ultrasound- fine needle aspiration (EUS-FNA) is often used for taking biopsies for establishing the diagnosis of pancreatic masses. Grieve et al. evaluated the feasibility of FF-OCT in evaluation of FNA specimens acquired during EUS.[85] Three images of pancreatic ductal adenocarcinomas (PDAC), two images of neuroendocrine pancreatic tumors and two images of pancreatic metastases from renal cell carcinomas were included in the analyses and compared to the histology. PDAC was recognized by intense dark malignant cell clusters with irregular borders and high nuclear density. Glandular differentiation was indicated by atypical tall columnar epithelium and the presence of luminal spaces. Neuroendocrine pancreatic tumors were also easily identified by areas with neoplastic endocrine tumor cells, which appeared darker than normal pancreatic tissue. Pancreatic renal cell metastases showed a fair matching with histology. One of the two images showed good correspondence and was recognised by sheets of large cells, which compressed the vessels.

SURGICAL RESECTED SPECIMEN

Iftimia et al. used OCT for detection of several types of pancreatic cystic tumors: mucinous cystic neoplasm (MCN), intrapapillary mucinous neoplasm (IPMN) and serous cystadenoma (SCA).[86] After developing OCT criteria for differentiating between MCNs, SCAs and IPMNs, the investigators (a gastroenterologist, a radiologist and a pathologist) underwent training based on 20 OCT images of fresh resected pancreatic specimens. After that, they were independently asked to evaluate 46 OCT images, resulting in a high sensitivity in distinguishing mucinous vs non mucinous cystic lesions (95.6% for the gastroenterologist and 100% for the radiologist and pathologist).

Van Manen et al. evaluated the accuracy of FF-OCT in detecting pancreatic tumors in resected surgical specimens.[87] Two pathologists were asked to evaluate 100 FF-OCT images after a training set, which resulted in a combined sensitivity and specificity of 72% and 74%, respectively, compared to histologic diagnosis. Moreover, they developed specific criteria for different types of pancreatic tumors. Especially, in case of pancreatic ductal adenocarcinoma, disorganization of glands and presence of tumor stroma were really well visible (Figure 4). However, due to low endogenous contrast, cell nuclei could not be visualized, whereas sometimes the collagen dominated the field of view due too much backscattering, which was mistaken for tumor stroma.

Zhu et al. evaluated the feasibility of FF-OCT in resected liver specimens.[88] Normal liver structures, such as blood vessels, bile ducts and sinusoidal spaces, could be really well identified. Hepatocellular carcinoma was recognized by the presence of nuclear atypia and large tumor nodules separated by thick fibrous bands.

CONCLUSION

The role of OCT was evaluated both during endoscopy and on resected specimens of both cystic and solid tumors. OCT during ERCP showed high accuracy in detection of pancreatic or biliary strictures. Mucinous cystic lesions could be really well identified and distinguished from non-mucinous lesions. FF-OCT was feasible in *ex vivo* EUS-FNA biopsies, pancreatic and liver specimens. Especially, in liver and pancreatic specimens, diverse tumor characteristics were found.

Oesophageal cancer

Oesophageal cancer, one of the most lethal cancers in the western world, is usually divided in adenocarcinoma and squamous cell carcinoma (SCC).[89] One of the independent risk factors for an oesophageal adenocarcinoma is a Barrett's oesophagus (BE), which is a transition of normal squamous mucosa into columnar (gastric) epithelium (=metaplasia), which could be considered as a pre-malignant stadium. Currently, most patients with BE undergo endoscopic surveillance, which is controversial. Moreover, development into dysplastic or neoplastic tissue could only be detected by taking biopsies, frequently accompanied with a sampling error.[90] Thirteen studies evaluated the role of OCT during endoscopy in patients with suspected oesophageal lesions.

BARRETT'S OESOPHAGUS AND ADENOCARCINOMA

Bouma et al. performed the first *in vivo* study in 32 patients, who underwent routine endoscopy, and developed some characteristics of BE on OCT images.[91] Due to high scattering of the metaplastic epithelium, there was a loss of normal layered architecture. In normal oesophageal tissue, the five oesophageal wall layers (squamous epithelium, lamina propria, muscularis mucosae, submucosa and muscularis propria) could easily be recognised by their relative difference in reflection.[91-94] Together with the presence of inhomogeneous tissue contrast and abnormal and disorganised glands below the epithelial surface, visible as pockets of low reflectance, it is called BE. Especially, patients with BE without dysplasia or low grade dysplasia, the muscularis mucosae and submucosal layers often could be preserved.[95,96] Poneros et al. applied these criteria in a validation cohort in patients, who underwent routine upper endoscopy, which resulted in a sensitivity and specificity of 100% and 93% for BE detection, respectively.[97] OCT was also used for detection of BE before and after radiofrequency ablation treatment. Unfortunately, in the minority of the patients (7.7%), OCT was capable to distinguish normal glands from buried Barrett's glands.[98] Another study showed a 81% sensitivity and 66% specificity in detection of BE, indicating that OCT is currently not accurate enough compared to histology.[99] One study evaluated the capacity of OCT for detection of oesophagus dysplasia.[100] Normally, dysplasia is divided in low-grade and high grade dysplasia, which consequently results in different clinical approach, i.e. resulting in oesophageal resection or not. Dysplasia was detected on OCT by reduced light scattering and loss of tissue architecture, which are currently the only known criteria. Evaluation of 314 OCT images of 33 patients by four endoscopists resulted in a sensitivity and

specificity (compared to histology of the biopsies) of 68% and 82%, respectively.[100] However, the authors did not make any difference between low-grade dysplasia, high-grade dysplasia or neoplasia. Chen et al. more specifically described high grade dysplasia as presence of irregular and distorted glandular architecture and closely packed glands.[95]

Adenocarcinomas were characterized on OCT images by a neoplastic epithelium, which contains large pockets of mucin surrounded by fibrotic and hypervascular tumor stroma.[91] Sometimes infiltration of heterogeneous structures into the muscular layers could be seen as a feature of tumor invasion. Irregular shape and crowd of submucosal glands also advocated the presence of adenocarcinoma (Figure 5).[95,101] Detection of adenocarcinoma in patients who underwent upper endoscopy for several reasons showed potential, with a detection rate of 95%.[102]

SQUAMOUS CELL CARCINOMA

Hatta et al. compared the capability of OCT for SCC invasion detection in the different layers of the oesophagus to histology.[93] Superficial invasion into the epithelium layer was difficult to distinguish from normal oesophagus tissue. However, the researchers were able to detect the tumor invasion level with a high overall accuracy: 92.7%. Furthermore, they compared the diagnostic accuracy of OCT with high-frequency EUS in a larger cohort of 123 patients.[103] OCT showed a significantly higher accuracy than high-frequency EUS (90.1% vs 77.1%; P=0.0046).

CONCLUSION

OCT has been evaluated for establishing the diagnosis of oesophageal SCC, BE and adenocarcinoma. Diverse characteristics of BE, dysplasia, adenocarcinoma, and SCC were applied, which showed promising results. However, differentiating between normal glands and Barrett's and tumor glands was really difficult.

Colon cancer

Screening for colon cancer is currently mainly performed by using fecal occult blood testing, in suspected cases followed by endoscopy.[104] Adenomatous polyps, which carry risk of cancer development are often found during colonoscopy. They can macroscopically be divided based on their growth pattern into tubular and villous polyps and microscopically they are generally classified as low-grade or high-grade dysplasia. Currently no studies have described the use of OCT for cancer detection, however six studies assessed the use of endoscopic OCT as a screening tool for premalignant polyp detection.

DETECTION OF (PRE)MALIGNANT TISSUE

Tearney et al. first described the feasibility of OCT during colonoscopy for premalignant tissue detection.[105] Normal colonic wall features were described by Westphal et al.[106] The mucosa was visible as a reflective layer, including an underlying thin hyperreflective line, whereas the submucosa appeared highly variable probably caused by compression related to the colonoscopy procedure. Pfau et al. described the different features visible on OCT concerning the most common forms of polyps and showed that adenomatous polyps were significantly more disorganized and more hypo-reflective than hyperplastic polyps.[107] Colorectal neoplasms were described as polyps

with an uneven surface. On OCT, areas of malignant cells appeared bright, whereas non-cellular regions were less reflecting.[92] Quantitative analysis was performed for colorectal cancer in two studies, which showed that malignant tissue has lower scattering properties and less variation of signal intensity from the surface yielding a 78% sensitivity and 74% specificity.[108,109]

CONCLUSION

The use of OCT during colonoscopy for tumor detection has not been frequently analysed. Currently, presumably quantitative analysis could be performed for both tumor and polyp detection, however the diagnostic accuracy lacks sensitivity.

Urological cancer

Most of the time surgery is not the first choice of treatment for urological cancers.. Establishing the correct diagnosis before chemoradiotherapy is of outmost important. Therefore, OCT has been mainly used as an additional tool during biopsy taking in both five studies for prostate, six studies for renal and seven studies for bladder cancer detection, respectively.

PROSTATE CANCER

D'Amico et al. first described the feasibility of OCT for detection of tumor in prostate biopsies.[110] The first large cohort study, performed by Dangle et al. included 100 samples of which 10 had positive surgical margins.[111] Using homogeneity of the prostate epithelium and presence of prostatic stroma as assessment criteria, OCT yielded a sensitivity of 70% and specificity of 84%. More detailed information about malignant features were visualized using FF-OCT, such as presence of irregular gland contours, infiltration of variably sized glands between benign glands, and the presence of cribriform patterns.[112] These characteristics were used during analysis by three independent pathologists, resulting in a 63% sensitivity and 74% specificity. However, a learning curve was observed, leading to a diagnostic accuracy of 82% at the end of the assessment. More recently, quantitative analysis of prostate biopsies showed significant differences in attenuation coefficient between normal and malign prostate tissue.[113,114]

RENAL CANCER

Linehan et al. performed the first *ex vivo* study on 20 resected renal specimens.[115] Generally, in malignant tissue there was a lack of normal structures, however in some cases tumor samples had heterogeneous areas, which mimicked normal kidney tissue. Furthermore, high sensitivities and specificities (up to 100%) for renal tumor detection were achieved in another study by Lee et al.[116] Three pathologists evaluated 35 OCT images of both normal and tumor resected specimens. Renal tumors were characterised by increased scattering tumor nests, which were separated by hyposcattering stroma.[116] More specific, distinguishing renal cell carcinoma and renal oncocytoma (benign renal tumor) was possible by both morphological characteristics and after quantitative analysis of the attenuation coefficient.[116-118] Computer analysis also showed the attenuation coefficient of normal renal parenchyma to be significantly differed from malignant tumors.[117,119] Moreover, several signatures of different kidney tumors could be recognized as described by Jain et al.[120] After training, the uropathologist was able to distinguish benign and malignant tumors (67 FF-OCT images) with a 100% accuracy and achieved a 80% accuracy for correct subtyping of these tumors.

BLADDER CANCER

Seven studies evaluated the diagnostic value of OCT for the detection of cancer in bladder biopsies or resected specimens in populations varying between 21 and 116 patients.[121-127] Disorganized tissue layers and sub-epithelial nests of tumor cells were often found in tumorous biopsies. By using these criteria, sensitivities between 84% and 100%, and specificities between 65% and 89% for tumor detection could be achieved. By using FF-OCT, more details of tumor cells, such as presence of large nuclei and newly formed blood vessels, appearing as small bright spots, could be visualized. After training of the reviewers, a diagnostic accuracy up to 96% could be obtained, as demonstrated by Montagne et al.[121]

CONCLUSION

OCT was capable to distinguish urological tumors from benign tissue with varying accuracies. For quantitative analysis, the attenuation coefficient seems the most informative parameter.

Ovarian cancer

Ovarian cancer is a disease with a dreadful prognosis, making it the most lethal gynaecological malignancy.[60] Treatment mainly consists of surgery, especially in early-stage disease. Eight studies, evaluated the use of OCT for detection of ovarian cancer, of which two during surgery.

RESECTED SPECIMEN

Two studies evaluated the tumor characteristics based on qualitative analysis using OCT and FF-OCT, respectively.[128,129] Ovarian malignancies were characterized by presence of hyperintense regions with irregular patterns, which turned out to be disorganised collagen fibers. Ovarian metastases could also be detected as shown by Stegehuis et al.[129] Metastatic tumor cells appeared light grey in a web-like organisation, resulting in a distorted ovarian cortex architecture. Furthermore, other studies analysed tumor images quantitatively, focussing on optical coefficients, which were derived from normalized histograms.[130-133] After building a logistic classifier model, Nandy et al. were able to achieve a 91.6% sensitivity and a 87.7% specificity for tumor detection based on FF-OCT images.[133]

LAPAROSCOPIC SURGERY

Boppart et al. first described the use of OCT, integrated in a laparoscopic system, in one resected ovary specimen, containing a serous papillary cystadenocarcinoma.[134] Presence of cysts, which are surrounding by papillary structures, were characterizing for this tumor type. *In vivo* application of laparoscopic OCT was performed by Hariri et al. in 30 ovaries of 17 patients, who underwent surgical resection.[135] They described different features of ovarian tumors, such as papillary serous cystadenoma or adenocarcinoma. An adenoma was characterized by large, simple cystic structure with a sharp, regular, well-demarcated cyst lining. Complex, multicystic signal void structures surrounding by tumor stroma, which have a more heterogeneous signal intensity than normal stroma, were suspect for adenocarcinomas.

CONCLUSION

Several subtypes of ovarian tumors could be recognized by using OCT both *ex vivo* and during laparoscopic surgery. However, until today no large patient cohort studies have been reported.

General conclusion and future perspectives

The introduction of OCT shows new opportunities during oncologic interventions. In this review, the role of OCT was evaluated for different tumor types. We have shown that several characteristics for both normal tissues and the different tumor types were established. In case of Barrett's oesophagus, even metaplasia could be detected. OCT could be integrated during bronchoscopic and endoscopic procedures. However, the diagnostic value of OCT was evaluated in limited studies, of which an overview is provided in Table 1. In general, it can be concluded, based on this overview, that use of OCT for guiding of biopsy location during bronchoscopy, intraoperative margin assessment in case of breast cancer surgery and for visualization of pancreatico-biliary strictures during ERCP might be useful. Especially, in case of breast cancer, a developed handheld device showed promising diagnostic accuracy, which could be valuable during surgical intervention.

The great advantage of OCT is its non-invasive, reproducible and well-tolerated characteristics for in human use. However, some drawbacks could be mentioned. First of all, OCT is a relatively new modality, which needs extensive training and setting-up new clinically relevant features by building extensive atlases for instance, before adopting into clinical practice. That also states the need for automatic feature extraction and even automatic tumor detection, which was recently performed by Marvdashti et al. who integrated an automatic classifier based on known characteristics and new features, resulting in a high diagnostic accuracy of 95.4%.[136] However, due to the availability of several OCT systems classification is difficult, although matching of optical properties is possible.[137] Standardization for signal intensities for each device, which has been done after the introduction of CT devices by using Hounsfield units, would make analysis easier.[138] Secondly, the imaging depth is restricted up to maximum 1-2 mm in OCT and to less than 1 mm in its high resolution variants (HD-OCT, FF-OCT). Conventional OCT with resolution between 7-10 μm showed less microscopic details compared to the current gold standard, histology. Nevertheless, further developing of new variants of conventional OCT with increased resolution, such as FF-OCT, could improve the quality of the images, which make tumor detection feasible into the clinical practice. However, even with FF-OCT, which provides images with resolution comparable to histology, the endogenous contrast of for instance cell nuclei is not good enough for visualization. Techniques to improve the subcellular contrast, such as dynamic FF-OCT, are being developed, enhancing both structural and functional information through the detection of the intracellular activity.[139] Recently, also a handheld FF-OCT rigid endoscope has been developed, with a faster and more sensitive camera integrated than current FF-OCT systems, which paves the way for intraoperative use.[140] Finally, sometimes signal of highly backscattering tissues, such as collagen vessels or tumor stroma, disturbed the OCT images and made distinguishing benign and malignant tissue from each other complicated. On the other hand, it was shown that stroma alignment is significantly different between benign and malignant tissue for pancreatic cancer [141] and breast cancer[142], and could therefore contributes to better detection of tumors on OCT images. Such information can be possibly obtained using polarization-sensitive OCT, which in addition to tissue microarchitecture can provide images of tissue birefringence.[136] Hariri et al. showed that Polarization Sensitive OCT (PS-OCT) has a potential to help in differentiation between lung tumor and fibrosis and Kiseleva et al. used PS-OCT to diagnose mucosal pathologies in *in vivo* human bladders.[143,144] Also, other functional OCT variants, such as Doppler-OCT that visualizes tissue vasculature and spectroscopic OCT that

differentiates tissue types based on signal attenuation, as well as multimodality approaches are currently a topic of research.[117,119,145,146]

In conclusion, OCT showed promising results in tumor detection and with the development of novel probes allowing integration in bronchoscopy, flexible or rigid endoscopy, needles [147], handheld cameras and tethered capsules [148,149] could add important value during both preoperative diagnosis as well for intraoperative use in obtaining tumor free resection margins in the nearby future.

Figure 1. Flow diagram of study inclusion.

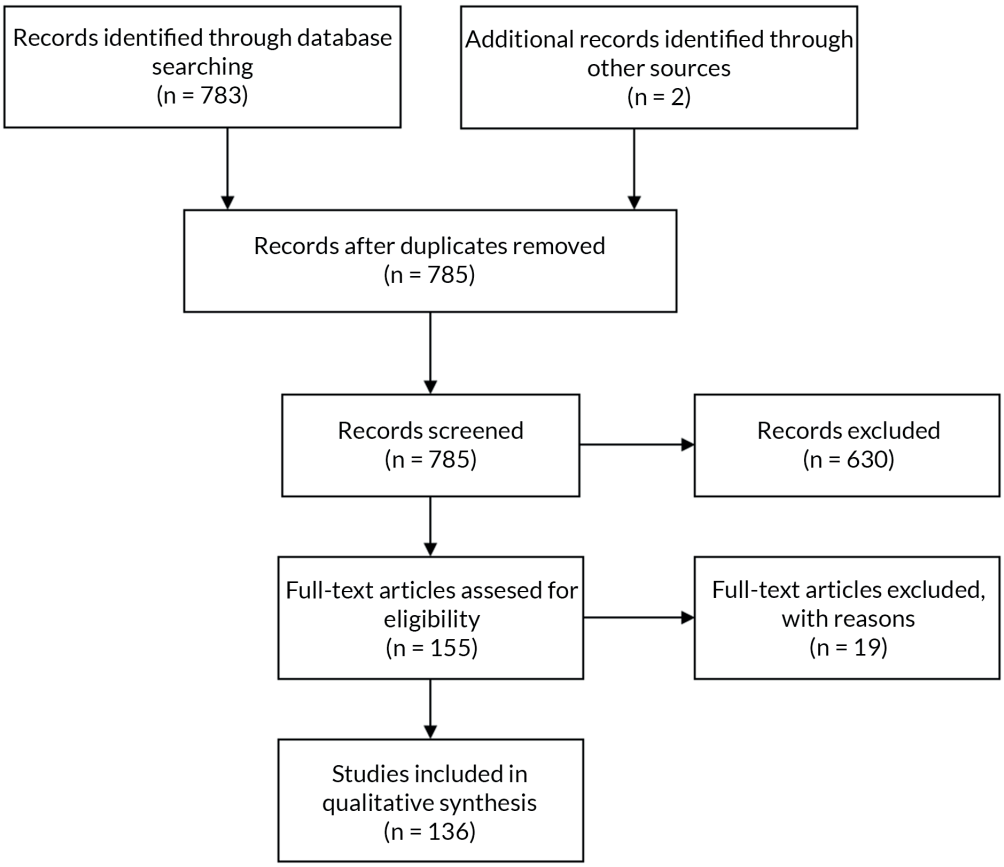

Table 1. Overview of clinical studies evaluating the diagnostic value of optical coherence tomography for tumor detection.

Tumor type	Reference	Technical specifications				Study design		Analysis	Diagnostic value		
		Technique, *Manufacturer*	Resolution: axial x lateral (µm)	Penetration depth (mm)	Acquisition time/image (seconds)	N (images)	Implementation	Samples		Sensitivity (%)	Specificity (%)	Detection rate (%)
Basal cell carcinoma	Mogensen et al. 2009	(Polarization-sensitive) OCT, *Technical University of Denmark*	8 x24	N.S.	3	220	*Ex vivo*	Suspected lesions	6 reviewers of which 2 reviewed all images.	79, 94	85, 96	-
	Jorgensen et al. 2008	OCT, *Riso National Laboratory, Roskilde, Denmark*	10 x 20	1.3	4	78	*Ex vivo*	Suspected lesions	Machine based learning	-	-	81
	Ulrich et al. 2015	OCT, *Vivosight Scanner, Michelson Diagnostics Ltd (Orpington, Kent, U.K.)*	5 x 7.5	1.2-2	N.S.	235	*In vivo*	Suspected lesions	Clinicians of participating centres	96	75	-
	Cunha et al. 2011	OCT, *EX1301, Michelson Diagnostics Ltd (Orpington, Kent, U.K.)*	10 x 7.5	1.5	N.S.	75	*Ex vivo*	Resection margin	2 Mohs surgeons	19	56	-
	Maier et al. 2014	HD-OCT, *Skintell, Agfa HealthCare, Belgium*	3 x 3	0.45-0.75	120	80	*Ex vivo*	Resection margin	1 experienced investigator	74	64	-
Oral cancer	Wilder-Smith et al. 2009	OCT, *Niris™ system, Imalux (Cleveland, OH)*	5-10 (not exactly specified)	1-2	1.5	50	*Ex vivo*	Biopsies	2 reviewers	93	93	-
	Hamdoon et al. 2016	OCT, *EX1301, Michelson Diagnostics Ltd (Orpington, Kent, U.K.)*	<10 x <10	1.5	<0.1	112	*Ex vivo*	Resected SCC specimens	2 reviewers	82	87	-
	De Leeuw et al. 2015	FF-OCT, *Light CT scanner, LL-Tech SAS (Paris, France)*	1.5 x 1.0	N.S.	N.S.	57	*Ex vivo*	Resected head and neck specimens	2 pathologists	88, 90	81, 87	-
Lung cancer	Hariri et al. 2015	OCT, *Harvard Medical School (Boston, USA)*	6 x 30	2-3	N.S.	82	*Ex vivo*	Resection specimens	1 pathologist 1 OCT expert 1 surgeon	80 (AC) 83 (SCC) 86 (PDC)	89 (AC) 87 (SCC) 98 (PDC)	-
Breast cancer	Nguyen et al. 2009	OCT, *University of Illinois, Urbana-Champaign (Illinois, USA)*	6 x 35	1-2	5	210	*Ex vivo*	Resection margin	1 trained researcher	100	82	-
	Zysk et al. 2015	Handheld OCT, *University of Illinois, Urbana-Champaign (Illinois, USA)*	<15 x <15	N.S.	N.S.	2,192	*In vivo* and *ex vivo*	Resection margin	1 pathologist 1 surgeon 1 radiologist	55-65	68-70	-
	Erickson-Bhatt et al. 2015	Handheld OCT, *University of Illinois, Urbana-Champaign (Illinois, USA)*	9 x 9	N.S.	N.S.	50	*Ex vivo*	Resection margin	5 trained OCT readers	92	92	-
	Nolan et al. 2016	OCT, *Bioptigen Inc. (Morrisville, USA)*	11 x 11	N.S.	300-600	184	*Ex vivo*	Lymph nodes	3 analists	59	81	-
	Grieve et al. 2016	FF-OCT, *LL-Tech SAS (Paris, France)*	1 x 1.6	0.20-0.30	600	71		Lymph nodes	1 pathologist 1 non-medical OCT expert	92 / 85	83 / 90	-

Tumor type	Reference	Technical specifications				Study design			Analysis	Diagnostic value		
		Technique, *Manufacturer*	Resolution: axial x lateral (µm)	Penetration depth (mm)	Acquisition time/image (seconds)	N (images)	Implementation	Samples		Sensitivity (%)	Specificity (%)	Detection rate (%)
Pancreatico-biliary cancer	Testoni et al. 2005	OCT, *Pentax, Lightlab Imaging (Westford, MA, USA)*	5-10 x 5-10	1	1 radial mm /s	100	*Ex vivo*	Resection specimens	3 observers	79	89	-
	Testoni et al. 2007	OCT, *Pentax, Lightlab Imaging (Westford, MA, USA)*	5-10 x 5-10	1	1 radial mm /s	11	*In vivo* (during ERCP)	Pancreatic duct strictures	N.S.	100	100	-
	Arvanitakis et al. 2009	OCT, *PENTAX Corporation (Tokyo, Japan) / Lightlab Imaging Ltd. (Boston, USA)*	10 (not exactly described)	1	N.S.	35	*In vivo* (during ERCP)	Biliary duct strictures	2 endoscopists	53	100	-
	Iftimia et al. 2011	OCT, *Physical Sciences, Inc. (Andover, USA)*	9.5 x 25	N.S.	N.S.	46	*Ex vivo*	Resected cysts	1 pathologist 1 gastroenterologist 1 radiologist	95	95	-
	Van Manen et al. 2017	FF-OCT, *Light CT scanner, LL-Tech SAS (Paris, France)*	1.5 x 1.0	>1	N.S.	100	*Ex vivo*	Resected specimens	2 pathologists	72	74	
Oesophageal cancer	Zuccaro et al. 2001	OCT, *manufacturer not specified*	12 x 20	1	3	138	*In vivo* (endoscopic)	AC	23 individuals	-	-	95
	Hatta et al. 2010	OCT, *Light Lab Imaging (Boston, Mass) and HOYA (Tokyo, Japan)*	11 x 30	1.5	N.S.	144	*In vivo* (endoscopic)	SCC	1 gastroenterologist	-	-	93
	Hatta et al. 2012	OCT, *Light Lab Imaging (Boston, Mass) and HOYA (Tokyo, Japan)*	11 x 30	1.5	N.S.	131	*In vivo* (endoscopic)	SCC	1 gastroenterologist	-	-	95
Colorectal cancer	Ashok et al. 2013	(Fourier Domain) OCT, *University of Edinburgh (Edinburgh, UK)*	6.2 x 17	1.2	5	62	*Ex vivo*	Resected specimens	Computer	78	74	-
Prostate cancer	Dangle et al. 2009	OCT, *Niris™ System, Imalux Corporation (Cleveland, OH, USA)*	10-20 x 10-20	2-3	1.5	100	*Ex vivo*	Resection margin	N.S.	70	84	-
	Lopater et al. 2016	FF-OCT, *Light CT scanner, LL-Tech SAS (Paris, France)*	1.5 x 1.5	>1	Mean: 261	119	*Ex vivo*	Biopsies	3 pathologists	63	74	-
Renal cancer	Lee et al. 2012	OCT, *manufacturer not specified*	4 x 14	N.S.	N.S.	35	*Ex vivo*	Resected specimens	Three observers	96	96	-
	Jain et al. 2015	FF-OCT, *Light CT scanner, LL-Tech SAS (Paris, France)*	1.5 x 0.8	N.S.	N.S.	67	*Ex vivo*	Resected specimens	1 uropathologist	100	100	-
	Wagstaff et al. 2016	OCT, *Ilumien™ Optis™ , St. Jude Medical (Saint Paul, MN, USA)*	15 x 20	N.S.	N.S.	40	*Ex vivo*	Renal biopsies	Computer	86	75	-

Tumor type	Reference	Technical specifications				Study design		Analysis	Diagnostic value		
		Technique, *Manufacturer*	Resolution: axial x lateral (µm)	Penetration depth (mm)	Acquisition time/image (seconds)	N (images)	Implementation	Samples		Sensitivity (%)	Specificity (%)	Detection rate (%)
Bladder cancer	Manyak et al. 2005	OCT, *manufacturer not specified*	10 x 15	1	1.5	87	*Ex vivo*	Biopsies	1 reviewer	100	89	-
	Hermes et al. 2008	OCT, *Aachen University (based on Sirius 713, Heidelberg Engineering GmbH, Lübeck, Germany)*	3 x 10	N.S.	4-16	142	*Ex vivo*	Resected specimens	1 reviewer	84	78	-
	Goh et al. 2008	OCT, *Niris Imaging System (Imalux, Cleveland, OH)*	10 x 20	1-2	1.5	94	*In vivo*	Biopsies and resected specimens	1 surgeon	100	90	-
	Ren et al. 2009	OCT, *Stony Brook University, (New York, USA)*	10 x 10	2.1	8 frames / s	110	*In vivo*	Biopsies	urologists/ OCT researchers	94	81	-
	Karl et al. 2010	OCT, *Niris Imaging System (Imalux, Cleveland, OH)*	10 x 20	1-2	1.5	102	*In vivo*	biopsies	N.S.	100	65	
	Gladkova et al. 2011	Cross-polarization OCT, *Institute of Applied Physics of the Russian Academy of Sciences (Nizhny Novgorod, Russia)*	15 x 25	N.S.	2	360	*Ex vivo*	Biopsies	7 reviewers	94	84	-
	Montagne et al. 2017	FF-OCT, *Light CT scanner, LL-Tech SAS (Paris, France)*	1.5 x 1.0	>1	N.S.	24	*Ex vivo*	Resected specimens	2 unexperienced reviewers; 1 FF-OCT expert	Unexperienced: 93 Expert:100	Unexperienced: 78 Expert: 89	-
Ovarian cancer	Nandy et al. 2016	FF-OCT, *manufacturer not specified*	1.6 x 3.9	N.S.	N.S.	56	*Ex vivo*	Resected specimens	Computer: logistic classifier model	92	88	-

Abbreviations:
OCT: optical coherence tomography
N.S.: not specified
HD-OCT: high definition optical coherence tomography
SCC: squamous cell carcinoma
AC: adenocarcinoma
PDC: poorly differentiated carcinoma
FF-OCT: full field optical coherence tomography

Figure 2. Example of corresponding OCT and histology images of two melanomas.

Upper panel (A and C): Hematoxylin and eosin (H&E) images of a superficial spreading melanoma. Lower panel (B and D): OCT images of distorted skin architecture, including large vertically arranged icicle-shaped structures (*). Prominent hyperreflective structures are corresponding to dense collagen cords of encapsulated tumor lobules. Reprinted by permission from Elsevier: Journal of the American Academy of Dermatology.[16] © 2007.

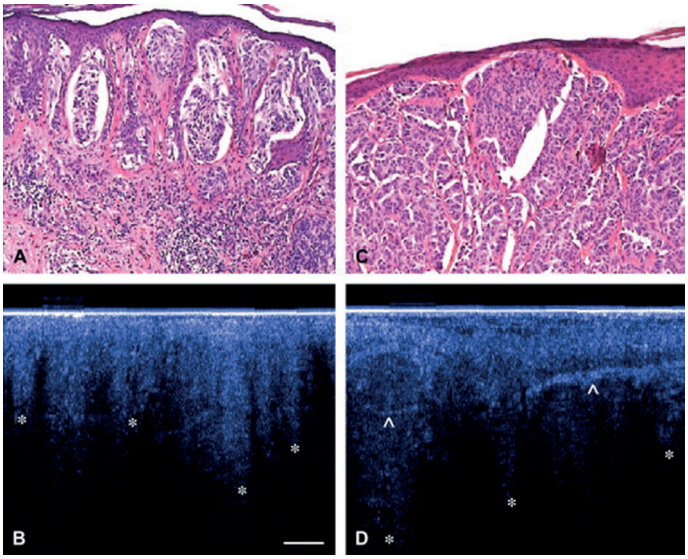

Figure 3. Handheld OCT during breast cancer surgery.

Upper panel: Normal breast tissue with well-defined boundaries, linear structures, and regular texture. Middle panel: Arrow shows an example of a ductal carcinoma in situ, characterized by irregular texture and significant shadowing. Lower panel: An example of an invasive ductal carcinoma (arrows) showing regions with disturbed tissue architecture. Reprinted by permission from Springer Nature: Annals of Surgical Oncology.[69] © 2015.

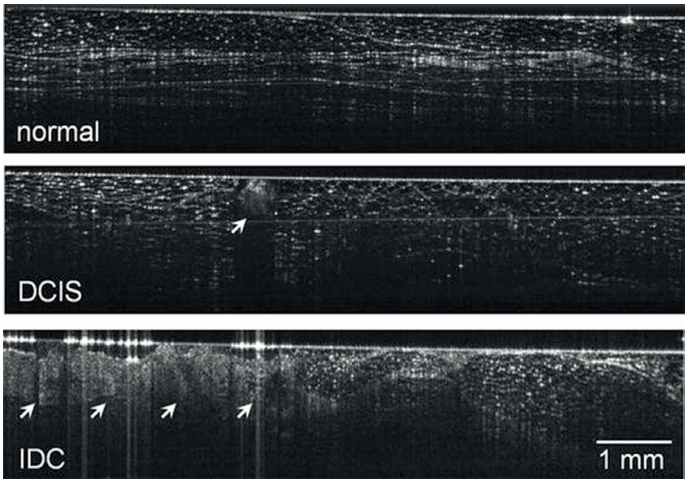

Figure 4. FF-OCT images of the pancreas.

Upper panel: FF-OCT image and corresponding Hematoxylin and eosin(H&E) image of normal pancreatic tissue. Lower panel: An example of a FF-OCT image of a moderately differentiated pancreatic adenocarcinoma with corresponding H&E image, showing tumor cells infiltrating into fat tissue (Bar= 250 µm).

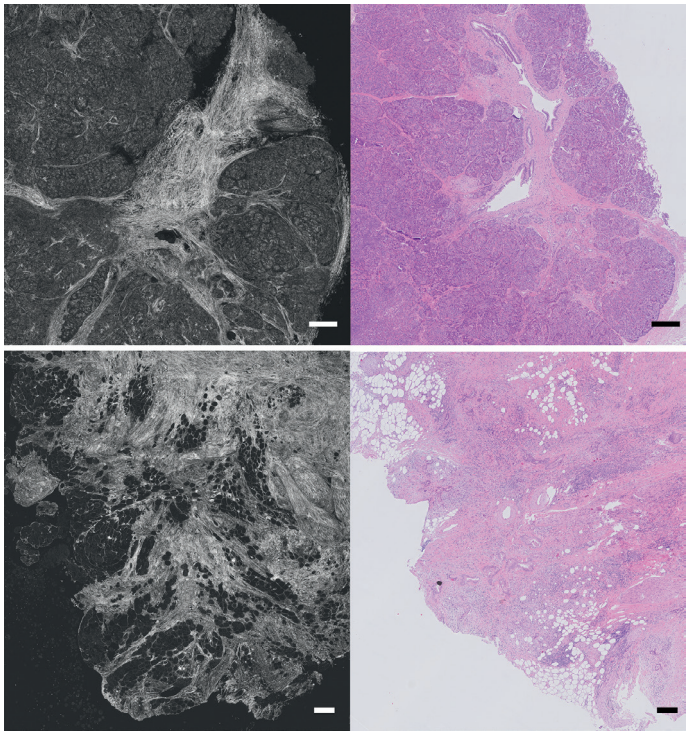

Figure 5. Example of endoscopic OCT of an esophageal squamous cell carcinoma.

Corresponding OCT (A) and histology (B) image of tumor invasion in the submucosal layer, resulting in a loss of the five-layered architecture (Bar= 1000 µm). Reprinted by permission from Elsevier: Gastrointestinal Endoscopy.[93] © 2010.

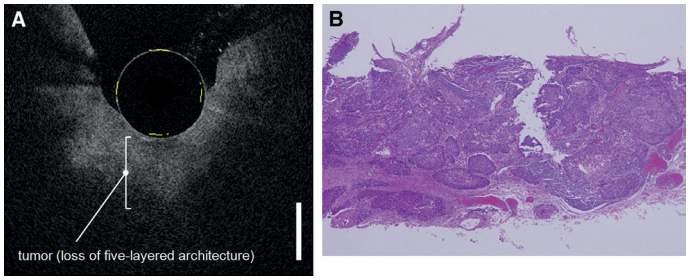

References

1. Kennedy S, Geradts J, Bydlon T, et al. Optical breast cancer margin assessment: an observational study of the effects of tissue heterogeneity on optical contrast. *Breast cancer research : BCR.* 2010;12(6):R91.
2. Haka AS, Volynskaya Z, Gardecki JA, et al. *In vivo* margin assessment during partial mastectomy breast surgery using raman spectroscopy. *Cancer research.* 2006;66(6):3317-3322.
3. Revesz E, Khan SA. What are safe margins of resection for invasive and in situ breast cancer? *Oncology (Williston Park, NY).* 2011;25(10):890-895.
4. Frangioni JV. New technologies for human cancer imaging. *Journal of clinical oncology : official journal of the American Society of Clinical Oncology.* 2008;26(24):4012-4021.
5. Keereweer S, Kerrebijn JD, van Driel PB, et al. Optical image-guided surgery--where do we stand? *Molecular imaging and biology : MIB : the official publication of the Academy of Molecular Imaging.* 2011;13(2):199-207.
6. Huang D, Swanson EA, Lin CP, et al. Optical coherence tomography. *Science (New York, NY).* 1991;254(5035):1178-1181.
7. Vakoc BJ, Fukumura D, Jain RK, Bouma BE. Cancer imaging by optical coherence tomography: preclinical progress and clinical potential. *Nature reviews Cancer.* 2012;12(5):363-368.
8. Tearney GJ, Brezinski ME, Bouma BE, et al. *In vivo* endoscopic optical biopsy with optical coherence tomography. *Science (New York, NY).* 1997;276(5321):2037-2039.
9. Jung W, Zhang J, Mina-Araghi R, et al. Feasibility study of normal and septic tracheal imaging using optical coherence tomography. *Lasers in surgery and medicine.* 2004;35(2):121-127.
10. Boone MA, Norrenberg S, Jemec GB, Del Marmol V. Imaging of basal cell carcinoma by high-definition optical coherence tomography: histomorphological correlation. A pilot study. *The British journal of dermatology.* 2012;167(4):856-864.
11. Popescu DP, Choo-Smith LP, Flueraru C, et al. Optical coherence tomography: fundamental principles, instrumental designs and biomedical applications. *Biophysical reviews.* 2011;3(3):155.
12. Dubois A, Grieve K, Moneron G, Lecaque R, Vabre L, Boccara C. Ultrahigh-resolution full-field optical coherence tomography. *Applied optics.* 2004;43(14):2874-2883.
13. Tripp MK, Watson M, Balk SJ, Swetter SM, Gershenwald JE. State of the science on prevention and screening to reduce melanoma incidence and mortality: The time is now. *CA: a cancer journal for clinicians.* 2016.
14. Verkouteren JAC, Ramdas KHR, Wakkee M, Nijsten T. Epidemiology of basal cell carcinoma: scholarly review. *The British journal of dermatology.* 2017.
15. Welzel J, Lankenau E, Birngruber R, Engelhardt R. Optical coherence tomography of the human skin. *Journal of the American Academy of Dermatology.* 1997;37(6):958-963.
16. Gambichler T, Regeniter P, Bechara FG, et al. Characterization of benign and malignant melanocytic skin lesions using optical coherence tomography *in vivo*. *Journal of the American Academy of Dermatology.* 2007;57(4):629-637.
17. Gambichler T, Plura I, Kampilafkos P, et al. Histopathological correlates of basal cell carcinoma in the slice and en face imaging modes of high-definition optical coherence tomography. *The British journal of dermatology.* 2014;170(6):1358-1361.
18. Boone MA, Norrenberg S, Jemec GB, Del Marmol V. High-definition optical coherence tomography imaging of melanocytic lesions: a pilot study. *Archives of dermatological research.* 2014;306(1):11-26.
19. Mogensen M, Joergensen TM, Nurnberg BM, et al. Assessment of optical coherence tomography imaging in the diagnosis of non-melanoma skin cancer and benign lesions versus normal skin: observer-blinded evaluation by dermatologists and pathologists. *Dermatologic surgery : official publication for American Society for Dermatologic Surgery.[et al]* 2009;35(6):965-972.
20. Bechara FG, Gambichler T, Stucker M, et al. Histomorphologic correlation with routine histology and optical coherence tomography. *Skin research and technology : official journal of International Society for Bioengineering and the Skin (ISBS).[and] International Society for Digital Imaging of Skin (ISDIS).[and] International Society for Skin Imaging (ISSI).* 2004;10(3):169-173.
21. Olmedo JM, Warschaw KE, Schmitt JM, Swanson DL. Optical coherence tomography for the characterization of basal cell carcinoma *in vivo*: a pilot study. *Journal of the American Academy of Dermatology.* 2006;55(3):408-412.
22. Olmedo JM, Warschaw KE, Schmitt JM, Swanson DL. Correlation of thickness of basal cell carcinoma by optical coherence tomography *in vivo* and routine histologic findings: a pilot study. *Dermatologic surgery : official publication for American Society for Dermatologic Surgery.[et al]* 2007;33(4):421-425; discussion 425-426.
23. Jorgensen TM, Tycho A, Mogensen M, Bjerring P, Jemec GB. Machine-learning classification of non-melanoma skin cancers from image features obtained by optical coherence tomography. *Skin research and technology : official journal of International Society for Bioengineering and the Skin (ISBS).[and] International Society for Digital Imaging of Skin (ISDIS).[and] International Society for Skin Imaging (ISSI).* 2008;14(3):364-369.
24. Mogensen M, Nurnberg BM, Forman JL, Thomsen JB, Thrane L, Jemec GB. *In vivo* thickness measurement of basal cell carcinoma and actinic keratosis with optical coherence tomography and 20-MHz ultrasound. *The British journal of dermatology.* 2009;160(5):1026-1033.
25. Forsea AM, Carstea EM, Ghervase L, Giurcaneanu C, Pavelescu G. Clinical application of optical coherence tomography for the imaging of non-melanocytic cutaneous tumors: a pilot multi-modal study. *Journal of medicine and life.* 2010;3(4):381-389.
26. Khandwala M, Penmetsa BR, Dey S, Schofield JB, Jones CA, Podoleanu A. Imaging of periocular basal cell carcinoma using en face optical coherence tomography: a pilot study. *The British journal of ophthalmology.* 2010;94(10):1332-1336.
27. Pomerantz R, Zell D, McKenzie G, Siegel DM. Optical Coherence Tomography Used as a Modality to Delineate Basal Cell Carcinoma prior to Mohs Micrographic Surgery. *Case reports in dermatology.* 2011;3(3):212-218.
28. Mogensen M, Nurnberg BM, Thrane L, Jorgensen TM, Andersen PE, Jemec GB. How histological features of basal cell carcinomas influence image quality in optical coherence tomography. *Journal of biophotonics.* 2011;4(7-8):544-551.
29. Hinz T, Ehler LK, Hornung T, et al. Preoperative characterization of basal cell carcinoma comparing tumour thickness measurement by optical coherence tomography, 20-MHz ultrasound and histopathology. *Acta dermato-venereologica.* 2012;92(2):132-137.
30. Wang T, Mallidi S, Qiu J, et al. Comparison of pulsed photothermal radiometry, optical coherence tomography and ultrasound for melanoma thickness measurement in PDMS

tissue phantoms. *Journal of biophotonics.* 2011;4(5):335-344.
31. Coleman AJ, Richardson TJ, Orchard G, Uddin A, Choi MJ, Lacy KE. Histological correlates of optical coherence tomography in non-melanoma skin cancer. *Skin research and technology : official journal of International Society for Bioengineering and the Skin (ISBS).[and] International Society for Digital Imaging of Skin (ISDIS).[and] International Society for Skin Imaging (ISSI).* 2013;19(1):10-19.
32. Alawi SA, Kuck M, Wahrlich C, et al. Optical coherence tomography for presurgical margin assessment of non-melanoma skin cancer - a practical approach. *Experimental dermatology.* 2013;22(8):547-551.
33. Maier T, Braun-Falco M, Hinz T, Schmid-Wendtner MH, Ruzicka T, Berking C. Morphology of basal cell carcinoma in high definition optical coherence tomography: en-face and slice imaging mode, and comparison with histology. *Journal of the European Academy of Dermatology and Venereology : JEADV.* 2013;27(1):e97-104.
34. Meekings A, Utz S, Ulrich M, et al. Differentiation of Basal Cell Carcinoma Subtypes in Multi-Beam Swept Source Optical Coherence Tomography (MSS-OCT). *Journal of drugs in dermatology : JDD.* 2016;15(5):545-550.
35. Ulrich M, von Braunmuehl T, Kurzen H, et al. The sensitivity and specificity of optical coherence tomography for the assisted diagnosis of nonpigmented basal cell carcinoma: an observational study. *The British journal of dermatology.* 2015;173(2):428-435.
36. Cunha D, Richardson T, Sheth N, Orchard G, Coleman A, Mallipeddi R. Comparison of *ex vivo* optical coherence tomography with conventional frozen-section histology for visualizing basal cell carcinoma during Mohs micrographic surgery. *The British journal of dermatology.* 2011;165(3):576-580.
37. Maier T, Kulichova D, Ruzicka T, Kunte C, Berking C. *Ex vivo* high-definition optical coherence tomography of basal cell carcinoma compared to frozen-section histology in micrographic surgery: a pilot study. *Journal of the European Academy of Dermatology and Venereology : JEADV.* 2014;28(1):80-85.
38. Durkin JR, Fine JL, Sam H, Pugliano-Mauro M, Ho J. Imaging of Mohs micrographic surgery sections using full-field optical coherence tomography: a pilot study. *Dermatologic surgery : official publication for American Society for Dermatologic Surgery. [et al]* 2014;40(3):266-274.
39. Coleman AJ, Penney GP, Richardson TJ, et al. Automated registration of optical coherence tomography and dermoscopy in the assessment of sub-clinical spread in basal cell carcinoma. *Computer aided surgery : official journal of the International Society for Computer Aided Surgery.* 2014;19(1-3):1-12.
40. Wang KX, Meekings A, Fluhr JW, et al. Optical coherence tomography-based optimization of mohs micrographic surgery of Basal cell carcinoma: a pilot study. *Dermatologic surgery : official publication for American Society for Dermatologic Surgery. [et al]* 2013;39(4):627-633.
41. Pelosini L, Smith HB, Schofield JB, Meeckings A, Dhital A, Khandwala M. *In vivo* optical coherence tomography (OCT) in periocular basal cell carcinoma: correlations between *in vivo* OCT images and postoperative histology. *The British journal of ophthalmology.* 2013;97(7):890-894.
42. Iftimia N, Peterson G, Chang EW, Maguluri G, Fox W, Rajadhyaksha M. Combined reflectance confocal microscopy-optical coherence tomography for delineation of basal cell carcinoma margins: an *ex vivo* study. *Journal of biomedical optics.* 2016;21(1):16006.
43. Neville BW, Day TA. Oral cancer and precancerous lesions. *CA: a cancer journal for clinicians.* 2002;52(4):195-215.
44. Wilder-Smith P, Lee K, Guo S, et al. *In vivo* diagnosis of oral dysplasia and malignancy using optical coherence tomography: preliminary studies in 50 patients. *Lasers in surgery and medicine.* 2009;41(5):353-357.
45. Hamdoon Z, Jerjes W, McKenzie G, Jay A, Hopper C. Optical coherence tomography in the assessment of oral squamous cell carcinoma resection margins. *Photodiagnosis and photodynamic therapy.* 2016;13:211-217.
46. Leeuw FD, Casiraghi O, Lakhdar AB, Abbaci M, Laplace-Builhé C. Full-field OCT for fast diagnostic of head and neck cancer. Paper presented at: SPIE BiOS2015.
47. Jerjes W, Upile T, Conn B, et al. In vitro examination of suspicious oral lesions using optical coherence tomography. *The British journal of oral & maxillofacial surgery.* 2010;48(1):18-25.
48. Adegun OK, Tomlins PH, Hagi-Pavli E, et al. Quantitative analysis of optical coherence tomography and histopathology images of normal and dysplastic oral mucosal tissues. *Lasers in medical science.* 2012;27(4):795-804.
49. Hamdoon Z, Jerjes W, Upile T, McKenzie G, Jay A, Hopper C. Optical coherence tomography in the assessment of suspicious oral lesions: an immediate *ex vivo* study. *Photodiagnosis and photodynamic therapy.* 2013;10(1):17-27.
50. Lee CK, Chi TT, Wu CT, Tsai MT, Chiang CP, Yang CC. Diagnosis of oral precancer with optical coherence tomography. *Biomedical optics express.* 2012;3(7):1632-1646.
51. Hamdoon Z, Jerjes W, Al-Delayme R, McKenzie G, Jay A, Hopper C. Structural validation of oral mucosal tissue using optical coherence tomography. *Head & neck oncology.* 2012;4:29.
52. Tsai MT, Lee HC, Lee CK, et al. Effective indicators for diagnosis of oral cancer using optical coherence tomography. *Optics express.* 2008;16(20):15847-15862.
53. Tsai MT, Lee CK, Lee HC, et al. Differentiating oral lesions in different carcinogenesis stages with optical coherence tomography. *Journal of biomedical optics.* 2009;14(4):044028.
54. Andolfi M, Potenza R, Capozzi R, Liparulo V, Puma F, Yasufuku K. The role of bronchoscopy in the diagnosis of early lung cancer: a review. *Journal of thoracic disease.* 2016;8(11):3329-3337.
55. Lam S, Standish B, Baldwin C, et al. *In vivo* optical coherence tomography imaging of preinvasive bronchial lesions. *Clinical cancer research : an official journal of the American Association for Cancer Research.* 2008;14(7):2006-2011.
56. Michel RG, Kinasewitz GT, Fung KM, Keddissi JI. Optical coherence tomography as an adjunct to flexible bronchoscopy in the diagnosis of lung cancer: a pilot study. *Chest.* 2010;138(4):984-988.
57. Whiteman SC, Yang Y, Gey van Pittius D, Stephens M, Parmer J, Spiteri MA. Optical coherence tomography: real-time imaging of bronchial airways microstructure and detection of inflammatory/neoplastic morphologic changes. *Clinical cancer research : an official journal of the American Association for Cancer Research.* 2006;12(3 Pt 1):813-818.
58. Hariri LP, Mino-Kenudson M, Lanuti M, Miller AJ, Mark EJ, Suter MJ. Diagnosing lung carcinomas with optical coherence tomography. *Annals of the American Thoracic Society.* 2015;12(2):193-201.
59. Jain M, Narula N, Salamoon B, et al. Full-field optical coherence tomography for the analysis of fresh unstained human lobectomy specimens. *Journal of pathology informatics.* 2013;4:26.
60. Siegel RL, Miller KD, Jemal A. Cancer statistics, 2018. *CA: a*

cancer journal for clinicians. 2018;68(1):7-30.
61. Pleijhuis RG, Graafland M, de Vries J, Bart J, de Jong JS, van Dam GM. Obtaining adequate surgical margins in breast-conserving therapy for patients with early-stage breast cancer: current modalities and future directions. *Annals of surgical oncology.* 2009;16(10):2717-2730.
62. Lyman GH, Giuliano AE, Somerfield MR, et al. American Society of Clinical Oncology guideline recommendations for sentinel lymph node biopsy in early-stage breast cancer. *Journal of clinical oncology : official journal of the American Society of Clinical Oncology.* 2005;23(30):7703-7720.
63. Assayag O, Antoine M, Sigal-Zafrani B, et al. Large field, high resolution full-field optical coherence tomography: a pre-clinical study of human breast tissue and cancer assessment. *Technology in cancer research & treatment.* 2014;13(5):455-468.
64. Zhou C, Cohen DW, Wang Y, et al. Integrated optical coherence tomography and microscopy for *ex vivo* multiscale evaluation of human breast tissues. *Cancer research.* 2010;70(24):10071-10079.
65. Yao X, Gan Y, Chang E, Hibshoosh H, Feldman S, Hendon C. Visualization and tissue classification of human breast cancer images using ultrahigh-resolution OCT. *Lasers in surgery and medicine.* 2017;49(3):258-269.
66. Nguyen FT, Zysk AM, Chaney EJ, et al. Intraoperative evaluation of breast tumor margins with optical coherence tomography. *Cancer research.* 2009;69(22):8790-8796.
67. Curatolo A, McLaughlin RA, Quirk BC, et al. Ultrasound-guided optical coherence tomography needle probe for the assessment of breast cancer tumor margins. *AJR American journal of roentgenology.* 2012;199(4):W520-522.
68. Patel R, Khan A, Kamionek M, Kandil D, Quinlan R, Yaroslavsky AN. Delineating breast ductal carcinoma using combined dye-enhanced wide-field polarization imaging and optical coherence tomography. *Journal of biophotonics.* 2013;6(9):679-686.
69. Zysk AM, Chen K, Gabrielson E, et al. Intraoperative Assessment of Final Margins with a Handheld Optical Imaging Probe During Breast-Conserving Surgery May Reduce the Reoperation Rate: Results of a Multicenter Study. *Annals of surgical oncology.* 2015;22(10):3356-3362.
70. Erickson-Bhatt SJ, Nolan RM, Shemonski ND, et al. Real-time Imaging of the Resection Bed Using a Handheld Probe to Reduce Incidence of Microscopic Positive Margins in Cancer Surgery. *Cancer research.* 2015;75(18):3706-3712.
71. Nguyen FT, Zysk AM, Chaney EJ, et al. Optical coherence tomography: the intraoperative assessment of lymph nodes in breast cancer. *IEEE engineering in medicine and biology magazine : the quarterly magazine of the Engineering in Medicine & Biology Society.* 2010;29(2):63-70.
72. McLaughlin RA, Scolaro L, Robbins P, Hamza S, Saunders C, Sampson DD. Imaging of human lymph nodes using optical coherence tomography: potential for staging cancer. *Cancer research.* 2010;70(7):2579-2584.
73. Nolan RM, Adie SG, Marjanovic M, et al. Intraoperative optical coherence tomography for assessing human lymph nodes for metastatic cancer. *BMC cancer.* 2016;16:144.
74. Scolaro L, McLaughlin RA, Klyen BR, et al. Parametric imaging of the local attenuation coefficient in human axillary lymph nodes assessed using optical coherence tomography. *Biomedical optics express.* 2012;3(2):366-379.
75. Grieve K, Mouslim K, Assayag O, et al. Assessment of Sentinel Node Biopsies With Full-Field Optical Coherence Tomography. *Technology in cancer research & treatment.* 2016;15(2):266-274.
76. Burnett AS, Calvert TJ, Chokshi RJ. Sensitivity of endoscopic retrograde cholangiopancreatography standard cytology: 10-y review of the literature. *The Journal of surgical research.* 2013;184(1):304-311.
77. Chen J, Yang R, Lu Y, Xia Y, Zhou H. Diagnostic accuracy of endoscopic ultrasound-guided fine-needle aspiration for solid pancreatic lesion: a systematic review. *Journal of cancer research and clinical oncology.* 2012;138(9):1433-1441.
78. Are C, Gonen M, Zazzali K, et al. The impact of margins on outcome after hepatic resection for colorectal metastasis. *Annals of surgery.* 2007;246(2):295-300.
79. Verbeke CS, Menon KV. Redefining resection margin status in pancreatic cancer. *HPB : the official journal of the International Hepato Pancreato Biliary Association.* 2009;11(4):282-289.
80. Testoni PA, Mangiavillano B, Albarello L, et al. Optical coherence tomography to detect epithelial lesions of the main pancreatic duct: an *Ex vivo* study. *The American journal of gastroenterology.* 2005;100(12):2777-2783.
81. Testoni PA, Mariani A, Mangiavillano B, et al. Main pancreatic duct, common bile duct and sphincter of Oddi structure visualized by optical coherence tomography: An *ex vivo* study compared with histology. *Digestive and liver disease : official journal of the Italian Society of Gastroenterology and the Italian Association for the Study of the Liver.* 2006;38(6):409-414.
82. Testoni PA, Mariani A, Mangiavillano B, Arcidiacono PG, Di Pietro S, Masci E. Intraductal optical coherence tomography for investigating main pancreatic duct strictures. *The American journal of gastroenterology.* 2007;102(2):269-274.
83. Testoni PA, Mariani A, Mangiavillano B, Arcidiacono PG, Masci E. Preliminary data on the use of intraductal optical coherence tomography during ERCP for investigating main pancreatic duct strictures. *Gut.* 2006;55(11):1680-1681.
84. Arvanitakis M, Hookey L, Tessier G, et al. Intraductal optical coherence tomography during endoscopic retrograde cholangiopancreatography for investigation of biliary strictures. *Endoscopy.* 2009;41(8):696-701.
85. Grieve K, Palazzo L, Dalimier E, Vielh P, Fabre M. A feasibility study of full-field optical coherence tomography for rapid evaluation of EUS-guided microbiopsy specimens. *Gastrointestinal endoscopy.* 2015;81(2):342-350.
86. Iftimia N, Cizginer S, Deshpande V, et al. Differentiation of pancreatic cysts with optical coherence tomography (OCT) imaging: an *ex vivo* pilot study. *Biomedical optics express.* 2011;2(8):2372-2382.
87. van Manen L, Stegehuis PL, Farina-Sarasqueta A, et al. Validation of full-field optical coherence tomography in distinguishing malignant and benign tissue in resected pancreatic cancer specimens. *PloS one.* 2017;12(4):e0175862.
88. Zhu Y, Gao W, Zhou Y, Guo Y, Guo F, He Y. Rapid and high-resolution imaging of human liver specimens by full-field optical coherence tomography. *Journal of biomedical optics.* 2015;20(11):116010.
89. Pennathur A, Gibson MK, Jobe BA, Luketich JD. Oesophageal carcinoma. *Lancet (London, England).* 2013;381(9864):400-412.
90. Falk GW, Rice TW, Goldblum JR, Richter JE. Jumbo biopsy forceps protocol still misses unsuspected cancer in Barrett's esophagus with high-grade dysplasia. *Gastrointestinal endoscopy.* 1999;49(2):170-176.
91. Bouma BE, Tearney GJ, Compton CC, Nishioka NS. High-resolution imaging of the human esophagus and stomach *in vivo* using optical coherence tomography. *Gastrointestinal endoscopy.* 2000;51(4 Pt 1):467-474.

92. Jackle S, Gladkova N, Feldchtein F, et al. *In vivo* endoscopic optical coherence tomography of the human gastrointestinal tract--toward optical biopsy. *Endoscopy.* 2000;32(10):743-749.
93. Hatta W, Uno K, Koike T, et al. Optical coherence tomography for the staging of tumor infiltration in superficial esophageal squamous cell carcinoma. *Gastrointestinal endoscopy.* 2010;71(6):899-906.
94. Li XD, Boppart SA, Van Dam J, et al. Optical coherence tomography: advanced technology for the endoscopic imaging of Barrett's esophagus. *Endoscopy.* 2000;32(12):921-930.
95. Chen Y, Aguirre AD, Hsiung PL, et al. Ultrahigh resolution optical coherence tomography of Barrett's esophagus: preliminary descriptive clinical study correlating images with histology. *Endoscopy.* 2007;39(7):599-605.
96. Cobb MJ, Hwang JH, Upton MP, et al. Imaging of subsquamous Barrett's epithelium with ultrahigh-resolution optical coherence tomography: a histologic correlation study. *Gastrointestinal endoscopy.* 2010;71(2):223-230.
97. Poneros JM, Brand S, Bouma BE, Tearney GJ, Compton CC, Nishioka NS. Diagnosis of specialized intestinal metaplasia by optical coherence tomography. *Gastroenterology.* 2001;120(1):7-12.
98. Swager AF, Boerwinkel DF, de Bruin DM, et al. Detection of buried Barrett's glands after radiofrequency ablation with volumetric laser endomicroscopy. *Gastrointestinal endoscopy.* 2016;83(1):80-88.
99. Evans JA, Bouma BE, Bressner J, et al. Identifying intestinal metaplasia at the squamocolumnar junction by using optical coherence tomography. *Gastrointestinal endoscopy.* 2007;65(1):50-56.
100. Isenberg G, Sivak MV, Jr., Chak A, et al. Accuracy of endoscopic optical coherence tomography in the detection of dysplasia in Barrett's esophagus: a prospective, double-blinded study. *Gastrointestinal endoscopy.* 2005;62(6):825-831.
101. Evans JA, Poneros JM, Bouma BE, et al. Optical coherence tomography to identify intramucosal carcinoma and high-grade dysplasia in Barrett's esophagus. *Clinical gastroenterology and hepatology : the official clinical practice journal of the American Gastroenterological Association.* 2006;4(1):38-43.
102. Zuccaro G, Gladkova N, Vargo J, et al. Optical coherence tomography of the esophagus and proximal stomach in health and disease. *The American journal of gastroenterology.* 2001;96(9):2633-2639.
103. Hatta W, Uno K, Koike T, et al. A prospective comparative study of optical coherence tomography and EUS for tumor staging of superficial esophageal squamous cell carcinoma. *Gastrointestinal endoscopy.* 2012;76(3):548-555.
104. Ali M, Yaqub M, Haider Z, Anees I, Bhargava S, Gian J. Yield of dual endoscopy for positive fecal occult blood test. *The American journal of gastroenterology.* 2003;98(1):82-85.
105. Tearney GJ, Brezinski ME, Southern JF, Bouma BE, Boppart SA, Fujimoto JG. Optical biopsy in human gastrointestinal tissue using optical coherence tomography. *The American journal of gastroenterology.* 1997;92(10):1800-1804.
106. Westphal V, Rollins AM, Willis J, Sivak MV, Izatt JA. Correlation of endoscopic optical coherence tomography with histology in the lower-GI tract. *Gastrointestinal endoscopy.* 2005;61(4):537-546.
107. Pfau PR, Sivak MV, Jr., Chak A, et al. Criteria for the diagnosis of dysplasia by endoscopic optical coherence tomography. *Gastrointestinal endoscopy.* 2003;58(2):196-202.
108. Ashok PC, Praveen BB, Bellini N, Riches A, Dholakia K, Herrington CS. Multi-modal approach using Raman spectroscopy and optical coherence tomography for the discrimination of colonic adenocarcinoma from normal colon. *Biomedical optics express.* 2013;4(10):2179-2186.
109. Zhang QQ, Wu XJ, Tang T, et al. Quantitative analysis of rectal cancer by spectral domain optical coherence tomography. *Physics in medicine and biology.* 2012;57(16):5235-5244.
110. D'Amico AV, Weinstein M, Li X, Richie JP, Fujimoto J. Optical coherence tomography as a method for identifying benign and malignant microscopic structures in the prostate gland. *Urology.* 2000;55(5):783-787.
111. Dangle PP, Shah KK, Kaffenberger B, Patel VR. The use of high resolution optical coherence tomography to evaluate robotic radical prostatectomy specimens. *International braz j urol : official journal of the Brazilian Society of Urology.* 2009;35(3):344-353.
112. Lopater J, Colin P, Beuvon F, et al. Real-time cancer diagnosis during prostate biopsy: *ex vivo* evaluation of full-field optical coherence tomography (FFOCT) imaging on biopsy cores. *World journal of urology.* 2016;34(2):237-243.
113. Muller BG, de Bruin DM, Brandt MJ, et al. Prostate cancer diagnosis by optical coherence tomography: First results from a needle based optical platform for tissue sampling. *Journal of biophotonics.* 2016;9(5):490-498.
114. Muller BG, Swaan A, de Bruin DM, et al. Customized Tool for the Validation of Optical Coherence Tomography in Differentiation of Prostate Cancer. *Technology in cancer research & treatment.* 2017;16(1):57-65.
115. Linehan JA, Bracamonte ER, Hariri LP, et al. Feasibility of optical coherence tomography imaging to characterize renal neoplasms: limitations in resolution and depth of penetration. *BJU international.* 2011;108(11):1820-1824.
116. Lee HC, Zhou C, Cohen DW, et al. Integrated optical coherence tomography and optical coherence microscopy imaging of *ex vivo* human renal tissues. *The Journal of urology.* 2012;187(2):691-699.
117. Barwari K, de Bruin DM, Faber DJ, van Leeuwen TG, de la Rosette JJ, Laguna MP. Differentiation between normal renal tissue and renal tumours using functional optical coherence tomography: a phase I *in vivo* human study. *BJU international.* 2012;110(8 Pt B):E415-420.
118. Wagstaff PG, Ingels A, de Bruin DM, et al. Percutaneous Needle Based Optical Coherence Tomography for the Differentiation of Renal Masses: a Pilot Cohort. *The Journal of urology.* 2016;195(5):1578-1585.
119. Barwari K, de Bruin DM, Cauberg EC, et al. Advanced diagnostics in renal mass using optical coherence tomography: a preliminary report. *Journal of endourology.* 2011;25(2):311-315.
120. Jain M, Robinson BD, Salamoon B, Thouvenin O, Boccara C, Mukherjee S. Rapid evaluation of fresh *ex vivo* kidney tissue with full-field optical coherence tomography. *Journal of pathology informatics.* 2015;6:53.
121. Montagne P, Ducesne I, Anract J, et al. Quality control and primo-diagnosis of transurethral bladder resections with full-field OCT. Paper presented at: SPIE BiOS2017.
122. Manyak MJ, Gladkova ND, Makari JH, et al. Evaluation of superficial bladder transitional-cell carcinoma by optical coherence tomography. *Journal of endourology.* 2005;19(5):570-574.
123. Goh AC, Tresser NJ, Shen SS, Lerner SP. Optical coherence tomography as an adjunct to white light cystoscopy for intravesical real-time imaging and staging of bladder cancer. *Urology.* 2008;72(1):133-137.

124. Gladkova N, Streltsova O, Zagaynova E, et al. Cross-polarization optical coherence tomography for early bladder-cancer detection: statistical study. *Journal of biophotonics.* 2011;4(7-8):519-532.
125. Karl A, Stepp H, Willmann E, et al. Optical coherence tomography for bladder cancer -- ready as a surrogate for optical biopsy? Results of a prospective mono-centre study. *European journal of medical research.* 2010;15(3):131-134.
126. Ren H, Waltzer WC, Bhalla R, et al. Diagnosis of bladder cancer with microelectromechanical systems-based cystoscopic optical coherence tomography. *Urology.* 2009;74(6):1351-1357.
127. Hermes B, Spoler F, Naami A, et al. Visualization of the basement membrane zone of the bladder by optical coherence tomography: feasibility of noninvasive evaluation of tumor invasion. *Urology.* 2008;72(3):677-681.
128. Yang Y, Biswal NC, Wang T, et al. Potential role of a hybrid intraoperative probe based on OCT and positron detection for ovarian cancer detection and characterization. *Biomedical optics express.* 2011;2(7):1918-1930.
129. Peters IT, Stegehuis PL, Peek R, et al. Noninvasive Detection of Metastases and Follicle Density in Ovarian Tissue Using Full-Field Optical Coherence Tomography. *Clinical cancer research : an official journal of the American Association for Cancer Research.* 2016;22(22):5506-5513.
130. Yang Y, Wang T, Brewer M, Zhu Q. Quantitative analysis of angle-resolved scattering properties of ovarian tissue using optical coherence tomography. *Journal of biomedical optics.* 2012;17(9):90503-90501.
131. Yang Y, Wang T, Biswal NC, et al. Optical scattering coefficient estimated by optical coherence tomography correlates with collagen content in ovarian tissue. *Journal of biomedical optics.* 2011;16(9):090504.
132. St-Pierre C, Madore WJ, De Montigny E, et al. Dimension reduction technique using a multilayered descriptor for high-precision classification of ovarian cancer tissue using optical coherence tomography: a feasibility study. *Journal of medical imaging (Bellingham, Wash).* 2017;4(4):041306.
133. Nandy S, Sanders M, Zhu Q. Classification and analysis of human ovarian tissue using full field optical coherence tomography. *Biomedical optics express.* 2016;7(12):5182-5187.
134. Boppart SA, Goodman A, Libus J, et al. High resolution imaging of endometriosis and ovarian carcinoma with optical coherence tomography: feasibility for laparoscopic-based imaging. *British journal of obstetrics and gynaecology.* 1999;106(10):1071-1077.
135. Hariri LP, Bonnema GT, Schmidt K, et al. Laparoscopic optical coherence tomography imaging of human ovarian cancer. *Gynecologic oncology.* 2009;114(2):188-194.
136. Marvdashti T, Duan L, Aasi SZ, Tang JY, Ellerbee Bowden AK. Classification of basal cell carcinoma in human skin using machine learning and quantitative features captured by polarization sensitive optical coherence tomography. *Biomedical optics express.* 2016;7(9):3721-3735.
137. Liu S, Sotomi Y, Eggermont J, et al. Tissue characterization with depth-resolved attenuation coefficient and backscatter term in intravascular optical coherence tomography images. *Journal of biomedical optics.* 2017;22(9):1-16.
138. Davis AT, Palmer AL, Pani S, Nisbet A. Assessment of the variation in CT scanner performance (image quality and Hounsfield units) with scan parameters, for image optimisation in radiotherapy treatment planning. *Physica medica : PM : an international journal devoted to the applications of physics to medicine and biology : official journal of the Italian Association of Biomedical Physics (AIFB).* 2018;45:59-64.
139. Apelian C, Harms F, Thouvenin O, Boccara AC. Dynamic full field optical coherence tomography: subcellular metabolic contrast revealed in tissues by interferometric signals temporal analysis. *Biomedical optics express.* 2016;7(4):1511-1524.
140. Benoit a la Guillaume E, Martins F, Boccara C, Harms F. High-resolution handheld rigid endomicroscope based on full-field optical coherence tomography. *Journal of biomedical optics.* 2016;21(2):26005.
141. Drifka CR, Tod J, Loeffler AG, et al. Periductal stromal collagen topology of pancreatic ductal adenocarcinoma differs from that of normal and chronic pancreatitis. *Modern pathology : an official journal of the United States and Canadian Academy of Pathology, Inc.* 2015;28(11):1470-1480.
142. Bredfeldt JS, Liu Y, Conklin MW, Keely PJ, Mackie TR, Eliceiri KW. Automated quantification of aligned collagen for human breast carcinoma prognosis. *Journal of pathology informatics.* 2014;5(1):28.
143. Hariri LP, Villiger M, Applegate MB, et al. Seeing beyond the bronchoscope to increase the diagnostic yield of bronchoscopic biopsy. *American journal of respiratory and critical care medicine.* 2013;187(2):125-129.
144. Kiseleva E, Kirillin M, Feldchtein F, et al. Differential diagnosis of human bladder mucosa pathologies *in vivo* with cross-polarization optical coherence tomography. *Biomedical optics express.* 2015;6(4):1464-1476.
145. Mavadia J, Xi J, Chen Y, Li X. An all-fiber-optic endoscopy platform for simultaneous OCT and fluorescence imaging. *Biomedical optics express.* 2012;3(11):2851-2859.
146. Welge WA, Barton JK. *In vivo* endoscopic Doppler optical coherence tomography imaging of the colon. *Lasers in surgery and medicine.* 2017;49(3):249-257.
147. Lorenser D, Quirk BC, Auger M, et al. Dual-modality needle probe for combined fluorescence imaging and three-dimensional optical coherence tomography. *Optics letters.* 2013;38(3):266-268.
148. Gora MJ, Sauk JS, Carruth RW, et al. Tethered capsule endomicroscopy enables less invasive imaging of gastrointestinal tract microstructure. *Nature medicine.* 2013;19(2):238-240.
149. Liang K, Ahsen OO, Lee HC, et al. Volumetric Mapping of Barrett's Esophagus and Dysplasia With en face Optical Coherence Tomography Tethered Capsule. *The American journal of gastroenterology.* 2016;111(11):1664-1666.

Chapter 9

Validation of full-field optical coherence tomography in distinguishing malignant and benign tissue in resected pancreatic cancer specimens

L. van Manen, P.L. Stegehuis, A. Fariña-Sarasqueta, L.M. de Haan, J. Eggermont, B.A. Bonsing, H. Morreau, B.P.F. Lelieveldt, C.J.H. van de Velde, A.L. Vahrmeijer, J. Dijkstra, J.S.D. Mieog

PLoS One. 2017 Apr 17;12(4).

Abstract

Background

Pancreatic cancer is the fourth leading cause of cancer-related mortality in the United States. The minority of patients can undergo curative-intended surgical therapy due to progressive disease stage at time of diagnosis. Nonetheless, tumor involvement of surgical margins is seen in up to 70% of resections, being a strong negative prognostic factor. Real-time intraoperative imaging modalities may aid surgeons to obtain tumor-free resection margins. Full-field optical coherence tomography (FF-OCT) is a promising diagnostic tool using high-resolution white-light interference microscopy without tissue processing. Therefore, we composed an atlas of FF-OCT images of malignant and benign pancreatic tissue, and investigated the accuracy with which the pathologists could distinguish these.

Materials and Methods

One hundred FF-OCT images were collected from specimens of 29 patients who underwent pancreatic resection for various indications between 2014 and 2016. One experienced gastrointestinal pathologist and one pathologist in training scored independently the FF-OCT images as malignant or benign blinded to the final pathology conclusion. Results were compared to those obtained with standard hematoxylin and eosin (H&E) slides.

Results

Overall, combined test characteristics of both pathologists showed a sensitivity of 72%, specificity of 74%, positive predictive value of 69%, negative predictive value of 79% and an overall accuracy of 73%. In the subset of pancreatic ductal adenocarcinoma patients, 97% of the FF-OCT images (n=35) were interpreted as tumor by at least one pathologist. Moreover, normal pancreatic tissue was recognised in all cases by at least one pathologist. However, atrophy and fibrosis, serous cystadenoma and neuroendocrine tumors were more often wrongly scored, in 63%, 100% and 25% respectively.

Conclusion

FF-OCT could distinguish normal pancreatic tissue from pathologic pancreatic tissue in both processed as non-processed specimens using architectural features. The accuracy in pancreatic ductal adenocarcinoma is promising and warrants further evaluation using improved assessment criteria.

Introduction

Pancreatic cancer is the fourth leading cause of cancer related deaths with a 5-year survival rate of 8% in the United States.[1] Many patients present with locally advanced or metastasized disease and are beyond cure. Patients diagnosed with localized disease can undergo a potentially curable treatment and have a 5-year survival rate around 20%.[2-4] Treatment consists of high-risk surgery (morbidity of 40-50% and mortality around 5% [5,6]) usually followed or preceded by chemo(radio) therapy. During surgery, it is important to achieve a complete (R0) resection, as a distance of the tumor from the resection margin of ≤1 mm (R1 resection) is one of the most important prognosticators for poor survival in Europe.[2,7-9] However, adequate intraoperative judgment is challenging, because the surgeon has to rely on visual inspection and palpation only. The presence of peritumoral inflammation in pancreatic cancer makes the distinction with normal tissue even more difficult. The incidence of R1 resections is up to 60-80% in published series of standardized pathological assessment [8-13], underlining the importance of adequate intraoperative resection margin assessment.

Although various imaging modalities (such as CT, MRI, EUS and PET) are used to diagnose pancreatic cancer and assess its resectability prior to surgery, only few techniques are suitable during surgery.[14] Frozen section analysis is currently the most used intraoperative modality, especially to assess extra-pancreatic lesions.[15] However, it has low sensitivity (38%) evaluating resection margins, and is therefore only used in selected cases at our institution.[15] Intraoperative ultrasound can be used to detect metastases or assess resectability, but its value in reducing positive resection margins is unknown [14] and is the study object of an ongoing clinical trial at our institution. An emerging technique is near-infrared fluorescence imaging, which is based on a fluorescent tracer and dedicated cameras. Pre-clinical results demarcating pancreatic tumor are promising, but use tracers that are currently not yet FDA approved.[16] Thus, the current state-of-the art surgical approach encompasses high-risk intervention with limited success and little to no intraoperative visualisation of the malignant process. Novel intraoperative imaging tools are needed to improve the assessment of resectability and to guide subsequent resection.

Optical coherence tomography (OCT) was first described in 1991 and uses low-coherence interferometry to produce 2-dimensional cross-sectional images.[17] It is already standard-of-care in ophthalmology and cardiology, and with the development of new OCT modalities, other fields of interest – like oncology – are being discovered.[18] Full-field OCT (FF-OCT) is such a newly developed modality, based on the principles of white light interference microscopy, and acquires en face images by illuminating the whole field of view without scanning.[19] It enables non-invasive high-resolution imaging up to several millimetres of tissue without the need for tissue processing, by measuring the backscattered light of tissue structures with different refractive indices. Several studies report the use of FF-OCT in the field of oncology, i.e. on ovarian [20], skin [21] and brain tissue.[22] All showed encouraging results; architectural changes could be identified, and in a quick fashion a large surface could be scanned. Only one study has been conducted in pancreatic cancer, but this was to evaluate fine needle aspirates.[23] FF-OCT has not yet been tested in pancreas resection specimens to discriminate malignant and benign tissues.

In this feasibility study, we investigated whether pathologists were able to distinguish malignant from normal and benign pancreatic tissue based on FF-OCT images, obtained from surgical specimens.

Materials and methods

Patient and sample selection

Twenty-nine patients who underwent surgery for suspect pancreatic cancer at the Leiden University Medical Center (LUMC) were included in this study. Fresh tissue samples were collected prospectively (October 2015 until January 2016) from surgical specimens from 17 patients with (pre)malignant pancreatic lesions. Formalin-fixed paraffin embedded (FFPE) samples from 12 patients were collected retrospectively (January 2014 until December 2014) from both benign and malignant pancreatic neoplasms to acquire FF-OCT images of different pancreatic neoplasms. No patients with a preoperative diagnosis of benign disease were included, for instance, patients with chronic or auto-immune pancreatitis were not included. From each of the 29 patients, if achievable, minimal one tissue section with presence of tumor and one tissue section without tumor were obtained. For the fresh samples, the selection was based on the macroscopic assessment by the pathologist; for FFPE samples, the selection was based on microscopic assessment. This resulted in 50 tissue samples (25 fresh samples and 25 FFPE samples). Per tissue sample, two regions of interest were selected by the study coordinator, LvM, based on the corresponding H&E slides. These two regions of interest from a single tissue sections could be either both benign, both malignant or one malignant and one benign.

FFPE tissue blocks were deparaffinised, using a standard protocol. The study protocol was approved by the local medical ethics committee of the LUMC. The prospective collection of the fresh tissue samples was performed within the framework of routine clinical care. Therefore patient consent was not obtained, as this study was not subject to the Dutch Medical Research Involving Human Subjects Act, according to our local medical ethics committee. One author (LvM) had access to patient information during clinical data acquisition after which patient data were anonymized. All patient samples and clinical data were handled in accordance with the medical ethics guidelines described in the Code of Conduct for the Proper Secondary Use of Human Tissue of the Dutch Federation of Biomedical Scientific Societies.[24]

FF-OCT imaging and sample processing

Images were obtained using a high resolution FF-OCT system (Light-CT™ scanner, LLTech SAS, Paris, France). In short, the setup consists of an upright microscope with a 10x objective, a halogen light-source with wavelength of 700±125 nm, and a reference arm in Linnik interferometric configuration.[25,26] It generates high resolution (1.5 µm isotropic), 0.8 by 0.8 mm en face images, but the field of view is increased using image mosaicking (with a maximum diameter of 25 mm), at an image rate of 35 Hz. Image depth is adjustable, with a maximum depth of several millimeters, depending on tissue properties.[27]

Tissue samples were placed in a sample holder in 0.9% NaCl solution with the surface to be imaged facing upward. A glass slide was positioned above the tissue to which it was gently flattened, and

a layer of silicone oil was applied between the optical window and the microscope objective. A macroscopic image was obtained using a wide-field camera, followed by FF-OCT images. To ensure good correspondence with the histology images, FF-OCT images were acquired at a depth of around 20 µm. Imaging time for one sample was on average 30 minutes. After FF-OCT imaging, tissue samples were formalin fixed and embedded in paraffin. H&E slides were obtained and digitalised with a digital pathology slide scanner (IntelliSite Ultra Fast Scanner, Philips, Eindhoven, the Netherlands). FF-OCT images were viewed using in-house developed analysis software based on MeVisLab (MeVis Medical Solutions AG and Fraunhofer MEVIS, Germany).

Study design

Two pathologists – one experienced and one resident – followed a brief training prior to assessment of the FF-OCT images. The training was divided in two parts: in the first part the technique and method of tissue imaging were explained, and in the second part FF-OCT images were shown with their corresponding H&E images. The images of this training atlas were magnified regions of interest showing details of the different pancreatic tissues (such as normal pancreas, pancreatitis and pancreatic ductal adenocarcinoma (PDAC)); the whole slide was not presented to the pathologists. Moreover, the regions of interest used in the training atlas were different in the test cohort.

The 100 regions of interest to be assessed by the pathologists were shown in the context of both the total FF-OCT image, and an enlarged (detail) image. They were offered to the pathologists in both the original and inverse setting, as shown in Figure 1. During assessment pathologists were able to digitally zoom the images. FF-OCT images were randomly presented in the same order to the pathologists who were blinded to the H&E slides, patient information and final pathological diagnosis of the specimen. The pathologists had to classify the marked region-of-interest as malignant or benign. If the pathologists found that the image quality was too poor to reach a decision, it was classified as not interpretable.

Statistical analysis

The results of the individual region-of-interest scores were put in a 2x2 contingency table to calculate sensitivity, specificity, positive predictive value (PPV), negative predictive value (NPV) and accuracy for the complete cohort. In addition, diagnostic test characteristics and the interobserver variability were calculated after each cohort of 25 consecutive FF-OCT images. SPSS version 23 (IBM Corporation, Armonk, NY, USA) was used to calculate the interobserver variability and to compare the agreement in tumor identification by both pathologists, for which chi-squared tests were used. Kappa values were interpreted as described by Landis et Koch.[28] $P<0.05$ was considered statistical significant. Graphs were created using Graphpad version 7 (Graphpad Software, La Jolla, CA, USA).

Results

In FF-OCT images of normal pancreatic tissue, the morphologic features of major components could be identified, like interlobular septae, acinar tissue, islet cells, pancreatic ducts and blood vessels (Figure 2). Recognition of nerve bundles in normal pancreatic tissue was difficult (Figure 2).

Interlobular septae are visible as light grey strands which are located between the lobuli. Islet cells were recognised as highlighted groups of cells located in acinar tissue.

Histomorphology of pancreatic cancer in general and especially of PDAC is complex, being sometimes challenging to distinguish between malignant and reactive, benign glands in the context of pancreatitis even on H&E images. On H&E images various criteria are used to distinguish between benign and malignant tissue. First of all, the pathologists look at low magnification level to detect the presence of normal pancreatic architecture. Desmoplastic stroma, irregular ducts and disorganised glands are characteristics that indicate potential malignancy. Atypical cell nuclei, intraluminal necrosis, perineural invasion and ingrowth into structures as lymph nodes, blood vessels and fat tissue are all characteristics that point toward malignancy. If the lobular structure is maintained even in the presence of irregular ducts with some cytonuclear atypia, pancreatitis should be considered. However, the difficulty resides in the fact that these essential features for the diagnostic on H&E slides are regularly not evaluable on the FF-OCT images. As shown in Table 1, only stroma and architectural distortion of pancreatic tissue and tumor glands are easily recognizable on FF-OCT images.

Scoring FF-OCT images

Fifty samples from 29 patients have been included in this study. Patient and tumor characteristics are presented in Table 2. Of these tissue samples, 100 FF-OCT images were available for assessment: 57 benign and 43 malignant sections. The results of the FF-OCT assessment by the pathologists are detailed in Table 3. The more experienced gastrointestinal pathologist scored 6 images as not interpretable, the pathologist in training none. Of these 6 images – 3 fresh and 3 deparaffinised FFPE – 3 were benign and 3 were malignant. These images were scored by the pathologist in training; 3 images were scored correctly, and 3 images were scored incorrectly. Leaving these 6 images out of the analysis, the experienced pathologist achieved a higher accuracy than the less experienced pathologist: 80% versus 67%, respectively. The combined results showed the following test characteristics: sensitivity of 72%, specificity of 74%, PPV of 67%, NPV of 79% and an accuracy of 73%.

A more detailed overview of the scores per histologic type is provided in Table 4. Normal pancreatic parenchyma was correctly recognised by both pathologists in 32 of the 40 cases. Atrophy and fibrosis (Figure 3) were wrongly scored by both pathologists in 63%, serous cystadenoma in 100% and neuroendocrine tumors in 25% of the cases. Pathologists evaluated 35 FF-OCT images of a PDAC (Figure 4), of which 34 were correctly scored as malignant by at least one pathologist. Well (grade 1) and moderately (grade 2) differentiated PDAC were scored as malignant by both pathologists in 67% and 57% of cases, respectively (Table 4). Whereas, poorly differentiated (grade 3) PDAC was scored as malignant by both pathologist in 1 out of 8 cases (13%).

The first 50 FF-OCT images given to the pathologists were taken from deparaffinised FFPE pancreatic tissue specimens, whereas the others were taken from fresh specimens. Univariate analysis showed no significant difference (P=0.24) in evaluating fresh or deparaffinised FFPE FF-OCT images, however, fresh FF-OCT images appear to provide a more detailed view and improved visualization of tumor stroma.

Interobserver variability

The overall interobserver variability (Kappa) was calculated and there was a fair agreement between the pathologists (Kappa: 0,33). After presentation of each set of 25 consecutive FF-OCT images the interobserver variability was measured and an increase of 0.1 to 0.5 was observed, as shown in Figure 5.

Discussion

In this study we investigated whether pathologists were able to distinguish malignant from benign pancreatic tissue based on FF-OCT images. We found that normal, healthy pancreatic tissue could be distinguished from malignant tissue very well due to the characteristic architecture of normal pancreatic parenchyma. Distinguishing other benign tissue types like chronic pancreatitis was harder. We also found that the experienced pathologist was better in assessing the FF-OCT images than the pathologist in training. To our knowledge this is the first study to evaluate the correlation between H&E slides and FF-OCT in detecting malignancies in fixated and fresh pancreatic resection specimens. The diagnostic accuracy of 73% obtained in this study is not yet adequate, but we believe this can be improved upon by taking several measures: using other contrast mechanisms, improving knowledge on collagen topology, and more extensive training.

Pancreatic pathology and in particular morphological differentiation between pancreatic ductal adenocarcinoma and pancreatitis is challenging even on H&E slides. On FF-OCT this differentiation is difficult as well; although FF-OCT provides high resolution, the endogenous contrast is not proficient to see cell nuclei. Techniques to reveal subcellular metabolic contrast are being developed, showing encouraging results.[30] Other contrast mechanisms can provide additional information and thereby increase diagnostic accuracy.

Secondly, improved knowledge on the collagen topology could increase the diagnostic accuracy. As collagen reflects light very well, tumor stroma is evidently visible on FF-OCT images. The pathologists mostly evaluated the FF-OCT images based on these architectural features. However in this study, both pathologists often misdiagnosed pancreatic atrophy and fibrosis as malignant. In these cases the presence of collagen fibers dominating the image could be mistaken for tumor stroma as PDAC is characterized by extensive and disorganized desmoplastic stroma.[31] Recently it was shown that its collagen topology differs significantly from that of pancreatitis.[32] Improved knowledge on the collagen topology of these benign conditions, and possibilities to detect these differences and correlation between stromal alignment and organization, and diagnosis, could increase the diagnostic accuracy. This feature could also be exploited in the future by automated detection of collagen characteristics, as was previously done for second harmonic generation images of breast cancer.[33]

Our study consisted of two parts: 50 image regions of deparaffinised tissue and 50 image regions of fresh tissue shown to the pathologists in that order. In tissue imaged both fresh and deparaffinised we see that the intensity of collagen is higher in fresh tissue (Supplementary Figure 1). We did not

find significant differences in the assessment between these parts. However, an increase in accuracy was shown for both pathologists in the second half (images 26-50 and 76-100) of each part, suggesting a learning curve. Another study on FF-OCT where they looked at prostate biopsies showed an overall accuracy of 70%, with a learning curve from 60% to 80% after evaluation of 119 images; this is concordant with our data.[34] A later study on FF-OCT images of prostate core biopsies showed, after extensive training an overall accuracy of 93%. This implies that for pancreatic tissues further improvement is possible [35], therefore we believe that more training could further improve the diagnostic accuracy. We made a flowchart for assessment of pancreatic FF-OCT images which could support pathologists, although it should be validated in future studies (Figure 6).

Finally, we did not provide any clinical data to the pathologists. This lack of clinical information made interpretation even more difficult as compared to daily practice when such information is available and taken into account in the interpretation of the histomorphology.

We have not imaged resection margins of the surgical specimens as that would have affected the clinical workflow too much, however, we included fresh pancreatic tissue for imaging to mimic the future application of intraoperative use. Moreover, we selected interesting and clinically relevant locations on the H&E and the corresponding FF-OCT images; for example, transition zones of infiltrating tumor glands and surrounding tissue (Supplementary Figure 2). Furthermore, to achieve an R0 resection margin in Europe, imaging up to 1 mm is necessary. In this study, we imaged at a depth of 20 μm to ensure good correspondence with reference H&E. As resolution decreases with increasing imaging depth, future studies should analyze the influence on accuracy with increased imaging depth.

The more experienced pathologist did not find the imaging quality good enough to give a diagnosis in six cases that were excluded from further analysis. These images were equally distributed between the different groups (malignant, benign, fresh, deparaffinised) we believe that this exclusion does not represent a specific bias.

Several other groups tried to identify pancreatic tumor tissue in order to reduce the amount of positive margins during surgery using various techniques. Hu et al.[36] used nonlinear optical microscopy to image pancreatic tumor xenografts harvested at different stages. They also saw an increased density of the collagen fibers in tumor compared with normal tissue. However, they did not do a blind reading of the images. Eberlin et al.[37], used mass spectrometry imaging and an automatic classifier to distinguish normal from cancer human pancreas tissue. They obtained a high agreement with pathology, but excluded cellular compositions that were not accounted for in their classifier, such as inflammation and necrosis, which is in contrast with our study, which included a broad spectrum of benign areas of disease to mimic clinical scenarios. Also our group studied the use of fluorescence-guided surgery during pancreatic resections. However, in human studies the results have been disappointing so far, as no useful tumor demarcation could be visualized with non-specific contrast agents.[38,39] Currently, studies using tumor-specific fluorescent contrast agents are ongoing (Trial ID:NTR5673).[40]

Resection margins can either be examined *in vivo* before and during resection and after resection in the resection bed, or *ex vivo* on the resected specimen. Erickson-Bhatt et al.[41], used a portable OCT system to image the resection bed after a wide local excision of breast cancer. Tao et al.[42], also looked at resection margins in breast cancer, but examined *ex vivo* frozen sections using nonlinear microscopy, reaching an accuracy of 94.1%. We envision that FF-OCT could eventually be used during surgery at clinically suspect resection margins to further improve radical resection rates by extending the resection margin to facilitate en bloc tumor removal or by resecting additional tissue after suggestion of residual disease.

The FF-OCT device used in this study is not yet applicable in surgery. For translation into the operating room for *in vivo* imaging a handheld and faster device is necessary; for *ex vivo* assessment of resected specimens a bench top system is sufficient. Progression is made on both accounts. The first handheld endomicroscope based on FF-OCT was recently described by Benoit a la Guillaume et al.[43], which opens new perspectives for *in vivo* imaging. Furthermore, a 7 times faster and 3 times more sensitive camera was introduced in the device, also bringing it closer to clinical implementation.[44]

In conclusion, FF-OCT could distinguish normal pancreatic tissue from pathologic pancreatic tissue, however, further development of the FF-OCT device and more experience in evaluating FF-OCT images of the pancreas is necessary before introduction in the clinical practice of pancreatic surgery.

Figure 1. Example FF-OCT image of a well-differentiated pancreatic ductal adenocarcinoma as shown to the pathologist for assessment. The whole FF-OCT images were shown to the pathologists, but they were asked to only assess the selected regions of interest (two per FF-OCT image). Both the original (A,C,E) and the inverse (B,D,F) FF-OCT images are shown. Scale bars, 5 mm (A,B), 2 mm (C,D), and 1 mm (E,F).

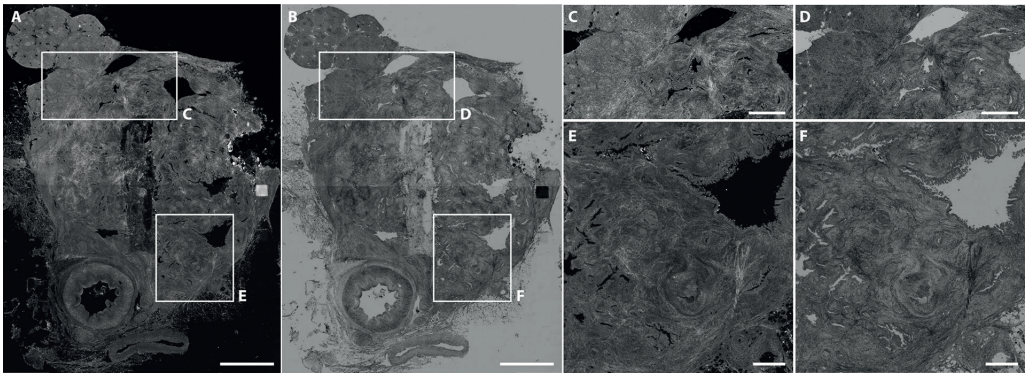

Table 1: Comparison of features of pancreatic ductal adenocarcinoma detectable on H&E and on FF-OCT images.

Features of malignancy	Detectable on H&E[a]	Detectable on FF-OCT
Disorganisation of lobuli and glands	+	+
Presence of atypical glands	+	±[b]
Atypical cell nuclei	+	-
Presence of tumor stroma	+	+
Ingrowth into structures (a.o. lymph nodes, blood vessels, fat)	+	±
Intraluminal necrosis	+	±
Perineural invasion	+	±

[a] *Adapted from Hruban et al..[29], these diagnostic characteristics are used in assessment of H&E images.*

[b] *Large atypical glands could be detected, but smaller glands are less visible and sometimes mistaken for blood vessels.*

Figure 2. Examples of FF-OCT images of normal pancreatic tissue and corresponding histology. Structures that are easily identified on FF-OCT images include normal pancreatic parenchyma (A-B), vessels (C-D), and a large pancreatic duct (E-F). Harder to recognize are nerve bundles (G-H). Scale bars, 250 µm (A-B, G-H), and 150 µm (C-F). Inset shows an islet of Langerhans (A-B) at 2.5 times higher magnification.

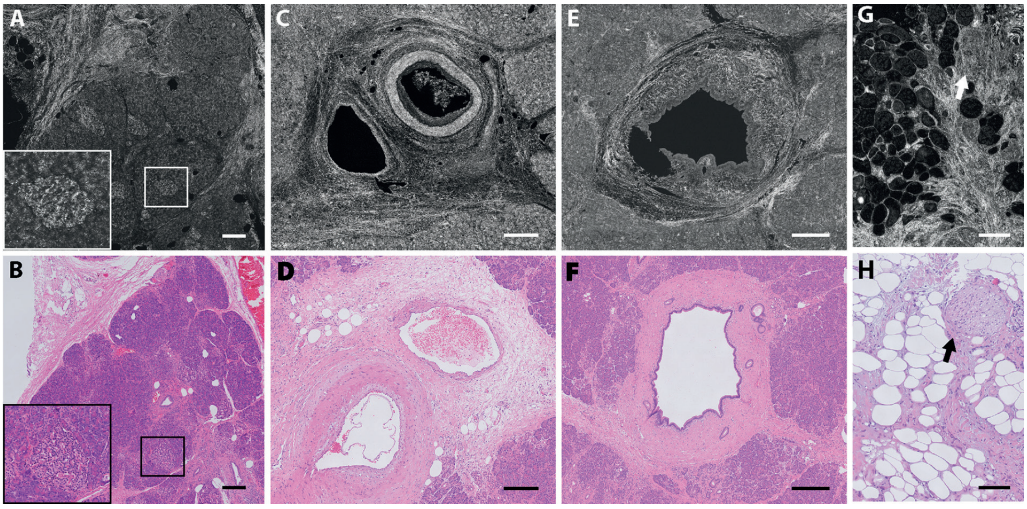

Figure 3. Example of benign pancreatic tissue FF-OCT images and corresponding histology. Fibrotic pancreatic tissue after neoadjuvant therapy (A-B), pancreatitis (C-D), and a serous cystadenoma (E-F). Scale bars all 500 µm.

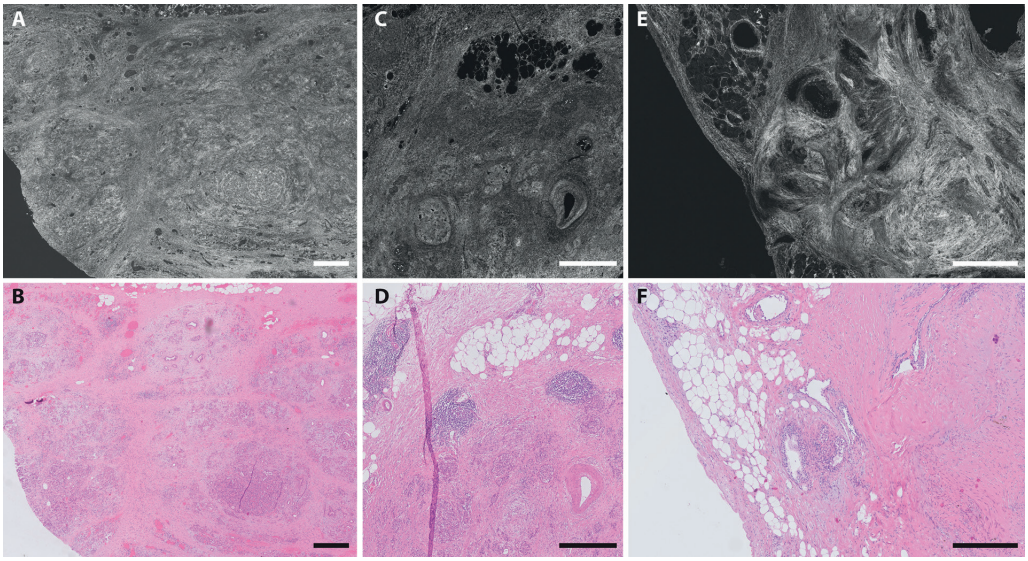

Figure 4. Example FF-OCT image of a well differentiated pancreatic ductal adenocarcinoma. A shows an overview. B shows a magnified view of stromal disorganization, and C shows nests of tumor cells. Scale bars, 2 mm (A), 1 mm (B), and 500 µm (C).

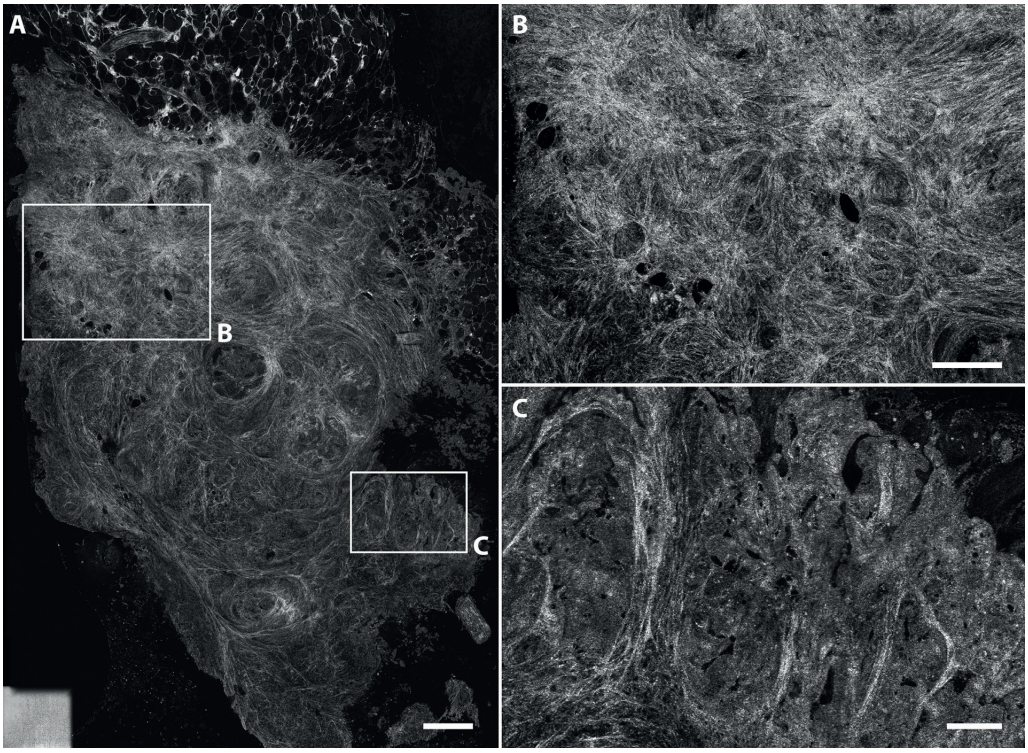

Table 2. Patient and tumor characteristics.

Characteristics	
Age, mean (y)	65.7
Sex, n (%)	
Male	13 (45)
Female	16 (55)
ASA score, n (%)	
1	5 (17)
2	19 (66)
≥3	5 (17)
Tumor size (mm), mean	33.2
Tumor location, n (%)	
Pancreatic head	13 (45)
Pancreas body/tail	10 (35)
Distal CBD	1 (3)
Peri-ampullar	5 (17)
Histological diagnosis, n (%)	
PDAC	23 (79)
Well differentiated	3
Moderately differentiated	10
Poorly differentiated	7
Unknown[a]	3
IPMN	1 (3)
MCN	2 (7)
NET	2 (7)
Serous cystadenoma	1 (3)
Surgical procedure, n (%)	
PPPD	17 (59)
Whipple	1 (3)
Distal pancreatectomy	9 (31)
Central pancreatectomy	1 (3)
Total pancreatectomy	1 (3)

[a] Differentiation grade could not be determined in 3 cases, because of pancreatic fibrosis after neoadjuvant (chemo)radiotherapy.

Abbreviations:
ASA: American Society of Anesthesiologists
CBD: Common bile duct
PDAC: Pancreatic ductal adenocarcinoma
IPMN: Intraductal papillary mucinous neoplasm
MCN: Mucinous cystic neoplasm
NET: *Neuroendocrine* tumor
PPPD: Pylorus-preserving pancreaticoduodenectomy

Table 3. Test characteristics of FF-OCT on pancreatic tissue. True positives are FF-OCT images which were correctly identified as malignant. True negatives are FF-OCT images which were correctly identified as benign. False positives are FF-OCT images which were incorrectly identified as malignant. False negatives are FF-OCT images which were incorrectly identified as benign. Pathologist 1 is the experienced pathologist, pathologist 2 is the pathologist in training.

Pathologist	True positive	True negative	False positive	False negative	Not inter-pretable	Sensitivity	Specificity	Accuracy
1	28	47	8	11	6	72%	85%	80%
2	30	37	21	12	0	71%	64%	67%
Overall (mean)	29	42	15	12	3	72%	74%	73%

Table 4. Accuracy per histological diagnosis.

	Correctly identified by both pathologists	Correctly identified by one pathologist	None correctly identified
Benign			
Normal pancreatic parenchyma	32	8	0
Pancreatitis	1	2	0
Atrophy or fibrosis	1	2	5
Serous cystadenoma	0	0	2
Mucinous cystic neoplasm	1	0	0
Malignant			
Grade 1 NET	0	1	1
Grade 2 NET	1	1	0
Grade 1 PDAC	4	2	0
Grade 2 PDAC	12	8	1
Grade 3 PDAC	1	7	0
Malignant IPMN	1		
Total[a]	**54**	**31**	**9**

[a] 6 images were scored as not interpretable by one of the pathologists, these are excluded from this analysis.

Figure 5. Accuracy and interobserver variability. Pathologist 1 is the experienced pathologist, pathologist 2 is the pathologist in training.

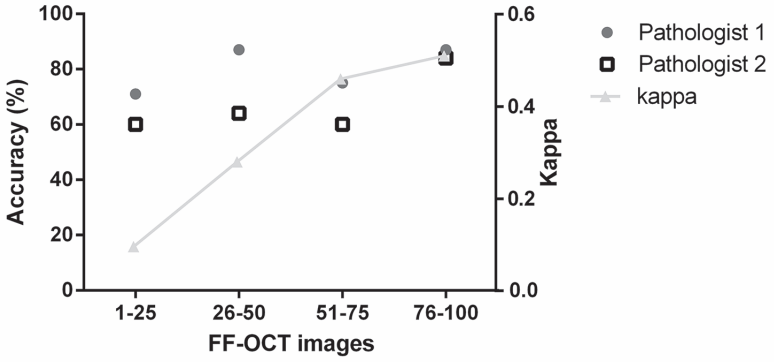

Figure 6. Proposed decision tree to evaluate pancreatic FF-OCT images. Scalebars are all 500 µm.
*The FF-OCT image and corresponding histology image only depict lymph node invasion.

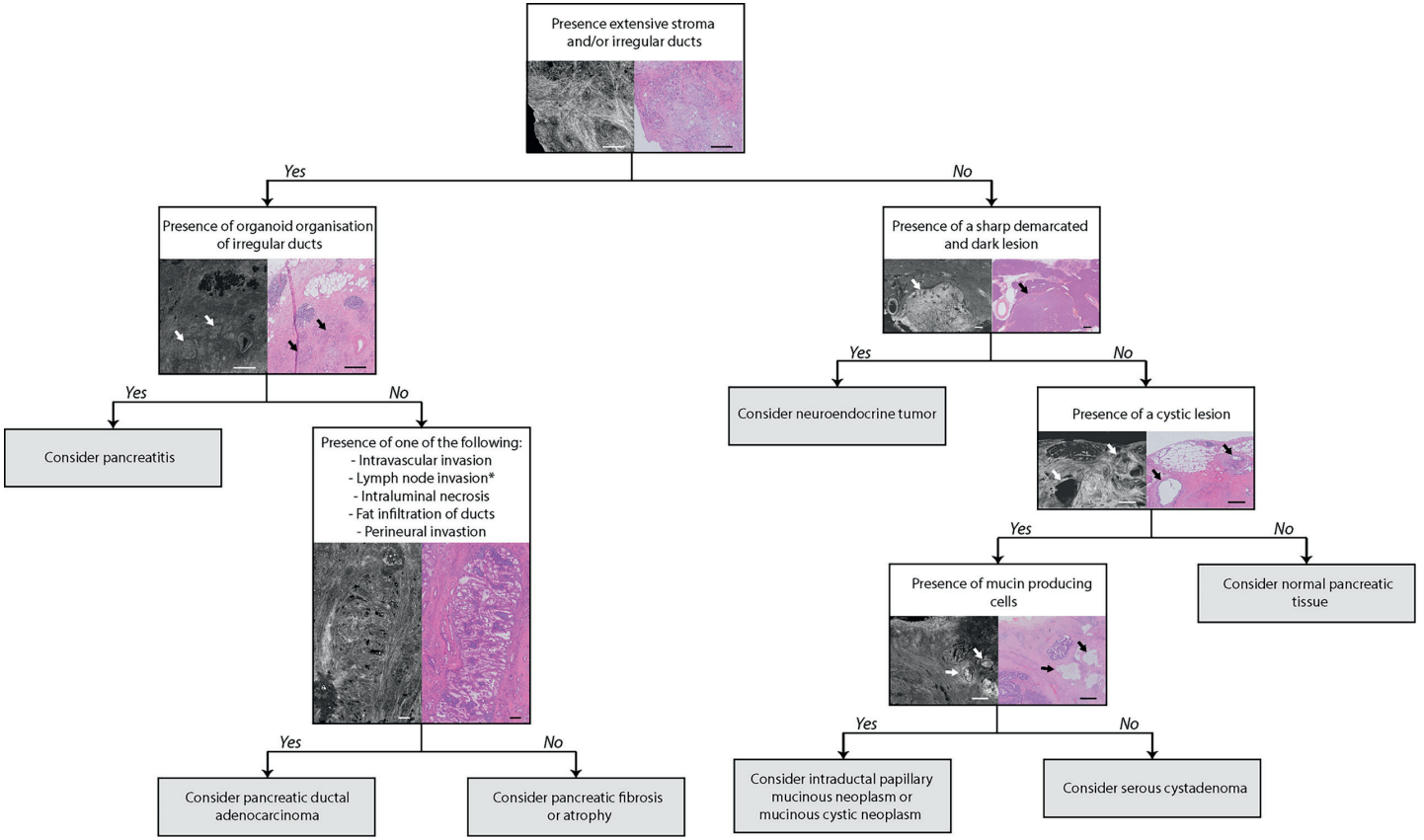

References

1. Siegel RL, Miller KD, Jemal A. Cancer statistics, 2016. *CA Cancer J Clin.* 2016;66(1):7-30.
2. Wagner M, Redaelli C, Lietz M, Seiler CA, Friess H, Buchler MW. Curative resection is the single most important factor determining outcome in patients with pancreatic adenocarcinoma. *Br J Surg.* 2004;91(5):586-594.
3. Reddy S, Wolfgang CL, Cameron JL, et al. Total pancreatectomy for pancreatic adenocarcinoma: evaluation of morbidity and long-term survival. *Ann Surg.* 2009;250(2):282-287.
4. Neoptolemos JP, Stocken DD, Bassi C, et al. Adjuvant chemotherapy with fluorouracil plus folinic acid vs gemcitabine following pancreatic cancer resection: a randomized controlled trial. *JAMA.* 2010;304(10):1073-1081.
5. Tran KT, Smeenk HG, van Eijck CH, et al. Pylorus preserving pancreaticoduodenectomy versus standard Whipple procedure: a prospective, randomized, multicenter analysis of 170 patients with pancreatic and periampullary tumors. *Ann Surg.* 2004;240(5):738-745.
6. Yeo CJ, Cameron JL, Sohn TA, et al. Pancreaticoduodenectomy with or without extended retroperitoneal lymphadenectomy for periampullary adenocarcinoma: comparison of morbidity and mortality and short-term outcome. *Ann Surg.* 1999;229(5):613-622; discussion 622-614.
7. Nitschke P, Volk A, Welsch T, et al. Impact of Intraoperative Re-resection to Achieve R0 Status on Survival in Patients With Pancreatic Cancer: A Single-center Experience With 483 Patients. *Ann Surg.* 2016.
8. Delpero JR, Bachellier P, Regenet N, et al. Pancreaticoduodenectomy for pancreatic ductal adenocarcinoma: a French multicentre prospective evaluation of resection margins in 150 evaluable specimens. *HPB (Oxford).* 2014;16(1):20-33.
9. Neoptolemos JP, Palmer DH, Ghaneh P, et al. Comparison of adjuvant gemcitabine and capecitabine with gemcitabine monotherapy in patients with resected pancreatic cancer (ESPAC-4): a multicentre, open-label, randomised, phase 3 trial. *Lancet.* 2017.
10. Esposito I, Kleeff J, Bergmann F, et al. Most pancreatic cancer resections are R1 resections. *Ann Surg Oncol.* 2008;15(6):1651-1660.
11. Campbell F, Smith RA, Whelan P, et al. Classification of R1 resections for pancreatic cancer: the prognostic relevance of tumour involvement within 1 mm of a resection margin. *Histopathology.* 2009;55(3):277-283.
12. Jamieson NB, Foulis AK, Oien KA, et al. Positive mobilization margins alone do not influence survival following pancreatico-duodenectomy for pancreatic ductal adenocarcinoma. *Ann Surg.* 2010;251(6):1003-1010.
13. Verbeke CS, Gladhaug IP. Resection margin involvement and tumour origin in pancreatic head cancer. *Br J Surg.* 2012;99(8):1036-1049.
14. Handgraaf HJ, Boonstra MC, Van Erkel AR, et al. Current and future intraoperative imaging strategies to increase radical resection rates in pancreatic cancer surgery. *Biomed Res Int.* 2014;2014:890230.
15. Nelson DW, Blanchard TH, Causey MW, Homann JF, Brown TA. Examining the accuracy and clinical usefulness of intraoperative frozen section analysis in the management of pancreatic lesions. *American journal of surgery.* 2013;205(5):613-617; discussion 617.
16. Boonstra MC, Tolner B, Schaafsma BE, et al. Preclinical evaluation of a novel CEA-targeting near-infrared fluorescent tracer delineating colorectal and pancreatic tumors. *Int J Cancer.* 2015;137(8):1910-1920.
17. Huang D, Swanson EA, Lin CP, et al. Optical coherence tomography. *Science (New York, NY).* 1991;254(5035):1178-1181.
18. Vakoc BJ, Fukumura D, Jain RK, Bouma BE. Cancer imaging by optical coherence tomography: preclinical progress and clinical potential. *Nat Rev Cancer.* 2012;12(5):363-368.
19. Dubois A. Full-Field Optical Coherence Microscopy. In: Liu G, ed. *Selected Topics in Optical Coherence Tomography.* InTech; 2012:3-20.
20. Peters IT, Stegehuis PL, Peek R, et al. Non-invasive detection of metastases and follicle density in ovarian tissue using full-field optical coherence tomography. *Clin Cancer Res.* 2016.
21. Assayag O, Antoine M, Sigal-Zafrani B, et al. Large field, high resolution full-field optical coherence tomography: a pre-clinical study of human breast tissue and cancer assessment. *Technology in cancer research & treatment.* 2014;13(5):455-468.
22. Binding J, Ben Arous J, Leger JF, Gigan S, Boccara C, Bourdieu L. Brain refractive index measured in vivo with high-NA defocus-corrected full-field OCT and consequences for two-photon microscopy. *Opt Express.* 2011;19(6):4833-4847.
23. Grieve K, Palazzo L, Dalimier E, Vielh P, Fabre M. A feasibility study of full-field optical coherence tomography for rapid evaluation of EUS-guided microbiopsy specimens. *Gastrointest Endosc.* 2015;81(2):342-350.
24. Federa F. Code for proper secondary use of human tissue in the Netherlands 2002; http://www.federa.org/codes-conduct.
25. Dubois A, Grieve K, Moneron G, Lecaque R, Vabre L, Boccara C. Ultrahigh-resolution full-field optical coherence tomography. *Applied optics.* 2004;43(14):2874-2883.
26. Dubois A, Vabre L, Boccara AC, Beaurepaire E. High-resolution full-field optical coherence tomography with a Linnik microscope. *Applied optics.* 2002;41(4):805-812.
27. Grieve K, Dubois A, Simonutti M, et al. In vivo anterior segment imaging in the rat eye with high speed white light full-field optical coherence tomography. *Opt Express.* 2005;13(16):6286-6295.
28. Landis JR, Koch GG. The measurement of observer agreement for categorical data. *Biometrics.* 1977;33(1):159-174.
29. Hruban RH, Fukushima N. Pancreatic adenocarcinoma: update on the surgical pathology of carcinomas of ductal origin and PanINs. *Modern pathology : an official journal of the United States and Canadian Academy of Pathology, Inc.* 2007;20 Suppl 1:S61-70.
30. Apelian C, Harms F, Thouvenin O, Boccara AC. Dynamic full field optical coherence tomography: subcellular metabolic contrast revealed in tissues by interferometric signals temporal analysis. *Biomed Opt Express.* 2016;7(4):1511-1524.
31. Erkan M, Hausmann S, Michalski CW, et al. The role of stroma in pancreatic cancer: diagnostic and therapeutic implications. *Nature reviews Gastroenterology & hepatology.* 2012;9(8):454-467.
32. Drifka CR, Tod J, Loeffler AG, et al. Periductal stromal collagen topology of pancreatic ductal adenocarcinoma differs from that of normal and chronic pancreatitis. *Modern pathology : an official journal of the United States and Canadian Academy of Pathology, Inc.* 2015;28(11):1470-1480.
33. Bredfeldt JS, Liu Y, Conklin MW, Keely PJ, Mackie TR, Eliceiri KW. Automated quantification of aligned collagen for human breast carcinoma prognosis. *Journal of pathology informatics.* 2014;5(1):28.

34. Lopater J, Colin P, Beuvon F, et al. Real-time cancer diagnosis during prostate biopsy: ex vivo evaluation of full-field optical coherence tomography (FFOCT) imaging on biopsy cores. *World journal of urology.* 2015.
35. Yang C, Ricco R, Sisk A, et al. High efficiency for prostate biopsy qualification with full-field OCT after training. *Proc SPIE 9689, Photonic Therapeutics and Diagnostics XII.* 2016;96891J.
36. Hu W, Zhao G, Wang C, Zhang J, Fu L. Nonlinear optical microscopy for histology of fresh normal and cancerous pancreatic tissues. *PLoS One.* 2012;7(5):e37962.
37. Eberlin LS, Margulis K, Planell-Mendez I, et al. Pancreatic Cancer Surgical Resection Margins: Molecular Assessment by Mass Spectrometry Imaging. *PLoS Med.* 2016;13(8):e1002108.
38. Hutteman M, van der Vorst JR, Mieog JS, et al. Near-infrared fluorescence imaging in patients undergoing pancreaticoduodenectomy. *Eur Surg Res.* 2011;47(2):90-97.
39. van der Vorst JR, Vahrmeijer AL, Hutteman M, et al. Near-infrared fluorescence imaging of a solitary fibrous tumor of the pancreas using methylene blue. *World J Gastrointest Surg.* 2012;4(7):180-184.
40. de Geus SW, Boogerd LS, Swijnenburg RJ, et al. Selecting Tumor-Specific Molecular Targets in Pancreatic Adenocarcinoma: Paving the Way for Image-Guided Pancreatic Surgery. *Mol Imaging Biol.* 2016.
41. Erickson-Bhatt SJ, Nolan RM, Shemonski ND, et al. Real-time Imaging of the Resection Bed Using a Handheld Probe to Reduce Incidence of Microscopic Positive Margins in Cancer Surgery. *Cancer research.* 2015;75(18):3706-3712.
42. Tao YK, Shen D, Sheikine Y, et al. Assessment of breast pathologies using nonlinear microscopy. *Proc Natl Acad Sci U S A.* 2014;111(43):15304-15309.
43. Benoit a la Guillaume E, Martins F, Boccara C, Harms F. High-resolution handheld rigid endomicroscope based on full-field optical coherence tomography. *Journal of biomedical optics.* 2016;21(2):26005.
44. LLTech. www.lltechimaging.com. 2016. Accessed 16-09-2016.

Chapter 10

Single fiber reflectance spectroscopy for pancreatic cancer detection during endoscopic ultrasound guided fine needle biopsy: a prospective cohort study

L. van Manen, I. Schmidt, A. Inderson, R.D. Houvast, J.J. Boonstra, J. Dijkstra, J.E. van Hooft, W.B. Nagengast, D.J. Robinson, A.L. Vahrmeijer, J.S.D. Mieog

International Journal of Medical Sciences 2022; 19(2): 205-212.

Abstract

This study aimed to determine the ability of single fiber reflectance (SFR) spectroscopy incorporated in endoscopic ultrasound fine needle biopsy (EUS-FNB) procedures in the pancreas to distinguish benign and malignant pancreatic tissue in patient with pancreatic masses suspected for malignancy.

Methods

This study was designed as a prospective observational single center study and included consecutive adult patients, who were scheduled for EUS-FNB of a solid pancreatic mass suspected for pancreatic ductal adenocarcinoma (PDAC). In total, seven optical parameters, derived from the absorption acquired spectra, were analyzed: blood volume fraction (BVF), microvascular saturation, average vessel diameter, bilirubin concentration (BIL), Mie amplitude, Mie slope and Rayleigh amplitude.

Results

Forty-five patients with a suspicious pancreatic lesion undergoing EUS-FNB were included, of which most of the patients (N=34) were ultimately diagnosed with PDAC. Finally, 27 out of 45 (60.0%) patients were used for the final analysis of the optical parameters. The median (IQR) BVF differed significantly in benign compared to malignant tissue (0.86 [0.30-2.03] and 4.49 [1.28-15.47]; p=0.046). Combining BVF and BIL to a new parameter (θ) improved the discrimination between PDAC and benign pancreatic tissue (p=0.026). The area under the curve of θ was 0.84, resulting in a 92.8%, 75.0%, 97.5%, 50.0% and 91.3% sensitivity, specificity, positive predictive value, negative predictive value and diagnostic accuracy for detection of PDAC.

Conclusion

Differentiation between PDAC and benign pancreatic tissue using SFR spectroscopy during EUS-FNB procedures is promising. Future work should focus on comparing the diagnostic performance combining SFR spectroscopy with EUS-FNB and EUS-FNB alone.

Introduction

Correct identification of pancreatic ductal adenocarcinoma (PDAC) can be difficult as it shows a considerable overlap with benign diseases like fibrosis or pancreatitis.[1] Discrimination between benign and malignant disease is of paramount importance in order to apply the most optimal treatment strategy. Next to conventional radiological imaging obtaining tissue is the cornerstone during the diagnostic process. Endoscopic ultrasound fine needle aspiration (EUS-FNA) or fine needle biopsy (EUS-FNB) are considered the least invasive and most effective procedures for establishing the diagnosis of pancreatic tumors. It has been suggested that EUS-FNA has some limitations such as the need of multiple tissue punctures ('passes') and preferably rapid onsite evaluation.[2-4] The introduction of fine needle biopsy in the endoscopy theatre, enabling acquisition of tissue cores, resulted in an improved diagnostic accuracy (between 85% and 95%), significantly lower number of passes, and similar diagnostic adequacy (between 87% and 96%) compared to EUS-FNA.[5-7] The presence of chronic pancreatitis is one of the factors mainly affecting the accuracy of both EUS-FNA and FNB, indicating that discriminating pseudotumoral masses from PDAC in the setting of chronic pancreatitis is of paramount importance in order to increase the diagnostic yield.[8,9] Therefore innovative techniques, such as contrast-enhanced EUS-FNA [10] or EUS elastography [11], are currently being investigated to determine the additional value during EUS in order to improve the differentiation between PDAC and pancreatitis or normal pancreatic tissue.

Multi-diameter single fiber reflectance spectroscopy is such an innovative technique that enables the non-invasive quantification of absorption and scattering parameters of tissue. This technique combines the data from two single fiber reflectance (SFR) spectra acquired with two different fiber diameters. Tissue characterization based on the quantification of physiological parameters, such as the blood volume fraction and microvascular oxygen saturation has the potential to differentiate between malignant and benign tissues directly during endoscopy. To extract and quantify these parameters from the obtained spectra a validated mathematical model, based on the knowledge of the absorption spectra of the chromophores, is applied.[12,13] However, this method can only measure superficial tissue and not in depth as is needed with pancreatic tissue. SFR spectroscopy using only one fiber diameter solves this problem as it reduces the diameter of the fiber. This fiber can be guided through a 22G needle used during EUS and measure at the same position, during the same needle pass as EUS-FNB is performed within the pancreatic mass.[14] Our group previously found a correlation between the acquired absorption spectra and cytology in a small group of patients with a variety of included pancreatic benign and malignant lesions.[14]

In this study the ability of SFR spectroscopy incorporated in EUS-FNB procedures of the pancreas to distinguish benign and malignant pancreatic tissue has been assessed in a larger patient cohort with optimised data exclusion procedures.

Material and methods

Study design

This study was designed as a prospective intention-to-measure single center trial. Consecutive adult patients, who were scheduled for EUS-FNB of a solid pancreatic mass suspected for carcinoma at the Leiden University Medical Center were eligible for inclusion, unless they refused participation or if insufficient time (≤ 3 days) was available to consider participation. Patients with cystic pancreatic lesions (either non-invasive intraductal papillary mucinous neoplasm, mucinous cystic neoplasm and serous cystadenoma) or a (suspicion of) neuro-endocrine tumor were not included. This trial was approved by the local Institutional Review Board (P17.316) and was performed in accordance with the ethical standards of the Helsinki Declaration of 1975. This trial was registered at the Dutch Trial Register (NL7613). All patients provided informed consent.

Endoscopic procedure

The EUS procedure was performed with the patient positioned in left lateral decubitus position under conscious (midazolam) or deep sedation (propofol). After introduction of a curved linear array echo endoscope (Fujinon EG-580UT, Fujifilm Corporation, Tokyo, Japan), visualization of the pancreatic mass, and decision to take a biopsy, a sterile 22-gauge biopsy needle (Acquire EUS FNB Needle, Boston Scientific, Marlborough, USA) was inserted in the endoscopic working channel. The stylet of the needle was replaced by a sterilized optical fiber (Light Guide Optics, Germany), which was placed in the pancreatic mass under ultrasound guidance (Figure 1). A minimum of three spectroscopic measurements were performed on the intended biopsy location before biopsies were taken. After each pass, the obtained material was directly placed into formalin and the adequacy of the samples was examined on-site by the endoscopist. In general, two passes were needed to obtain sufficient amount of tissue. For each biopsy area, the spectroscopic measurement procedure was repeated as described if feasible during the procedure. After each procedure, the spectroscopic fiber was calibrated in 2% Intralipid 20% and a dark container with water. The acquired tissue samples were paraffin embedded, cut into sections and stained using hematoxylin and eosin. If necessary, additional immunohistochemical staining was performed. All histology sections were examined by an experienced pancreatic pathologist for final histologic diagnosis.

SFR spectroscopy

The spectroscopy setup used in this study has been previously described in more detail.[14] In brief, the setup consists of a spectrophotometer (SD-2000; Ocean Optics, The Netherlands) to measure the white light reflectance, a halogen light source (HL-2000-FHSA; Ocean Optics, The Netherlands), and a quadfurcated optical fiber that is connected to a single optical fiber (Light Guide Optics, Germany). Sterilized single-use fibers had a core diameter of 230 µm, an outer diameter of 400 µm, a SMA905 connector, a distal fiber tip polished at 5°, with a numerical aperture of 0.27, and a length of 3 m (± 0.1 m). All measurements were analysed using a previously described fitting procedure.[14] The absorption coefficient of the measured spectra is modelled using a modified Beer-Lambert law. An assumption is made for the reduced scattering coefficient (μ'_s) and phase function (PF) at one wavelength, with wavelength dependent changes estimated by a background scattering model as there is no a priori knowledge of these parameters.[15,16] Next, a Levenberg-Marquardt algorithm was applied to extract parameter values and the confidence

interval was calculated from the square root of the diagonal of the covariance matrix. In total, seven optical parameters were evaluated for the differentiation between malignant and benign tissue: blood volume fraction (BVF), microvascular saturation parameter (StO_2), vessel diameter (VD), bilirubin concentration (BIL), Mie amplitude, Mie slope and Rayleigh amplitude. The first four parameters are physiological (absorption) parameters and the last three are morphological (scattering) tissue parameters.

Exclusion criteria SFR data

Spectra were evaluated by applying four predefined rejection criteria, which were developed before the data analysis by two members of our study team (IS and DR), who were not involved in the clinical procedures: (1) non-convergence of model fit, (2) absolute residual > 25% (between 450-900 nm) and (3) confidence interval (CI) which was >100x higher as the mean of the remaining CI parameters using the same calibration procedure (4) blood volume fraction higher than 40% indicating a blood pool. For the non-convergence fit, the fit did not converge due to imaginary numbers and values were set to not-a-number. The absolute residual is increased when a systematic error in the fitting model is present. A low absolute value, below 25%, therefore indicates the goodness of the fitting procedure. A high CI shows the statistical error of a parameter. A high CI indicates a low signal to noise ratio for the measurement. Finally, blood pool causes measurements of blood instead of the tissue we are interested in.[14]

Power calculation and statistical analysis

A sample size calculation using A'Hern's single stage phase II trial design with alpha=0.05 and power=80%, showed that 45 patients are needed to distinguish between a detected pancreatic mass by SFR spectroscopy of 90% and 75% or less (unacceptable outcome).[17] This requires at least 39 patients with biopsies positive for PDAC and six with biopsies negative for PDAC to reach the positive endpoint (i.e. diagnostic accuracy of 90%), which is concordance with the diagnostic yield of EUS-FNB.[2]

The optical parameters were calculated by averaging repeated measurements of the same location per patient weighted by the individual fit confidence intervals. Continuous variables were presented as mean values including standard deviation (SD) in normal distributed data or as median values including interquartile range (IQR) in non-normal distributed data, respectively. Differences between two groups were analyzed using the Mann-Whitney U test (non-normally distributed data). The most clinically relevant optical parameters and serum bilirubin were further evaluated in a multivariate binary logistic regression model to investigate to effect on differentiation between malignant and benign tissue. Data was standardized to a normal distribution $x_{new} =^{*}= (x - \mu)/sd$, where μ is the mean and *sd* the standard deviation of parameter *x*. Outliers were identified using the ROUT method.[18] Using a linear discriminant analysis, variables with a *p*-value below 0.200 were combined to create a new variable θ. Receiver-operating characteristic curve analyses were used, after which the sensitivity, specificity, positive predictive value (PPV), negative predictive value (NPV), and diagnostic accuracy were calculated. A *p*-value below 0.05 (two-sided) was considered statistically significant. Statistical analysis was performed with SPSS statistical software (Version 25.0, Chicago, Illinois) and graphs were created with Graphpad 9.0 (GraphPad Software, Inc., San Diego, CA).

Results

Patient characteristics

Forty-five patients with a suspicious lesion in the pancreas undergoing EUS-FNB were included in this study, of which two-thirds (N=30) had a lesion in the pancreatic head (Table 1). Thirty-four (75.6%) were diagnosed with PDAC. In total, 11 (24.4%) of the included patients underwent surgery (Table 1). Figure 2 shows an overview of all in- and excluded data. Thirty-seven out of the 45 patients were included for analysis. Reasons for exclusion were not performing biopsies during the procedure (N=5) and difficulties during the endoscopic procedure interfering spectroscopic measurements (N=3). For eight patients the fitting procedure was not possible due to an incorrect calibration procedure, resulting in 29 patients in which optical parameter evaluation was possible. Of the remaining 29 patients, 12% of the measurements were rejected based on the previously mentioned exclusion criteria. This resulted in the exclusion of two additional patients as all measurements of these patients were rejected. Ultimately, 27 patients were used for the final analysis of the optical parameters. In two patients the pancreatic mass was found out to be a colon carcinoma metastasis and a lymphoma, respectively. Four benign areas were measured in three patients and malignant tissue was measured in 42 areas in 22 patients. None of the patients had measurements of both benign and malignant tissue.

SFR spectra and optical parameters

Representative SFR spectra for both benign and malignant tissue including the corresponding histology are shown in Figure 3. Both residuals show low noise suggesting a correct fitting model. The malignant tissue shows a higher absorption between 500-600 nm, compared to the benign tissue, that is consistent with a higher blood volume fraction.

Table 2 shows the median and interquartile range (IQR) for all analyzed optical parameters for both malignant and benign tissue. BVF and BIL were the two most significant parameters (p=0.046; p=0.138) with a median (IQR) of 0.86 (0.30-2.03) and 22.2 (6.92-38.07) for malignant and 4.49 (1.28-15.47) and 32.9 (24.90-175.00) for benign tissue, respectively (Figure 4).

Sensitivity analysis

Within the BVF values, seven outliers were identified. To determine the effect of these outliers, the blood volume exclusion criteria was reduced from 40 to 10%. This reduction resulted in 1.3% extra measurements rejected, but still resulted in six new outliers. Furthermore, it did not show an improvement in differentiation between benign and malignant tissue (Table 2). Therefore, the exclusion criteria were not adjusted based on these results.

A binomial logistic regression was performed on the weighted mean to determine the effect on the serum bilirubin, physiological and morphological parameters on the discrimination between malignant and benign tissue. In the multivariate analysis, the BVF, StO_2, BIL, and serum BIL were not statistically significant associated with presence of malignancy (Table S1).

Combining parameters

Using linear discriminant analysis, the BVF and BIL were combined to a new parameter θ, as BVF and BIL were the most significantly different parameters (Table 2). This combined parameter

improved the discrimination between PDAC and benign pancreatic tissue (p=0.026; Figure 5 and Figure S1). The area under the curve (AUC) of θ increased from 0.80 and 0.73 for BVF or BIL alone to 0.84, which results in a 92.9%, 75.0%, 97.5%, 50.0% and 91.3% sensitivity, specificity, PPV, NPV, accuracy respectively.

Discussion

The aim of this study was to assess the ability of SFR spectroscopy to differentiate between benign pancreatic tissue and PDAC in consecutive patients with suspected PDAC, scheduled for EUS-FNB. Optical parameters were derived from the acquired spectra and consequently evaluated. A combined biomarker θ from the blood volume fraction and bilirubin concentration was created from SFR spectroscopy during EUS-FNB. This biomarker allowed for differentiation between malignant and benign pancreatic tissue (p=0.026), with an AUC of 0.84, resulting in 92.8%, 75.0%, 97.5%, 50.0% and 91.3% for sensitivity, specificity, PPV, NPV, and accuracy. These results suggest that the addition of SFR spectroscopy during EUS-FNB could potentially increase the diagnostic accuracy of such procedures.

Previously, a pilot study was performed with SFR spectroscopy during EUS-FNA procedures in the same patient population.[14] This study showed that microvascular saturation (StO_2) and bilirubin concentration were the physiological parameters that could differentiate between malignant and benign tissue most effectively. The low number of included patients, three benign and six malignant, could explain the discrepancy in results, concerning the StO_2 and BVF. Furthermore, in two out of the six malignant lesions, other neoplastic types than PDAC were included in the former analysis. As described previously, PDAC is a hypovascular tumor as a result of impaired tumor vasculature and a decrease in angiogenesis.[19] Together, this limits the blood flow and reduces the oxygen delivery to the tumor. It is suggested that the blood flow and blood volume in PDAC are lower in patients with PDAC compared to chronic pancreatitis and normal pancreatic tissue, which is in concordance with our results.[20]. One another study described the use of intraoperative optical spectroscopy to distinguish pancreatic cancer from normal pancreas and chronic pancreatitis. Using principal component analysis instead of deriving physiological and optical parameters from the reflectance measurements, these tissue types could be accurately identified with a sensitivity of 91%, specificity of 82%, PPV of 69% and NPV of 95%, and AUC of 0.89.[21]

In our study, all reflectance measurements during FNB were histologically confirmed with tissue that was taken from the same location. This ensures that our reflectance results correspond directly to the histopathological diagnosis. Furthermore, a bigger sample size of patients was included in this study compared to the previous pilot study of Stegehuis et al.[14] Nevertheless, our study has some limitations. First, although we were able to include our powered sample size of 45 patients, a total of 27 patients could be included in the final analysis meaning that our results should be interpreted with caution. Data had to be excluded due to clinical and technical decisions. In some patients no biopsies were taken as the lesion could not be visualized or considered not to be malignant and in other patients difficulties during the endoscopic procedure interfered with the

spectroscopic measurements. Furthermore, due to inaccurate calibrations a substantial number of patients had to be excluded. The frequency of this effect, which is necessary to obtain an optimal data set was not anticipated prior to designing the study. During the calibration procedure we did not attempt to feedback data on the calibration accuracy, which made it challenging for the involved clinicians to check the calibration quality as this is the first large prospective study that uses SFR spectroscopy in a clinical setting. In future trials, a calibration quality check will be implemented in the spectroscopy software. Finally, exclusion criteria also reduced the number of patients available for analysis, however the exclusion of data based on the technical criteria ensured that only optimal measurements were analyzed reducing the possibility of variance due to wrongly acquired data. All together this resulted in only a limited number of patients with benign areas making a fair comparison of optical parameters between malignant and benign tissue more difficult. Additionally, no patients had measurements of both benign and malignant tissue. For the last group this could have helped in determining the intraindividual instead of the interindividual variability in physiological parameters.

Implementation of this technique into clinical practice is relatively easy, as it is compatible with the endoscope and FNB needles that are currently used during these diagnostic procedures. According to a recent meta-analysis, that includes 18 high-quality designed randomized controlled trials, the introduction of FNB has led to a diagnostic adequacy of 86-90% and a diagnostic accuracy of 85-87%.[6] The results of this study demonstrated that the addition of SFR spectroscopy could potentially increase this diagnostic accuracy, although the results of this study should be interpreted with some uncertainty because of underpowering due to the amount of excluded patients. Nevertheless, even with this number of patients we could already distinguish PDAC from benign pancreatic tissue with similar diagnostic accuracy to what has been reported for EUS-FNB. Therefore the results of this study first warrant a clinical trial comparing the diagnostic accuracy of EUS-FNB combined with SFR spectroscopy or EUS-FNB alone.

In conclusion, differentiation between PDAC and benign pancreatic tissue using SFR spectroscopy during EUS-FNB procedures is promising, however technical improvements in the software and further clinical trials are necessary to demonstrate the added value during EUS procedures of the pancreas.

Figure 1. Overview on implementation of SFR spectroscopy during endoscopic procedure. (a) Overview of spectroscopy device. (b) identification of pancreatic mass using endoscopic ultrasound. (c) insertion of the optical fiber under white light endoscopic guidance (d) performing spectroscopic measurement in the suspicious lesion under endoscopic ultrasound guidance. (e) representative reflectance spectra of a malignant lesion. (f) histological confirmation of malignant cells in the acquired tissue.

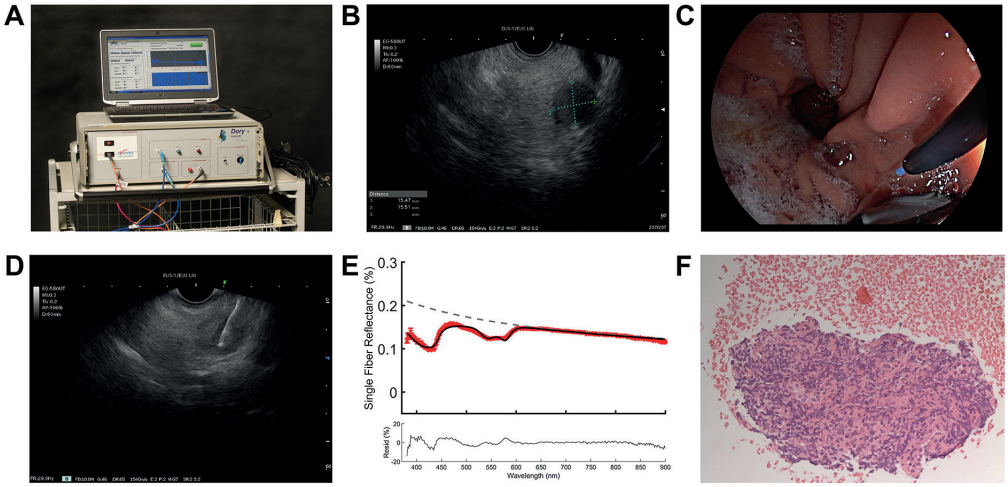

Table 1. Baseline patient characteristics.

Variable	
Age (y), mean (SD)	66.2 (9.5)
Sex, n (%)	
Male	24 (53.3)
Female	21 (46.7)
Bilirubin (µmol/L), median (IQR)	18 (8-210)
(Suspected) tumor location, n (%)	
Head	30 (66.7)
Body	9 (20.0)
Tail	6 (13.3)
Preoperative tumor stadium, n (%)	
Ia	2 (4.4)
Ib	3 (6.7)
IIa	3 (6.7)
IIb	7 (15.6)
III	14 (31.1)
IV	6 (13.3)
Not applicable	10 (22.2)
Patients undergoing FNB, n (%)	41 (91.1)
Pathological diagnosis, n (%)	
Pancreatic ductal adenocarcinoma	34 (75.6)
(Auto-immune) pancreatitis	3 (6.6)
Neuroendocrine tumor	1 (2.2)
Pancreatic fibrosis	1 (2.2)
Lymphoma	1 (2.2)
Benign pancreatic tissue	5 (11.1)
Patients undergoing surgery, n (%)	11 (24.4)

Figure 2. Flowchart of the included patients.

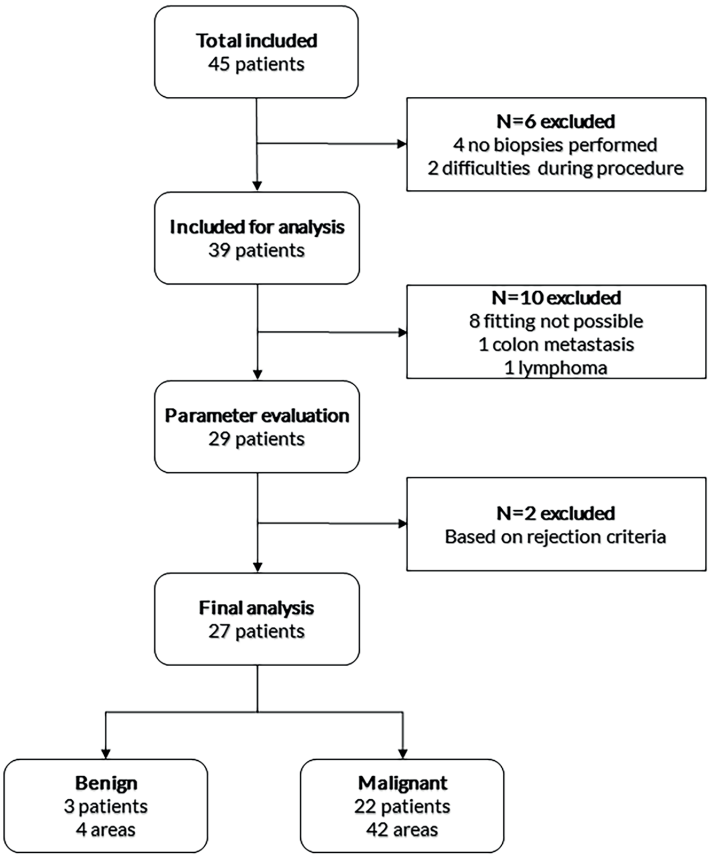

Figure 3. Representative fitted spectra with corresponding histology. (a) Spectra of benign lesion in the pancreas and (b) corresponding hematoxylin and eosin (H&E) image. (c) Spectra of a malignant pancreatic lesion and (d) corresponding H&E image.

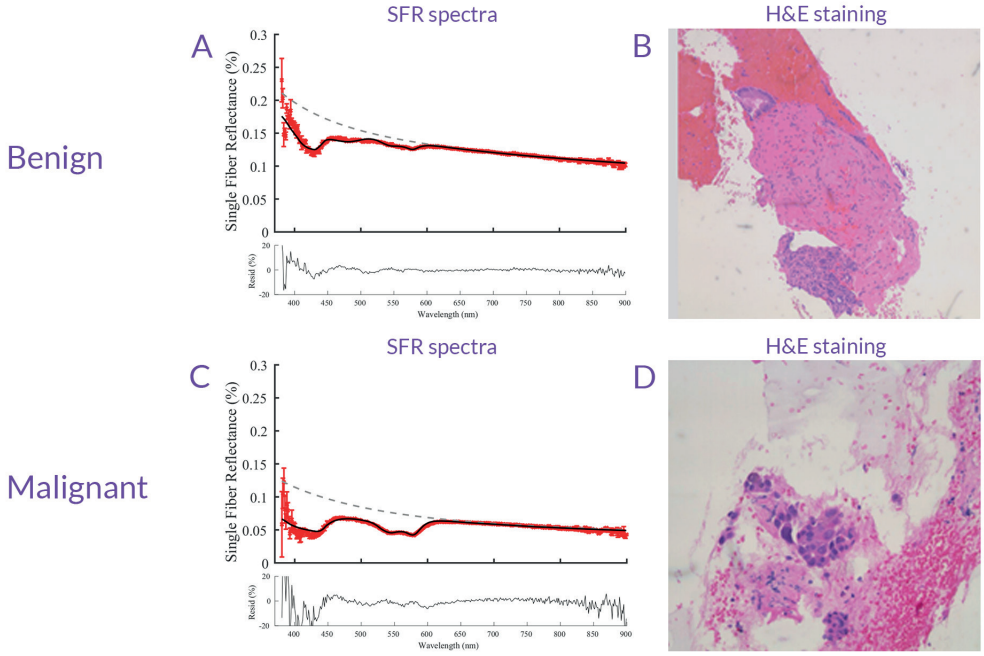

Figure 4. Overview of optical properties for both tumor and benign tissue. The top row shows the scattering properties and the bottom row the absorption properties. *P*-values are displayed above each graph.

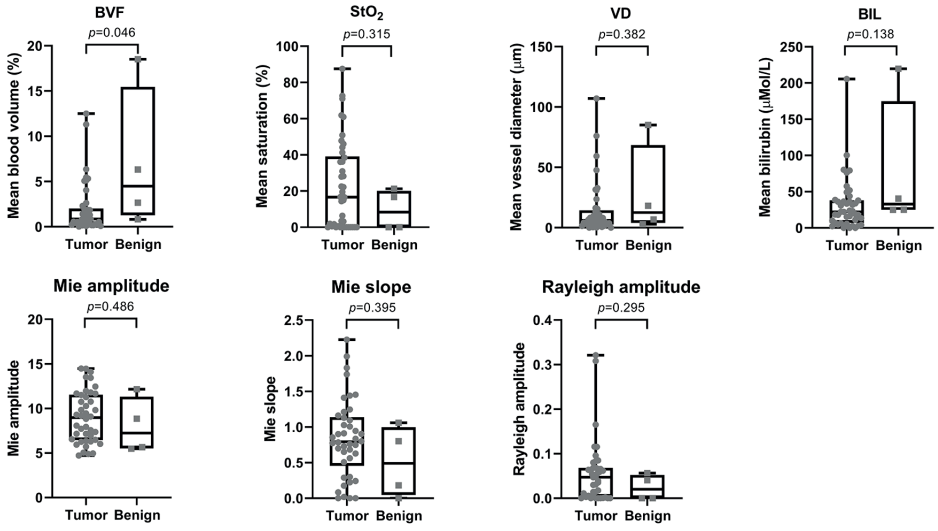

Table 2. Differences in optical parameters between malignant and benign pancreatic tissue.

	Malignant *Median*	*IQR*	Benign *Median*	*IQR*	*p*-value *40% BVF*	*10% BVF*
BVF (%)	0.86	0.30-2.03	4.49	1.28-15.47	0.046	0.146
StO_2 (%)	16.61	0.00-39.16	8.36	0.00-20.15	0.315	0.223
VD (µm)	6.04	2.66-14.40	12.5	3.92-68.38	0.382	0.947
BIL (µMol/L)	22.2	6.92-38.07	32.9	24.90-175.0	0.138	0.241
Mie amplitude	8.96	6.44-11.55	7.24	5.52-11.3	0.486	0.999
Mie slope	0.79	0.46-1.14	0.49	0.05-0.99	0.395	0.189
Rayleigh amplitude	0.05	0.00-0.07	0.02	0.00-0.05	0.295	0.527

Abbreviations: BVF: blood volume fraction; StO_2: microvascular saturation; VD: blood vessel diameter; BIL: bilirubin concentration; IQR: interquartile range.

Figure 5. ROC curve of biomarker θ. Biomarker θ is composed of blood volume fraction (BVF) and bilirubin concentration (BIL). The area under the curve (AUC) is 0.84 (p=0.026).

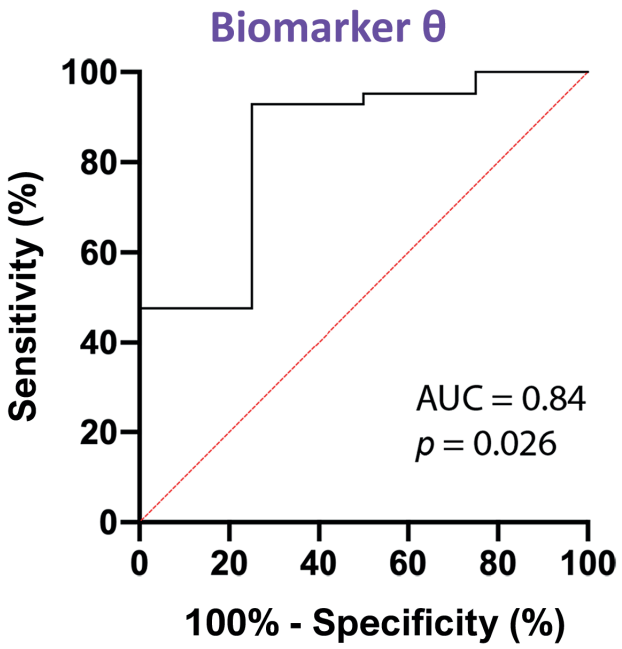

Supplementary data

Table S1 Binomial logistic regression model.

	Odds ratio	95% confidence interval	*p*-value
BVF (%)	0.51	0.22-1.19	0.118
StO2 (%)	1.10	0.99-1.23	0.090
BIL (µMol/L)	0.99	0.96-1.01	0.331
Serum BIL (µMol/L)	1.01	0.99-1.03	0.224

Abbreviations: BVF: blood volume fraction; StO2: microvascular saturation; BIL: bilirubin concentration.

Figure S1. Overview on receiver-operating characteristic (ROC) curves of individual parameters after linear discriminant analysis. *Abbreviations: S1: Mie amplitude; S2: Mie slope; S3: Rayleigh amplitude; BVF: blood volume fraction; StO_2: microvascular saturation; VD: blood vessel diameter; BIL: bilirubin concentration.*

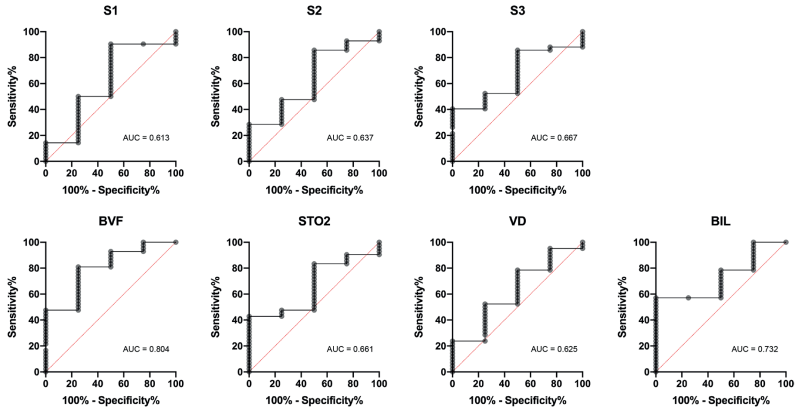

Figure S2. An example of reflectance spectra of normal pancreatic tissue. In two patients it was possible to perform measurements in normal pancreatic tissue (based on endoscopic ultrasound (EUS) view of the endoscopist) during the retraction of the fiber after a biopsy in a suspicious lesion. Due to the risk on EUS induced pancreatitis no biopsy has been taken in normal looking pancreatic tissue, so these measurement could not be histologically confirmed.

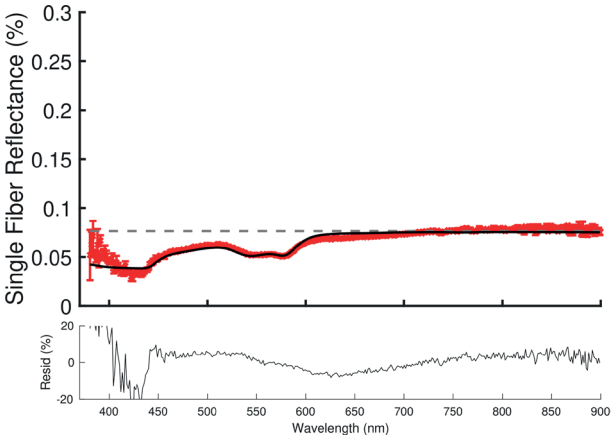

References

1. Zhang L, Sanagapalli S, Stoita A. Challenges in diagnosis of pancreatic cancer. World journal of gastroenterology. 2018; 24: 2047-60.
2. Cheng B, Zhang Y, Chen Q, Sun B, Deng Z, Shan H, et al. Analysis of Fine-Needle Biopsy vs Fine-Needle Aspiration in Diagnosis of Pancreatic and Abdominal Masses: A Prospective, Multicenter, Randomized Controlled Trial. Clinical gastroenterology and hepatology : the official clinical practice journal of the American Gastroenterological Association. 2018; 16: 1314-21.
3. Crinò SF, Di Mitri R, Nguyen NQ, Tarantino I, de Nucci G, Deprez PH, et al. Endoscopic Ultrasound-guided Fine-needle Biopsy With or Without Rapid On-site Evaluation for Diagnosis of Solid Pancreatic Lesions: A Randomized Controlled Non-Inferiority Trial. Gastroenterology. 2021; 161: 899-909.e5.
4. Dumonceau JM, Deprez PH, Jenssen C, Iglesias-Garcia J, Larghi A, Vanbiervliet G, et al. Indications, results, and clinical impact of endoscopic ultrasound (EUS)-guided sampling in gastroenterology: European Society of Gastrointestinal Endoscopy (ESGE) Clinical Guideline - Updated January 2017. Endoscopy. 2017; 49: 695-714.
5. Facciorusso A, Del Prete V, Buccino VR, Purohit P, Setia P, Muscatiello N. Diagnostic yield of Franseen and Fork-Tip biopsy needles for endoscopic ultrasound-guided tissue acquisition: a meta-analysis. Endosc Int Open. 2019; 7: E1221-e30.
6. van Riet PA, Erler NS, Bruno MJ, Cahen DL. Comparison of fine-needle aspiration and fine-needle biopsy devices for endoscopic ultrasound-guided sampling of solid lesions: a systemic review and meta-analysis. Endoscopy. 2021; 53: 411-23.
7. Rimbaş M, Crino SF, Gasbarrini A, Costamagna G, Scarpa A, Larghi A. EUS-guided fine-needle tissue acquisition for solid pancreatic lesions: Finally moving from fine-needle aspiration to fine-needle biopsy? Endosc Ultrasound. 2018; 7: 137-40.
8. Grassia R, Imperatore N, Capone P, Cereatti F, Forti E, Antonini F, et al. EUS-guided tissue acquisition in chronic pancreatitis: Differential diagnosis between pancreatic cancer and pseudotumoral masses using EUS-FNA or core biopsy. Endosc Ultrasound. 2020; 9: 122-9.
9. Varadarajulu S, Tamhane A, Eloubeidi MA. Yield of EUS-guided FNA of pancreatic masses in the presence or the absence of chronic pancreatitis. Gastrointestinal endoscopy. 2005; 62: 728-36; quiz 51, 53.
10. Facciorusso A, Mohan BP, Crinò SF, Ofosu A, Ramai D, Lisotti A, et al. Contrast-enhanced harmonic endoscopic ultrasound-guided fine-needle aspiration versus standard fine-needle aspiration in pancreatic masses: a meta-analysis. Expert Rev Gastroenterol Hepatol. 2021; 15: 821-8.
11. Carrara S, Di Leo M, Grizzi F, Correale L, Rahal D, Anderloni A, et al. EUS elastography (strain ratio) and fractal-based quantitative analysis for the diagnosis of solid pancreatic lesions. Gastrointestinal endoscopy. 2018; 87: 1464-73.
12. Kanick SC, Robinson DJ, Sterenborg HJ, Amelink A. Monte Carlo analysis of single fiber reflectance spectroscopy: photon path length and sampling depth. Phys Med Biol. 2009; 54: 6991-7008.
13. Kanick SC, Sterenborg HJ, Amelink A. Empirical model of the photon path length for a single fiber reflectance spectroscopy device. Opt Express. 2009; 17: 860-71.
14. Stegehuis PL, Boogerd LS, Inderson A, Veenendaal RA, van Gerven P, Bonsing BA, et al. Toward optical guidance during endoscopic ultrasound-guided fine needle aspirations of pancreatic masses using single fiber reflectance spectroscopy: a feasibility study. Journal of biomedical optics. 2017; 22: 24001.
15. Kanick SC, Robinson DJ, Sterenborg HJ, Amelink A. Method to quantitate absorption coefficients from single fiber reflectance spectra without knowledge of the scattering properties. Optics letters. 2011; 36: 2791-3.
16. Kanick SC, van der Leest C, Djamin RS, Janssens AM, Hoogsteden HC, Sterenborg HJ, et al. Characterization of mediastinal lymph node physiology in vivo by optical spectroscopy during endoscopic ultrasound-guided fine needle aspiration. J Thorac Oncol. 2010; 5: 981-7.
17. A'Hern RP. Sample size tables for exact single-stage phase II designs. Statistics in medicine. 2001; 20: 859-66.
18. Motulsky HJ, Brown RE. Detecting outliers when fitting data with nonlinear regression - a new method based on robust nonlinear regression and the false discovery rate. BMC bioinformatics. 2006; 7: 123.
19. Feig C, Gopinathan A, Neesse A, Chan DS, Cook N, Tuveson DA. The pancreas cancer microenvironment. Clinical cancer research : an official journal of the American Association for Cancer Research. 2012; 18: 4266-76.
20. Yadav AK, Sharma R, Kandasamy D, Pradhan RK, Garg PK, Bhalla AS, et al. Perfusion CT - Can it resolve the pancreatic carcinoma versus mass forming chronic pancreatitis conundrum? Pancreatology : official journal of the International Association of Pancreatology (IAP) [et al]. 2016; 16: 979-87.
21. Wilson RH, Chandra M, Scheiman JM, Lee SY, Lee OE, McKenna BJ, et al. Tissue Classification Using Optical Spectroscopy Accurately Differentiates Cancer and Chronic Pancreatitis. Pancreas. 2017; 46: 244-51.

Chapter 11

Detection of cutaneous oxygen saturation using a novel snapshot hyperspectral camera: a feasibility study

L. van Manen, W.A.J. Birkhoff, J. Eggermont, R.J. Hoveling, P. Nicklin, J. Burggraaf, R. Wilson, J.S.D. Mieog, D.J. Robinson, A.L. Vahrmeijer, M.S. Bradbury, J.Dijkstra

Quantitative Imaging in Medicine and Surgery. 2021 Sep;11(9):3966-3977.

Abstract

Background

Tissue necrosis, a consequence of inadequate tissue oxygenation, is a common post-operative complication. As current surgical assessments are often limited to visual and tactile feedback, additional techniques that can aid in the interrogation of tissue viability are needed to improve patient outcomes. In this bi-institutional pilot study, the performance of a novel snapshot hyperspectral imaging camera to detect superficial cutaneous oxygen saturation (StO_2) was evaluated.

Methods

Healthy human volunteers were recruited at two participating centers. Cutaneous StO_2 of the forearm was determined by a snapshot hyperspectral camera on two separate study days during occlusion-reperfusion of the brachial artery and after induction of local vasodilation. To calculate the blood StO_2 at each pixel in the multispectral image, spectra were selected, and fitting was performed over wavelengths ranging from 470 to 950 nm.

Results

Quantitative detection of physiological changes in cutaneous StO_2 levels was feasible in all sixteen volunteers. A significant ($P<0.001$) decrease in cutaneous StO_2 levels from 78.3% (SD:15.3) at baseline to 60.6% (SD:19.8) at the end of occlusion phase was observed, although StO_2 levels returned to baseline after five minutes. Mean cutaneous StO_2 values were similar in the same subjects on separate study days (Pearson R^2: 0.92 and 0.77, respectively) at both centers. Local vasodilation did not yield significant changes in cutaneous StO_2 values.

Conclusions

This pilot study demonstrated the feasibility of a snapshot hyperspectral camera for detecting quantitative physiological changes in cutaneous StO_2 in normal human volunteers, and serves as a precursor for further validation in perioperative studies.

Introduction

The restoration of normal tissue function and wound healing following surgery is critically dependent on tissue oxygen saturation (StO_2) and perfusion, among other factors. Tissue ischemia and soft tissue necrosis, caused by inadequate tissue oxygenation, commonly occurs in patients with (micro)vascular diseases requiring surgical interventions. However, in the post-operative period, wound complications can arise, such as tissue necrosis that necessitates a second surgical procedure. Traditionally, surgeons use tactile and visual feedback, sometimes in combination with handheld Doppler ultrasound, for intraoperatively evaluating tissue perfusion. Nevertheless, healing complications can occur, for instance, in up to 8 and 15% of patients undergoing breast reconstructive surgery or surgical amputations (i.e., below-the-knee), respectively.[1,2] Therefore, additional techniques that can reliably monitor perfusion and oxygenation status in post-operative settings and accurately predict and stratify patients at-risk for delayed surgical wound healing are essential for timely surgical management and for improved quality of life.

Although, transcutaneous oxygen saturation mapping ($TcPO_2$) and optical coherence tomography (OCT) are techniques that could be used for StO_2 monitoring, only $TcPO_2$ is currently used as a standard of care procedure. Both techniques can measure StO_2 levels *in vivo* by detecting optical absorption coefficient differences between oxygenated and deoxygenated haemoglobin.[1,3] However, these techniques have a limited field of view and require contact with the tissue for accurate assessments. Therefore, handheld cameras with a larger field of view, but not requiring direct skin contact, may serve as a practical alternative, in addition to being readily implemented in the perioperative setting.

One emerging technique is hyperspectral imaging, which has been used for biomedical applications, including the assessment of tumour margins and detection of tissue StO_2 in pathologic conditions.[4-6] This device detects the skin diffuse reflectance spectrum of light reflected from tissues after it has been scattered and absorbed by tissue chromophores, such as haemoglobin, fat, or water illuminated with a full spectrum light source.[4] Current available camera systems are mostly push-broom or band sequential scanners, which are limited by the long acquisition times needed to sequentially acquire spectral wavelength bands, precluding real-time imaging evaluations. Therefore, snapshot hyperspectral cameras have recently evolved to address this drawback. The first *in vivo* application of such a snapshot hyperspectral camera system was demonstrated by Gao et al. for the detection of retinal StO_2 levels.[7,8]

We have developed a novel snapshot hyperspectral imaging camera with a large field of view as a prototype system for non-invasively interrogating superficial anatomic structures and for monitoring changes in microvascular perfusion and oxygenation. This feasibility study herein aims to explore the novel capabilities of this hyperspectral snapshot camera system for detecting quantitative physiological changes in cutaneous StO_2 in healthy human volunteers under ambient light conditions, and without the need for direct skin contact.

Material and Methods

Study design

This study was an open observational multicenter feasibility study at the Leiden University Medical Center (LUMC), The Netherlands, and Memorial Sloan Kettering Cancer Center (MSKCC), USA. Healthy human volunteers, equally divided between these Centers, were recruited for participation in this study. Informed consent was obtained from all patients. All patients had a normal Body Mass Index (between 18.5 and 29,9 kg/m2)[9], were not taking medications, and had no past medical history. The study exclusion criteria were hypertension, regular tobacco use, and any confirmed allergies to medications. Furthermore, alcohol and caffeine consumption were prohibited within 12 hours of initiating each imaging session.[10,11] Approval for conducting the clinical trial was obtained at both Centers from their Institutional Review/Regulatory Boards. This trial was registered at the Dutch Trial Register (NL6381).

Study population

Sixteen human volunteers, equally divided between trial sites, were included in this feasibility study. Subject demographics are provided in Table 1. Age, vital signs (basal blood pressure, heart rate), and the BMI, were in the range of those measured in normal healthy adults, and were similar in both patient cohorts. Skin temperatures between cohorts showed statistically significant differences (32.2 [1.1] versus 36.0 [0.5] °C; $P<0.001$). Skin types, assessed according to the Flitzpatrick scale, were similar between the two groups ($P=0.637$).

Hyperspectral imaging system

A snapshot hyperspectral camera system (Hyperea, Quest Medical Imaging B.V., Middenmeer, The Netherlands), which acquires 41 spectral bands across the visual (VIS) and near-infrared (NIR) spectrum, ranging between 470 and 950 nm, was used for image acquisition.[12] The camera system consists of three sensors (RGB, VIS and NIR), which are combined to facilitate simultaneous colour and spectral imaging. The effective sensor resolution is 2048 x 1080 pixels. The spectral bands are acquired using two mosaic sensors, one (4x4 filter pattern) having a spectral range of 470 - 630 nm, and one sensor (5x5 filter pattern) having a spectral range of 600 – 950 nm (Figure 1). This hyperspectral camera system is based on a tiled-filter approach where pixels are individually filtered with narrow Fabry-Pérot bandpass filters (bandwidth ≈ 12 nm each). The camera sensors are pixel aligned on the prism, with a maximum deviation of 1/3 pixel. In this study a camera lens of 35 mm with an aperture size of f/2.8 was used. The camera allows real-time imaging at video frame rates (max. frame rate: 16 frames per second) without the need to scan in either the x- or y- direction. The camera lens was 35 mm. The field of view of the camera is 5 by 10 cm using a 40 cm working distance, which makes this system suitable for clinical use. A signal to noise ratio of maximum 14 could be achieved. The hyperspectral imaging set-up used for this study has four 50 Watt halogen light sources (Philips Lighting B.V., Eindhoven, The Netherlands), which were mounted on the top of a black box, for optimal control of the lighting conditions (Figure 1).

Laser speckle contrast imager

For superficial skin perfusion analysis, a Laser Speckle Contrast Imager (LSCI) (PSI; Perimed, Järfälla, Sweden) was used at one participating center (LUMC). This non-invasive technique is capable of detecting the subcutaneous movement of light-scattering particles.[13,14] The measurement depth of the LSCI device is approximately 0.5 mm. The system uses a divergent laser beam with a

wavelength of 785 nm. Measurements were performed on an area of 3x3 cm, with a frequency of 22 images per second (averaged for capsaicin snapshots). Point density was normal (resolution 0.45 mm). The LSCI data obtained were analysed using PIMsoft software (Perimed, Järfälla, Sweden).

Imaging procedure

To assess the imaging characteristics of the hyperspectral camera, its output was compared with contact measurements obtained using a fiber optic probe and multi-diameter reflectance spectroscopy.[15,16] During each measurement, the reflectance spectra are collected at effective diameters of 200, 600, and 1000 µm; StO_2, and blood volume fraction, was determined using the largest effective single fiber diameter with an interrogation depth of approximately 500 µm.[17] The pathlength of light in the interrogated volume for the point spectroscopy is fixed by the fiber (equal to approximately ½ the fiber diameter). For hyperspectral imaging, the illumination spot size is similar to that of the spectroscopy measurements but longer pathlength light from other points elsewhere are present in the illuminated field of the snapshot camera. Occlusion-reperfusion experiments were performed to characterize tissue optical properties. In each human volunteer, baseline skin StO_2 measurements were made of the right forearm over a two-minute interval. After acquiring these measurements, StO_2 of the right forearm was monitored for five minutes following occlusion of the right brachial artery; this procedure was repeated during the subsequent reperfusion period. In total, the arms of the included subjects did stay for 12 minutes in front of the camera and lamps during the occlusion-reperfusion experiments. Both snapshot images and spectroscopy measurements were taken every 30 seconds, except for the first minute after reperfusion, during which phase images and measurements were taken every second.

To validate this technique, human volunteers were recruited to undergo occlusion-reperfusion at two separate times, separated by more than three days. The patients' vital signs were obtained, namely their blood pressure, heart rate, basal finger oxygenation, and skin temperature, at the start of the measurements. Occlusion-reperfusion experiments were performed, as described above. Hereafter, capsaicin cream, a vasodilator, was applied on the right forearm. It works by activating the vanilloid type-1 receptor that, in turn, results in cutaneous vasodilation.[18] Capsaicin was administered on the same arm over an area of 3 by 3 cm, with an average distance of 5 cm under the radiocarpal joint, after the occlusion-reperfusion measurement. However, this was done only after the subject had rested for approximately 15 minutes, thereby restoring normal cutaneous blood flow. Subsequently, and before the capsaicin challenge, surgical tape was placed about the region of interest (ROI) to prevent spillage of capsaicin beyond the region of application. Thirty minutes after application of the crème, it was removed from the skin, and a superficial skin StO_2 measurement was acquired over a 30-minute time interval, with snapshots taken every 5 minutes. Results were compared with those of control regions located on the same forearm. In the LUMC cohort, blood flow was imaged simultaneously using LSCI.

Data processing

Due to the configuration of the 4x4 and 5x5 mosaic in the sensors and the different offsets that are applied for the placement of this mosaic pattern on the sensor pixels, specific demosaicing of the sensor information into the different spectral datacube components was required. By comparing the differences between the different planes in the spectral datacube, the alignment, cropping and scaling of the sensor data could be optimized. Based on the filter characteristics of both the sensors and the filters in the

camera system, a camera-specific correction matrix could be generated for the correction of the spectral artifacts that occur due to the configuration of the filters on the sensor pixels and the nature of the interference filters, e.g. crosstalk and higher-order transmission. The correction matrix for the spectral data was validated with reference spectra (Figure 1). Next, acquired images were normalized using white and dark reference images, as previously described by Lu et al.[4] Furthermore, a correction for the second-order light effect due to light diffraction [19], provided by the manufacturer, was performed after the normalization of images. Lastly, in order to calculate the blood StO_2 at each pixel in the hyperspectral images, all spectral bands (N=41) were selected in the full range of 470 - 950 nm to enable fitting using a method described previously, although implemented for hyperspectral imaging. [17,20,21] Reflectance spectra were analyzed using an analytical model to describe the wavelength-dependent optical properties to extract physiological and morphological information from the sampled tissue as previously described.[17] In short, attenuation due to absorption within the tissue is modeled using a modified Beer–Lambert law and is a function of both the tissue absorption coefficient (μ_a) and the single fiber photon path length. The reflectance amplitude, as well as the single fiber photon path length, depend on the scattering properties of the tissue, with a dependence on the reduced scattering coefficient (μ'_s) and on the angular distribution of scattering (phase function). Our initial model assumed that absorption was attributable to oxygenated and deoxygenated hemoglobin confined within the local microvasculature. A Levenberg–Marquardt algorithm was used to estimate the parameter values for the microvascular hemoglobin StO_2, the blood volume fraction and average blood vessel diameter by minimizing the chi-squared metric between measured reflectance data and model predictions.[17] Confidence intervals on parameter estimates were calculated from the square root of the diagonal of the covariance matrix.[9] Parameter values were averaged over repeated measurements, weighted by the confidence interval of individual spectral fits, and reported with the associated weighted standard deviation.

This fitting method assumed that blood is the dominant absorber in the field-of view, and that each wavelength travels an equal pathlength in the tissue with scattering losses approximately equal across the wavelength range of interest. The wavelength dependence of the penetration depth is not a confounding factor for the spectroscopy measurements because the fiber (probe) determines the penetration depth and is approximately equal over the wavelength range measured. This is not the case for the hyperspectral camera where longer wavelength photons also contribute to the acquired signal. We determined the effective light collection area of the camera system to be approximately 320 by 320 microns per pixel. StO_2 fitting was performed using software developed in-house, written in C++ programming language. It has been shown that the recovery of blood StO_2 in patients with skin types 1-3 is not affected by skin type.[15] Hyperspectral data were not corrected for skin type. Saturation maps were converted to color-based maps for improved interpretation (blue: low StO_2; red: high StO_2). The fitted StO_2 was not allowed to be greater than 100%, nor lower than 0%, for both spectroscopy and the hyperspectral camera system. The StO_2 maps were imported into MeVisLab (MeVis Medical Solutions AG, Bremen, Germany), and skin StO_2 subsequently calculated based on selecting corresponding ROI, which were located on a planar surface of the forearm and marked with a dermatological marker at the beginning of each measurement procedure. For all analyses, the marked area on the volar side of the forearm was chosen as the ROI. Care was taken during the repeated measurements to choose an ROI as close as possible to

the previous used ROI, using the LSCI and hyperspectral images as reference. In the analysis software, the ROI was manually selected using the dermatological markers as reference point.

Statistical analysis

Continuous variables were presented as mean values + standard deviations ([SD]) in normal distributed data or as median values (interquartile range [IQR]) in non-normal distributed data, respectively. The Mann-Whitney U-test, independent t-test, paired t-test and ANOVA test were used for comparison of continuous variables. For categorical variables, a Chi-Squared test was used to compare groups. Correlations were calculated by using the mean correlation coefficient (Pearson R^2). Correlation coefficients were interpreted according to Schober et al.[22] A P-value below 0.05 (two-sided) was considered statistically significant. SPSS Statistics for Windows, version 23.0 (IBM Corp., Armonk, N.Y., USA) was used for the statistical analysis. Graphs were created using Graphpad 8.0 (GraphPad Software, Inc., San Diego, CA).

Results

Spectral fitting

Figure 2 shows the variation in the percentage (%) of StO_2 measured using single fiber reflectance and hyperspectral imaging. The baseline StO_2 measured before occlusion using the fiber optic reflectance technique is significantly lower than that using hyperspectral imaging, but is consistent with previous measurements in the skin of the inner forearm.[15] During occlusion, the skin blood volume fraction is reduced (data not shown); consequently, there are large confidence intervals on these data points. Upon reperfusion, blood volume increases and subsequently returns to near baseline levels; in this regime, no significant differences in StO_2 levels were found using these measurement techniques. However, it is important to note that there are substantial uncertainties in both measurements of StO_2 due to the relatively low blood volume in the interrogated region, as we have described previously.[9]

Occlusion-reperfusion experiments

Measurement of StO_2 levels using a linear fitting algorithm was feasible in all volunteers during all phases of occlusion and reperfusion. General analysis showed a statistically significant ($P<0.001$) decrease in cutaneous StO_2 levels from 78.3% (SD: 15.3) at baseline to 60.6% (SD: 19.8) at the end of occlusion phase (Figure 3). Subgroup analysis showed that baseline StO_2 differed significantly between the subjects recruited at LUMC and MSKCC (mean StO_2: 69.9 versus 86.6 %, $P<0.001$), with a decrease in StO_2 of 20.3 and 14.3 %, respectively. Overall StO_2 levels returned to baseline at the end of the reperfusion phase, which was after 12 minutes (mean StO_2: 70.4 versus 85.1 %, for the two cohorts respectively). An additional perfusion analysis was performed in the LUMC cohort using LSCI and showed a strong correlation (Pearson R^2: 0.86) of blood flow with StO_2 levels during occlusion-reperfusion phases (Figure 4).

Moreover, StO_2 correlations between the two measurement days were analysed, resulting in an overall Pearson R^2 of 0.85, although a higher correlation was observed in the LUMC cohort (Pearson R^2: 0.92)

compared to the MSKCC cohort (Pearson R^2: 0.77). Individual analyses of all patients showed an excellent correlation in 13 (81%), a strong correlation in 2 (13%) and a fair correlation in 1 (6%) subject.

Effect of local vasodilatation

After application of capsaicin cream, statistically significant increases in blood flow due to vasodilatation (P<0.001) were measured (with LSCI) within the most superficial layers of the skin; blood flow increased from 76.7 (SD:11.1) to 146.9 (SD: 38.4) arbitrary units (AU). However, cutaneous StO_2 did not change significantly (P=0.927) after application of capsaicin in the most superficial layers (Figure 5). Nevertheless, mean StO_2 levels in the MSKCC cohort were significantly (P<0.001) higher compared to the LUMC cohort.

Discussion

In this multicenter study, we explored the feasibility of a novel snapshot hyperspectral camera system for non-invasive detection of superficial cutaneous StO_2 under different physiological conditions in normal, healthy human volunteers. Strong correlations were found between the StO_2 measurements acquired during occlusion-reperfusion experiments. Furthermore, local vasodilation did result in an increased cutaneous vascular flux, but not in a significantly higher tissue StO_2 level in the most superficial layers of the skin.

In general, non-invasive imaging using endogenous contrast for the detection and monitoring of cutaneous StO_2 levels is advantageous, and may offer distinct benefits over methods requiring injection of exogenous contrast agents for specific indications. In the perioperative setting, there is a general lack of real-time non-invasive imaging tools for reliably monitoring alterations in perfusion and oxygenation status. In the future, such tools could potentially improve patient care outcomes by their ability to detect decreased StO_2 about surgical margins, wound sites, and sites of graft placement, for instance, in addition to guiding clinical management. Moreover, direct skin contact is not needed for such measurements. To our knowledge, this is the first study implementing an existing and validated algorithm for quantitatively analysing cutaneous StO_2 by utilizing a snapshot hyperspectral camera system in human subjects. Recently, more systems have been introduced into the clinic for StO_2 monitoring of the bowel, skin and cerebral cortex.[23-27] Current available hyperspectral camera systems have longer acquisition times than those used by this snapshot hyperspectral camera system, precluding the types of evaluations performed herein. Moreover, other camera systems lack the ability to quantitatively monitor changes in tissue StO_2 by using relative oxyhemoglobin or deoxyhemoglobin measurements as surrogate markers for tissue StO_2. Our data supports the hypothesis that quantitative cutaneous StO_2 imaging is feasible and reproducible with good correlations in human volunteers. This is also underlined by the fact that the performance of this system was independently evaluated at two different centers.

However, a few limitations are noteworthy. First, as the study recruited a relatively small number of normal, healthy human volunteers, the results may not be representative of larger patient populations, who may exhibit a variety of baseline characteristics. Second, the hyperspectral camera system has 41 wavelength bands divided over two mosaic sensors, which implies a lower spatial resolution (i.e., either

2 or 2.5 times) that of the original resolution, noted earlier, although this was found not to be a limiting factor in the current study. Furthermore, we decided to use contact point optical spectroscopy as a reference for comparing the StO_2 of the most superficial layers of tissue. Based on these comparisons, a fitting algorithm was proposed, in order to quantify StO_2, which has been validated in other clinical studies.[21] Nevertheless, we acknowledge that other reference hyperspectral imaging devices suitable for StO_2 detection could have also been used to supplement the perfusion data obtained by LSCI, which was unfortunately only performed one center. Moreover, a general drawback of hyperspectral imaging is that penetration depths of only several hundred micrometres to a maximum of multiple millimetres can be interrogated, which are wavelength-dependent, limiting the applicability of this optical tool to assessments of the most superficial layers of the target tissue of interest (up to the dermis at the red end of the spectrum).[28] Nevertheless, compared to contact point spectroscopy, it seems that the sampling depth is greater for the hyperspectral camera, resulting in higher StO_2 values (Figure 2). The simple linear model of light transport in tissue we have used in the present study is based on assumptions that the scattering remains constant, and that the pathlength travelled is equal for all photons over the wavelength range of interest. The reduced scattering coefficient is known to vary across the visible spectrum. This means that the calculated absorbance of the tissue may be overestimated at the red end of the spectrum. Furthermore, the algorithm did not account for the effect of melanin, as it is very difficult to separate the influence of scattering and the absorption due to melanin without measuring in the blue-green portion of the visible spectrum. Finally, alterations in penetration depth and sampling volume may occur during occlusion, given that the distribution of absorbers changes. While these changes were not accounted for in our analysis, it was felt that the scattering properties of tissues in the forearm would not be significantly affected by occlusion remote from that site.

A high inter-patient variability in cutaneous StO_2 values was observed in this study, both within and across patient cohorts, however the differences in StO_2 values were not significant between the two measurement days in both cohorts, which was also demonstrated by a Pearson R^2 value of 0.85. Controversial data has been published for baseline cutaneous StO_2 values in the range of 50-96%, depending on the camera system used and region of interest in which the measurement was taken.[27,29-32] One explanation for the differences in StO_2 within cohorts may be attributed to gender differences. For example, in the LUMC cohort, females tended to have a higher baseline StO_2 or more subcutaneous fat. It has been demonstrated that fatty tissues are relatively poorly oxygenated, although the BMI included for all volunteers was within the normal range.[9,33] A high inter-patient variability may also be attributed to known wavelength-dependent and depth-dependent variations in cutaneous StO_2 values, that is, superficial skin layers exhibit lower StO_2 values than those found for the well-perfused deeper tissue layers. Another possible explanation is that skin temperature might have led to differences in cutaneous StO_2 between the two cohorts, as this parameter was significantly different at baseline. The large differences in baseline StO_2 between both cohorts could probably be explained by the room temperature, which was significantly higher at MSKCC, leading to increased vasodilatation with subsequent higher StO_2 levels, as previously demonstrated.[31] Moreover, the skin temperature could have been affected by the heat of the light sources, although StO_2 levels in both groups were similar at the beginning and at the end of the measurement period. Interestingly, capsaicin interventions did not result in significantly higher StO_2 levels for either patient cohort. Through activation of the TLPRV1 receptor, capsaicin is known to cause an increased neurogenic vasodilation (amongst other

responses, such as flare, pain, heat, and cutaneous hypersensitivity). This challenge showed that a flare and increased vasodilation did not significantly influence StO_2 measurements, which might be explained by the fact that healthy volunteers are already well oxygenated under normal circumstances and consequently the effect of local vasodilation is minimal. Nevertheless, there is still a trend towards higher saturation levels after application of capsaicin, however due to the expected limited effect on the StO_2 and the small sample size of our study, the detected StO_2 values are not changed significantly.

Besides hyperspectral imaging, other non-invasive techniques for StO_2 mapping, such as optical coherence tomography (near-infrared) spectroscopy, or photoacoustic imaging can be used, although these techniques have significant shortcomings, including the offering of only a limited field of view and/or an inability to acquire imaging data, respectively.[3,34] Recently, another imaging technique termed Single Snapshot of Optical Properties (SSOP), which is based on the Spatial Frequency Domain Imaging (SFDI) principle, allows real-time quantitative imaging of tissue oxygenation.[35,36]

Future work will focus on developing a more user-friendly system and evaluating other sources for better controlled light conditions. Furthermore, data analysis steps and software will be improved to enable real-time intraoperative StO_2 mapping, as current frame rate settings are only about 16 frames per second. Additional refinements, such as mounting the camera head, including light sources, on a stable arm, are needed to efficiently translate and implement such a prototype system into a variety of clinical settings. Importantly, StO_2 measurements are expected to be similar for both elderly adults and younger individuals.[21] In this proof-of-concept study, we focused on the assessment of cutaneous oxygenation status. For intraoperative applications, however, additional technical issues that may limit accuracy e.g., variations in skin thickness, would need to be addressed. In the present work, we attempted to minimize such contributions by imaging the inner aspect of the arm. Different applications and clinical conditions may necessitate specific mechanical solutions to be advanced, which will need to be evaluated and tested. These additional capabilities, however, would also enable high-resolution, full-field StO_2 imaging to be combined, in the same setting, with other real-time imaging strategies, such as fluorescence imaging that utilizes near-infrared wavelengths for the visualisation of multiple fluorophores. Such a hybrid system could also potentially allow for the simultaneous assessment of tissue StO_2 and perfusion. As this camera system has only been evaluated in healthy volunteers, it will be necessary to validate its clinical utility in a more heterogenous patient population. Future implementation will therefore focus on assessing feasibility under clinical circumstances such as patients with vascular conditions arising from, for example, diabetes mellitus, or during reconstructive surgical procedures.

Conclusions

In conclusion, this early-stage multicenter clinical trial demonstrated the feasibility of utilizing a novel snapshot hyperspectral camera system for the detection of cutaneous StO_2 in normal, healthy human volunteers. These findings are being used to inform next-stage camera system developments for monitoring oxygenation status in both non-surgical oncologic and peri-operative settings. In these settings, patients with vascular disease might potentially be risk-stratified for improving clinical decision-making and outcomes.

Table 1. Demographics of study population and overall results of cutaneous oxygen saturation measurements.

	LUMC cohort (N=8)	MSKCC validation cohort (N=8)	*P*- value
Sex, male (%)	4 (50)	2 (25)	0.302
Age (year), median (IQR)	23.5 (22.3-24.0)	23.5 (21.3-38.0)	0.798
BMI (kg/m^2), mean (SD)	24.6 (2.7)	23.3 (2.4)	0.348
Blood pressure, mean (SD)			
Systolic	120 (6.1)	119 (9.9)	0.834
Diastolic	77 (7.7)	73 (5.3)	0.309
Skin temperature (°C), mean (SD)	32.3 (1.1)	36.0 (0.5)	<0.001
Heart rate (BPM), mean (SD)	77 (16.5)	81 (11.8)	0.497
Skin type flitzpatrick (n, %)			
I	3 (37.5)	2 (25.0)	0.637
II	3 (37.5)	5 (62.5)	
III	1 (12.5)	1 (12.5)	
IV	1 (12.5)	-	
V	-	-	
VI	-	-	
Cutaneous StO_2, mean (SD)			
Basal phase	69.9 (15.3)	86.6 (10.0)	<0.001
Max. Occlusion	49.6 (16.5)	72.3 (15.9)	
Reperfusion	70.4 (16.4)	85.5 (9.9)	

Abbreviations: IQR: interquartile range; SD: standard deviation; BMI: body mass index; BPM: beats per minute; StO_2: oxygen saturation.

Figure 1. Overview of the hyperspectral snapshot camera system and its specifications. Images of the forearm of human volunteers were acquired by the hyperspectral snapshot camera, which was mounted in a black box containing four halogen light (broad band illumination) spots on top of each corner (A). The spectral response covers the wavelength range of 470-630 nm for the VIS sensor and 600-950 nm for the NIR sensor (B). The experimental prototype of the camera consists of three camera sensors (RGB-VIS-NIR) which are pixel aligned on the prism [37,38] and a 35 mm lens with a f/2.8 aperture (C). The camera is based on a tiled filter approach where pixels are individually filtered with narrow Fabry-Pérot bandpass filters (bandwidth ≈ 12 nm each). Each image acquisition leads to a hypercube with a spatial resolution of 2048 x 1080 pixels and 41 spectral bands after processing (D).

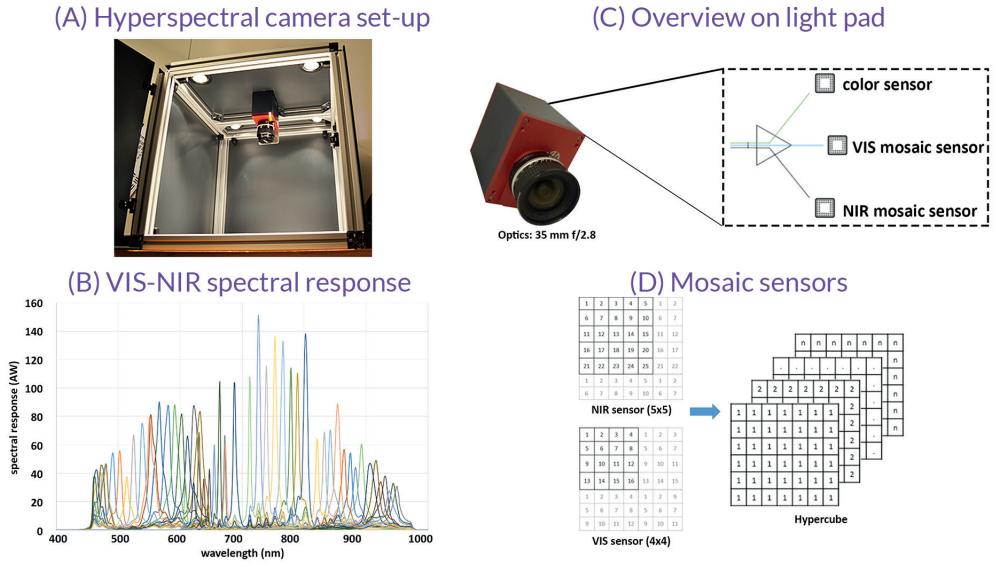

Figure 2. Comparison of single fiber reflectance spectroscopy with hyperspectral imaging for blood oxygen saturation (StO_2) detection. It shows the variation in the percentage (%) of StO_2 measured using single fiber reflectance and hyperspectral imaging. The baseline StO_2 measured before occlusion using the fiber optic reflectance technique is significantly lower than that using hyperspectral imaging. During occlusion, the skin blood volume fraction is reduced. Upon reperfusion, blood volume increases and subsequently returns to near baseline levels. It is important to note that there are substantial uncertainties in both measurements of StO_2 due to the relatively low blood volume in the interrogated region. *Abbreviation: StO_2: oxygen saturation.*

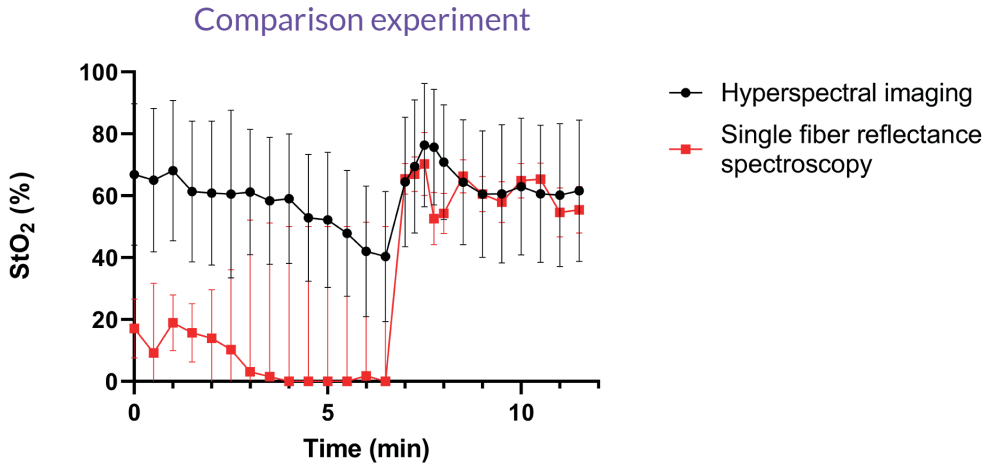

Figure 3. A typical example of the effect of vascular occlusion on superficial cutaneous oxygen saturation determined using hyperspectral imaging (color, saturation and saturation overlay maps) and perfusion determined by Laser Speckle Contrast Imaging (LSCI, perfusion maps).

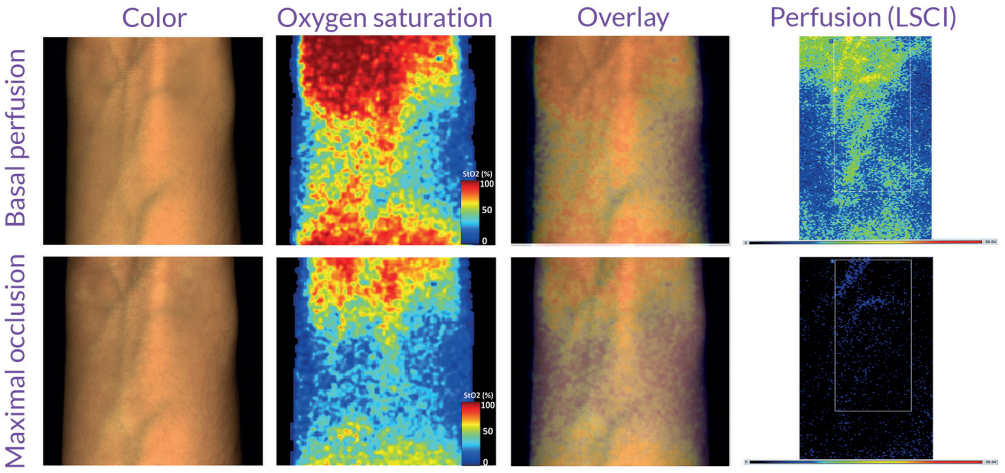

Figure 4. Correlation of cutaneous blood oxygen saturation with vascular perfusion during occlusion-reperfusion experiments in the LUMC cohort. Average of separate measurements of cutaneous blood oxygen saturation on measurement day 1 and 2 show a strong correlation with corresponding perfusion assessments by laser speckle imaging during occlusion-reperfusion experiments. Occlusion was performed after two minutes baseline measurements for a total of five minutes. Both oxygen saturation and blood flow levels returned to baseline after 12 minutes. *Abbreviations: AU: arbitrary units; StO_2: oxygen saturation.*

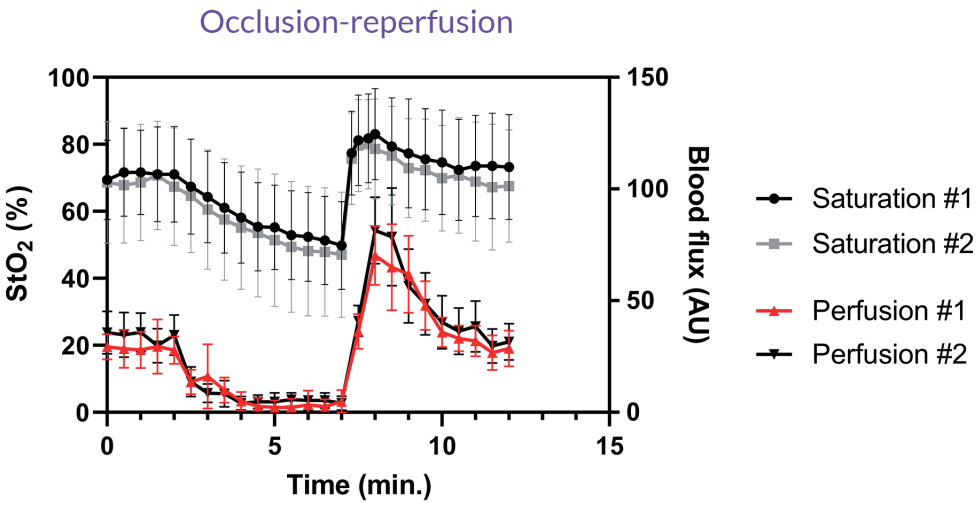

Figure 5. Tissue oxygen saturation levels after application of capsaicin cream, including subgroup analysis per cohort (LUMC *vs* MSKCC validation cohort). Cutaneous StO_2 levels did not change significantly after application of capsaicin in the most superficial layers. *Abbreviations: MSKCC: Memorial Sloan Kettering Cancer Center; LUMC: Leiden University Medical Center; StO_2: oxygen saturation.*

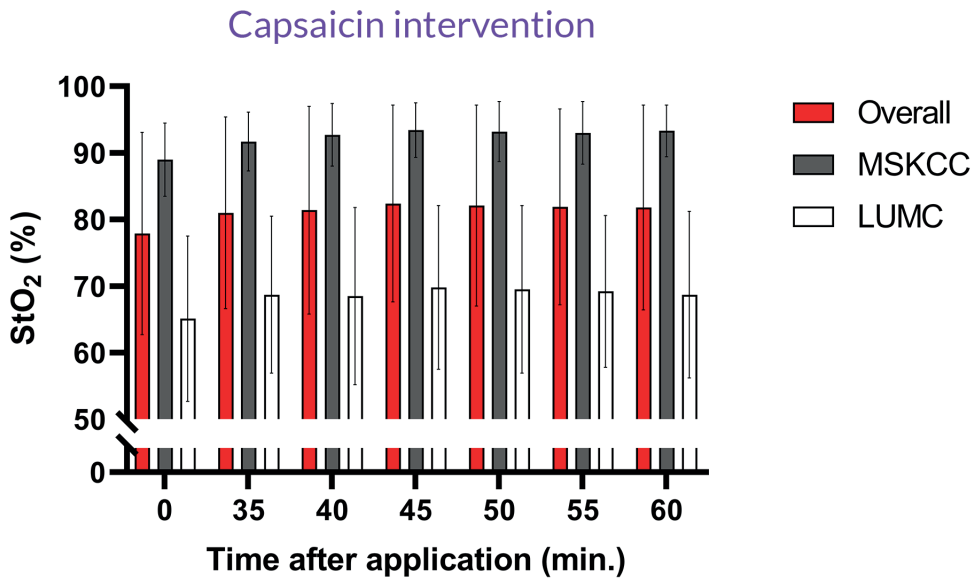

References

1. Arsenault KA, Al-Otaibi A, Devereaux PJ, Thorlund K, Tittley JG, Whitlock RP. The use of transcutaneous oximetry to predict healing complications of lower limb amputations: a systematic review and meta-analysis. *European journal of vascular and endovascular surgery : the official journal of the European Society for Vascular Surgery.* 2012;43(3):329-336.
2. Wilkins EG, Hamill JB, Kim HM, et al. Complications in Postmastectomy Breast Reconstruction: One-year Outcomes of the Mastectomy Reconstruction Outcomes Consortium (MROC) Study. *Annals of surgery.* 2018;267(1):164-170.
3. Yi J, Chen S, Backman V, Zhang HF. In vivo functional microangiography by visible-light optical coherence tomography. *Biomedical optics express.* 2014;5(10):3603-3612.
4. Lu G, Fei B. Medical hyperspectral imaging: a review. *Journal of biomedical optics.* 2014;19(1):10901.
5. Zherebtsov E, Dremin V, Popov A, et al. Hyperspectral imaging of human skin aided by artificial neural networks. *Biomedical optics express.* 2019;10(7):3545-3559.
6. Dremin V, Marcinkevics Z, Zherebtsov E, et al. Skin complications of diabetes mellitus revealed by polarized hyperspectral imaging and machine learning. *IEEE transactions on medical imaging.* 2021;Pp.
7. Kashani AH, Kirkman E, Martin G, Humayun MS. Hyperspectral computed tomographic imaging spectroscopy of vascular oxygen gradients in the rabbit retina in vivo. *PloS one.* 2011;6(9):e24482.
8. Gao L, Smith RT, Tkaczyk TS. Snapshot hyperspectral retinal camera with the Image Mapping Spectrometer (IMS). *Biomedical optics express.* 2012;3(1):48-54.
9. Amelink A, Robinson DJ, Sterenborg HJ. Confidence intervals on fit parameters derived from optical reflectance spectroscopy measurements. *Journal of biomedical optics.* 2008;13(5):054044.
10. Noguchi K, Matsuzaki T, Sakanashi M, et al. Effect of caffeine contained in a cup of coffee on microvascular function in healthy subjects. *Journal of pharmacological sciences.* 2015;127(2):217-222.
11. Gillespie JA. Vasodilator properties of alcohol. *British medical journal.* 1967;2(5547):274-277.
12. Manni F, van der Sommen F, Zinger S, et al. Hyperspectral Imaging for Skin Feature Detection: Advances in Markerless Tracking for Spine Surgery. *Applied Sciences.* 2020;10(12):4078.
13. Matheus ASM, da Matta MFB, Clemente ELS, Rodrigues MLG, Valenca DCT, Gomes MB. Sensibility and specificity of laser speckle contrast imaging according to Endo-PAT index in type 1 diabetes. *Microvascular research.* 2018;117:10-15.
14. Birkhoff WAJ, Heuberger J, Post TE, et al. Recombinant human erythropoietin does not affect several microvascular parameters in well-trained cyclists. *Physiological reports.* 2018;6(24):e13924.
15. Brooks S, Hoy CL, Amelink A, Robinson DJ, Nijsten TE. Sources of variability in the quantification of tissue optical properties by multidiameter single-fiber reflectance and fluorescence spectroscopy. *Journal of biomedical optics.* 2015;20(5):57002.
16. Hoy CL, Gamm UA, Sterenborg HJ, Robinson DJ, Amelink A. Method for rapid multidiameter single-fiber reflectance and fluorescence spectroscopy through a fiber bundle. *Journal of biomedical optics.* 2013;18(10):107005.
17. Stegehuis PL, Boogerd LS, Inderson A, et al. Toward optical guidance during endoscopic ultrasound-guided fine needle aspirations of pancreatic masses using single fiber reflectance spectroscopy: a feasibility study. *Journal of biomedical optics.* 2017;22(2):24001.
18. Buntinx L, Vermeersch S, de Hoon J. Development of anti-migraine therapeutics using the capsaicin-induced dermal blood flow model. *British journal of clinical pharmacology.* 2015;80(5):992-1000.
19. Toivonen ME, Rajani C, Klami A. Snapshot hyperspectral imaging using wide dilation networks. *Machine Vision and Applications.* 2020;32(1):9.
20. Amelink A, Bard MP, Burgers SA, Sterenborg HJ. Single-scattering spectroscopy for the endoscopic analysis of particle size in superficial layers of turbid media. *Applied optics.* 2003;42(19):4095-4101.
21. Middelburg TA, Kanick SC, de Haas ER, et al. Monitoring blood volume and saturation using superficial fibre optic reflectance spectroscopy during PDT of actinic keratosis. *Journal of biophotonics.* 2011;4(10):721-730.
22. Schober P, Boer C, Schwarte LA. Correlation Coefficients: Appropriate Use and Interpretation. *Anesthesia and analgesia.* 2018;126(5):1763-1768.
23. Barberio M, Longo F, Fiorillo C, et al. HYPerspectral Enhanced Reality (HYPER): a physiology-based surgical guidance tool. *Surgical endoscopy.* 2020;34(4):1736-1744.
24. Giannoni L, Lange F, Davies AL, et al. Hyperspectral Imaging of the Hemodynamic and Metabolic States of the Exposed Cortex: Investigating a Commercial Snapshot Solution. *Advances in experimental medicine and biology.* 2018;1072:13-20.
25. He Q, Liu T, Wang RK. Enhanced spatial resolution for snapshot hyperspectral imaging of blood perfusion and melanin information within human tissue. *Journal of biophotonics.* 2020;13(5):e202000019.
26. Rubins U, Marcinkevics Z, Cimurs J, Saknite I, Kviesis-Kipge E, Grabovskis A. Multimodal Device for Real-Time Monitoring of Skin Oxygen Saturation and Microcirculation Function. *Biosensors.* 2019;9(3).
27. Nkengne A, Robic J, Seroul P, Gueheunneux S, Jomier M, Vie K. SpectraCam(®) : A new polarized hyperspectral imaging system for repeatable and reproducible in vivo skin quantification of melanin, total hemoglobin, and oxygen saturation. *Skin research and technology : official journal of International Society for Bioengineering and the Skin (ISBS) [and] International Society for Digital Imaging of Skin (ISDIS) [and] International Society for Skin Imaging (ISSI).* 2018;24(1):99-107.
28. Zhang R, Verkruysse W, Choi B, et al. Determination of human skin optical properties from spectrophotometric measurements based on optimization by genetic algorithms. *Journal of biomedical optics.* 2005;10(2):024030.
29. Yudovsky D, Pilon L. Retrieving skin properties from in vivo spectral reflectance measurements. *Journal of biophotonics.* 2011;4(5):305-314.
30. Vyas S, Banerjee A, Burlina P. Estimating physiological skin parameters from hyperspectral signatures. *Journal of biomedical optics.* 2013;18(5):57008.
31. Jafari-Saraf L, Wilson SE, Gordon IL. Hyperspectral image measurements of skin hemoglobin compared with transcutaneous PO2 measurements. *Annals of vascular surgery.* 2012;26(4):537-548.
32. Chin MS, Freniere BB, Lo YC, et al. Hyperspectral imaging for early detection of oxygenation and perfusion changes in

irradiated skin. *Journal of biomedical optics.* 2012;17(2):026010.
33. Kabon B, Nagele A, Reddy D, et al. Obesity decreases perioperative tissue oxygenation. *Anesthesiology.* 2004;100(2):274-280.
34. Li M, Tang Y, Yao J. Photoacoustic tomography of blood oxygenation: A mini review. *Photoacoustics.* 2018;10:65-73.
35. Ghijsen M, Lentsch GR, Gioux S, et al. Quantitative real-time optical imaging of the tissue metabolic rate of oxygen consumption. *Journal of biomedical optics.* 2018;23(3):1-12.
36. Ghijsen M, Choi B, Durkin AJ, Gioux S, Tromberg BJ. Real-time simultaneous single snapshot of optical properties and blood flow using coherent spatial frequency domain imaging (cSFDI). *Biomedical optics express.* 2016;7(3):870-882.
37. IMEC (2021, April 2) https://www.imec-int.com/en/hyperspectral-imaging.
38. Geelen B, Tack N, Lambrechts A. *A compact snapshot multispectral imager with a monolithically integrated per-pixel filter mosaic.* Vol 8974: SPIE; 2014.

Part IV

Chapter 12

Summary and discussion

In the treatment of solid tumors, surgery has been the cornerstone for decades. The idea of radical surgery is inseparably linked to dr. Willem Stewart Halsted (1852-1922), who was one of the first surgeons advocating that sufficient local resection of the tumor ('the more the better') will cure the cancer patient, based on the idea that cancer spreads through the bloodstream. In principle, his theory was right, although local disease control is not effective if the tumor already has been metastasized to other organs. It took years to discover that tumor staging is of outmost importance to provide the right therapy for the individual cancer patient. In this new era of technological and digital development, the diagnosis and treatment of cancer is being dominated by technical advances, minimally invasive treatment approaches and image-guided technologies.[1,2] Advances in neoadjuvant therapies have led to improved survival for cancer patients. For some cancer types, neoadjuvant therapy showed tumor complete response, meaning that these patients did not have to undergo surgical resection.[3] Furthermore, more patients are eligible for surgical exploration, since locally advanced tumors could shrink due to the therapy, which is also the case for pancreatic cancer. However, these advances also offer new challenges for the clinician, such as preoperative evaluation of tumor response to neoadjuvant therapy and intraoperative detection of tumor tissue when it is surrounded by fibrotic tissue after neoadjuvant therapy.

Biomarkers

Biochemical markers, such as Cancer Antigen 19-9 (CA19-9) and Carcinoembryonic Antigen (CEA), are both associated with advanced disease at diagnosis, response to neoadjuvant therapy, poor survival and early recurrence in pancreatic ductal adenocarcinoma (PDAC) patients (**Chapters 2 and 3**). As discussed in this thesis, this could indicate that patients with elevated CA19-9 and CEA levels should undergo meticulous preoperative staging. Patients with locally advanced disease, which could not undergo surgical resection, often undergo induction chemotherapy (mostly FOLFIRINOX) in order to downstage the tumor, allowing radical surgical resection.[4] It has been demonstrated that a >30% decrease of CA19-9 levels is associated with response on induction chemotherapy in this patient category, which illustrates that besides CT-imaging, mainly focusing on the tumor anatomy, extracting information of the tumor biology by measuring circulating biomarkers is of additional value in the diagnostic work-up.[5] Novel biochemical markers could be extracted from circulating immune cells and their subtypes, such as exosomes, which contain microRNA.[6] Correlation of levels of a specific cell surface proteoglycan (Glypican-1) in circulating exosomes with tumor burden and survival were found, thereby serving as a potential biochemical marker in PDAC patients.[7] Evaluation of the most sensitive microRNA markers and role of these markers in the prediction of advanced stage, i.e. irresectable, pancreatic cancer should be investigated in future studies. Besides these biochemical markers, imaging technologies are currently playing the most important role. Treatment response to neoadjuvant chemotherapy is currently assessed using CT-imaging and scored with the Response Evaluation Criteria in Solid Tumors (RECIST criteria). It has to be expected that the role of imaging techniques will become more important.[8] In this thesis, several optical imaging techniques applied to pancreatic cancer diagnostics and surgery have been discussed of which some of them will probably be incorporated in the toolbox of clinicians in the future.

Exogenous contrast imaging

Near-infrared fluorescence (NIRF) imaging is one of the techniques being used and developed for intraoperative guidance.[9] Surgeons want an imaging technique which is easy to use for different applications simultaneously (in pancreatic cancer for instance both for tumor identification and visualization of the vasculature and surrounding anatomical structures [10]) and minimally interfering with the surgical field. NIRF imaging has the potential to be such a technique, which is fairly straightforward, although it could still be challenging for surgeons to implement such a technique in daily practice. Therefore, a practical guide for the abdominal surgeon was provided in this thesis (**Chapter 4**). Non-specific NIRF imaging using Indocyanine green (ICG) is already being used in daily practice for perfusion mapping, lymph node detection and tumor imaging.[11] The clinical relevance of this technique has been demonstrated for bowel perfusion imaging and is currently being investigated in a prospective trial for prediction of the tumor margin *in vivo* (consequently leading to higher resection rates and therefore survival) during resection of colorectal liver metastasis.[12,13] In pancreatic cancer imaging, NIRF imaging using ICG showed contradictory results, with low dose ICG not showing tumor-specific signals, although high dose ICG demonstrated tumor-specific accumulation of ICG in selected cases.[14,15] Furthermore, a randomized controlled trial has been performed for visualization of the bile ducts using ICG, demonstrating the benefit compared to normal white light inspection, although they have not been able to demonstrate a statistical significant different in bile duct injuries, due to the few incident cases.[16] Even in difficult cases, such as obesity and severe inflammation, NIRF imaging of the biliary ducts is very useful and is therefore currently no longer considered as experimental and in some hospitals part of standard surgical care (**Chapter 5**).[17]

As ICG accumulates non-specifically in tumor tissue, molecular-targeted fluorescence imaging, by labeling fluorescent dyes to a targeting moiety, has been introduced (**Chapter 6**). For tumor-targeted fluorescence imaging three aspects are of outmost importance: target selection, probe design, and a dedicated camera system.

First, the ideal tumor target could be scored by using the TASC scoring system, of which the most important criteria are extracellular protein localization, diffuse upregulation through tumor tissue, high expression in tumor versus normal tissue (>10) and upregulation in a large percentage of the patients.[18] For pancreatic cancer several tumor (-associated) targets have been identified.[19,20] Until now, for intraoperative tumor-targeted fluorescence imaging of pancreatic cancer monoclonal antibodies against CEA, epidermal growth factor receptor (EGFR) and vascular endothelial growth factor (VEGF) receptor, which have been conjugated to a NIR fluorophore have been evaluated in clinical studies.[21-23](NCT02743975) Most recently, Panitumumab-IRDYe800CW (EGFR-targeted) showed promising results for pancreatic cancer visualization, even during minimally invasive surgical procedures.[23] However, important to realize is the effect of neoadjuvant therapy on the expression of the target in the tissue. It has been demonstrated that neoadjuvant therapy significantly affected the expression patterns of EGFR and VEGF in pancreatic tumors, which is not the case for CEA and integrin $\alpha_v\beta_6$.[24] This is clinically relevant, since more PDAC patients are treated with neoadjuvant therapies. In the nearby future, it would be interesting to select the most optimal target (and consequently the most suitable tracer for this patient) based on the expression pattern on the diagnostic FNB biopsies.[25] Designing fluorescence tracers also comes with

challenges, amongst others choosing the targeting moiety, a NIR fluorophore and conjugation strategy, to obtain the most optimal pharmacokinetics and specificity. Currently, clinically translated fluorescent tracers mostly consist of a fluorescently labeled monoclonal antibody, as these are capable of effectively recognizing specific cell-surface expressed antigens and are readily available. Recently, smaller particles, such as antibody fragments, protein scaffolds, peptides, and small molecules are also being investigated, as these have advantages such as better tumor penetration and more rapid clearance from non-targeted tissues with similar binding characteristics.[26] An example of antibody fragments are nanobodies, which are derived from camelid heavy-chain only antibodies.[27] Conjugation of a CEA nanobody to the zwitterionic fluorescent dye ZW800-1 results in fast tumor delineation, good tumor visualization and rapid background clearance through renal excretion (**Chapter 7**). Our study showed similar results concerning tumor-to-background ratio compared to labeling with IRDye800CW.[28] Furthermore, our results were in concordance with a recent paper of Baart et al. demonstrating that smaller fragments result in earlier tumor visualization, however at the expense of peak fluorescence.[29] Another strategy to improve intraoperative tumor visualization would be to use tracers, that are activated by tumor-specific biochemical processes and therefore decreasing background fluorescence.[30]

Lastly, the camera system should closely match the used fluorophore.[31] Currently, many camera systems are FDA approved for the use of ICG, however, are being used off-label for other fluorescent dyes. It is important to realize that the excitation light waves should match the optimal excitation wavelengths of the injected fluorophore.

To take this promising technique to the next level, it should overcome its limitations, such as lack of quantification and standardization, limited penetration depth, and providing clinical benefit.[26,32] First, quantification is an important step to provide quantitative objective measures instead of subjective, user-dependent values. Quantification methods include temporal analysis of fluorescence dynamic signals, ratiometric imaging using additional reflectance channel to normalize fluorescence and quantitative fluorescence imaging using spectral or spatial modulation of light.[33-35] The first method is currently being used in vascular and colorectal surgery, to determine tissue perfusion.[34,36] Implementation of this quantification method has been realized by displaying the quantitative results in a heatmap next to the RGB and NIR image. The first results of quantitative fluorescence imaging using spectral and spatial modulation of light have been published in 2017 and (pre)clinical validation of this technique is currently ongoing.[33,37] To overcome limited depth penetration, instead of imaging in the NIR-1 window, using other camera systems one can also image in the second NIR window (1000-1400 nm). In the NIR-2 window there is less autofluorescence and less scattering, which could result in improved tumor delineation and improved perfusion detection.[38,39] The last years also organic dyes, being less toxic and also suitable for conjugation to target moieties, have been developed.[40] Another option to deal with the limited penetration depth would be to develop hybrid fluorescent and radioactive targeted tracers, since gamma rays are hardly attenuated by overlying tissues.[41] Third, phase-III studies are ongoing to demonstrate the clinical benefit of tumor-targeted fluorescence imaging. For these studies it is paramount to propose clinically meaningful (surrogate) endpoints that are acceptable to authorities, such as percentage of tumor-positive margins, to convince the regulatory authorities and reimbursement agencies.[32]

Endogenous contrast imaging

Three different techniques using endogenous contrast have been described in this thesis. First, OCT has been mainly used during endoscopic interventions (**Chapter 8**). For pancreatic cancer, one study demonstrated its use for detection of cancer causing obstruction of the bile ducts.[42] With the introduction of FF-OCT, higher resolution could be achieved. FF-OCT could potentially also being used during FNB on a back-table, similar to rapid on-site evaluation, in order to prevent unnecessary secondary endoscopies, which is already demonstrated for intestinal biopsies.[43,44] In our study we validated FF-OCT on *ex vivo* resected specimen, which could pave the way for intraoperative use of the technique as back-table frozen section analysis (**Chapter 9**). For pancreatic cancer, this could be significant clinical relevance due to the difficulties with distinguishing fibrosis (caused by neoadjuvant therapy), pancreatitis, and viable tumor tissue, for instance at the vascular resection margin.[45] Furthermore it could be of significant use in patients with an intraductal papillary mucinous neoplasm or a distal cholangiocarcinoma, where it is sometimes challenging to determine the margin of the grade of dysplasia. Current developments are focusing on building a handheld FF-OCT camera, that can be used intraoperatively.[46] Nevertheless, improvements in image quality (i.e. contrast), acquisition times and more training in interpretation of FF-OCT images are necessary to make this technique part of the toolbox of the future clinician. Improvements in contrast is currently being implemented in the next generation FF-OCT systems, in which dynamic cell imaging is implemented.[47] Dynamic cell imaging is based on measuring temporal fluctuations of back-scattered light, thereby revealing sub-cellular structures having weak back-scattering. Furthermore, acquisition times are being improved (1 minute for a 1 cm^2 region of interest of tissue) as well as snapshot FF-OCT cameras have been developed, however not evaluated in clinical studies.[48,49] Lastly, image interpretation is difficult since pathologist are familiar with histology images, which illustrates the need for training using an atlas. This also offers opportunities to use computer-based learning (using for instance artificial neural networks) techniques to assist in the interpretation of the FF-OCT image. For instance, for detection of collagen topology, which differs significantly between normal pancreatic tissue, pancreatitis and pancreatic tumors.[50] Moreover, it has been suggested that collagen topology is correlated with chemosensitivity in breast cancer.[51] It would also be interesting to assess whether this is also the case for pancreatic tumors in future studies.

Secondly, reflectance spectroscopy has been used for several applications over the last years. In the diagnostic process of pancreatic cancer, it could have potential to aid during EUS-FNB (**Chapter 10**). It has also been used for intraoperative use to distinguish tumor from pancreatitis and normal pancreatic tissue. Semi-automatic analysis showed significant feature differences for these tissue types.[52] However as in our study, both methods are lacking real-time visualization of the acquired spectra, which is necessary to provide feedback to the clinician. Another application would be to intraoperatively sample lymph node metastases from pancreatic cancer, since lymph nodes are solid masses with typical spectra and already demonstrated to be highly accurate in intraoperative detection of lymph node metastases from head-neck cancers.[53] During pancreatic cancer surgery, sampling of para-aortal lymph nodes is controversial, as tumor-positive lymph nodes are considered as metastatic disease. However, some groups are advocating that resection of the primary tumor including the tumor-positive lymph nodes could be beneficial for the patient with

respect to overall survival.[54] Reflectance spectroscopy has also been used for screening of upper gastrointestinal and respiratory tract cancers, by measuring the optical field effect in the mucosal area of the oral cavity.[55] Contradictory results have been published on this effect, however this would be interesting and relevant to investigate this hypothesis in high-risk population of pancreatic cancer patients (for instance in CDKN2A-P16-Leiden mutation carriers). Instead of undergoing yearly EUS-FNB and/or MRI a spectroscopic measurement of the oral mucosa is less invasive. A certain disadvantage of reflectance spectroscopy is its reliance on reference methods and model ('spectral fitting') development. Furthermore, the measurements are located at one point corresponding to the fiber's diameter and thereby not providing an image. For this purpose hyperspectral cameras have been developed.

In this thesis a study of a novel hyperspectral snapshot camera for oxygen saturation imaging was presented (**Chapter 11**). As this system had multiple wavelength bands in the VIS-NIR window it could potentially also be used for detection of different tissue types. However, due to the snapshot design it lacks resolution and it is difficult to perform real-time imaging as image analysis is time-consuming. Currently, other hyperspectral cameras, dedicated for oxygen saturation imaging (thereby only including a certain combination of wavelength bands specific for oxygen saturation detection), have been approved for clinical use and evaluated for bowel, liver and kidney oxygenation analysis. Comparison of hyperspectral imaging with NIRF imaging showed similar performance in terms of detection between well and poorly perfused tissue in colorectal anastomosis.[56] In pancreatic cancer surgery, it is relevant to determine the oxygen saturation at the anastomotic sites since leakage of the pancreatojejunostomy, which is a main source of major morbidity and even mortality after a pancreaticoduodenectomy, is associated with poor perfusion and oxygenation.[57] Furthermore, during distal pancreatic resection, the splenic artery often needs to be dissected, resulting in less perfusion of the spleen followed by a splenectomy. In order to determine the sufficiency of the perfusion of the spleen via the gastric vasa brevia, intraoperative oxygen saturation mapping using hyperspectral imaging would therefore be useful to evaluate in future studies. For breast and colorectal cancer detection, hyperspectral imaging (using a pushbroom or line scan camera) demonstrated interesting results on *ex vivo* resected specimen, although the imaged tissue has to be fixed on a moving table below the camera and imaging could not be performed real-time.[58,59] Therefore, for intraoperative tumor visualization it seems that current state-of-the-art hyperspectral cameras are not yet suitable. Incorporating hyperspectral cameras capable of imaging in the SWIR or NIR-2 window (InGAas sensors) next to the VIS-NIR cameras will improve the spectral resolution, probably resulting in better capabilities to delineate tumor tissue, however current application into the clinic is far away.[60]

Other imaging techniques

Other optical techniques, which were out of the scope of this thesis include confocal laser endomicroscopy, Cherenkov luminescence imaging, laser speckle contrast imaging and Raman spectroscopy and could potentially also be of significant value for the clinician in both intraoperative and preoperative diagnostic process.[2] For instance Raman Spectroscopy, which is providing

chemical and structural information on the illuminated tissue, showed interesting results in preclinical studies, however implementation of fast and automatic feature extraction is necessary to perform the first clinical studies.[61] Also combining nuclear or photoacoustic imaging with optical imaging is an interesting opportunity being explored pre- and intraoperatively. In the diagnostic process of pancreatic cancer, PET-CT using a 18F-FDG labeled tracer seems already to be specific in monitoring tumor response on neoadjuvant therapy.[62] Therefore, molecular targeted PET-CT is currently being investigated. Both single-photon emission computerized tomography and photoacoustic imaging can overcome the limited penetration depth of NIRF imaging, thereby acting as additional tools to visualize pancreatic tumors in the future.[63]

Conclusions

In conclusion, many optical techniques have been developed the last years, of which some of them have the potential to be incorporated in existing endoscopic, laparoscopic or robotic systems, enabling improved diagnostics and more precise surgery. Interdisciplinary collaboration is therefore necessary to implement these techniques into daily practice. In this thesis, main topic was to investigate biomarkers and novel optical techniques in patient undergoing surgical exploration, however most pancreatic cancer patients have advanced disease at time of diagnosis. This illustrates that it is paramount to focus future research also on efficient screening methods and improvement of systemic therapies for locally advanced and metastasized patients, thereby enabling improved survival.

References

1. Ruers TJM. The future of surgical oncology. *Br J Surg.* 2019;106(6):663-664.
2. Mascagni P, Longo F, Barberio M, et al. New intraoperative imaging technologies: Innovating the surgeon's eye toward surgical precision. *J Surg Oncol.* 2018;118(2):265-282.
3. van der Valk MJM, Hilling DE, Bastiaannet E, et al. Long-term outcomes of clinical complete responders after neoadjuvant treatment for rectal cancer in the International Watch & Wait Database (IWWD): an international multicentre registry study. *Lancet.* 2018;391(10139):2537-2545.
4. Janssen QP, van Dam JL, Doppenberg D, et al. FOLFIRINOX as Initial Treatment for Localized Pancreatic Adenocarcinoma: A Retrospective Analysis by the Trans-Atlantic Pancreatic Surgery (TAPS) Consortium. *J Natl Cancer Inst.* 2022.
5. van Veldhuisen E, Vogel JA, Klompmaker S, et al. Added value of CA19-9 response in predicting resectability of locally advanced pancreatic cancer following induction chemotherapy. *HPB (Oxford).* 2018;20(7):605-611.
6. van der Sijde F, Mustafa DAM, Vietsch EE, Katsikis PD, van Eijck CHJ. Circulating Immunological Biomarkers: Prognosis of Pancreatic Cancer Patients Reflected by the Immune System. *Pancreas.* 2021;50(7):933-941.
7. Melo SA, Luecke LB, Kahlert C, et al. Glypican-1 identifies cancer exosomes and detects early pancreatic cancer. *Nature.* 2015;523(7559):177-182.
8. Handgraaf HJ, Boonstra MC, Van Erkel AR, et al. Current and future intraoperative imaging strategies to increase radical resection rates in pancreatic cancer surgery. *Biomed Res Int.* 2014;2014:890230.
9. Vahrmeijer AL, Hutteman M, van der Vorst JR, van de Velde CJ, Frangioni JV. Image-guided cancer surgery using near-infrared fluorescence. *Nature reviews Clinical oncology.* 2013;10(9):507-518.
10. de Muynck L, White KP, Alseidi A, et al. Consensus Statement on the Use of Near-Infrared Fluorescence Imaging during Pancreatic Cancer Surgery Based on a Delphi Study: Surgeons' Perspectives on Current Use and Future Recommendations. *Cancers.* 2023;15(3).
11. van Manen L, Handgraaf HJM, Diana M, et al. A practical guide for the use of indocyanine green and methylene blue in fluorescence-guided abdominal surgery. *Journal of surgical oncology.* 2018;118(2):283-300.
12. Achterberg FB, Sibinga Mulder BG, Meijer RPJ, et al. Real-time surgical margin assessment using ICG-fluorescence during laparoscopic and robot-assisted resections of colorectal liver metastases. *Ann Transl Med.* 2020;8(21):1448.
13. Jafari MD, Wexner SD, Martz JE, et al. Perfusion assessment in laparoscopic left-sided/anterior resection (PILLAR II): a multi-institutional study. *J Am Coll Surg.* 2015;220(1):82-92. e81.
14. Newton AD, Predina JD, Shin MH, et al. Intraoperative Near-infrared Imaging Can Identify Neoplasms and Aid in Real-time Margin Assessment During Pancreatic Resection. *Ann Surg.* 2019;270(1):12-20.
15. Hutteman M, van der Vorst JR, Mieog JS, et al. Near-infrared fluorescence imaging in patients undergoing pancreaticoduodenectomy. *Eur Surg Res.* 2011;47(2):90-97.
16. Dip F, LoMenzo E, Sarotto L, et al. Randomized Trial of Near-infrared Incisionless Fluorescent Cholangiography. *Ann Surg.* 2019;270(6):992-999.
17. Dip F, Boni L, Bouvet M, et al. Consensus Conference Statement on the General Use of Near-infrared Fluorescence Imaging and Indocyanine Green Guided Surgery: Results of a Modified Delphi Study. *Ann Surg.* 2022;275(4):685-691.
18. van Oosten M, Crane LM, Bart J, van Leeuwen FW, van Dam GM. Selecting Potential Targetable Biomarkers for Imaging Purposes in Colorectal Cancer Using TArget Selection Criteria (TASC): A Novel Target Identification Tool. *Transl Oncol.* 2011;4(2):71-82.
19. Tummers WS, Farina-Sarasqueta A, Boonstra MC, et al. Selection of optimal molecular targets for tumor-specific imaging in pancreatic ductal adenocarcinoma. *Oncotarget.* 2017;8(34):56816-56828.
20. de Geus SW, Boogerd LS, Swijnenburg RJ, et al. Selecting Tumor-Specific Molecular Targets in Pancreatic Adenocarcinoma: Paving the Way for Image-Guided Pancreatic Surgery. *Mol Imaging Biol.* 2016;18(6):807-819.
21. Tummers WS, Miller SE, Teraphongphom NT, et al. Intraoperative Pancreatic Cancer Detection using Tumor-Specific Multimodality Molecular Imaging. *Ann Surg Oncol.* 2018;25(7):1880-1888.
22. Hoogstins CES, Boogerd LSF, Sibinga Mulder BG, et al. Image-Guided Surgery in Patients with Pancreatic Cancer: First Results of a Clinical Trial Using SGM-101, a Novel Carcinoembryonic Antigen-Targeting, Near-Infrared Fluorescent Agent. *Ann Surg Oncol.* 2018;25(11):3350-3357.
23. Lu G, van den Berg NS, Martin BA, et al. Tumour-specific fluorescence-guided surgery for pancreatic cancer using panitumumab-IRDye800CW: a phase 1 single-centre, open-label, single-arm, dose-escalation study. *Lancet Gastroenterol Hepatol.* 2020;5(8):753-764.
24. Vuijk FA, de Muynck L, Franken LC, et al. Molecular targets for diagnostic and intraoperative imaging of pancreatic ductal adenocarcinoma after neoadjuvant FOLFIRINOX treatment. *Sci Rep.* 2020;10(1):16211.
25. Houvast RD, van Duijvenvoorde M, Chua J, et al. Prediction of Biomarker Expression on Primary Pancreatic Ductal Adenocarcinoma Tissues Using Fine-Needle Biopsies: Paving the Way for a Patient-Tailored Molecular Imaging Approach. *Molecular diagnosis & therapy.* 2023.
26. Hernot S, van Manen L, Debie P, Mieog JSD, Vahrmeijer AL. Latest developments in molecular tracers for fluorescence image-guided cancer surgery. *Lancet Oncol.* 2019;20(7):e354-e367.
27. Debie P, Devoogdt N, Hernot S. Targeted Nanobody-Based Molecular Tracers for Nuclear Imaging and Image-Guided Surgery. *Antibodies (Basel).* 2019;8(1).
28. Lwin TM, Hernot S, Hollandsworth H, et al. Tumor-specific near-infrared nanobody probe rapidly labels tumors in an orthotopic mouse model of pancreatic cancer. *Surgery.* 2020;168(1):85-91.
29. Baart VM, van Manen L, Bhairosingh SS, et al. Side-by-Side Comparison of uPAR-Targeting Optical Imaging Antibodies and Antibody Fragments for Fluorescence-Guided Surgery of Solid Tumors. *Mol Imaging Biol.* 2021.
30. Voskuil FJ, Steinkamp PJ, Zhao T, et al. Exploiting metabolic acidosis in solid cancers using a tumor-agnostic pH-activatable nanoprobe for fluorescence-guided surgery. *Nat Commun.* 2020;11(1):3257.
31. Gioux S, Choi HS, Frangioni JV. Image-guided surgery using invisible near-infrared light: fundamentals of clinical translation. *Mol Imaging.* 2010;9(5):237-255.

32. Mieog JSD, Achterberg FB, Zlitni A, et al. Fundamentals and developments in fluorescence-guided cancer surgery. *Nature reviews Clinical oncology.* 2022;19(1):9-22.
33. Valdes PA, Angelo JP, Choi HS, Gioux S. qF-SSOP: real-time optical property corrected fluorescence imaging. *Biomed Opt Express.* 2017;8(8):3597-3605.
34. Diana M, Agnus V, Halvax P, et al. Intraoperative fluorescence-based enhanced reality laparoscopic real-time imaging to assess bowel perfusion at the anastomotic site in an experimental model. *Br J Surg.* 2015;102(2):e169-176.
35. Ntziachristos V, Turner G, Dunham J, et al. Planar fluorescence imaging using normalized data. *J Biomed Opt.* 2005;10(6):064007.
36. Van Den Hoven P, Tange F, Van Der Valk J, et al. Normalization of Time-Intensity Curves for Quantification of Foot Perfusion Using Near-Infrared Fluorescence Imaging With Indocyanine Green. *J Endovasc Ther.* 2022:15266028221081085.
37. Ségaud S, van Manen L, de Muynck LDA, et al. *Widefield quantitative fluorescence imaging applied to tumor margin assessment*. Vol 11625: SPIE; 2021.
38. Hu Z, Fang C, Li B, et al. First-in-human liver-tumour surgery guided by multispectral fluorescence imaging in the visible and near-infrared-I/II windows. *Nat Biomed Eng.* 2020;4(3):259-271.
39. Byrd B, Marois M, Tichauer K, et al. First experience imaging short-wave infrared fluorescence in a large animal: indocyanine green angiography of a pig brain. *Journal of Biomedical Optics.* 2019;24(8):080501.
40. Zhu S, Tian R, Antaris AL, Chen X, Dai H. Near-Infrared-II Molecular Dyes for Cancer Imaging and Surgery. *Adv Mater.* 2019;31(24):e1900321.
41. van Leeuwen FWB, van Oosterom MN, Meershoek P, et al. Minimal-Invasive Robot-Assisted Image-Guided Resection of Prostate-Specific Membrane Antigen-Positive Lymph Nodes in Recurrent Prostate Cancer. *Clin Nucl Med.* 2019;44(7):580-581.
42. Arvanitakis M, Hookey L, Tessier G, et al. Intraductal optical coherence tomography during endoscopic retrograde cholangiopancreatography for investigation of biliary strictures. *Endoscopy.* 2009;41(8):696-701.
43. Zhou W, Li SY, Li J, et al. Comparison of full-field optical coherence tomography imaging for pancreatic tissue sample obtained by EUS-fine-needle biopsy and conventional histological examination: A study protocol for a prospective trial. *Endosc Ultrasound.* 2020;9(6):380-384.
44. Quénéhervé L, Olivier R, Gora MJ, et al. Full-field optical coherence tomography: novel imaging technique for extemporaneous high-resolution analysis of mucosal architecture in human gut biopsies. *Gut.* 2021;70(1):6-8.
45. Groen JV, van Manen L, van Roessel S, et al. Resection of the Portal-Superior Mesenteric Vein in Pancreatic Cancer: Pathological Assessment and Recurrence Patterns. *Pancreas.* 2021;50(8):1218-1229.
46. Tang Y, Gao W. Effects of orientation deviation of a beam splitter and a reference mirror on the stability of a two-interferometer-based handheld FFOCT imaging probe. *Appl Opt.* 2021;60(20):5942-5952.
47. Scholler J, Groux K, Goureau O, et al. Dynamic full-field optical coherence tomography: 3D live-imaging of retinal organoids. *Light Sci Appl.* 2020;9:140.
48. Iyer RR, Žurauskas M, Cui Q, Gao L, Theodore Smith R, Boppart SA. Full-field spectral-domain optical interferometry for snapshot three-dimensional microscopy. *Biomed Opt Express.* 2020;11(10):5903-5919.
49. Aquyre Biosciences. https://aquyre.com/celtivity-tm/.
50. Drifka CR, Tod J, Loeffler AG, et al. Periductal stromal collagen topology of pancreatic ductal adenocarcinoma differs from that of normal and chronic pancreatitis. *Mod Pathol.* 2015;28(11):1470-1480.
51. Dekker TJ, Charehbili A, Smit VT, et al. Disorganised stroma determined on pre-treatment breast cancer biopsies is associated with poor response to neoadjuvant chemotherapy: Results from the NEOZOTAC trial. *Mol Oncol.* 2015;9(6):1120-1128.
52. Wilson RH, Chandra M, Scheiman JM, et al. Tissue Classification Using Optical Spectroscopy Accurately Differentiates Cancer and Chronic Pancreatitis. *Pancreas.* 2017;46(2):244-251.
53. Bugter O, Aaboubout Y, Algoe M, et al. Detecting head and neck lymph node metastases with white light reflectance spectroscopy; a pilot study. *Oral Oncol.* 2021;123:105627.
54. Pranger BK, Tseng DSJ, Ubels S, et al. How to Approach Para-Aortic Lymph Node Metastases During Exploration for Suspected Periampullary Carcinoma: Resection or Bypass? *Ann Surg Oncol.* 2020;27(8):2949-2958.
55. Post AL, de Groof AJ, Zhang XU, et al. Toward improved endoscopic surveillance with multidiameter single fiber reflectance spectroscopy in patients with Barrett's esophagus. *J Biophotonics.* 2021;14(4):e202000351.
56. Jansen-Winkeln B, Germann I, Köhler H, et al. Comparison of hyperspectral imaging and fluorescence angiography for the determination of the transection margin in colorectal resections-a comparative study. *Int J Colorectal Dis.* 2021;36(2):283-291.
57. Bassi C, Marchegiani G, Dervenis C, et al. The 2016 update of the International Study Group (ISGPS) definition and grading of postoperative pancreatic fistula: 11 Years After. *Surgery.* 2017;161(3):584-591.
58. Kho E, de Boer LL, Van de Vijver KK, et al. Hyperspectral Imaging for Resection Margin Assessment during Cancer Surgery. *Clin Cancer Res.* 2019;25(12):3572-3580.
59. Baltussen EJM, Kok END, Brouwer de Koning SG, et al. Hyperspectral imaging for tissue classification, a way toward smart laparoscopic colorectal surgery. *J Biomed Opt.* 2019;24(1):1-9.
60. Lu G, Fei B. Medical hyperspectral imaging: a review. *J Biomed Opt.* 2014;19(1):10901.
61. Lauwerends LJ, Abbasi H, Bakker Schut TC, et al. The complementary value of intraoperative fluorescence imaging and Raman spectroscopy for cancer surgery: combining the incompatibles. *Eur J Nucl Med Mol Imaging.* 2022.
62. de Jong TL, Koopman D, van der Worp CAJ, et al. Added value of digital FDG-PET/CT in disease staging and restaging in patients with resectable or borderline resectable pancreatic cancer. *Surg Oncol.* 2023;47:101909.
63. Tummers WS, Willmann JK, Bonsing BA, Vahrmeijer AL, Gambhir SS, Swijnenburg RJ. Advances in Diagnostic and Intraoperative Molecular Imaging of Pancreatic Cancer. *Pancreas.* 2018;47(6):675-689.

Chapter 13
Nederlandse samenvatting

Alvleesklierkanker is een agressieve vorm van kanker met een slechte prognose, aangezien ongeveer 80% van de patiënten op het moment van de diagnose lokaal gevorderde ziekte of uitzaaiingen heeft. Alleen patiënten met gelokaliseerde tumoren kunnen worden geopereerd, al dan niet voorafgegaan door neoadjuvante (chemo/radio)therapie. De diagnostiek van een patiënt met alvleesklierkanker bestaat uit preoperatieve stadiëring met behulp van specifieke beeldvormingstechnieken, waarvan computertomografie (CT) momenteel de belangrijkste is. Tumormarkers, zoals cancer antigen 19-9 (CA19-9) en carcinoembryonaal antigeen (CEA) kunnen ook worden gebruikt om het biologische gedrag van alvleesklierkanker te voorspellen. In het diagnostisch traject speelt het verkrijgen van histologisch bewijs middels een biopt tijdens echogeleide endoscopie een belangrijke rol om de diagnose te verkrijgen. Desalniettemin, in het geval van pancreatitis, wat het tumorweefsel vaak omringt, is het soms moeilijk om weefsel met tumorcellen te verkrijgen, ter bevestiging van de diagnose. Intra-operatief moet de alvleesklierchirurg bepaalde uitdagingen het hoofd bieden, zoals een adequate intra-operatieve beoordeling van de omvang van de tumor en/of detectie van uitzaaiingen, waarvan het laatstgenoemde ervoor zorgt dat de operatie afgebroken moet worden. De aanwezigheid van peri-tumorale ontsteking of weefselfibrose na neoadjuvante therapie maakt het onderscheid maken met tumorweefsel nog ingewikkelder. Momenteel is niet bewezen dat intra-operatieve beeldvormingstechnieken een significante toegevoegde waarde hebben, zodat de chirurg moet vertrouwen op visuele inspectie en palpatie, waarvan het laatste alleen mogelijk is bij open chirurgie. De prognose van de patiënt na de operatie hangt voornamelijk af van de volledigheid van de chirurgische resectie. Momenteel voeren alvleesklierchirurgen operaties uit met een hoog risico (5% mortaliteit; 50% grote complicaties) en daarbij tot 75% van de operaties waarbij er (op microscopisch niveau) tumorweefsel achterblijft, wat aantoont dat er verbetering mogelijk is.

Dit proefschrift beschrijft de potentiële rol van tumormarkers en experimentele beeldvormingstechnieken in zowel het diagnostisch als intra-operatieve traject van een patiënt met alvleesklierkanker.

Deel 1 De rol van tumormarkers in de diagnostiek

Deel I bespreekt de klinische implicaties van de tumormarkers CA19-9 en CEA bij patiënten met alvleesklierkanker. **Hoofdstuk 2** beschrijft de diagnostische nauwkeurigheid van deze tumormarkers voor de voorspelling van gevorderd alvleesklierkanker en stelt voor om een combinatie van CA19-9 en CEA serumspiegels te gebruiken als extra hulpmiddel voor het preoperatief inschatten van de resectabiliteit van de tumor tijdens multidisciplinaire teambesprekingen. De combinatie van beide tumormarkers hebben een hoge positief voorspellende waarde van 91% voor het voorspellen van uitgezaaid en/of lokaal gevorderd alvleesklierkanker.

Hoofdstuk 3 analyseert de prognostische waarde van CA19-9 en CEA als tumormarkers voor overleving en recidief in patiënten met alvleesklierkanker in een retrospectieve cohort studie en bovendien zijn deze bevindingen vergeleken met bestaande literatuur. Hieruit werd geconcludeerd dat patiënten met een preoperatief verhoogd CA19-9, die een resectie hebben ondergaan, een verhoogde kans hebben op een vroeg recidief, terwijl een verhoogd preoperatief CEA niet een duidelijke associatie heeft met een vroeg recidief. Zowel een verhoogd CEA als CA19-9 preoperatief zijn wel geassocieerd met een slechtere overleving.

Deel 2 Beeldvorming met exogene contrastmiddelen

Deel II richt zich op optische beeldvorming van alvleesklierkanker met behulp van exogene contrastmiddelen voor intra-operatieve beeldvorming in het nabij-infraroodgebied (NIR). **Hoofdstuk 4** geeft een praktische handleiding, inclusief optimale doses en injectietijden, voor NIR fluorescentie beeldvorming met behulp van fluorescerende stoffen tijdens abdominale (oncologische) chirurgie. Indocyanine groen (ICG) kan gebruikt worden voor visualisatie van schildwachtklieren, galwegen, weefselperfusie en levertumoren. Methyleenblauw is tot op heden beperkt getest voor visualisatie van de ureteren, alhoewel dit klinisch minder goed toepasbaar is vanwege het hoge achtergrondsignaal.

Hoofdstuk 5 toont een voorbeeld van succesvolle intra-operatieve visualisatie van de anatomie van de galwegen en illustreert dat NIR fluorescentie beeldvorming met behulp van ICG tijdens moeilijke robot-geassisteerde chirurgische ingrepen van de galwegen effectief is en daarom ten zeerste wordt aanbevolen.

Hoofdstuk 6 bespreekt preklinische studies, lopende klinische studies en de laatste ontwikkelingen op het gebied van moleculaire NIR tracers voor fluorescentie-geleide oncologische chirurgie. De eerste moleculair gerichte fluorescerende stoffen, waarvan de meeste bestaan uit goedgekeurde therapeutische antilichamen die zijn geconjugeerd aan een fluorescerende stof, zijn geëvalueerd in verschillende klinische studies. Bovendien hebben ontwikkelingen op het gebied van proteïne-engineering en geneesmiddelenontwerp geleid tot de productie van een verscheidenheid aan tracers die geschikt zijn voor moleculaire fluorescentie-geleide chirurgie.

In hoofdstuk 7 is een CEA-gerichte tracer in de vorm van een nanobody geconjugeerd aan een fluorescente stof (ZW800-1) preklinisch geëvalueerd voor intra-operatieve visualisatie van alvleesklierkanker. Het voordeel van deze fluorescente tracer is dat het snel door de nieren geklaard wordt en ook binnen een paar uur goede opname in de tumor heeft, wat significant sneller is dan bij het gebruik van een monoklonaal antilichaam als target. Bovendien kan deze tracer potentieel ook gebruikt worden voor andere tumoren, zoals dikke darm tumoren, waarbij CEA als tumormarker ook tot overexpressie komt.

Deel 3 Beeldvorming met endogene contrastmiddelen

Deel III beschrijft de optische beeldvorming van alvleesklierkanker met behulp van endogene (lichaamseigen) contrastmiddelen. **Hoofdstuk 8** geeft een overzicht van de klinische bruikbaarheid van optische coherentie tomografie (OCT) tijdens oncologische interventies. In de nabije toekomst zou OCT kunnen worden gebruikt als extra hulpmiddel tijdens bronchoscopische of endoscopische interventies en zou het ook kunnen worden toegepast bij margebeoordeling tijdens (laparoscopische) oncologische chirurgie als een laparoscopisch of handheld OCT-apparaat verder zal worden ontwikkeld om routinematig klinisch gebruik mogelijk te maken.

In **hoofdstuk 9** wordt het gebruik van hoge resolutie (Full-Field) OCT beschreven om onderscheid te maken tussen kwaadaardig en goedaardig alvleesklierweefsel. Vergeleken met conventionele histologie werd er een algemene accuraatheid van 73% voor het aantonen van een maligniteit, wat

verbeterde in patiënten met adenocarcinoom, waarin 97% van de hoge resolutie OCT beelden beoordeeld werden als tumor door tenminste 1 patholoog. Deze studie toont aan dat deze techniek de potentie heeft om intra-operatief gebruikt te worden voor het beoordelen van de resectiemarges.

Hoofdstuk 10 bevat de resultaten van een prospectieve cohort studie, die de diagnostische nauwkeurigheid evalueert van reflectiespectroscopie tijdens echogeleide endoscopie voor het detecteren van alvleesklierkanker. Na analyse van de optische spectra, werd er in een cohort van 45 patiënten met verdenking op alvleesklierkanker een hoge diagnostische accuratesse bereikt van 91% voor het detecteren van alvleesklierkanker.

Hoofdstuk 11 bespreekt de resultaten van een nieuw hyperspectraal snapshot camerasysteem voor detectie van intra-operatieve zuurstofsaturatie. In twee separate onderzoekscentra werd er op afzonderlijke studiedagen zuurstofsaturatie metingen van de huid uitgevoerd met een hoge mate van betrouwbaarheid. Hiermee wordt de weg vrijgemaakt voor toekomstige studies in bijvoorbeeld vaatchirurgie en tevens eventuele implementatie tijdens alvleesklierchirurgie.

Concluderend beschrijft dit proefschrift het nut van het gebruik van tumormarkers in het diagnostisch traject van een patiënt met alvleesklierkanker. Tevens worden er diverse optische technieken besproken, die in de toekomst een essentiële rol kunnen spelen als diagnostisch en intra-operatief hulpmiddel om patiënten met alvleesklierkanker beter te kunnen behandelen.

List of publications

2023 **van Manen L**, de Muynck LDAN, Baart VM, Bhairosingh S, Debie P, Vahrmeijer AL, Hernot S, Mieog JSD. Near-Infrared Fluorescence Imaging of Pancreatic Cancer Using a Fluorescently Labelled Anti-CEA Nanobody Probe: A Preclinical Study. Biomolecules. 2023; 13(4):618.

2022 **van Manen L**, Schmidt I, Inderson A, Houvast RD, Boonstra JJ, Dijkstra J, van Hooft JE, Nagengast W, Robinson DJ, Vahrmeijer AL, Mieog JSD. Single fiber reflectance spectroscopy for pancreatic cancer detection during endoscopic ultrasound guided fine needle biopsy: a prospective cohort study. Int. J. Med. Sci. 2022; 19(2): 205-212.

2021 Groen JV, **van Manen L**, van Roessel S, van Dam JL, Bonsing BA, Doukas M, van Eijck CHJ, Farina Sarasqueta A, Morreau H, Putter H, Vahrmeijer AL, Verheij J, Besselink MG, Groot Koerkamp B, Mieog JSD. Resection of the Portal-superior Mesenteric Vein in Pancreatic Cancer: Pathological Assessment and Recurrence Patterns. Pancreas. 2021 Sep 1;50(8):1218-1229.

2021 Baart VM, **van Manen L**, Bhairosingh SS, Vuijk FA, Iamele L, de Jonge H, Scotti C, Resnati M, Cordfunke RA, Kuppen PJK, Mazar AP, Burggraaf J, Vahrmeijer AL, Sier CFM. Side-by-Side Comparison of uPAR-Targeting Optical Imaging Antibodies and Antibody Fragments for Fluorescence-Guided Surgery of Solid Tumors. Mol Imaging Biol. 2021 Oct 12.

2021 **van Manen L**, Birkhoff WAJ, Eggermont J, Hoveling RJ, Nicklin P, Burggraaf J, Wilson R, Mieog JSD, Robinson DJ, Vahrmeijer AL, Bradbury MS, Dijkstra J. Detection of cutaneous oxygen saturation using a novel snapshot hyperspectral camera: a feasibility study. Quantitative Imaging in Medicine and Surgery. 2021 Sep;11(9):3966-3977.

2021 Meijer RPJ, **van Manen L**, Hartgrink HH, Burggraaf J, Gioux S, Vahrmeijer AL, Mieog JSD. Quantitative dynamic near-infrared fluorescence imaging using indocyanine green for analysis of bowel perfusion after mesenteric resection. J Biomed Opt. 2021 Jun;26(6):060501.

2021 Ségaud S, **van Manen L**, de Muynck LDAN, Mieog JSD, Vahrmeijer AL, Lecler S, Gioux S. Widefield quantitative fluorescence imaging applied to tumor margin assessment. Proc. SPIE 11625, Molecular-Guided Surgery: Molecules, Devices, and Applications VII, 116250F (2021).

2020 **van Manen L**, Groen JV, Putter H, Pichler M, Vahrmeijer AL, Bonsing BA, Mieog JSD. Stage-specific value of Carbohydrate Antigen 19-9 and Carcinoembryonic Antigen serum levels on survival and recurrence in pancreatic cancer: a single center study and meta-analysis. Cancers (Basel). 2020 Oct 14;12(10).

2020 **van Manen L**, Groen JV, Putter H, Vahrmeijer AL, Swijnenburg RJ, Bonsing BA, Mieog JSD. Elevated CEA and CA19-9 serum levels independently predict advanced pancreatic cancer at diagnosis. Biomarkers. 2020 Mar;25(2):186-193.

2020 Birkhoff WAJ, **van Manen L**, Dijkstra J, de Kam ML, van Meurs JC, Cohen AF. Retinal oximetry and fractal analysis of capillary maps in sickle cell disease patients and matched healthy volunteers. Graefes Arch Clin Exp Ophthalmol. 2020 Jan;258(1):9-15.

2019 **van Manen L**, Tummers QRJG, Inderson A, Bhalla A, Vahrmeijer AL, Bonsing BA, Mieog JSD. Intraoperative detection of the remnant cystic duct during robot-assisted surgery using near-infrared fluorescence imaging: a case report. BMC Surg. 2019 Aug 7;19(1):104.

2019 Hernot S, **van Manen L**, Debie P, Mieog JSD, Vahrmeijer AL. Latest developments in molecular tracers for fluorescence image-guided cancer surgery. Lancet Oncol. 2019 Jul;20(7).

2019 Van den Hoven P, Ooms S, **van Manen L,** van der Bogt KEA, van Schaik J, Hamming JF, Vahrmeijer AL, van der Vorst JR, Mieog JSD. The use of near-infrared fluorescence imaging in patients with peripheral artery disease - A systematic review of the literature. J Vasc Surg. 2019 Jul;70(1).

2019 **van Manen L**, Eggermont J, Fariña-Sarasqueta A, Vahrmeijer AL, Mieog JSD, Dijkstra J. Snapshot hyperspectral imaging for detection of breast tumors in resected specimens. Proc. SPIE 10856, Diseases in the Breast and Reproductive System V, 108560I (2019).

2019 **van Manen L**, Birkhoff W, Eggermont J, Dzyubachyk O, Burggraaf J, Vahrmeijer AL, Mieog JSD, Dijkstra J. Feasibility of a snapshot hyperspectral imaging for detection of local skin oxygenation. Proc. SPIE 10873, Optical Biopsy XVII: Toward Real-Time Spectroscopic Imaging and Diagnosis, 108730Q (2019).

2018 **van Manen L**, Handgraaf HJM, Diana M, Dijkstra J, Ishizawa T, Vahrmeijer AL, Mieog JSD. A practical guide for the use of indocyanine green and methylene blue in fluorescence-guided abdominal surgery. J Surg Oncol. 2018 Aug;118(2):283-300.

2018 **van Manen L,** Dijkstra J, Boccara C, Benoit E, Vahrmeijer AL, Gora MJ, Mieog JSD. The clinical usefulness of optical coherence tomography during cancer interventions. J Cancer Res Clin Oncol. 2018 Oct;144(10):1967-1990.

2018 **van Manen L,** Mieog JSD, Vahrmeijer AL. Optics In Surgery: the surgeon perspective. Proc. SPIE 10677, Unconventional Optical Imaging, 106771J (2018).

2017 **van Manen L**, Stegehuis PL, Fariña-Sarasqueta A, de Haan LM, Eggermont J, Bonsing BA, Morreau H, Lelieveldt BPF, van de Velde CJH, Vahrmeijer AL, Dijkstra J, Mieog JSD. Validation of full-field optical coherence tomography in distinguishing malignant and benign tissue in resected pancreatic cancer specimens. PLoS One. 2017 Apr 17;12(4).

Curriculum Vitae

Labrinus van Manen werd op 15 juli 1994 geboren te Veenendaal. Na het behalen van zijn gymnasiumdiploma in 2012 aan het IchthusCollege te Veenendaal, startte hij met de studie Geneeskunde aan de Universiteit van Leiden. Gedurende zijn bachelor was hij een aantal jaar werkzaam als student-assistent op de anatomie-afdeling van het Leids Universitair Medisch Centrum (LUMC). In de wachttijd van zijn coschappen, begon hij zijn wetenschapsstage bij de Heelkunde onder leiding van Dr. J.S.D. Mieog, wat uiteindelijk leidde tot een eerste publicatie. Hierop begon de interesse voor het doen van wetenschappelijk onderzoek, waardoor zijn coschappen tijdelijk onderbroken werden voor promotieonderzoek. In 2017 startte hij een promotietraject bij de Heelkunde (Prof. dr. J.F. Hamming, Dr. J.S.D. Mieog en Dr. A.L. Vahrmeijer) in samenwerking met de afdeling Radiologie (Dr. ir. J. Dijkstra) met als focus de evaluatie van nieuwe intra-operatieve optische beeldvormende technieken bij pancreascarcinoom, waarvan de resultaten beschreven staan in dit proefschrift. Tijdens zijn promotietraject schreef hij mee aan diverse onderzoeksbeurzen. In 2020 hervatte hij zijn reguliere coschappen en verrichte hij zijn semiartsstage bij de gastro-intestinale en oncologische chirurgie in het LUMC, gevolgd door een keuzecoschap kinderchirurgie in het Sophia kinderziekenhuis te Rotterdam. Na het afronden van zijn geneeskunde studie heeft hij één jaar gewerkt als arts-assistent Heelkunde in het Groene Hart Ziekenhuis, waar hij nu sinds maart 2023 werkzaam is als arts-assistent bij de Keel-, neus- en oorheelkunde. Daarnaast beoefent hij tevens met veel plezier het ambacht van goudsmeden.

Dankwoord

Allereerst wil ik hierbij mijn waardering uitspreken voor de patiënten en vrijwilligers, die ondanks hun soms ernstige aandoeningen, bereid waren om deel te nemen aan de studies. Dit proefschrift is het resultaat van een leerzame periode, wat ik niet had kunnen doen zonder de hulp van velen, waarvan ik een aantal personen hieronder in het bijzonder wil bedanken.

Prof. Hamming, beste Jaap, hartelijk dank dat je mijn promotor wilde zijn. Ondanks je drukke werkzaamheden, reageerde je altijd snel en wist je direct alles te regelen of advies te geven.

Dr. Vahrmeijer, beste Alexander, wat een geweldige onderzoeksgroep heb je opgezet. Ongetwijfeld kan het niet anders zijn dan dat je leiderschap, enthousiasme en het vertrouwen dat je mij gaf en wat je ook je andere PhD studenten geeft, één van de redenen is dat het zo succesvol loopt.

Dr. Mieog, beste Sven, dank voor je begeleiding, de vrijheid en juist daardoor ook het vertrouwen die je me gaf tijdens mijn promotietraject. Daarnaast stond je ook altijd klaar om adviezen te geven, wat ik erg gewaardeerd heb.

Dr. Dijkstra, beste Jouke, naast je begeleiding op met name technisch en optisch vlak, stond de deur altijd open voor een gesprek met een bakje koffie.

Daarnaast wil ik ook de afdelingen Radiologie (in het bijzonder LKEB), Maag-, darm- en leverziekten (MDL), het Heelkunde onderzoekslab en de Pathologie, die nauw betrokken waren bij het onderzoek bedanken. Wat betreft de MDL-afdeling, wil ik in het bijzonder Akin Inderson bedanken voor de goede samenwerking en het motiverende enthousiasme tijdens de spectroscopie studies. Also special thanks to the lab of Professor Sylvain Gioux in Strasbourg. Sylvain and also Silvère, I enjoyed visiting your lab and Strasbourg, except for that Tuesday night…

Het Greenlight team, de trein die maar door blijft gaan. Wat een ongelofelijke prestaties elke keer maar weer, mooi om te zien dat de houdbaarheidsdatum nog lang niet bereikt is. Een speciale dank voor mijn mede pancreas-onderzoekers, Jesse en Lizzie, het was fijn samenwerken met jullie. Mijn kamergenoten op de C7, Annelieke, Floris, Meaghan, Ruben, Sophie en Victor, dank voor de borrels en alle gezelligheid. Zonder jullie was dit promotietraject ongetwijfeld een stuk moeizamer en saaier verlopen. Mijn collega's in het Goudse Groene Hart Ziekenhuis, dank voor alles wat ik heb mogen leren, de collegialiteit en de vriendschappen die er zijn ontstaan.

Ik wil mijn vrienden en familie bedanken voor jullie betrokkenheid en vriendschap. Een aantal personen wil ik in het bijzonder noemen. Frans, Robbin en Taco, ik waardeer onze vriendschap, de gezelligheid en met name jullie luisterend oor al die jaren sinds we elkaar ontmoetten als huisgenoten op KonQ. Speciale dank aan Taco dat je mijn paranimf wilde zijn. Dirk en Adrianus, *'Los Tres Musqueteros'*, wat een mooie reizen en avonturen hebben we beleefd, wat voor een leuke afleiding zorgde tijdens het promotietraject. Dirk, dankjewel dat je mijn paranimf wilde zijn; over een aantal jaar zal jij ongetwijfeld ook de doctorstitel mogen dragen. Marije en Teunis, wat toevallig dat we binnen onze familie tegelijkertijd begonnen zijn met een promotietraject en jullie me lieten zien hoe je succesvol zo'n traject afrondt. Peter, dank voor alle adviezen en hulp toen ik begon met dit promotietraject; hier heb ik veel aan gehad.

Lieve Anne-Marie en Ernst, veel dank voor jullie steun en de gezelligheid binnen onze familie samen met jullie meiden.

Lieve mam en pap, heel veel dank voor alle onvoorwaardelijke steun en vertrouwen die jullie me altijd gegeven hebben.

Lieve Jan-Willem, wat had ik graag gewild dat je als broertje dit promotietraject ook van de zijlijn had kunnen volgen en naast me had mogen staan om dit moment mee te maken. Dit proefschrift wil ik aan je opdragen.